EVALUATION OF DESIGN CRITERIA FOR STORAGE TANKS WITH FRANGIBLE ROOF JOINTS

by

Zhi Lu

B.S., Tianjin University, 1982

M.S., Tianjin University, 1984

A DISSERTATION

submitted in partial fulfillment of the

requirements for the degree

Doctor of Philosophy

Department of Mechanical Engineering

College of Engineering

Kansas State University

Manhattan, Kansas 66506

1994

Approved by:

Major Professor

EVALUATION OF DESIGN CRITERIA FOR STORAGE TANKS WITH FRANGIBLE ROOF JOINTS

Zhi Lu

1994

Abstract

API 650 gives rules for the design of frangible roof joints in fluid storage tanks. In the event of over-pressurization, the frangible roof-to-shell joint is designed to fail before the tank shell or the shell-to-bottom joint. This failure is intended to vent the tank and contain any remaining fluid. However, experience shows that the frangible joint may not always perform as intended. This dissertation describes research to evaluate the API 650 rules.

The API 650 design formulas for frangible roof joints were rederived and the reasoning behind these rules recovered. Scoping calculations were performed using the ANSYS finite element code. A combustion model was developed to predict the pressure rise in a tank due to deflagration of the contents. Weld joint specimens were tested to evaluate sensitivity of the frangible joint to weld dimensions. Small scale model tanks were tested statically to verify the failure mechanism and the effect of different roof slopes. Two large scale model tanks were tested dynamically under deflagration loads to improve understanding of frangible joint behavior, verify analysis and examine alternate designs.

Integrating the knowledge from analysis and testing, API-Tank, a computer program running on a PC in the Microsoft Windows™ environment, was developed. The program can design tanks following API guidelines. A nonlinear finite element analysis can be performed to calculate the deformation and stresses in the tank at critical pressures. The combustion module, including joint failure and venting, can be used to predict the peak pressure in the tank during deflagration. The program has post-processing capability to display the results and make hard copies.

Based on this research, the present API 650 calculation of frangible joint failure predicts too low a pressure and is not conservative. The margin of safety between frangible joint failure and bottom joint failure is larger for larger tanks. If empty during the over-pressurization, uplift of the bottom can be expected in most tanks. An alternate design approach is suggested.

TABLE OF CONTENTS

LISTS OF FIGURES

LISTS OF TABLES

ACKNOWLEDGMENTS

I would like to express my sincere gratitude and appreciation to my advisor, Dr. Daniel Swenson, for his valuable guidance, patience, participate and encouragement throughout the course of my Ph. D. studies.

The appreciation is extended to Dr. Stanley Clark for his kindly serving as outside chair for my final defense, and to Dr. Chi-Lung Huang, Dr. Stuart Swartz, and Dr. Qisu Zou, for their consideration, invaluable guidance and help on the project, and serving on my supervisory committee.

This work was supported by the Pressure Vessel Research Council (PVRC), Subcommittee on Dynamic Analysis and Testing, and the American Petroleum Institute (API). I especially thank Jerry Bitner, Martin Prager, Guido Karcher, and Richard Basile for useful discussions.

I appreciate the support of Texaco, El Dorado Plant, in allowing us to examine actual tanks and in constructing the scale model tanks; the Agriculture Department at Kansas State, in providing the test sites; and the Kinesiology Departments at Kansas State and the University of Kansas who provided and ran the high-speed cameras.

I would like to acknowledge Dr. Kuo Kuang Hu, Dr. Lige Li, Dr. Huanan Yang, Dr. Don Fenton, Joe Baalman, Mark Devries, Asif Ghori, for their invaluable advice and help in the project.

Acknowledgment is also given to faculty members, friends and secretarial staff in the Department of Mechanical Engineering for their friendships and valuable discussion.

I deeply indebted to my parents and parent in-laws for their sacrifices and inspiration.

I want to say thanks to my wife Menglin Ren for her love, patience and support and to my son Zouyan Lu for his childhood evenings and weekend that he sacrificed so his father could accomplish his dream.

1.0 INTRODUCTION

Liquid storage tanks are widely used in the petroleum and chemical industries. These tanks consist of a vertical, cylindrical, above-ground shell, a conical roof and a flat or slightly conical bottom. The roof is typically supported by rafters, which are themselves supported by columns inside the tanks. The roof is not attached to the rafters, but rests on them. The bottom of the tanks typically rests on sand with a hard concrete ringwall at the periphery of the tank. The tanks are manufactured in the field using steel plates that are either overlapped or seam welded. Diameters of the tanks range from 10 feet to over 200 feet. The material used in construction is steel, with yield strengths ranging from 30,000 to 60,000 psi. Figure 1.1 is a photograph of a large tank in a tank field and Figure 1.2 is the overall layout of a 25 feet diameter tank.

Due to filling and emptying of the tanks, the vapor above the liquid surface inside the tank may be within its flammability limits. Overpressurization could occur due to the ignition of this vapor and could exceed the capability of the pressure relief vents specified in storage tank design.

Sudden overpressurization can lead to the catastrophic loss of tank integrity. One undesirable mode of failure is the loss of the shell-to-bottom joint, which results in loss of containment and spillage of the contents. Figure 1.3 is an example of unexpected tank failure (Gugan, 1978). If the shell or bottom fails, the neighboring tanks and structures are in great danger of being ignited or damaged. To reduce this hazard, the frangible roof-to-shell joint is designed to fail before failure occurs in the tank shell or the shell-to-bottom joint. When the frangible joint fails, the roof of the tank becomes free to move, thereby providing a large venting capability to dissipate the pressure.

The design rules for frangible roof joints of fuel storage tanks are described by the American Petroleum Institute in API 650 (API, 1993). That standard has been used or referenced in many countries. A roof-to-shell joint designed according to API 650 rules is considered to be frangible and in case of excessive internal pressure, intended to fail before failure occurs in the tank shell or shell-to-bottom joint. However, practice has confirmed that a roof-to-shell joint so designed may not perform as intended, especially for smaller tanks, as shown in Figure 1.4. A means to prevent such catastrophic failure is needed by tank manufacturers as well as users.

The two main objectives of the research are to evaluate the present design criteria and to establish new design tools to ensure the desired frangible joint behavior. Particular questions to be answered include:

- Evaluation of the area inequality as a method to predict the buckling response of the compression ring.
- Evaluation of the effect of roof slope, tank diameter, and weld size on the frangible joint.
- Evaluation of the relative strength of the roof-to-shell joint compared to the shell-to-bottom joint.
- Characterization of dynamic loading on the tank caused by internal combustion.
- Creating design tables and a PC-based program, with graphical user interface, for designing and evaluating storage tanks.

The project was supported by the Pressure Vessel Research Council (PVRC) and American Petroleum Institute (API). Dr. Daniel Swenson and Dr. Don Fenton are the main Co-Investigators. Dr. Don Fenton directed Joe Baalman (a Master's student) in the original development of the combustion

model. The code was then modified further and completely rewritten in C by the author for use in the structural analysis. The description of the combustion model is similar to that given by Joe Baalman (Baalman, 1992).

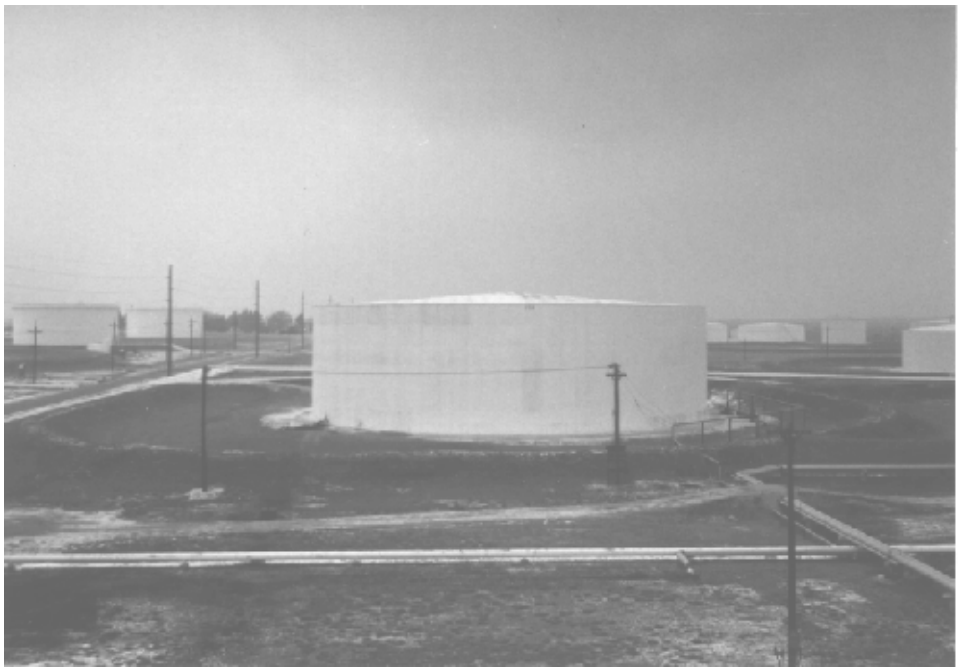

Figure 1.1 Photograph of Typical Tank

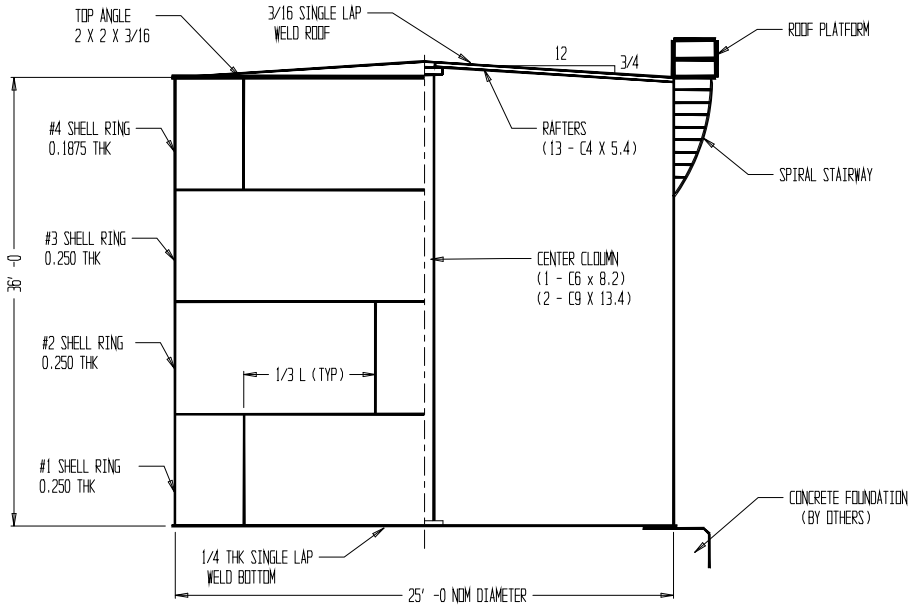

Figure 1.2: Overall Layout of a 25 feet Diameter Tank

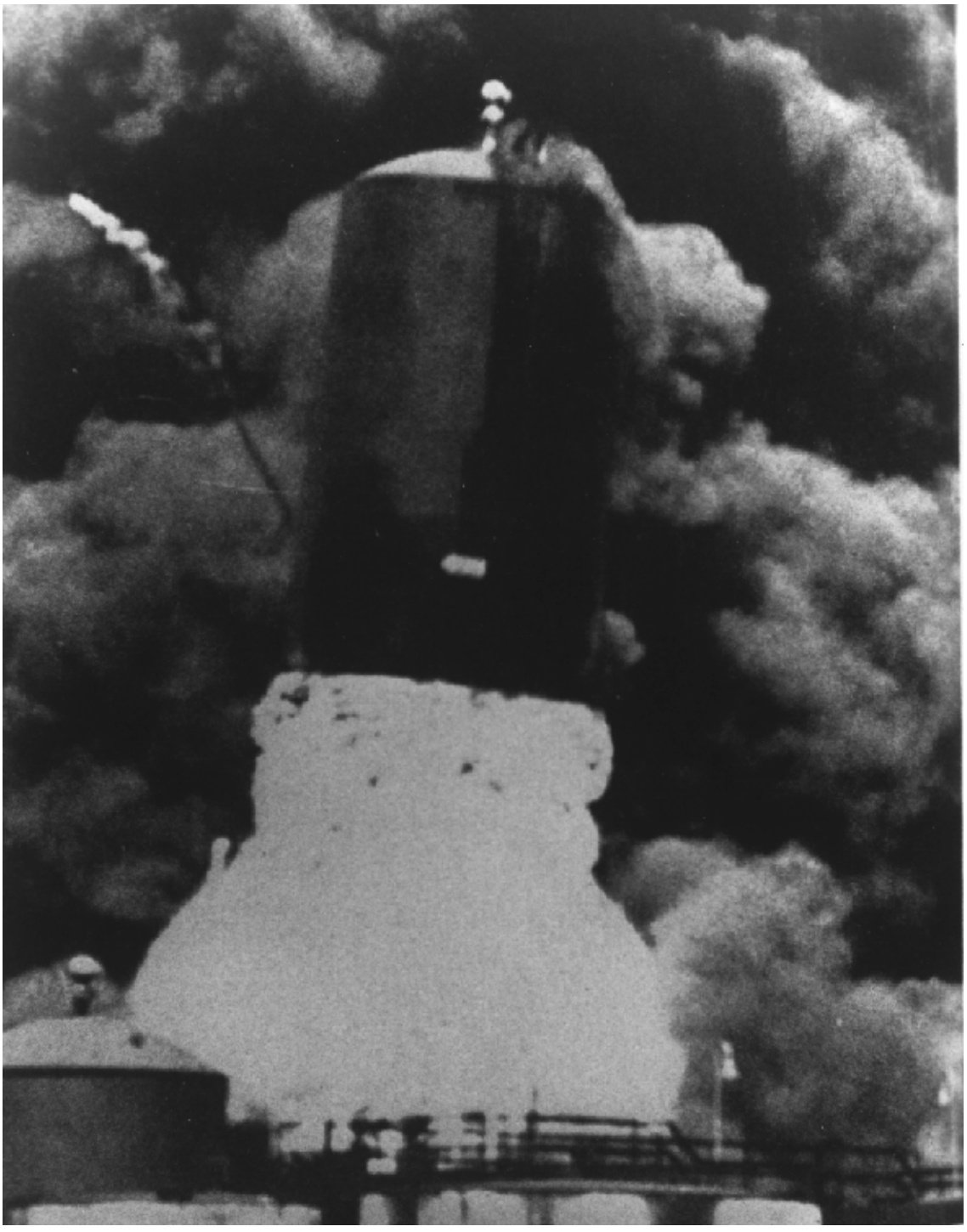

Figure 1.3 An Undesired Tank Failure

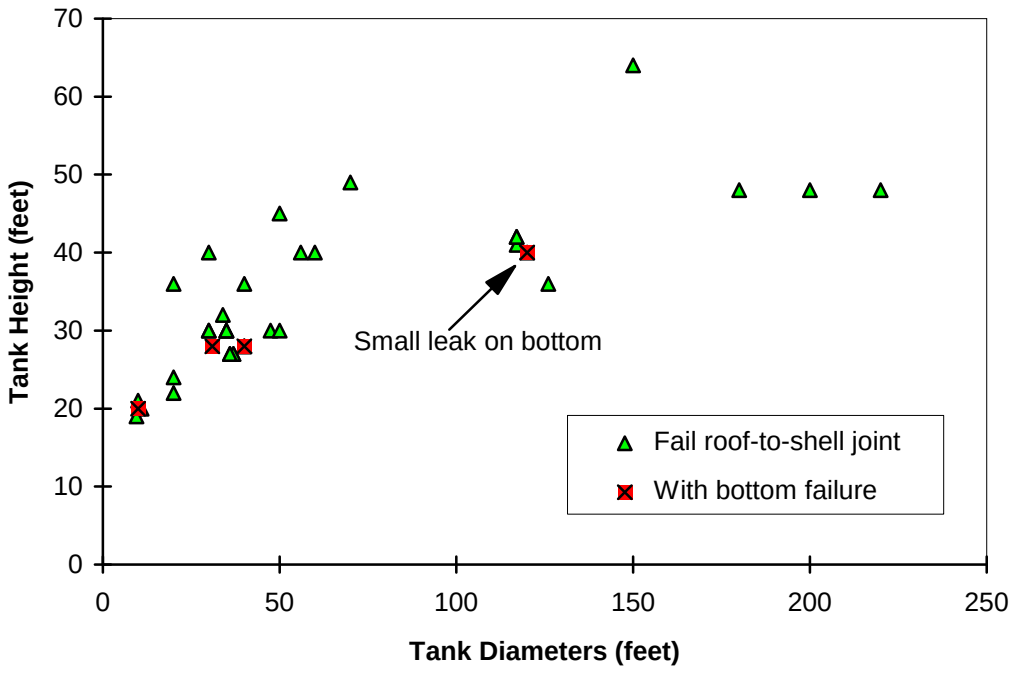

Figure 1.4: Cases of Tank Failure

2.0 LITERATURE REVIEW

The API standard 650: "Welded Steel Tanks for Oil Storage" was first published in 1961. It has been used and referenced by many countries throughout the world. The current issue is the ninth edition, revised in 1993. A counterpart of API 650 is the British Standard BS 2654 (1984). During the years, many cases of tank fires have occurred. In the majority cases, the tanks performed as intended, but there are exceptions. Also, certain tanks that marginally violated API 650 rules did behave as frangible roof joint (Bone, 1993). The question of validity of API 650 rules was first raised by E. Morgenegg (Morgenegg, 1978). API and the Pressure Vessel Research Council sponsored research at Kansas State University to review design procedures.

2.1 Structural Analysis on Components of the Tanks

The storage tanks consist of a cylindrical shell, a conical roof and a flat or slightly conical bottom. The differential equations for small and finite displacements of simple thin shells have been analyzed and developed by many researchers. The conical roof under internal pressure and edge loading can be described by the following differential equation (Timoshenko and Woinowsky-Krieger, 1959):

$$y\frac{d^2(yQ_y)}{dy^2}+\frac{d(yQ_y)}{dy}-Q_y \pm i\lambda y Q_y = 0 \qquad (2.1)$$

Equation 2.1 is valid when the lateral displacement of the shell is much smaller than its thickness and axisymmetric loading. It has a solution in terms of Kelvin's functions. When the displacement is of the same order as the thickness, the stretching of the center surface needs to be considered as well as the bending of the shell. The governing equation becomes a set of partial different equations (Famili, 1965):

$$D\nabla^4 w = \frac{1}{s}(\cot\alpha + w_{,s} + \frac{w_{,ss}}{s\sin^2\alpha})\Phi_{,ss} + \frac{2}{s^2\sin^2\alpha}(\frac{1}{s}w_{,s} - w_{,s\theta})\Phi_{,s\theta} + \frac{1}{s}w_{,ss}\Phi_{,s} + \frac{w_{,ss}\Phi_{,\theta\theta}}{s^2\sin^2\alpha} + \frac{2}{s^2\sin^2\alpha}(w_{,s\theta} - \frac{1}{s}w_{,\theta})\Phi_{,s\theta} + P_z \quad (2.2a)$$

$$\frac{1}{Eh}\nabla^4\Phi = -(\cot\alpha + w_{,s} + \frac{w_{,\theta\theta}}{s_2\sin^2\alpha})\frac{1}{s}w_{,ss} - \frac{1}{s^2\sin^2\alpha}(\frac{2}{s}w_{,\theta} - w_{,s\theta})w_{,s\theta} + \frac{1}{s^2\sin^2\alpha}(\frac{1}{s}w_{,\theta})^2 \quad (2.2b)$$

The corresponding ordinary linear differential equations for the axisymmetric case are:

$$D\nabla^4 w = \frac{1}{s}(\cot\alpha + w_{,s})\frac{d\Phi^2}{ds} + \frac{1}{s}\frac{d\Phi}{ds}w_{,ss} + P_z \quad (2.3a)$$

$$\frac{1}{Eh}\nabla^4\Phi = -\frac{1}{s}(w_{,s} + \cot\alpha)w_{,ss} \quad (2.3b)$$

Equations (2.2) and (2.3) are nonlinear and cannot be solved analytically. They can be solved by applying the variational method, perturbation, or the finite element method (Vol'mir, 1967; Krätzig, 1990).

The problem of a cylindrical shell can be solved by similar differential equations. The most commonly used are Donnell theory and Sanders theory (Yamaki, 1984). Donnell theory is based on the assumptions that the displacements u and v are infinitesimal, while w is of the same order as the shell thickness, and the derivatives of w are small, but their squares and products are of the same order as the strain here considered. The governing equation can be written as:

$$\nabla^4 F + Eh(\frac{1}{r}w_{,xx} - w_{,xy}^2 + w_{,xx}w_{,yy}) = 0 \quad (2.4a)$$

$$D\nabla^4 w - \frac{1}{r}F_{,xx} - F_{,yy}w_{,xx} + 2F_{,xy}w_{,xy} - F_{,xx}w_{,yy} - P = 0 \quad (2.4b)$$

Sanders theory takes the in-plane displacement into consideration and has a set of more complicated governing equations.

The bottom of the tank can be considered a circular plate on an elastic foundation. The linear case can be solved in terms of Kelvin's functions (Timoshenko, and Woinowsky-Keirger, 1959). The nonlinear deformation of a plate is described by Von Karman equations:

$$D\nabla^4 w = h\left(\frac{\partial^2\varphi}{\partial x^2}\frac{\partial^2 w}{\partial y^2} + \frac{\partial^2\varphi}{\partial y^2}\frac{\partial^2 w}{\partial x^2} - 2\frac{\partial^2\varphi}{\partial x\partial y}\frac{\partial^2 w}{\partial x\partial y}\right) + q \tag{2.5a}$$

$$\nabla^4\varphi = E\left[\left(\frac{\partial^2 w}{\partial x\partial y}\right)^2 - \frac{\partial^2 w}{\partial x^2}\frac{\partial^2 w}{\partial y^2}\right] \tag{2.5b}$$

In case of axisymmetry, the equations (2.5) become a set of ordinary differential equations:

$$\frac{1}{r}D\frac{d}{dr}\left\{r\frac{d}{dr}\left[\frac{1}{r}\frac{d}{dr}\left(r\frac{dw}{dr}\right)\right]\right\} - \frac{1}{r}\frac{d}{dr}\left(rN_r\frac{dw}{dr}\right) = q \tag{2.6a}$$

$$r\frac{d}{dr}\left[\frac{1}{r}\frac{d}{dr}\left(r^2 N_r\right)\right] + \frac{Eh}{2}\left(\frac{dw}{dr}\right)^2 = 0 \tag{2.6b}$$

Many stress-strain and stability solutions have been obtained for all three cases, mainly for clamped or simply supported boundaries either moveable or immovable in the in-plane direction, loaded by torsion, external pressure or axial compression (Famili, 1965; Yamaki, 1984; Niordson, 1985; Bert and Martindale, 1988; NASA, 1962). No solution was found in the literature for the case with a large transverse displacement at the boundary.

2.2 Structural Analysis of Whole Tanks

Considering the tank as a whole, only local portions of the shell close to the joints undergo large deflection, with circumferential compression and meridional tension stresses. The combination of a conical roof and a long

cylindrical shell under internal pressure has been solved by C. E. Taylor (1974) for asymmetric small deformation. Both analytical and experimental studies have been made for the response of oil storage tanks to earthquake and ground motion (Liu, and Uras, 1989; Nagashima, 1989; Yoshida and Miyoshi, 1990). The recent paper by Yoshida and Miyoshi (1992) calculated the bifurcation buckling pressure of the top end closure of oil storage tanks under internal pressure by axisymmetric finite element analysis. No literature about the relative strength of the top and bottom joints was found.

2.3 Summary of Frangible Joint Study by British Researchers

A similar review has been performed by British researchers. The Tank Committee of the Engineering Equipment and Materials Users Association (including all major oil, chemical and gas companies in Britain) studied frangible roof joints and prepared a report in January 1990 (The Tank Committee, 1990). Their results are mainly consistent with our initial ones, but the basic quistions for safety design were remain unsolved.

They noted that the sudden high vapor pressure in a tank may be caused by:

- An explosion inside the tank due to misoperation.
- Welding operations on the tank, causing an internal explosion.
- A lightning strike on the tank, causing an internal explosion.
- Discharge of static electricity, causing an internal explosion.
- A fire in an adjacent tank.
- Water entering a tank storing a product with a temperature over 100 °C.
- Pyroghoric iron sulphide deposits inside the tank.
- Carbonaceous deposits (glowing coke deposits) in bitumen tanks.

The report mentioned that bottom-to-shell failures occurred only in a few cases with small tanks having diameters not exceeding 12.5 meter (41 feet). Most failures occurred with dome roof tanks. A number of failures also occurred in tanks with heavy welds at the roof-to-shell connection.

Assuming ideal material properties, critical vapor pressures were calculated. It was shown that pressures up to 1.5 bar (21 psi) might be reached before failure at either the roof-to-shell or bottom-to-shell connections. The details of these analyses are unknown, but this result could be valid for tanks with large slopes.

Both BS 2654 and API 650 specify a maximum strength value for the roof-to-shell connection acting as a compression ring. When this maximum strength is exceeded, the compression ring cannot be considered a frangible roof joint. The British report stated that, for small tanks, the compression ring exceeds this value in almost all cases.

They concluded that the roof slope of 1:5 specified in BS 2654 is a reasonable compromise for the frangible joint and maximum design internal pressure. They also concluded that dome roofs should not be used. Our calculations show that a 1:5 roof slope may greatly increase the failure pressure. A slope of 1:16, which is used in most of the large tanks, gives a much smaller failure pressure.

The British researchers also found that in many cases the seal weld on existing tanks was made as a full fillet weld. They suggested that double fillet welds (not allowed in API 650) shall not be used and a 3 mm (1/8 inch) leg length seal weld should be preferred. However, from the view point of manufacturing, it is difficult to make a small weld joint.

The lap welded bottom plates under the tank were considered a weak spot for the bottom-to-shell connection. It was recommended to use butt-

welded annular plates under the tank shell. It was considered effective to require a minimum plat thickness of 8 mm (5/16 inch) for the bottom annular plates and the lowest shell course. The current API 650 requires 1/4 inch thickness bottom plate (6.4 mm). Our analysis shows that only the outer ring of the bottom plate undergoes large loading and may need to be reinforced.

In the report, concrete foundation ringwalls with anchor bolts are considered only to prevent overturning by wind and not recommended to compensate for the high internal pressure. API 650 requires anchors for some tanks to increase overturning stability and reduce the uplift of the bottom and hence the stresses at the bottom-to-shell joint.

2.4 Combustion Analysis

The available literature provided sufficient information concerning flame temperature (Ferguson, 1986), and burning velocity data (Lind, et al., 1977). There has been research done in the area of unconfined and confined explosions (Lee, 1984; Sherman, 1991). No work was found that considered the effects of different ignition source locations in tanks. The location of the ignition source could be important because it determines when the flame front will come in contact with the surfaces of the tank. Because fuel storage tanks can be of different sizes, with liquid fuel levels varying from full to empty, the location of the ignition source will influence the rate of pressure rises in the tank. The pressure rise and vent area relations for industrial dust explosions (which is a much faster process than the deflagration of oil storage tanks) can be found in book by Bartknecht (1989) and ASTM special technical publication 958 (ASTM, 1987), but no reference for the slow burning in the tank with changing venting area could be found.

3.0 RE-DERIVATION OF API 650 RULES

The design rules given in API 650 cover vertical cylindrical aboveground, welded steel storage tanks for small internal pressures. Several sections of the code address the design of a frangible roof joint for supported cone roofs. Summary descriptions of these sections and formulas are given below. By the time the project started, the original derivations of the design formulas for frangible roof joints were not known by API. It is necessary to understand the intentions of those rules before making any modification.

3.1 Summary descriptions of API 650 rules

The present description is based on wording in the Ninth Edition of API Standard 650, July 1993.

- Section 3.1.5.9.e: For tanks with diameters of 35 feet and smaller, the minimum size for the top angle is 2 by 2 by 3/16 inches; for tanks with diameters of 35 to 60 feet, 2 by 2 by 1/4 inches; for larger tanks 3 by 3 by 3/8 inches.
- Section 3.10.2.2: Roof plates shall have a minimum thickness of 3/16 inch.
- Section 3.10.2.3: Roof plates of supported cone roofs shall not be attached to the supporting members.
- Section 3.10.2.5.1: The continuous fillet weld between the roof plates and the top angle cannot exceed 3/16 inch. The slope of the roof at the top angle attachment not exceed 2 inches in 12 inches. The roof-to-shell compression ring details are limited to those shown in Details a-d of Figure F-1.
- Section 3.10.2.5.3: The cross-sectional area at the roof-to-shell junction shall not exceed:

$$A = \frac{0.153\,W}{30{,}800 \tan\theta} \qquad (3.1.1)$$

Where:

A = Area resisting the compressive force, in square inches,

W = Total weight of the shell and any framing (but not roof plates) supported by the shell and roof, in pounds,

θ = Angle between the roof and a horizontal plane at the roof-to-shell junction, in degrees.

- Section 3.10.2.5: For a frangible joint, the top angle may be smaller than that specified in Section 3.1.5.9.
- Section 3.10.4.1: Roof plates shall be welded on the top side with continuous full-fillet welds on all seams. The size of the roof-to-top angle weld shall be 3/16 inch or smaller if so specified on the purchase order.
- Section 3.10.4.2: The slope of the roof shall be 3/4 inch in 12 inches, or greater if specified by purchaser. (Note: Section 10.2.5 limits maximum slope to 2 inches in 12 inches.)
- Section 3.10.4.5: Rafters shall be spaced so that at the outer edges their center shall be not more than 6.28 feet apart. Spacing on inner rings shall not be less than 5 1/2 feet.
- Appendix F.2.2.1: While the construction of the compression ring conforms to but does not exceed the minimum requirements of Item e of 3.1.5.9, 3.10.2, and 3.10.4, the frangible characteristic of the ring is retained, and additional emergency venting devices are not required. (Note: The Appendix F requirement to conform to 3.1.5.9.e is not consistent with Section 10.3.2.5 which allows compression ring area to be reduced for frangible joints.)

- Appendix F.4.1: Maximum design pressure is given by the following:

$$P = \frac{(30.800)(A)(\tan\theta)}{D^2} + 8t_h \qquad (3.1.2)$$

where

P = internal design pressure, in inches of water,

D = tank diameter, in feet,

t_h = nominal roof thickness, in inches.

- Appendix F.4.2: The maximum design pressure, limited by uplift at the base of the shell, shall not exceed the following (Note the last term is not used in Eighth Edition of API 650 (1988)):

$$P_{max} = \frac{0.245W}{D^2} + 8t_h - \frac{0.735M}{D^3} \qquad (3.1.3)$$

where

M = wind moment, in foot-pounds.

- Appendix F.5.1: Where the maximum design pressure has already been established (not higher than that permitted by F.4.2 or F.4.3), the total required compression area at the roof-to-shell junction may be calculated from the following:

$$A = \frac{D^2(P - 8t_h)}{30{,}800(\tan\theta)} \qquad (3.1.4)$$

- Appendix F.5.6: Failure can be expected to occur when the stress in the compression ring area reaches the yield point, as given by:

$$P_f = 1.6P - 4.8t_h \qquad (3.1.5)$$

where

P_f = calculated failure pressure, in inches of water.

In addition to the rules given above, only certain configurations of joint design are allowed. These are given in Appendix F and are shown in Figure 3.1. As the roof lifts due to internal pressure, it applies an inward radial force on the compression area. The compression area calculations in Figure 3.1 allow the designer to calculate the area available to resist this compressive force.

3.2 Intent of API 650 Rules

In the above section, we listed the rules that govern frangible joint design. In order to understand the rules, it is necessary to understand the intent of the rules. As stated in API 650 Section 3.10.2.5.1, if the frangible joint rules are met "... the roof-to-shell joint may be considered to be frangible and, in case of excessive internal pressure, will fail before failure occurs in the tank shell joints or the shell-to-bottom joint. Failure of the roof-to-shell joint is usually initiated by buckling of the top angle and followed by tearing of the 3/16 inch continuous weld of the periphery of the roof plates."

Although the rules use the term buckling as the initiation of the failure, if we examine the area inequality rule (3.10.2.5.3), we see that this rule was developed based on yielding of the compression ring. Figure 3.2 shows the equilibrium forces (per unit circumference) on the compression ring. The weight of the plates and the pressure acting on this region and bending moment are all neglected here to obtain the API 650 design formulas. The forces consist of a downward force, caused by stresses in the shell and an inward force, caused by stresses in the roof. The roof force can be separated into vertical and radial components.

Using equilibrium in the vertical direction, we obtain:

$$V = F_{shell} = \frac{rP}{2} \tag{3.2.1}$$

$$H = \frac{V}{\tan\theta} = \frac{rP}{2\tan\theta} \tag{3.2.2}$$

where:

V = Vertical component of roof force per unit circumference,

F_{shell} = Force in shell per unit circumference,

H = Horizontal component of roof force per unit circumference,

P = Internal pressure in the tank,

r = radius of the tank,

Looking at the top of the compression ring, we can derive an expression that gives the horizontal force that will cause the compression ring to yield. The equilibrium of the compression force in the ring and the horizontal force, as shown in Figure 3.3, gives:

$$2rH = 2F_{comp} \tag{3.2.3}$$

The force in the compression ring F_{comp} is equal to the compression stress σ_{comp} times the compression area A:

$$F_{comp} = \sigma_{comp} A \tag{3.2.4}$$

Substituting equations (3.2.1) and (3.2.3) into (3.2.4), we obtain:

$$A = \frac{rH}{\sigma_{comp}} = \frac{r^2 H}{2\sigma_{comp}\tan\theta} \tag{3.2.5}$$

We can assume yielding occurs when the bottom is about to uplift, then equation (3.2.5) can be written as:

$$A = \frac{W}{2\pi\sigma_{yield}\tan\theta} \tag{3.2.6}$$

where W is the total weight of the shell.

Equation (3.2.6) is the basis of the area inequality rule. The remaining equations that are given in API 650 for frangible roofs can be derived from this equation.

In order to avoid uplift of the bottom, consider a factor of safety n = 1.6 and neglect wind moment, then the maximum design pressure and the weight of shell are related by (Note: in API 650, the unit of P is inches of water, and the density of the roof plate is about 8 times of that of water):

$$(P - 8\rho_{water} t_h)\frac{\pi D^2}{4} = \frac{W}{n} \tag{3.2.7}$$

Substituting W in equations (3.2.6) into (3.2.7) we have:

$$P = \frac{8A\sigma_{yield} \tan\theta}{nD^2} + 8\rho_{water} t_h \tag{3.2.8}$$

If we assume a compressive yield stress of 32,000 psi (as described in Appendix F, Section F.6), substitute into equation (3.2.8), and convert units of pressure by 1 inch of water = 0.03606 psi, we obtain the exact equation for calculating maximum design pressure given in API 650 F.4.1:

$$P = \frac{30{,}800A \tan\theta}{D^2} + 8 t_h \tag{3.2.9}$$

If design pressure P has already been established, we can invert equation (3.2.9) to obtain the total required area expression as given by API 650 F.5.1:

$$A = \frac{(P - 8 t_h)D^2}{30{,}800 \tan\theta} \tag{3.2.10}$$

Modifying (3.2.9) by equating the maximum uplift force by pressure P_{max} to the weight of the shell gives:

$$0.25\pi D^2 (P_{max} - 8\rho_{water} t_h) = W \tag{3.2.11}$$

Rearranging equation (3.2.11) and converting pressure units to inches of water gives the equation in API F.4.2 less the wind moment term which is new in the API 650 ninth edition:

$$P_{max} = \frac{0.245W}{D^2} + 8t_h \qquad (3.2.12)$$

If the area A satisfies equation (3.2.6), then the uplift pressure P_{max} is also the calculated failure pressure, P_f. From equation (3.2.7), the relation between P_f and the design pressure P is:

$$0.25\pi D^2(P_f - 8\rho_{water}t_h) = W = 0.25\pi D^2 n(P - 8\rho_{water}t_h) \qquad (3.2.13)$$

or, in terms of inches of water:

$$P_f = 1.6P - 4.8t_h \qquad (3.2.14)$$

This is identical to equation API 650 F.6.

The above derivations are based on using static equilibrium and the original geometry to calculate the inward force on the compression ring due to roof lifting. The resulting equations demonstrate that the objective of the inequality rule is to ensure that yielding of the compression ring will occur before uplift of the bottom. Initial yielding and subsequent loss of stiffness are expected to cause buckling of the compression ring, followed by gross deformation of the roof, shell, and associated failure of the roof-to-shell wild. As discussed in Section 5.5, our testing proved this to be the mode in which failure occurred.

The area of the compression ring (which is used to evaluate yielding) is determined using W_c, the maximum width of participating shell, and W_h, the maximum width of the participating roof. To verify the validity of the rules, it is necessary to know the basis for the derivations of W_c and W_h.

As shown below, W_c and W_h can be derived from linear approximations of cylindrical and conical shells loaded by a shearing force at the edge. Internal pressure, bending moments (which are large near the joint), and the effect of large deflection are all neglected in the derivation.

3.3 Derivation of W_c

For a long cylindrical shell submitted to the action of a shearing force Q_o as shown in Figure 3.4, the governing differential equation is:

$$\frac{d^4w}{dx^4} + 4\beta^4 w = \frac{p}{D} \tag{3.3.1}$$

where:

$\beta^4 = \frac{3(1-\nu^2)}{R^2h^2}$,

w = lateral displacement,

R = radius of the shell,

h = thickness of the shell,

p = internal pressure,

D = flexural rigidity.

The general solution can be written as (Timoshenko and Woinowsky-Krieger, 1959):

$$w = e^{-\beta x}(c_3 \cos\beta x + c_4 \sin\beta x) \tag{3.3.2}$$

Using the boundary condition of zero moment at the end of the shell:

$$(M_x)_{x=0} = -D\left(\frac{d^2w}{dx^2}\right)_{x=0} = 0$$

$$\frac{d^2w}{dx^2} = \beta e^{-\beta x}(c_3 \cos\beta x + c_4 \sin\beta x) - 2\beta^2 d^{-\beta x}(-c_3 \sin\beta x + c_4 \cos\beta x)$$
$$+ \beta^2 e^{-\beta x}(-c_3 \cos\beta x - c_4 \sin\beta x)$$

$$(\frac{d^2w}{dx^2})_{x=0} = 0 = -2\beta^2 e^{-\beta x} c_4 = 0 \qquad \Rightarrow c_4 = 0 \tag{3.3.3}$$

We get:

$$w = e^{-\beta x} c_3 \cos\beta x \tag{3.3.4}$$

$$\frac{d^2w}{dx^2} = \beta^2 e^{-\beta x} c_3 \cos\beta x + 2\beta^2 e^{-\beta x} c_3 \sin\beta x - \beta^2 e^{-\beta x} c_3 \cos\beta x$$
$$= 2c_3 \beta^2 e^{-\beta x} \sin\beta x$$

$$\frac{d^3w}{dx^3} = 2c_3 \beta^3 e^{-\beta x}(\cos\beta x - \sin\beta x) \tag{3.3.5}$$

Under the shearing force Q_0 at edge where x = 0:

$$(Q_0)_{x=0} = -Q_0$$
$$= -D(\frac{d^3w}{dx^3})_{x=0}$$
$$= -2D\beta^3 c_3$$

$$c_3 = \frac{Q_0}{2\beta^3 D} \tag{3.3.6}$$

The solution for the given problem is:

$$w = \frac{Q_0}{2\beta^3 D} e^{-\beta x} \cos\beta x \tag{3.3.7}$$

The circumferential force per unit length of meridian (compression) is:

$$N_\theta = -\frac{Ehw}{R}$$
$$= -\frac{EhQ_0}{2R\beta^3 D} e^{-\beta x} \cos\beta x \tag{3.3.8}$$

where E is the Young's modulus and the circumferential stress can be written as:

$$\begin{aligned}\sigma_\theta &= \frac{N_\theta}{h} \\ &= -\frac{EQ_0}{2R\beta^3 D} e^{-\beta x} \cos\beta x\end{aligned} \tag{3.3.9}$$

The maximum value of compression stress is located at the edge of the shell where x = 0, given by:

$$\sigma_{\theta\max} = -\frac{EQ_0}{2R\beta^3 D} \tag{3.3.10}$$

Then:

$$\sigma_\theta = \sigma_{\theta\max} e^{-\beta x} \cos\beta x \tag{3.3.11}$$

The change of normalized force with βx is plotted in Figure 3.5. If one considers the region of W_c to be the region where the circumferential stress is equal or greater than 1/3 of the maximum value, its width would be:

$$e^{-\beta W_c} \cos\beta W_c = \frac{1}{3} \qquad \Rightarrow \beta W_c = 0.76865 \tag{3.3.12}$$

Assume Poisson's ratio ν = 0.3 we finally get:

$$\begin{aligned}W_c &= \frac{0.76865}{\beta} \\ &= \frac{0.76865}{\left[3\left(1-0.3^2\right)\right]^{1/4}} \sqrt{Rh} \\ &= 0.59798\sqrt{Rh} \\ &\cong 0.6\sqrt{Rh}\end{aligned} \tag{3.3.13}$$

This is the formula given by API 650. Thus, the value 0.6 in API 650 arises from considering the shear force acting on a shell and finding the distance for the stress to drop to 1/3 of the maximum value.

3.4 Derivation of W_h

Consider a complete cone shown in Figure 3.6. Define:

$$m^4 = 12(1-\nu^2),$$

$$\lambda^4 = \frac{m^4}{t_h}\tan^2\alpha,$$

$$\xi = 2\lambda\sqrt{y},$$

where the t_h is the thickness of the cone and ν is Poisson's ratio.

The linear governing differential equation for the cone can be written as (Timoshenko and Woinowsky-Krieger, 1959):

$$y\frac{d^2(yQ_y)}{dy^2} + \frac{d(yQ_y)}{dy} - Q_y \pm i\lambda^2 yQ_y = 0 \tag{3.4.1}$$

where the Q_y is the shearing force per unit circumference. The solutions in terms of Kelvin's functions have the form:

$$H = -\frac{\csc\alpha}{y}(c_1 ber_2\xi + c_2 bei_2\xi) \tag{3.4.2}$$

$$M_y = \frac{h}{2m^2 y}\left[c_1\left(bei_2'\xi + 2\nu bei_2\xi\right) - c_2\left(\xi ber_2'\xi + 2\nu ber_2\xi\right)\right] \tag{3.4.3}$$

$$N_\theta = \frac{1}{2}\left(c_1 ber_2'\xi + c_2 bei_2'\xi\right) \tag{3.4.4}$$

where ber_2 and bei_2 are second order Kelvin's functions and prime denotes the derivative with respect to ξ. For a cone acted by unit radial stress resultant only, the boundary conditions are:

$$(H)_{\xi=\xi_0} = -1; \qquad (M_y)_{\xi=\xi_0} = 0 \tag{3.4.5}$$

Substitute (3.4.5) into (3.4.3):

$$c_1 = \frac{\xi_0 \mathrm{ber}_2'\xi_0 + 2\nu \mathrm{ber}_2\xi_0}{\xi_0 \mathrm{bei}_2'\xi_0 + 2\nu \mathrm{bei}_2\xi_0} c_2 \tag{3.4.6}$$

Substitute (3.4.5),(3.4.6) into (3.4.3), the constants can be determined as:

$$c_1 = \frac{y\left(\xi_0 \mathrm{ber}_2'\xi_0 + 2\nu \mathrm{ber}_2\xi_0\right)}{\csc\alpha\left[\left(\xi_0 \mathrm{ber}_2'\xi_0 + 2\nu \mathrm{ber}_2\xi_0\right)\mathrm{ber}_2\xi_0 + \left(\xi_0 \mathrm{bei}_2'\xi_0 + 2\nu \mathrm{bei}_2\xi_0\right)\mathrm{bei}_2\xi_0\right]}$$

$$c_2 = \frac{y\left(\xi_0 \mathrm{bei}_2'\xi_0 + 2\nu \mathrm{bei}_2\xi_0\right)}{\csc\alpha\left[\left(\xi_0 \mathrm{ber}_2'\xi_0 + 2\nu \mathrm{ber}_2\xi_0\right)\mathrm{ber}_2\xi_0 + \left(\xi_0 \mathrm{bei}_2'\xi_0 + 2\nu \mathrm{bei}_2\xi_0\right)\mathrm{bei}_2\xi_0\right]} \tag{3.4.7}$$

Using asymptotic expansion, for a real, positive and large x, the Kelvin's functions of zero order can be written as (Tranter, 1968):

$$\mathrm{ber}(x) = \frac{e^{\alpha_1}}{\sqrt{2\pi x}} \cos\beta_1$$

$$\mathrm{bei}(x) = \frac{e^{\alpha_1}}{\sqrt{2\pi x}} \sin\beta_1 \tag{3.4.8}$$

where

$$\alpha_1 \sim \frac{x}{\sqrt{2}} + \frac{1}{8\sqrt{2}\,x} - \frac{25}{384\sqrt{2}\,x^3} + \cdots,$$

$$\beta_1 \sim \frac{x}{\sqrt{2}} - \frac{\pi}{8} - \frac{1}{8\sqrt{2}\,x} - \frac{1}{16x^2} - \frac{25}{384\sqrt{2}\,x^3} - \cdots.$$

Assume x is large enough and neglecting 0(1/x) and all higher order terms, we get the approximation:

$$\mathrm{ber}(x) \sim \frac{e^{\frac{x}{\sqrt{2}}}}{\sqrt{2\pi x}} \cos\left(\frac{x}{\sqrt{2}} - \frac{\pi}{8}\right)$$

$$\mathrm{bei}(x) \sim \frac{e^{\frac{x}{\sqrt{2}}}}{\sqrt{2\pi x}} \sin\left(\frac{x}{\sqrt{2}} - \frac{\pi}{8}\right)$$

The second and zero order Kelvin's functions have the following relations:

$$\text{ber}_2(x) = -\text{ber}(x) + \frac{2}{x}\text{bei}'(x)$$

$$\text{bei}_2(x) = -\text{bei}(x) + \frac{2}{x}\text{ber}'(x) \tag{3.4.9}$$

Neglecting all the 0(1/x) terms, the second order Kelvin's functions and their derivatives are:

$$\text{ber}_2(x) \approx -\text{ber}(x)$$

$$\approx -\frac{e^{\frac{x}{\sqrt{2}}}}{\sqrt{2\pi x}}\cos\left(\frac{x}{2} - \frac{\pi}{8}\right)$$

$$\text{ber}_2'(x) \approx \frac{e^{\frac{x}{\sqrt{2}}}}{\sqrt{2\pi x}}\left[-\cos\left(\frac{x}{\sqrt{2}} + \frac{\pi}{8}\right) + \frac{1}{2x}\cos\left(\frac{x}{\sqrt{2}} - \frac{\pi}{8}\right)\right] \tag{3.4.10}$$

$$\approx -\frac{e^{\frac{x}{\sqrt{2}}}}{\sqrt{2\pi x}}\cos\left(\frac{x}{\sqrt{2}} + \frac{\pi}{8}\right)$$

$$\text{bei}_2(x) \approx -\text{bei}(x)$$

$$\approx -\frac{e^{\frac{x}{\sqrt{2}}}}{\sqrt{2\pi x}}\sin\left(\frac{x}{2} - \frac{\pi}{8}\right) \tag{3.4.11}$$

$$\text{bei}_2'(x) \approx \frac{e^{\frac{x}{\sqrt{2}}}}{\sqrt{2\pi x}}\left[-\sin\left(\frac{x}{\sqrt{2}} - \frac{\pi}{8}\right) + \frac{1}{2x}\sin\left(\frac{x}{\sqrt{2}} - \frac{\pi}{8}\right)\right] \tag{3.4.12}$$

$$\approx -\frac{e^{\frac{x}{\sqrt{2}}}}{\sqrt{2\pi x}}\sin\left(\frac{x}{\sqrt{2}} + \frac{\pi}{8}\right)$$

Substituting (3.4.9) through (3.4.12) into (3.4.7), the coefficients are:

$$c_1 \approx \frac{y\sqrt{2\pi\xi_0}\, e^{\frac{-\xi_0}{\sqrt{2}}}[\xi_0 \cos(\frac{\xi_0}{\sqrt{2}}+\frac{\pi}{8})+2\nu\cos(\frac{\xi_0}{\sqrt{2}}-\frac{\pi}{8})]}{\csc\alpha[\xi_0\cos(\frac{\pi}{4})+2\nu]}$$

$$c_2 \approx \frac{y\sqrt{2\pi\xi_0}\, e^{\frac{-\xi_0}{\sqrt{2}}}[\xi_0 \sin(\frac{\xi_0}{\sqrt{2}}+\frac{\pi}{8})+2\nu\sin(\frac{\xi_0}{\sqrt{2}}-\frac{\pi}{8})]}{\csc\alpha[\xi_0\cos(\frac{\pi}{4})+2\nu]} \qquad (3.4.13)$$

Substituting c_1 and c_2 into (3.4.4), the circumferential force per unit meridional length is:

$$N_\theta \approx -\frac{\sqrt{\xi\xi_0}}{\csc\alpha(\sqrt{2}\,\xi_0+2\sqrt{2}\,\nu)} e^{\frac{\xi_0-\xi}{\sqrt{2}}}[\xi_0\cos(\frac{\xi_0-\xi}{\sqrt{2}})+2\nu\cos(\frac{\xi_0-\xi}{\sqrt{2}}+\frac{\pi}{4})] \quad (3.4.14)$$

Since in our case $\xi_0 >> \nu$ and $(\xi_0-\xi)/\sqrt{2}$ is small, the ν terms can be neglected with less than 0.5% error. Then equation (3.4.14) becomes:

$$N_\theta \approx -\frac{\sqrt{\xi\xi_0}}{2\csc\alpha} e^{\frac{\xi_0-\xi}{\sqrt{2}}}\cos(\frac{\xi_0-\xi}{\sqrt{2}}) \qquad (3.4.15)$$

At the edge of the shell where $\xi = \xi_0$, there exists the maximum compression:

$$(N_\theta)_{\xi=\xi_0} = -\frac{\xi_0}{\sqrt{2}\csc\alpha} \qquad (3.4.16)$$

The ratio of force at any place to the edge force is:

$$\frac{N_\theta}{(N_\theta)_{\xi=\xi_0}} = \sqrt{\frac{\xi}{\xi_0}}\, e^{\frac{\xi_0-\xi}{\sqrt{2}}}\cos(\frac{\xi_0-\xi}{\sqrt{2}}) \cong e^{\frac{\xi_0-\xi}{\sqrt{2}}}\cos(\frac{\xi_0-\xi}{\sqrt{2}}) \qquad (3.4.17)$$

Notice (3.4.17) is exactly the same curve as given by equation (3.3.11) and shown in Figure 3.5.

If one considers the region where the stress is greater or equal to 1/3 of the edge compression stress as the compression zone, then W_h could be the distance from the edge that will make the above ratio equal 1/3. We have the relation:

$$\frac{\xi_0 - \xi}{\sqrt{2}} = 0.76865$$

$$\begin{aligned}\xi_0 - \xi &= 0.76865\sqrt{2} \\ &= 2\lambda(\sqrt{y_0} - \sqrt{y}) \\ &= 2\lambda\left(\frac{y_0 - y}{\sqrt{y_0} + \sqrt{y}}\right) \\ &\cong \lambda\frac{y_0 - y}{\sqrt{y_0}}\end{aligned} \qquad (3.4.18)$$

The width of participating roof W_h would be:

$$\begin{aligned}W_h &= y_0 - y \\ &= 0.76865\frac{\sqrt{2y_0}}{\lambda} \\ &= 1.087\frac{\sqrt{y_0 t_h \tan\alpha}}{[12(1-\nu^2)]^{1/4}}\end{aligned} \qquad (3.4.19)$$

Take $\nu = 0.3$, then:

$$\begin{aligned}W_h &= 1.087\frac{\sqrt{y_0 t_h \tan\alpha}}{1.8178} \\ &= 0.598\sqrt{\frac{R}{\sin\alpha}\frac{\sin\alpha}{\cos\alpha}t_h} \\ &\cong 0.6\sqrt{R_2 t_h}\end{aligned} \qquad (3.4.20)$$

In API 650 W_h is half the value given by equation 3.4.20, but in BS 2654 W_h is exactly as given above. Since α is close to $\pi/2$, W_h is much larger than W_c. It seems that API 650 uses half of the calculated width based on the stress dropping to 1/3 of the maximum.

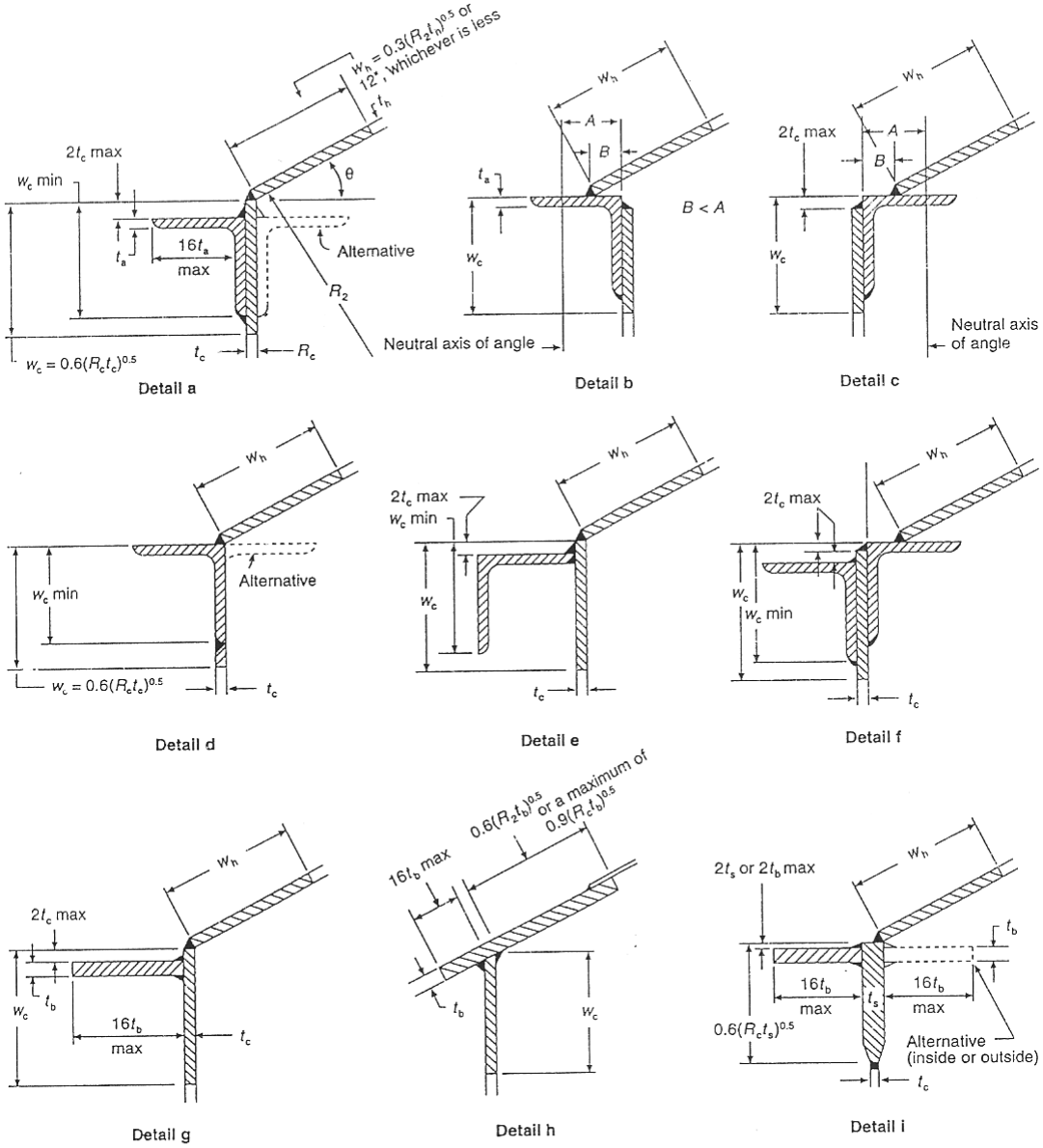

t_a = thickness of angle leg.
t_b = thickness of bar.
t_c = thickness of shell plate.
t_h = thickness of roof plate.
t_s = thickness of thickened plate in shell.
w_c = maximum width of participating shell.
= $0.6\,(R_c t_s)^{0.5}$

w_h = maximum width of participating roof.
= $0.3(R_2 t_h)^{0.5}$ or 12 inches, whichever is less.
R_c = inside radius of tank shell.
R_2 = length of the normal to the roof, measured from the vertical centerline of the tank.
= $R_c/(\sin\theta)$.

Note: All dimensions and thicknesses shown are in inches.

Figure 3.1: Permissible Details of Compression Rings (from API 650)

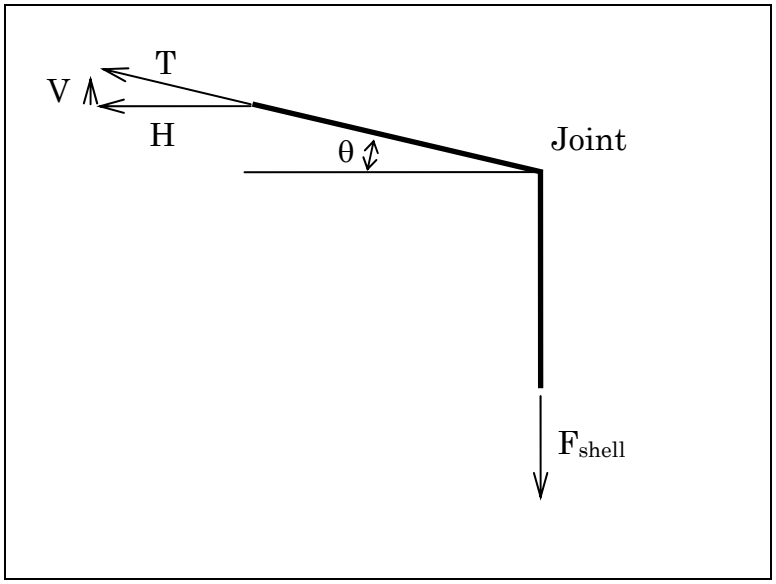

Figure 3.2: Side View of Equilibrium Forces on Compression Ring

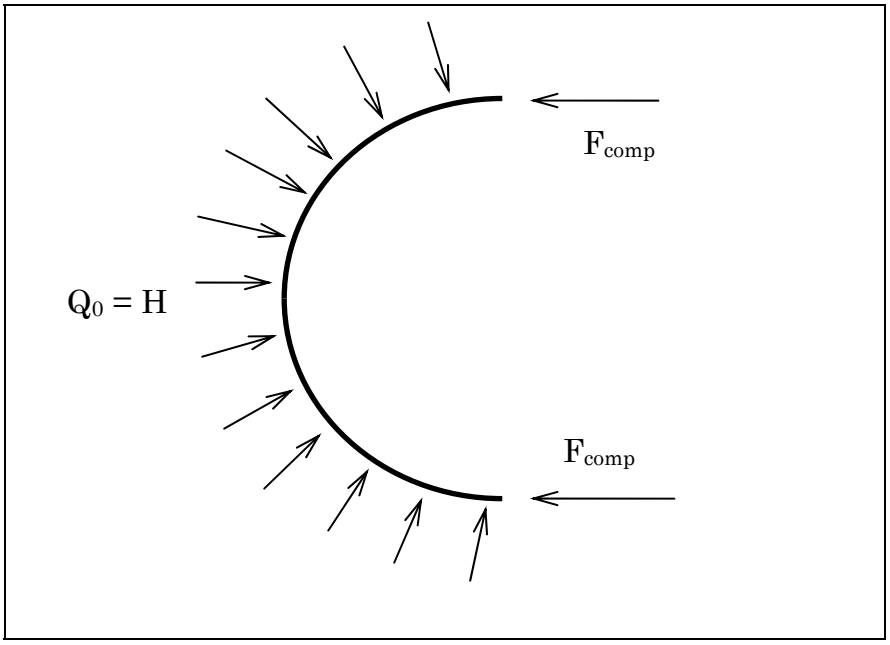

Figure 3.3: Top View of Equilibrium Forces on Compression Ring

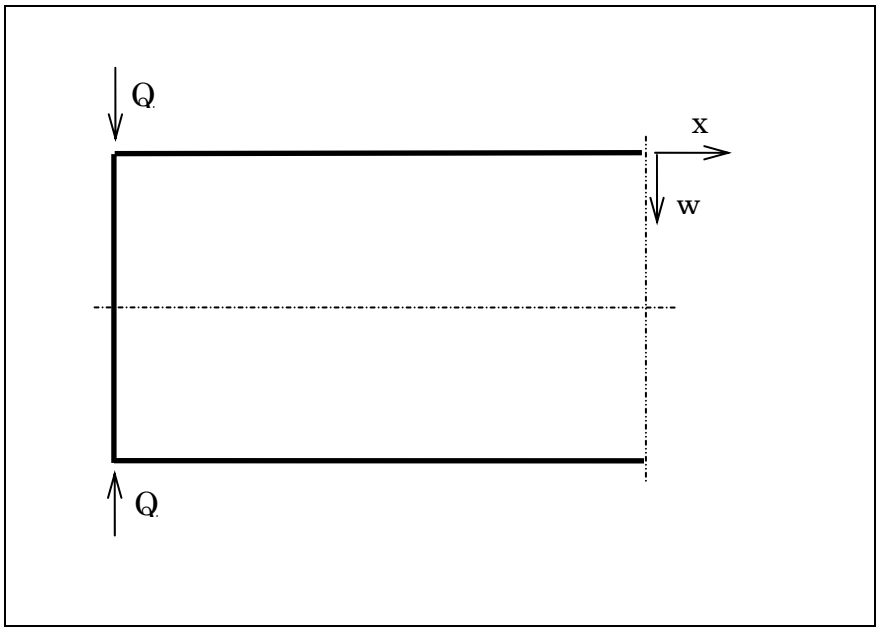

Figure 3.4: A Long Shell with Edge Shear Loading

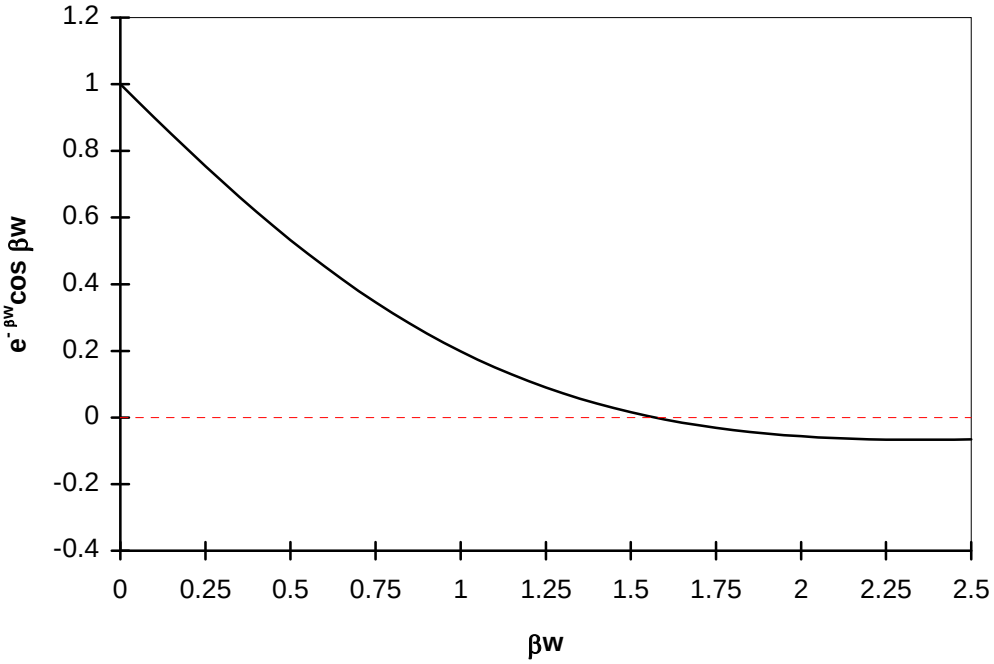

Figure 3.5: Change of Circumferential Force along Meridian

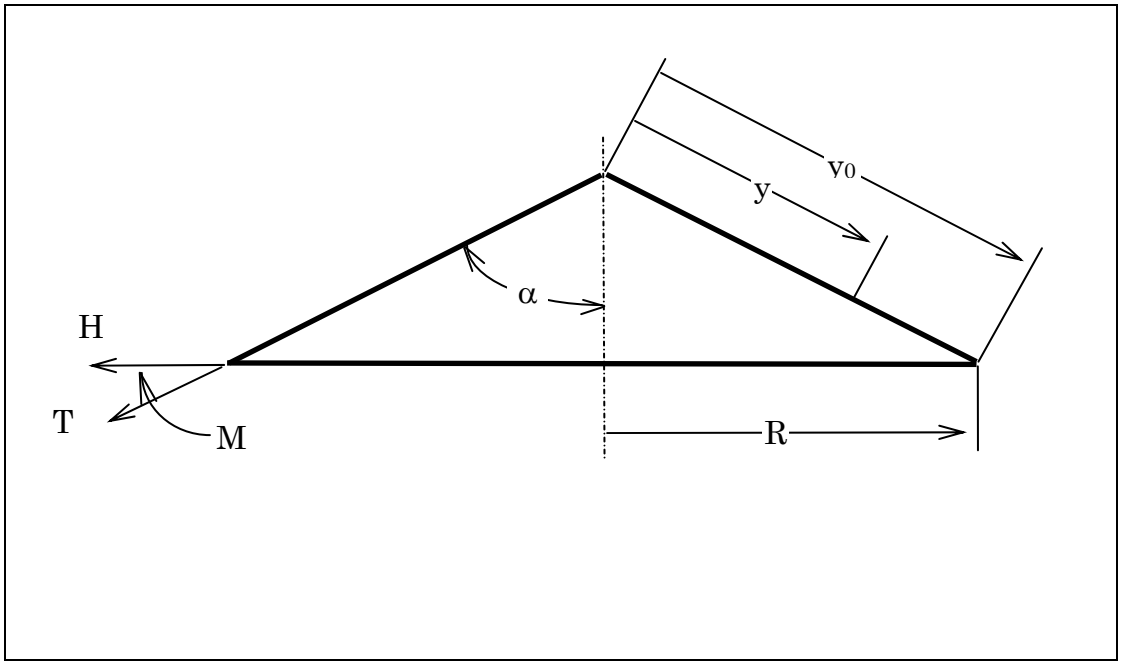

Figure 3.6: A Complete Cone Loaded by Edge Moment and Forces

4.0 PRELIMINARY ANALYSIS AND TESTS

Supported by the Pressure Vessel Research Council (PVRC) Subcommittee on Dynamic Analysis and Testing and the American Petroleum Institute (API), research on evaluation of design criteria for storage tanks with frangible roof joints has been performed since 1991. The following initial analysis and tests were done in order to gain basic understanding of the behavior of the tank (Swenson, et al., 1992, 1993).

4.1 Structural analysis

The objective of the structural analysis is to predict the failure mode and failure pressure of tanks with frangible roof joints. This was done using a combination of axisymmetric and 3-D analysis. The ANSYS finite element code was used for calculation in the preliminary analysis.

4.1.1 Approach

Our fundamental assumption is that failure of the frangible joints will occur as a result of gross deformation at the joint. This deformation could be the result of either elastic buckling, yielding of the compression ring, or a combination of elastic-plastic buckling. Elastic bucking of the relatively thin roof can occur, leading to a stable post-buckling shape before yielding.

Two generic tanks have been chosen for the initial structural analysis: a "small" (25 feet diameter) and "large" tank (140 feet diameter). Details of the tank geometry are given in Table 4.1. Figure 4.1 shows the axisymmetric finite element model using the ANSYS Shell-61, a biaxial shell with both membrane and bending capabilities and linear material properties. The element has four degrees of freedom at each node: translations in the nodal x, y, and z directions and a rotation about the nodal z axis. The loading may be axisymmetric or non-axisymmetric.

Figure 4.2 shows a typical three-dimensional model for linear buckling analysis. This model uses ANSYS Shell-93, an 8-node isoparametric shell with plasticity stress stiffening and large deflection capabilities. The element has six degrees of freedom at each node. The deformation shapes are quadratic in both in-plane directions. The three-dimensional model represents the local structure at the joint, with sufficient size so that boundary effects are not significant. In linear buckling analysis, boundary loads for the three-dimensional model are obtained from axisymmetric calculations. Gravity loads are not included.

4.1.2 Axisymmetric and 3-D Linear Elastic Analysis

A basic calculation is the static linear elastic analysis of the tanks. It provides a basic understanding of the response of the tanks to internal pressure. Figure 4.3 shows the circumferential stress in the 25 feet diameter tank, and Figure 4.4 shows the corresponding results for the 140 feet diameter tank. It is noticed that the combination of roof lifting and constraint at the top angle result in compressive stresses in the roof-to-shell joint. The compression zone in the shell is smaller than that of the roof. An important feature is that, as the roof slope increases, the peak compressive stress becomes smaller and more local to the joint.

The axisymmetric results were used to verify the three-dimensional model, which was used in the buckling analysis. The axisymmetric and three-dimensional results were essentially identical. Also, these results are very close to those obtained by using the closed form solution of a cylindrical shell with a conical top under uniform internal pressure, as shown in Figure 4.3.

For comparison with the compressive area calculation in API 650, Figures 4.5 and 4.6 show the compression stresses in the roof of the small tank for different roof slopes and different diameters, respectively.

Superimposed are the calculations of W_h and W_c as specified in API 650 Appendix F. The calculated values are bounded inside the compression region and are an approximation of the region with the highest compressive stresses. The effective compressive areas calculated using W_h and W_c are smaller than would be obtained using the averaged analytic stress. This makes the determination of maximum design pressure a bit conservative; on the other hand, the calculated failure pressure, based on W_h and W_c may be lower than true failure pressure. This is not conservative, since this could lead one to predict a frangible joint failure when it would not actually occur.

4.1.3 Axisymmetric Modal Analysis

To determine the natural frequencies of the tanks, modal analyses of the tanks were performed using the axisymmetric model. These results were used to determine if dynamic calculations are required to capture the tank response to combustion. Figure 4.7 shows the first two modes for the small tank with an internal pressure of 0.1 psi and a roof slope of 3/4 inch in 12 inches. The remainder of the results are summarized in Table 4.2. It shows that the higher the internal pressure, the higher the natural frequencies will be.

Based on these results, it is likely that static analyses will be sufficient. The frequencies of pressure rise in the tanks are much slower than the natural frequency of the tanks (see 4.2: Combustion Analysis). As a result, dynamic effects should not significant for the tanks before failure initiation occurs at the roof-to-shell joint.

4.1.4 Elastic Buckling Analysis

Using the verified three-dimensional model of the joint, buckling calculations were performed to determine the buckling mode and the critical load. Because the shell was expected to buckle in a high mode (many waves), it was not necessary to model the entire shell. Instead, for the small tank, a

60 degree section was modeled, with a length from the joint of 33 inches along the shell and a length of 51 inches along the roof. The boundary conditions on the 3-D model were based on the nodal forces calculated by 2-D analysis. Very close stress results were obtained from the two kinds of models. The buckling calculations were performed using an elastic analysis.

Figures 4.8.a through 4.8.b show the lowest two buckling modes for the roof. As can be seen, the lowest critical load is not associated with the lowest mode. The lowest critical internal pressure is 0.42 psi with a mode of 21. The results show that a 60 degree section is more than sufficient to capture the buckling behavior. The buckling occurs locally at the roof joint where the circumferential stresses are compressive. Most of the buckling deformation occurs in the roof, with only minor participation of the shell.

One goal of this research is to determine the sensitivity of the failure mode to roof slope. Figures 4.9 and 4.10 show the buckling calculations for roof slopes of 2 inches in 12 inches and 4 inches in 12 inches. As the roof slope increases, the critical mode becomes higher and the deformation becomes more localized around the joint. This is because, as noted in the static analysis, the compressive region becomes smaller as the roof slope becomes larger. Of more significance, the critical internal pressure increases to 1.5 psi for the 2 inches in 12 inches slope and to 6 psi for a slope of 4 inches in 12 inches.

Figure 4.11 summarizes the results of the buckling calculations for the small tank. As the roof slope increases, both the critical load and the mode increase significantly.

A similar buckling calculation was performed of the 140 feet diameter tank with a roof slope of 3/4 inch in 12 inches. The buckling mode is displayed in Figure 4.12 (Note that the large model covers a 30 degree

section). The critical load for this mode is 0.004 psi, much lower than for the small tank. The mode number is 42. Recall, that gravity loads are not included in the analysis, so that buckling would not actually occur until the roof lifted from the rafters, but, in any case, the buckling load is very small.

Based on results provided by Marvin Ringer of Mansanto (1991), this low load is realistic for large tanks. In addition, based on examination of large tanks, where one could feel the deflection and bending as one walked on the roof, a low buckling load is possible.

The calculated buckling and compression ring yielding loads (based on equivalent stress on middle surface) are plotted in Figure 4.13. Using this graph, one can predict the failure mode and the load at which failure is expected to occur for the 25 feet diameter tank with different roof slopes. Elastic buckling does not imply failure in our case, since the stresses will redistribute and the structure will remain stable. Elastic buckling of roof plates means that the roof no longer sustains compressive circumferential stress. However, the radial tensile stress is still applied to the compression ring. This radial load will eventually cause yielding of the compression ring. As can be seen, for the smaller roof slopes, the buckling may occur before yielding of the ring. However, for roofs with larger slopes, failure will occur by yielding of the compression ring without elastic buckling. In addition, this failure will occur at a higher pressure than that for roofs with smaller slopes.

As part of the design of the small scale model tests and to verify the analysis capability, 3-D shell analyses were performed of two small scale models, one with a flat roof and one with a conical roof. For these analyses, large deformation calculations were performed with buckling analysis at different loads. A bilinear stress-strain curve was used with a yield strength of 36 ksi and a plastic modulus of 300 ksi.

The results predicted that for the flat roof model, elastic buckling should occur at 0.85 psi with about 16 waves, as shown in Figure 4.14, with yielding of the compression ring at 1.5 psi. For the model with a roof slope of 4 inches in 12 inches, buckling was predicted at 7 psi, with a much higher node, and yielding of the middle surface at 4 psi. The main conclusion from these calculations is that the flat roof model tank was expected to elasticity buckle and then yield at a higher pressure. In contrast, the model with 4 inches in 12 inches roof slope was expected to yield before buckling occurred. In addition, the compression ring yield pressure was expected to be significantly higher for the model with sloped roof. The tests performed later confirmed our prediction.

4.2 Combustion model development

The initial work on developing the combustion model were done by Dr. Don Fenton and Joe Baalman (Swenson, et al., 1993). The author made modifications to the formulations of combustion wave geometry, burning velocity, and venting. The author also modified the computer program and recalculated all the examples in pressure sensitivity study. The following description is based on that given by Baalman (1992).

4.2.1 Analysis Approach

To evaluate the tank response after the enclosed combustible vapor ignites, a characterization of the pressure time history inside the tank is required. The calculations for the pressure rise inside the tank are done numerically. Analytical solutions are not possible because of the chemical equilibrium and variable ignition source location assumptions.

Deflagration and detonation are the two extreme combustion processes. A deflagration is characterized by relatively low burning velocities and small pressure rises across the combustion wave. In contrast, detonations are identified by supersonic burning velocities and large pressure

increases across the combustion wave. Detonation requires two orders higher ignition energy as required to start a deflagration. Because fuel storage tanks consist of steel shells and are electrically grounded, the possibility of a lightning strike initiating a detonation is considered remote. This analysis assumes that the combustion wave will burn as a radial deflagration, having a smooth spherical shaped flame front from a point source ignition.

The calculation of the adiabatic constant volume flame temperature is essential to calculating the pressure time history inside a fuel storage tank. The approach taken uses chemical equilibrium given by Ferguson (1986).

The calculation assumes the flame front maintains a spherical shape throughout combustion with a point source ignition located in the vapor space, most likely along the side or top surface of the tank. If the flame is in contact with the tank or the liquid, the fireball will be constrained by the tank or liquid in the tank. Numerical integration is necessary to calculate the volume of the fireball with sufficient accuracy. The calculation of the fireball volume is given in Appendix A. The surface area of the fireball is obtained by taking numerical derivative of the volume with respect to the radius of the fireball

To determine the pressure-time history inside a storage tank during combustion the tank is assumed to be adiabatic and the structure of the tank rigid. The analysis also assumes no net effect due to radiation heat transfer between the flame front and wall of the tank. The combustion process is continuous, but to calculate the pressure rise numerically, the pressure is calculated at small increments of time. The volume swept out by the flame front is the outer shell of a sphere or partial sphere. The thickness of the shell equals the burning velocity multiplied by a time increment. For the calculation procedure there exist three volumes during combustion: products, which are enclosed by the inner surface of the flame front; the volume swept

out by the flame front, which are the reactants burned during a small increment of time; and the reactants, which is the volume of fuel vapor outside the flame front.

To calculate a pressure rise during a time increment, an adiabatic flame temperature is calculated for the flame front, assuming constant volume combustion using chemical equilibrium. The pressure inside the volume swept out by the flame front, during a single time increment, is increased due to the burning of the reactants at constant volume. The volume swept by the flame front is then allowed to expand causing the reactants and products to compress, with no mixing, until the pressure inside the tank is uniform. After the pressure in the tank is balanced, the time is incremented and the process repeats itself until all the reactants are burned.

4.2.2 Flame Temperature Calculation

To determine the adiabatic flame temperature, the vapor is allowed to react with air consisting of 21% oxygen and 79% nitrogen by volume. The following chemical reaction equation describes the fuel, air, and their products (Ferguson, 1986).

$$\varepsilon = \frac{0.210}{\alpha + 0.25\beta - 0.5\gamma} \tag{4.2.1}$$

$$\varepsilon\lambda C_\alpha H_\beta O_\gamma N_\delta + 0.21O_2 + 0.79N_2 \rightarrow \nu_1 CO_2 + \nu_2 H_2O + \nu_3 N_2 + \nu_4 O_2 + \nu_5 CO + \nu_6 H_2 + \nu_8 O + \nu_9 OH + \nu_{10} NO \tag{4.2.2}$$

where

ε = molar fuel-air ratio,

λ = fuel-air ratio: actual fuel-air ratio divided by the stoichiometric fuel-air ratio,

α = number of Carbon atoms,

β = number of Hydrogen atoms,

γ = number of Oxygen atoms,

δ = number of Nitrogen atoms,

ν = mole numbers of each respective product.

The fuel-air ratio λ is assumed to be well mixed and can be arbitrarily chosen, or calculated directly from known properties of the fuel and the conditions at which the fuel exists:

$$F = \frac{m_f}{m_a} = \frac{M_a (P_t - P_f)^2}{M_f P_f^2} \tag{4.2.3}$$

$$F_s = \frac{\varepsilon(12.01\alpha + 1.008\beta + 16.00\gamma + 14.01\delta)}{28.85} \tag{4.2.4}$$

$$\lambda = \frac{F}{F_s} \tag{4.2.5}$$

where

F = actual fuel-air ratio by mass,

F_s = stoichiometric fuel-air ratio by mass,

m_f = mass of the fuel vapor (kg),

m_a = mass of the air (kg),

M_f = molecular weight of the fuel (kg/kmol),

M_a = molecular weight of the air (kg/kmol),

P_t = total pressure of the fuel-air mixture (Pa),

P_f = vapor pressure of the fuel (Pa).

Following the procedure described by Ferguson (1986) for equilibrium combustion, the mole numbers for the products of equation (4.2.2) are

calculated using data from Gordon and McBride (1971) to calculate the enthalpy, specific heat at constant pressure, specific volume, and the internal energy of the reactants and products. Two derivatives are calculated numerically,

$$\left(\frac{\partial \ln v}{\partial \ln T}\right)_P \quad \text{and} \quad \left(\frac{\partial \ln v}{\partial \ln P}\right)_T$$

These are used to determine the constant volume adiabatic flame temperature employing the Newton-Raphson iteration in the following procedure:

1. Guess an initial flame temperature and pressure.
2. Calculate the change in internal energy from reactants to products.
3. Calculate the change in specific volume from reactants to products.
4. Solve the following equations to obtain the new guess for the flame temperature and pressure.

Equations (4.2.6) through (4.2.10) are solved during the Newton-Raphson iteration to yield the adiabatic constant volume flame temperature. Define:

$$DET = \frac{v^2}{2}\left[-\frac{\partial \ln v}{\partial \ln P}\left(\frac{10 C_p T}{Pv}+\frac{\partial \ln v}{\partial \ln T}\right)+\frac{\partial \ln v}{\partial \ln T}\left(\frac{\partial \ln v}{\partial \ln T}+\frac{\partial \ln v}{\partial \ln P}\right)\right] \tag{4.2.6}$$

then:

$$\Delta T = \frac{-v}{DET}\left[\frac{10\Delta U}{P}\frac{\partial \ln v}{\partial \ln P}+\Delta v\left(\frac{\partial \ln v}{\partial \ln T}+\frac{\partial \ln v}{\partial \ln P}\right)\right] \tag{4.2.7}$$

$$\Delta P = \frac{-vP}{T\cdot DET}\left[\left(\frac{10 C_p T}{Pv}-\frac{\partial \ln v}{\partial \ln T}\right)\Delta v-\frac{10\Delta U}{P}\frac{\partial \ln v}{\partial \ln T}\right] \tag{4.2.8}$$

$$T_{new} = T - \Delta T \tag{4.2.9}$$

$$P_{new} = P - \Delta P \qquad (4.2.10)$$

where

v = specific volume (cm^3/g),

P = pressure (bars),

T = flame temperature (K),

ΔU = internal energy of the reactants minus that of the products (J/g),

Δv = specific volume of the reactants minus that of the products (cm^3/g),

C_p = specific heat capacity at constant pressure (J/gK).

4.2.3 Burning Velocity

Confusion can arise due to the difference between the apparent flame speed and the burning velocity. The apparent flame speed is the flame speed actually measured by an observer during an experiment. The apparent flame speed includes expansion of the combustion products. As result the apparent flame speed is larger than the burning velocity which describes the amount of reactants that experience combustion during a time increment. The following equations fit experimental observations, and thus are apparent flame speeds. During the calculation, the burning velocity was calculated using the apparent flame speed and the expansion ratio.

The laminar burning velocity, S_o, for a hydrocarbon fuel vapor mixed uniformly in air is readily available (Gordon and McBride, 1971; Barnett and Hibbard, 1957; Kuo, 1986). Significant variations of S_o occur with alkynes (C_NH_{2N-2}) and alkenes (C_NH_{2N}) as a function of the number of carbon atoms in the fuel molecule. However, alkanes exhibit very little change in S_o with the carbon atom number. Information regarding S_o for a particular fuel is readily available, and consequently, the numerical value of S_o is considered to incorporate the effect of fuel type.

Physical conditions influencing the burning velocity include: equivalence ratio, pressure, temperature, and turbulence level. These are incorporated in a mathematical function yielding the burning velocity in a hydrocarbon vapor-air mixture. The mixture is assumed premixed and of uniform concentration throughout the vapor space above the liquid surface in the tank. Each of the above four physical characteristics are now considered regarding the effect on burning velocity.

Equivalence ratio, Φ, defined as the actual mass air-fuel ratio divided by the stoichiometric air-fuel ratio, represents the relative concentration of the hydrocarbon fuel in the air. For all the hydrocarbon fuels, stoichiometric conditions where $\Phi = 1$ yield maximum linear burning velocity. The following equation is used to represent the change in laminar burning velocity with Φ for hydrocarbon fuels (Lee, 1984):

$$\frac{S_o}{S_o\big|_{\Phi=1}} = -2.614 + 7.228\Phi - 3.614\Phi^2 \qquad (4.2.11)$$

The effect of pressure on the laminar burning velocity when $S_o < 0.5$ m/s is such that S_o decreases with increasing pressure. When $0.5 < S_o < 1.0$ m/s, S_o is independent of pressure, and when $S_o > 1.0$ m/s, then S_o increases with increasing pressure. For the hydrocarbons: 100 Octane gasoline, and JP4, the respective laminar burning velocities in air at standard conditions are: 0.37, 0.36, and 0.38 m/s (Lee, 1984). Thus, a reasonable assumption is that increasing pressure reduces the burning velocity for hydrocarbon fuels. Both Kanury (1975) and Kuo (1986) report experimental results identifying the influence of pressure on burning velocity as

$$S_0 \propto \left(\frac{P_u}{P_0}\right)^n \qquad (4.2.12)$$

where a burning velocity of 0.4 m/s suggests that $n = -0.04$.

The influence of temperature actually involves two temperatures: reactants temperature and the flame temperature. Regarding the reactants temperature, the burning velocity is given by the following relationship:

$$S = S_o \left(\frac{P_u}{P_o} \right)^{-0.04} \left(\frac{T_u}{T_o} \right)^2 \tag{4.2.13}$$

where:

S = burning velocity (m/s),

P_u = reactant pressure (Pa),

P_o = initial Pressure (Pa),

T_u = reactant temperature (K),

T_o = initial temperature (K).

In our case, when pressure rises from zero to 20 psi, the pressure term in (4.2.13) reduces only 4%. Compared to the effects of flame temperature and turbulence, the pressure change can be neglected without significant change in the results.

Using the approach taken by Lee (1984), equation (4.2.13) is modified to accommodate the level of turbulence that may exist in the mixture,

$$S = a S_o \left(\frac{T_u}{T_o} \right)^2 \tag{4.2.14}$$

where a is the turbulence factor that ranges from 1 to 15. The laminar case is obtained when a equals 1. A large-scale balloon test at the China Lake Naval Weapons Center (Lind and Whitson, 1977) yielded an apparent horizontal flame speed of 3.9 to 23.7 m/s for different fuels, corresponding to a burning velocity of 0.46 to 2.65 m/s. For the vapor space above the liquid surface inside a storage tank, the hydrocarbon-air mixture is assumed to be quiescent, suggesting low values for a. The obstructions inside a storage tank

are considered as minimal and therefore assumed insignificant relative to the burning velocity variation.

The burning velocity starts at the laminar speed and increases with the generation of turbulence in the reactants. The turbulent factor varies throughout combustion and can be calculated as a function of time by the following equation (Abdel-Gayed, et al., 1987):

$$a = \frac{U_t}{S_0}\left[1 - e^{-0.2\left(\frac{T_k}{\tau_a}\right)^{0.75}}\right]^{0.5} \qquad (4.2.15)$$

where:

a = turbulent burning factor, ranges from 1 to 15,

U_t = fully developed turbulent burning velocity (m/s),

T_k = elapsed time from ignition (s),

τ_a = integral time scale (s).

Equation (4.2.15) is a best fit curve through test data for propagation of burning velocity due to turbulence from a point source ignition. The combustion calculation procedure used here determines the flame speed (as observed relative to the structure) for each increment of reactant mass burned. Consequently, the burning velocity, flame temperature, and volume increase associated with the combustion products are included in the flame speed calculation. The result is the pressure-time variation in the vapor space above the liquid surface inside the storage tank. Combining equations (4.2.11), (4.2.13), and (4.2.15) yields

$$S = U_t\left[1 - e^{-0.2\left(\frac{T_k}{\tau_a}\right)^{0.75}}\right]^{0.5}\left(\frac{T_u}{T_o}\right)^2(-2.614 + 7.288\,\Phi - 3.614\,\Phi^2) \qquad (4.2.16)$$

The above expression for the burning velocity allows for variation of the fuel type, equivalence ratio, temperature, and changes in turbulence levels of the reactants.

4.2.4 Convergence of Combustion

The adiabatic flame temperature can be evaluated by one of two types of combustion processes, constant pressure or constant volume. Both of the calculation procedures provide the same pressure time history curves when complete combustion is assumed.

The combustion process inside a fuel storage tank is simulated by evaluating the pressure at small increments in time. This is done by multiplying the burning velocity by the time increment to obtain the thickness of the layer of reactants to be burned in that time step. The flame will raise the temperature and expand the gases within the flame envelope. This expansion causes the flame to have a higher velocity than it would have if no expansion occurred. Thus, the apparent flame speed is made up of an expansion component and the basic burning velocity. The basic burning velocity may be calculated by multiplying the apparent flame speed by the density ratio across the flame (Lind, and Whitson, 1977).

The combustion process is actually a continuous process, but the calculation procedure evaluates the pressure at small increments in time. Figure 4.15 shows the convergence of pressure curves for different time increments. These curves show the solution converging at a time increment of 0.01 seconds which is the maximum value used in the calculation procedure.

4.2.5 Venting

Most tanks are equipped with small pipes, approximately 6 inches in diameter and bent in a "U" shape, to allow venting during loading or unloading of the tank. As the pressure in the tank is beyond the setting

value of the vent, some of the over-pressure is relieved through these "U" shaped venting pipes. Venting is also important during the failure process of the frangible joint, since a large opening will be formed to vent the over-pressure in the tank. A venting model is included in the combustion analysis.

A venting mass flow rate is calculated based on the pressure, temperature, and density of the vapor inside the tank, as well as the atmospheric pressure and temperature. The total mass that has left the tank during an individual time step is used to determine the pressure drop due to venting for that given time step. The mass flow rate is calculated assuming constant pressure and temperature inside the tank for the time increment. The pressure and temperature are then recalculated based on the amount of mass that is left inside the tank.

For venting during frangible joint failure, a simplified analysis assuming adiabatic incompressible open-channel flow through a sluice gate is made (Fox and McDonald, 1985). For a given value of the joint opening area, the volume flow rate though the opening can be written as:

$$Q = C_D A \sqrt{\frac{2\Delta P}{\rho}} \tag{4.2.17}$$

where

ρ = density of the mixture (kg/m$^{3)}$,

ΔP = pressure deference (Pa),

A = opening area on the roof to shell joint (m^2),

C_D = coefficient of contraction, commonly between 0.6 to 0.9.

Since the time increment is small, the change in pressure due to venting over the time increment is sufficiently low for the temperature to be assumed to remain constant for venting during each time increment. After

the mass flow rate is calculated for each small time step, a new pressure is found based on the amount of mass that has left the tank during that small time increment by the use of the ideal gas law.

4.2.6 Pressure Sensitivity Study

Predictions of the pressure rise inside tanks of different sizes containing different fuels were made. The location of the ignition source and the air-to-fuel ratio (by mass) were also varied. These calculations show the sensitivity of pressure rise to the different parameters inside the tank.

4.2.6.1 Effects of Ignition Source Location

The ignition source location can be anywhere in the tank, but the most likely positions are along the inside surface of the roof or shell above the stored liquid. The amount of reactants burned in an instant of time is determined by the surface area of the flame front. The location of the ignition source determines when the flame front will intersect the tank's internal surface. When the flame front is intersected by the tank's internal surface, the surface area of the flame front is reduced, by an amount proportional to the surface area of the object of intersection.

As the ignition source location is moved along the inside surface of the tank's roof and shell, the rate of pressure rise changes from a maximum when the ignition source is in the center to a minimum when in the corner, as shown in Figures 4.16 through 4.19. This change in pressure rise is due to the surface area of the flame front. As the ignition source location moves toward the corner, the area of the flame front lessens because interception occurs with the tank's internal surface. When the ignition source is located in the center of the tank's roof, this yields the longest time before the flame front will intersect the tank surface and explains why the pressure rise is faster with the ignition source located at the center of the tank's roof.

4.2.6.2 Effects of Tank Size on Pressure Rise

The amount of vapor space, defined as the volume of combustible vapor above the stored liquid, influences the pressure rise inside the tank. The amount of reactants burned by the flame front in a time increment is a function of the burning velocity and the surface area of the flame front. The pressure rise then depends on the ratio of the amount of reactants burned and the total vapor space volume. As a result, larger empty tanks have a slower pressure rise than that of smaller full tanks, but there is no direct proportional relationship. Figures 4.20 through 4.23 show the effect of tank size on pressure rise.

4.2.6.3 Effects of different Fuels and Air-to-Fuel Ratios

The pressure rise also changes for different fuels. Of the fuels considered, nitromethane (CH3OH) gives the fastest pressure rise as well as the largest total pressure, providing the structure could remain intact throughout the combustion process. The other fuels are about the same in pressure rise and total pressure. For the scope of this project, the only concern is before the pressure reaches 20 psi. For hydrocarbons the laminar burning velocities range from 0.34 to 0.40 m/s (Obert, 1973). It is expected that the combustion of hydrocarbons generates similar turbulence during the first several seconds, so the data of methane will represent general fuels.

As the equivalence ratio, which is defined to be the stoichiometric air-to-fuel ratio divided by the actual air-to-fuel ratio, changes from rich to lean the pressure rise also changes. The rate of pressure rise increases as the equivalence ratio approaches one. Changing the equivalence ratio effects the flame temperature and the burning velocity. As the equivalence ratio changes from 1.0 to 1.2, and from 1.0 to 0.8, the flame temperature decreases by approximately 5% and the burning velocity decreases by approximately 9%. The burning velocity determines the radius of the flame front, which is a

squared function, and the flame temperature is used for finding the pressure, which is a linear function, this implies that a change in burning velocity has a greater influence on the rate of pressure rise than a change in flame temperature.

4.3 Testing of welded joints

Testing of joint details was used to evaluate sensitivity of the failure to weld dimensions. It is also used to determine the necessary deformation and load for the weld joint to fail. The test set up and specimens are shown in Figure 4.25.

It is difficult to exactly simulate the three deformational conditions that will occur during an actual tank joint failure. However, since most of the circumferential stress on the buckled region may be released, testing of the joints to failure in a tensile machine does subject the joint to the gross deformation that is expected to occur. In an attempt to bound the possible deformation of the weld during loading, the specimens were tested in pairs, with and without and internal spacer between them. If the internal restraint is not included, large rotation occurs at the joint and a significant amount of bending results at the weld. When the internal constraint is included, the rotation is reduced and the failure mode is in tension.

Two sets of specimens were tested. The small sized welds were of equal-leg, with cross-section of about 3/16 inch. The big welds were unequal-leg fillet noes, with one leg of about 3/8 inch. The specimens were made of 1020 steel angle and 1020 hot roll flat stock, with yielding strength of 38,000 psi, and welded together with rod AWS-ASTM E6013.

For the small welded size specimens without a spacer, bending occurs at the joints and the specimens fail after about 30 degrees of rotation at the weld, under a maximum load of 65 lb. per inch. The loading-rotation curve is

shown in Figure 4.26. With the spacer, the rotation at the weld is much reduced and the specimens essentially fail in direct tension. The specimen was broken at the roof-to-angle weld at a load of 4000 lb. per inch, as shown in Figure 4.27.

The tests on specimens with large welds were performed similarly. Even though the large sized weld joints on the specimens looked similar to the small joints, they failed differently. The specimens without the spacer did not fail at the weld joint, but bent the angle at a load of 90 lb. per inch. The ones with a spacer sustained 7200 lb. per inch width, and one of the weld shell-to-angle joints failed. In this case, the double butt weld of the shell-to-angle joint had not been welded completely through the plates, but the butt weld of the shell-to-angle joint had been stretched to yielding stress. If the joint had been well welded, the failure might have happened somewhere on the shell or roof plates.

The testing shows clearly that the weld size on the joint is an important parameter of tank design. In case of unequal-leg fillet welds, the joint may be stronger than the plate. Making the weld larger than needed may cause the failure to happen elsewhere rather than on the joint as desired. The dynamic test of the continuously welded scale model tank showed that failure can also occur on top angel and roof plate, indicating that the weld joint was no weaker than the roof plate.

4.4 Static Test of Small Scale Model Tanks

Two scale models of small tanks were built and tested. The scale models were constructed of 20 gauge sheet steel (with thickness about 0.036 inch), with a measured yield stress of 38,000 psi. The tanks had a diameter of 4 feet, with shells 2 feet tall. The bottoms of the tanks were made of 3/4 inch plywood with steel reinforce beams. There was no internal support of

the roofs or walls. Assuming a linear scaling factor on the thickness, this corresponds to a tank of 20 feet in diameter.

Because of difficulties encountered with distortion while welding the sheet metal, the tanks were constructed using spot welding on the shell and pop rivets at the roof-to-shell joint. This was very satisfactory, since this method of joining did not distort the model and still gave the appropriate stiffness of the joint. One tank was constructed with a flat roof and the other with a roof that had a slope of 4 inches in 12 inches. These dimensions were chosen so as to give extremes of elastic bucking behavior. As mentioned before, elastic buckling was expected for the flat roof but not the large sloped roof.

The setting of the test is shown in Figure 4.28. The tanks were tested statically until significant buckling occurred. The internal pressure was controlled by flowing water into the tank while taking pressure readings with a barometer. Measurements of the vertical displacement of the tank roofs were taken using dial indicators on a rotating arm.

For the tank with the flat roof, elastic buckling occurred in the tank roof below 1 psi (the exact pressure is not known due to initial difficulties in running the test). This elastic buckling was very pronounced. The measured vertical displacements on the roof at a radius 1/2 inch inward from the joint are plotted in Figure 4.29. Sixteen waves formed around the entire circumference with an amplitude of about 0.1 inch. An important point to note is that this elastic buckling did not result in significant deformation of the roof-to-shell joint. In fact, the buckling was stable and we were able to continue to load the tank. At a pressure of about 1.2 psi, a large inelastic buckle formed at the joint as shown in Figure 4.30. This is approximately the pressure at which yielding of the ring was expected. An increase in pressure to 1.5 psi resulted in the formation of four buckles spaced about 90 degree

apart. These buckles are shown in Figure 4.31. These buckles essentially flatten the joint and would have caused the joint to fail (at least locally). The sequence of first elastic buckling, then yielding of the ring matches the analytical prediction.

The test with the sloped roof was performed in a similar manner. However, no elastic buckling was observed. The roof was smooth and without buckles until 4.0 psi as shown in Figure 4.32. At about 4.0 psi small sharp buckles formed closer to the edge than that in the flat roof tank, and the buckling mode was much higher (about 30). Finally, at a pressure of about 5.5 psi, large wrinkles formed on the roof at the joint. This was followed by failure due to yielding of the ring (matching the analysis), as shown in Figure 4.33. Also, as predicted, the failure pressure was much higher than that for the flat roof tank, although the observed pressure at yielding was larger than that predicted.

	Small Tank	Large Tank
Height (ft)	36	40
Diameter (ft)	25	140
Roof Thickness (in)	3/16	3/16
Top Shell Thickness (in)	3/16	5/16
Top Angle	2 x 2 x 3/16 (in)	3 x 3 x 3/8 (in)
	Outside Shell	Outside Shell
Roof Slope (in)	3/4 ~ 4 in 12	3/4 in 12
Containing of Tank	empty	empty

Table 4.1: Geometric data for tanks used in analysis

Prestress Pressure:	**0.0 psi**		
		Frequency	**(Hertz.)**
	Mode	**Small Tank**	**Large Tank**
	1	7.7	0.95
	2	21.2	3.03
	3	26.6	3.36
	4	34	3.83
	5	41.9	4.23
Prestress Pressure:	**0.1 psi**		
		Frequency	**(Hertz.)**
	Mode	**Small Tank**	**Large Tank**
	1	8.1	1.67
	2	22.4	4.55
	3	28.3	5.67
	4	35.7	6.84
	5	43.9	7.88

Table 4.2: Natural frequencies of small tank with low pressure

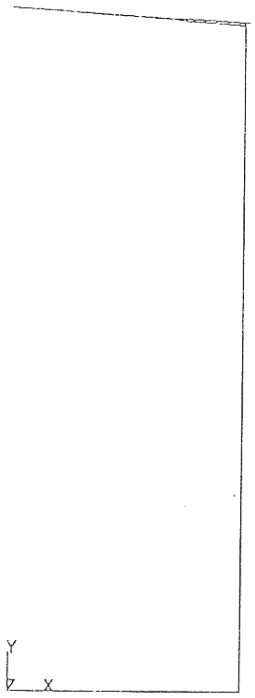

Figure 4.1: Axisymmetric Model of 25 feet Diameter Tank

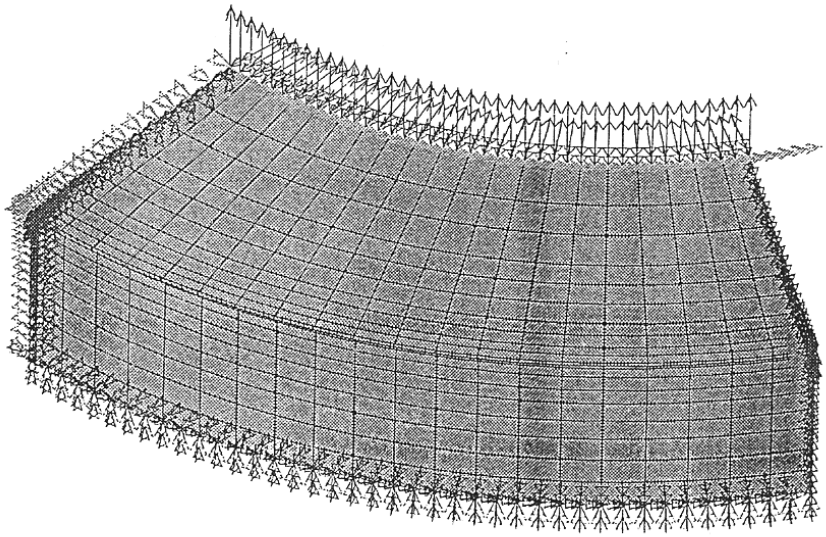

Figure 4.2: 3-D Model of 25 feet Diameter Tank

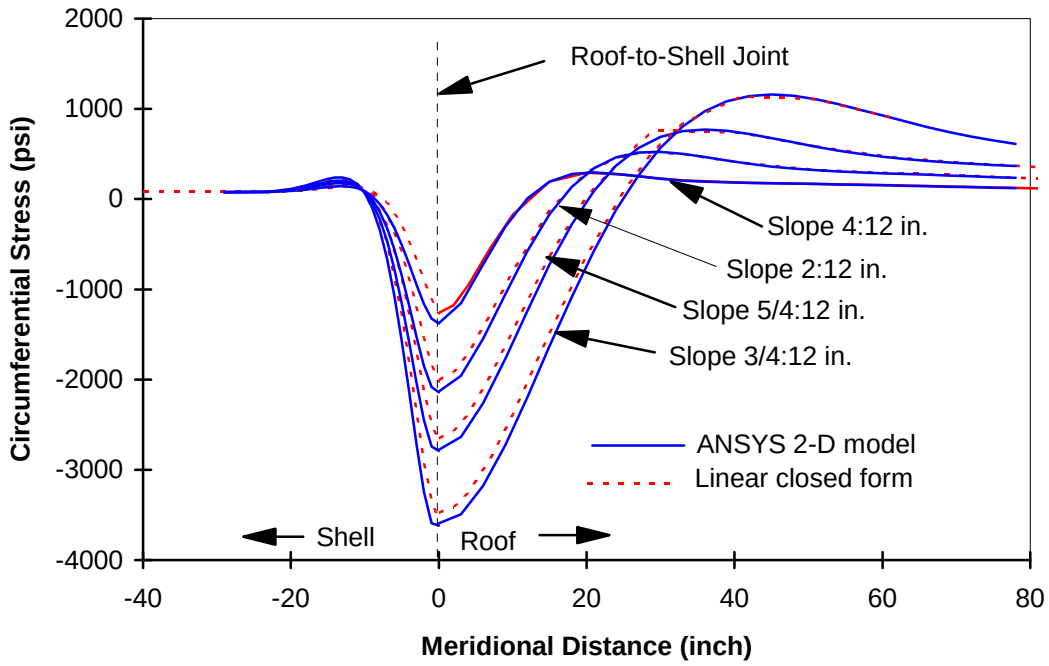

Figure 4.3: Circumferential stress in 25 feet diameter tank due to 0.1 psi pressure

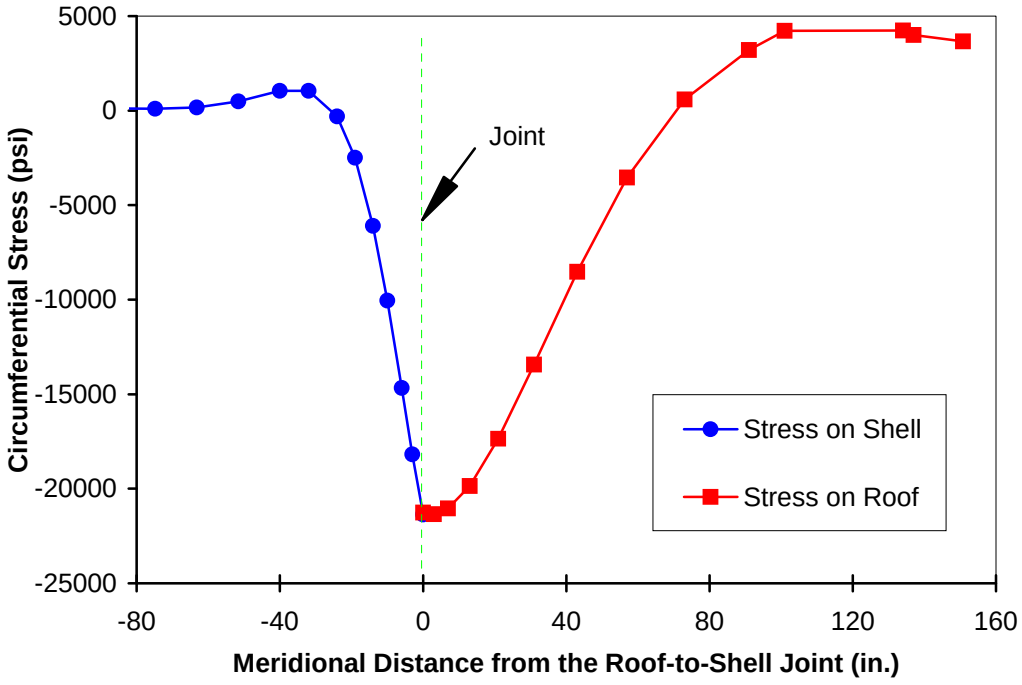

Figure 4.4: Circumferential Stress in 140 feet Diameter Tank due to 0.1 psi Pressure

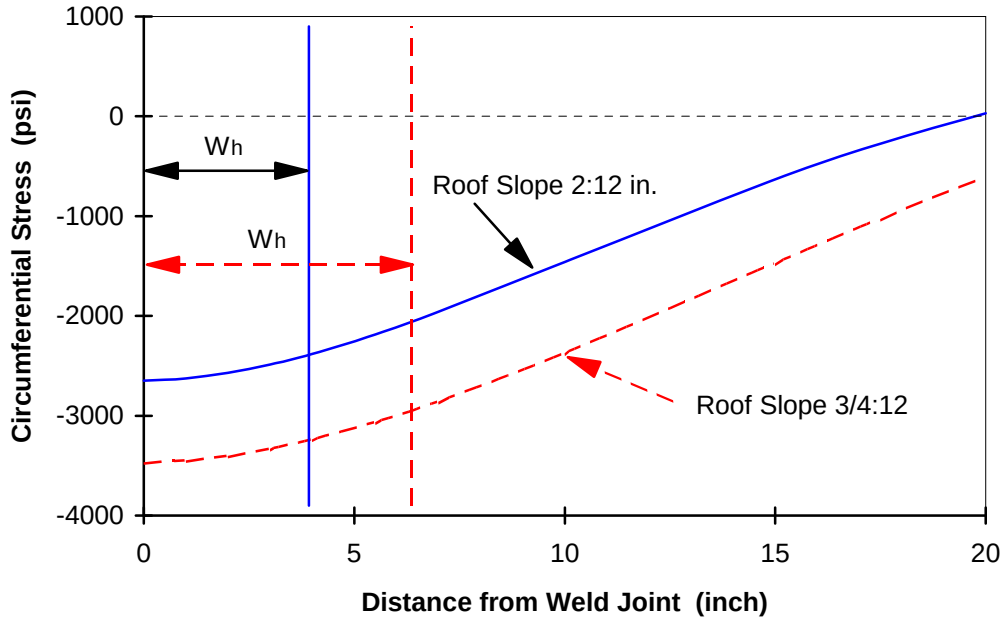

a: Calculation of W_h vs. circumferential stress

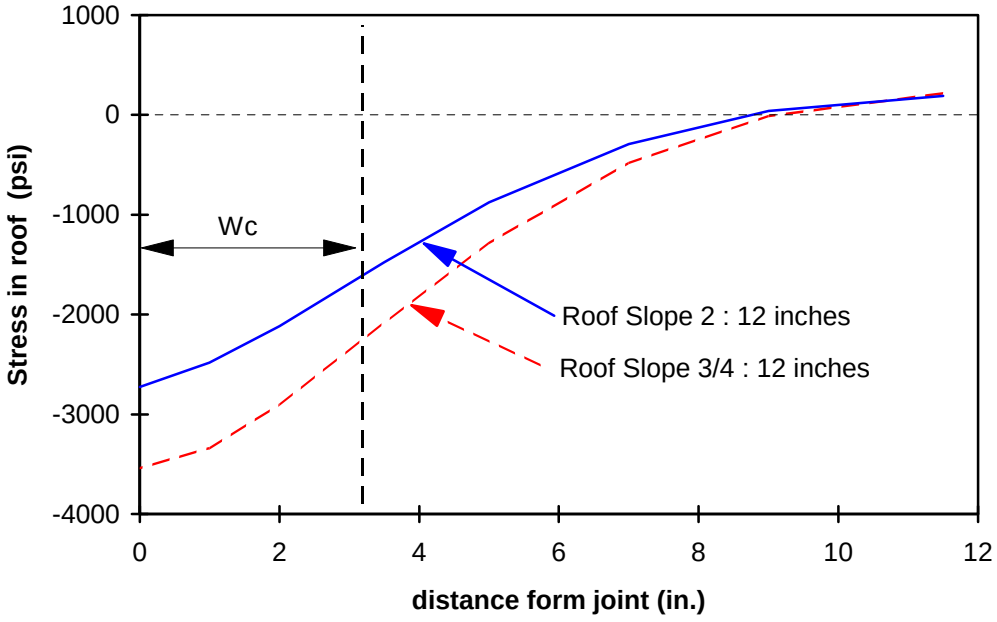

b. Calculation of W_c

Figure 4.5: Compression zone for D = 25 feet Tank of Different Roof Slopes

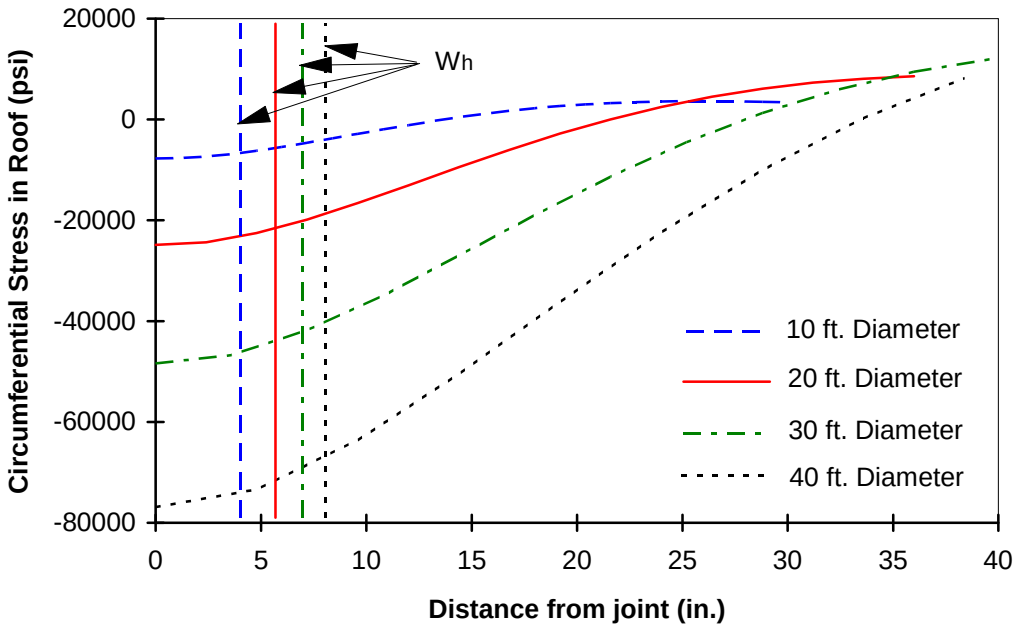

a: Calculation of W_h vs. circumferential stress

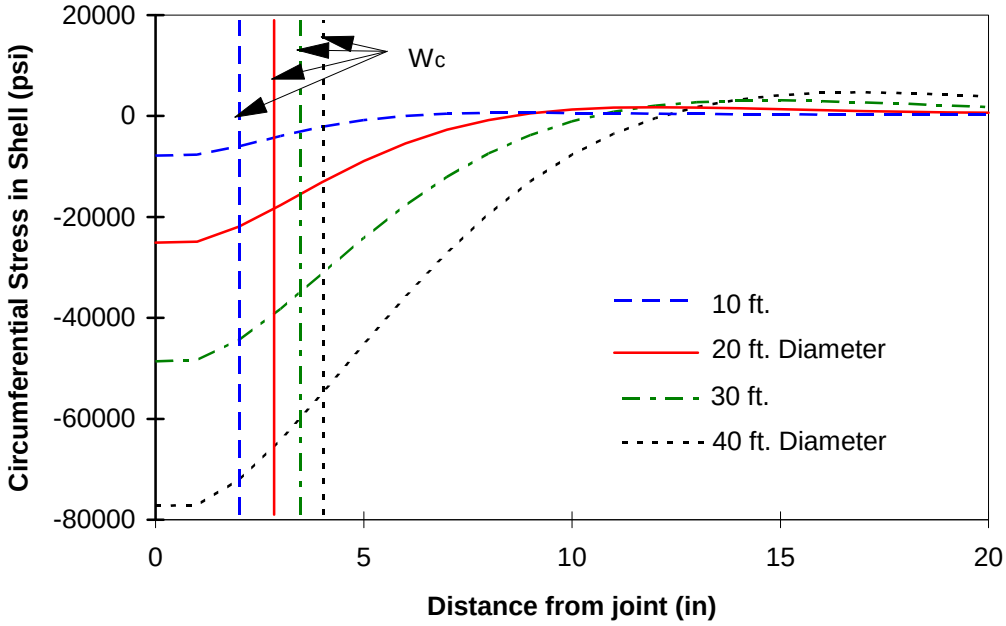

b: Calculation of W_c vs. circumferential stress

Figure 4.6: W_h and W_c for Different Tank Diameters. Linear Analysis; Roof Slope 0.75 inch in 12 inches; 1.0 psi Pressure.

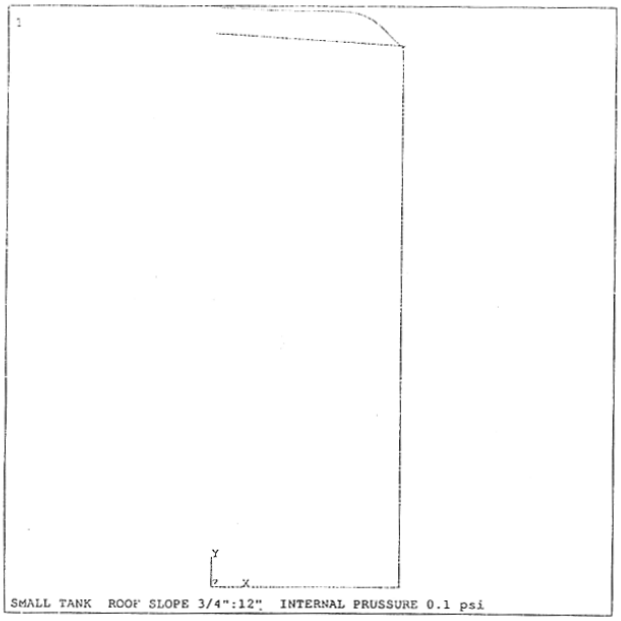

a. Lowest mode (8.1 Hertz)

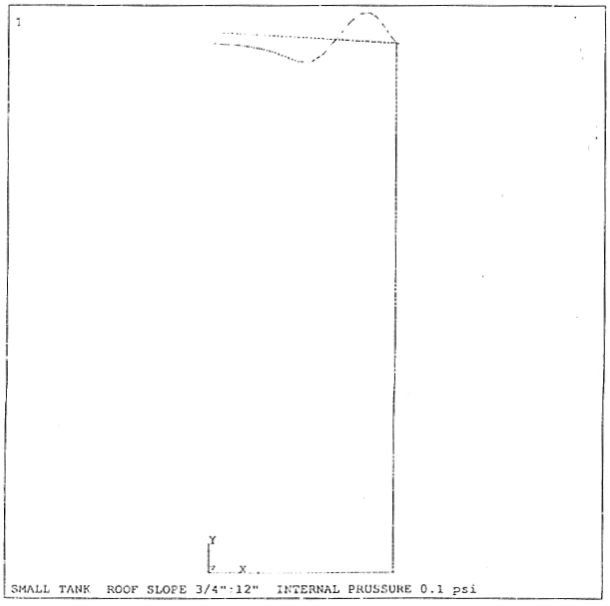

b. Second mode (22.4 Hertz)

Figure 4.7: Natural Frequencies of 25 feet Diameter Tank

(0.1 psi pressure prestress)

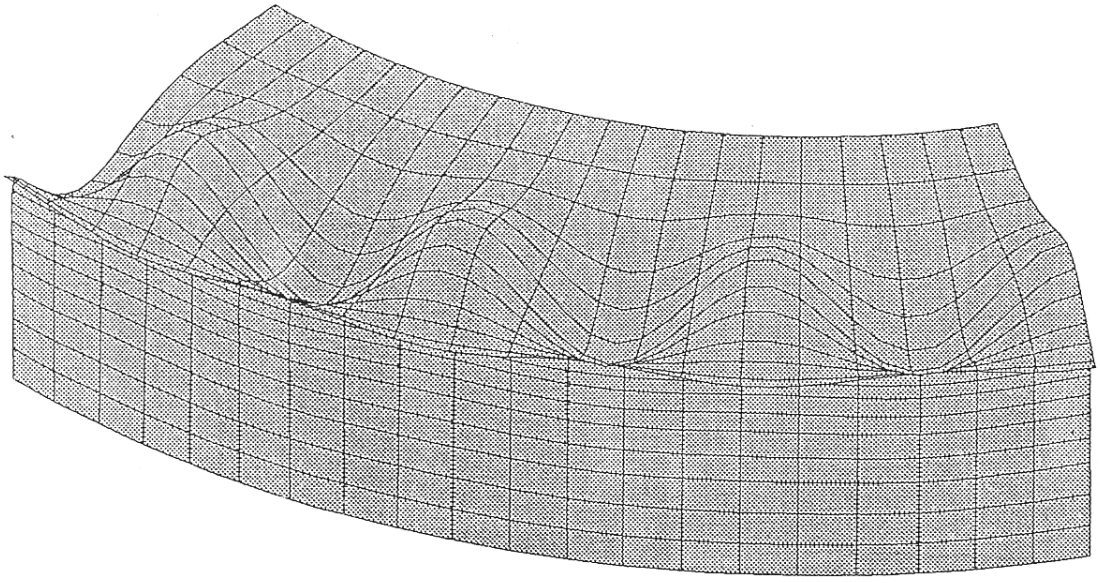

a. Lowest buckling mode (P_{cr} = 0.418 psi, mode = 21)

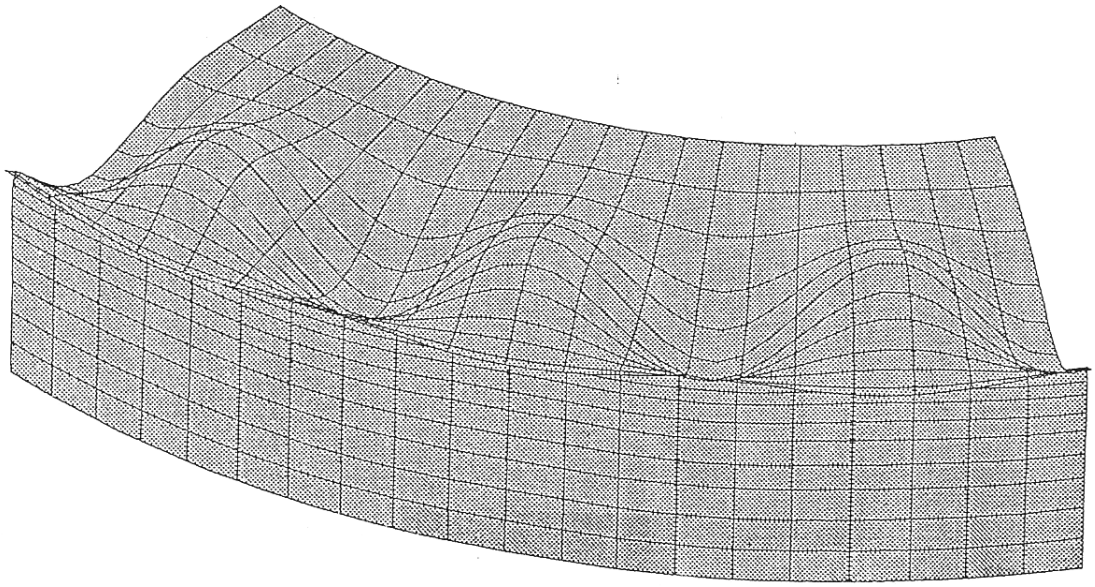

b. Second lowest buckling mode (P_{cr} = 0.421 psi, mode = 18)

Figure 4.8: Buckling of 25 feet Diameter Tank with 3/4 : 12 inches Slope

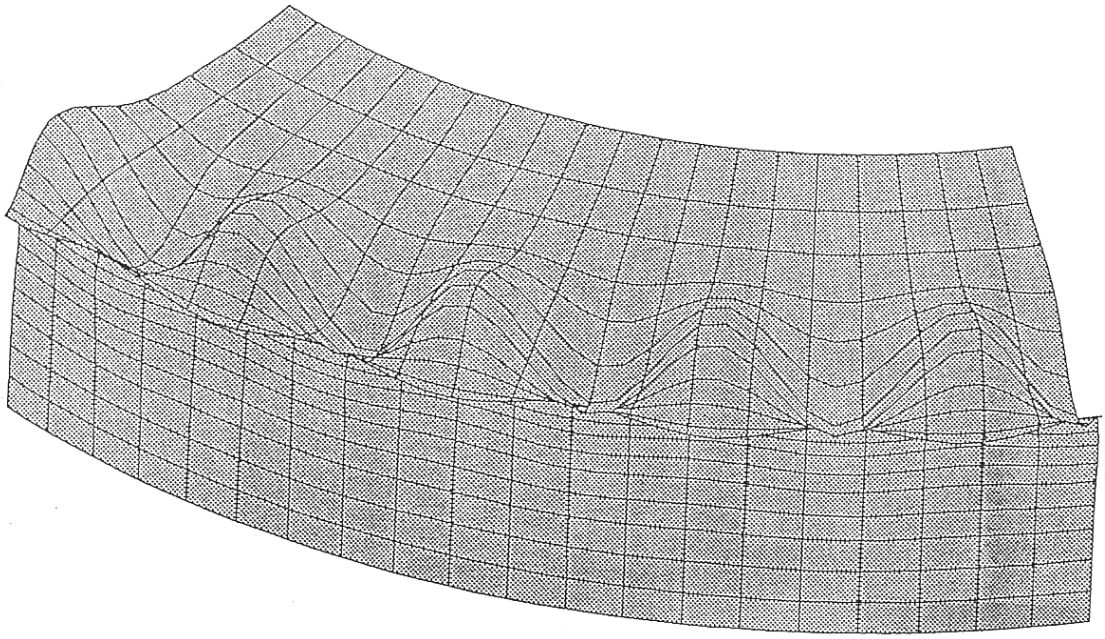

Figure 4.9: Buckling of 25 feet Diameter Tank with 2 : 12 inches Slope
(P_{cr} = 1.5 psi, Mode = 27)

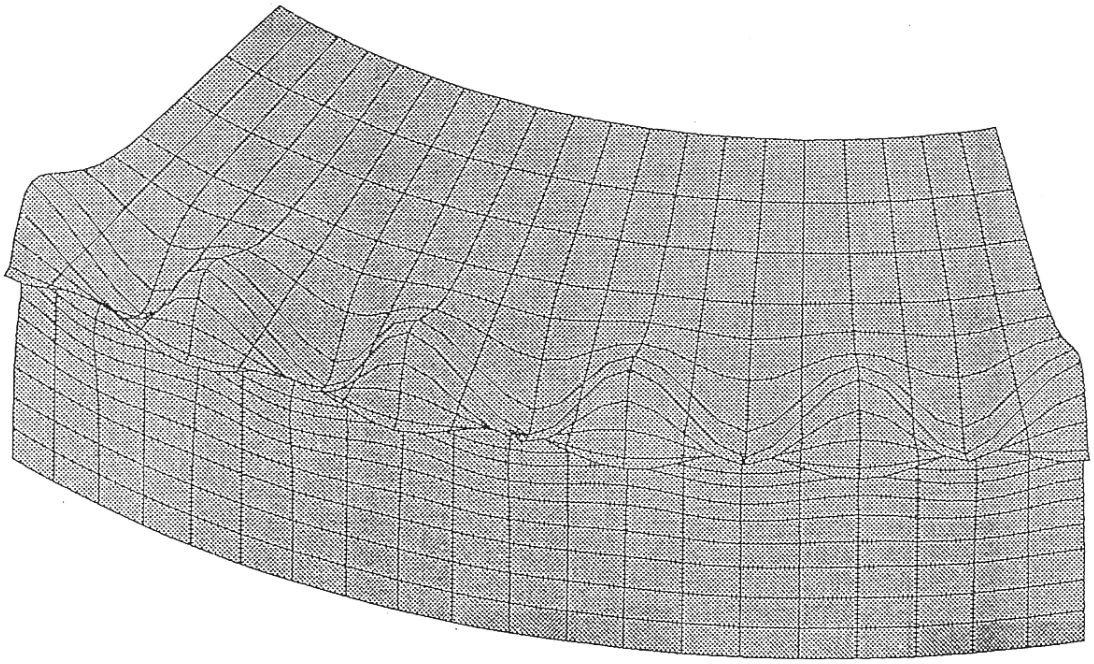

Figure 4.10: Buckling of 25 feet Diameter Tank with 4 : 12 inches Slope (P_{cr} = 6.0 psi, Mode = 30)

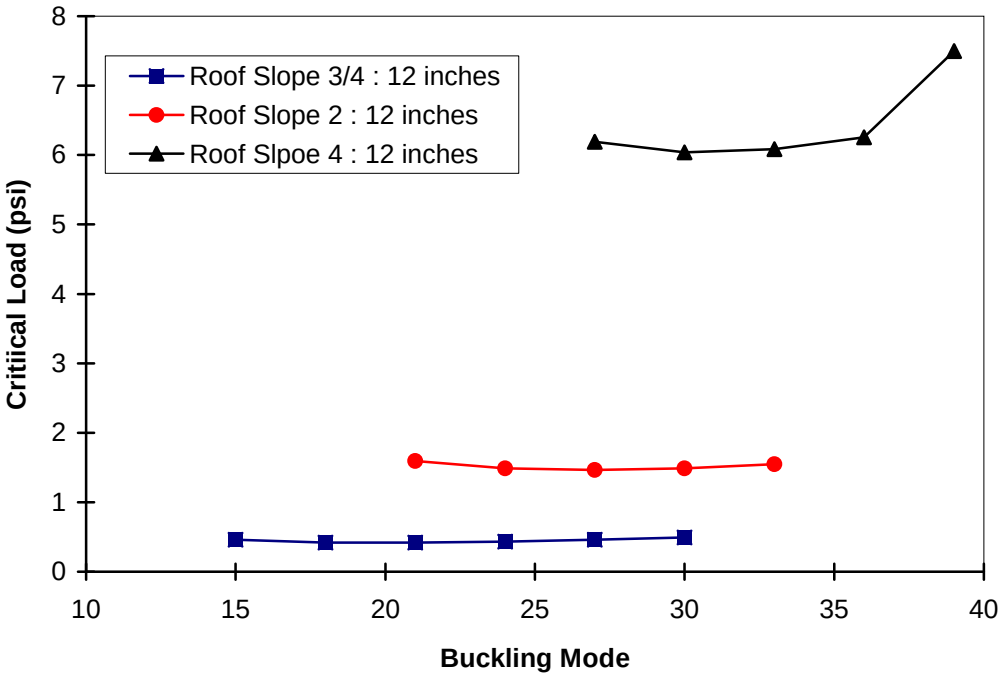

Figure 4.11: Summary of Buckling Analysis Results for 25 feet Diameter Tank with Different Roof Slopes

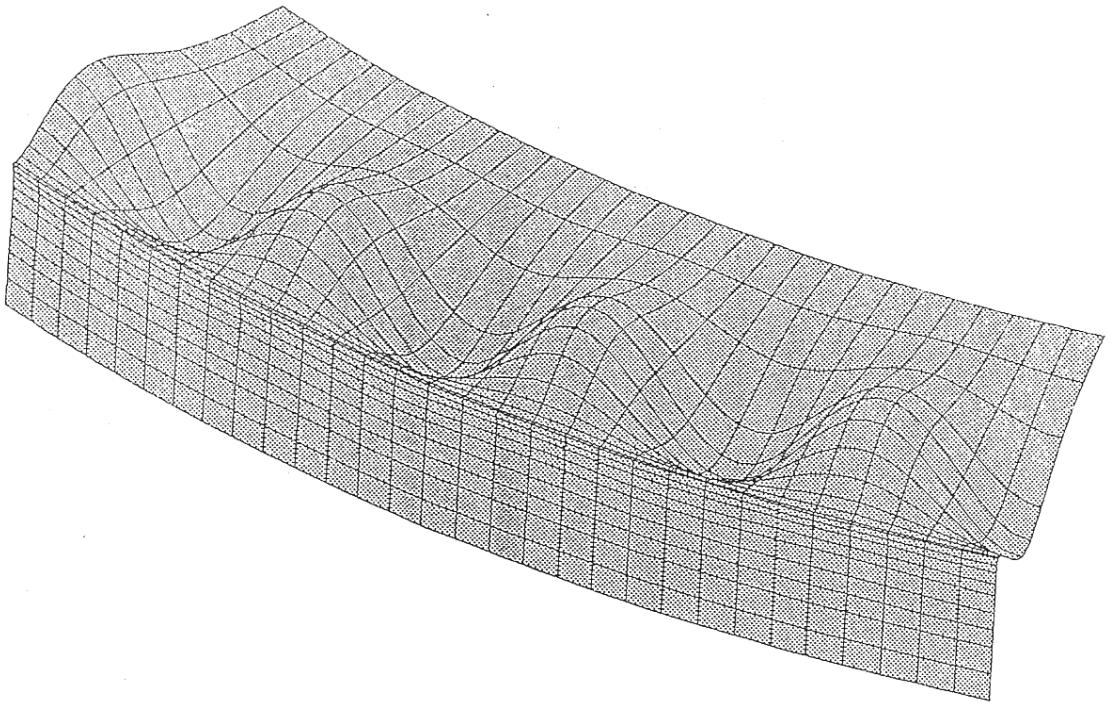

Figure 4.12: Buckling of 140 feet Diameter Tank with 3/4 : 12 inches Slope (P_{cr} = 0.004 psi)

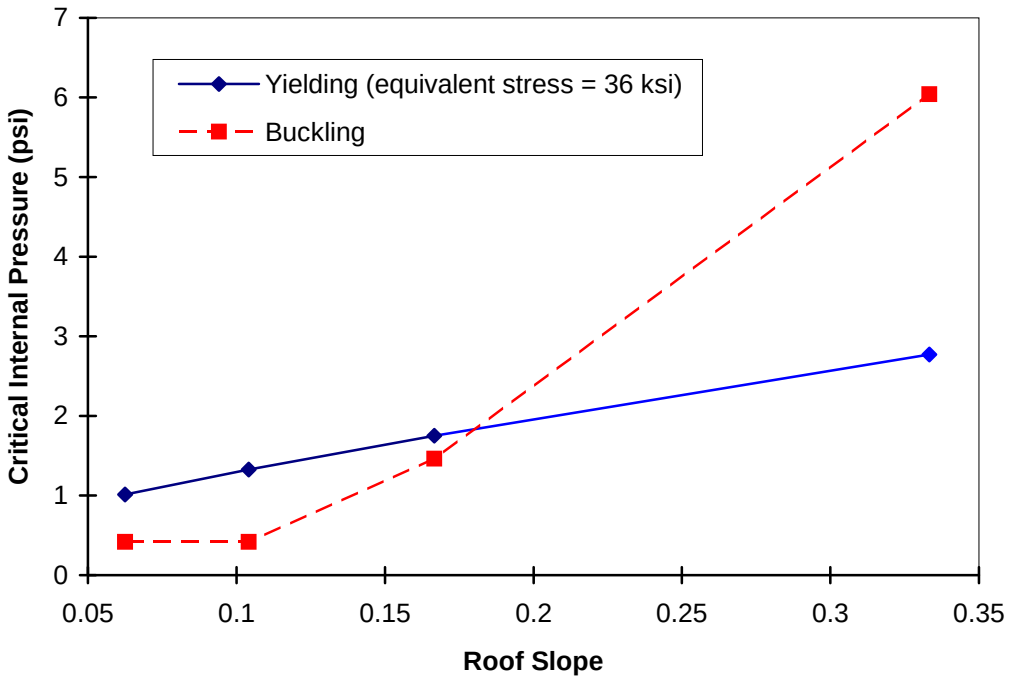

Figure 4.13: Combined Buckling and Compression Yielding of 25 feet Diameter Tank

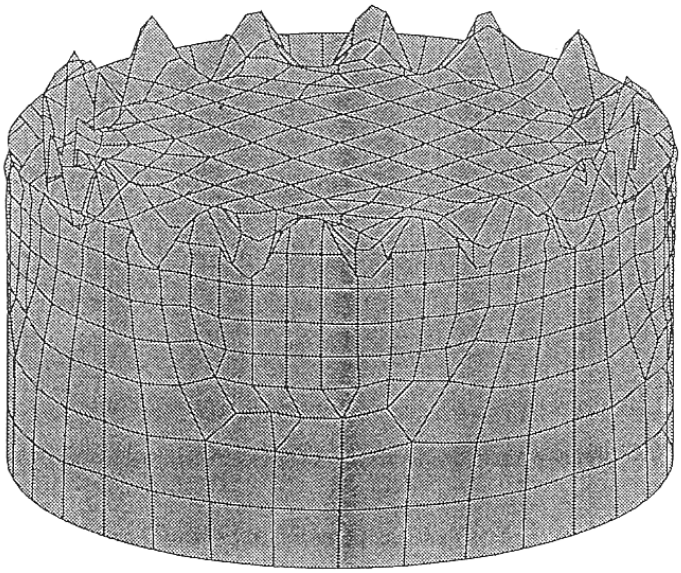

a: buckling mode of flat roof tank $P_{cr} = 0.87$

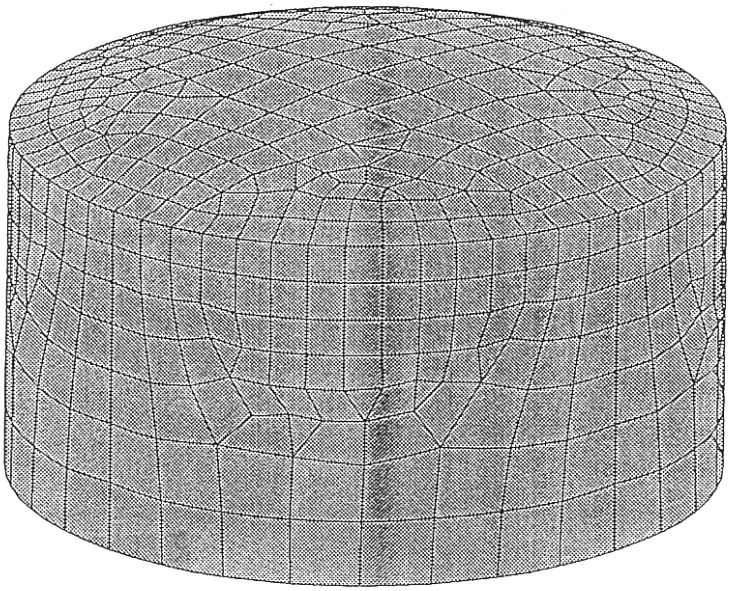

b: displacement

Figure 4.14: Large Deformation Analysis of Flat Roof Tank under 1 psi Pressure

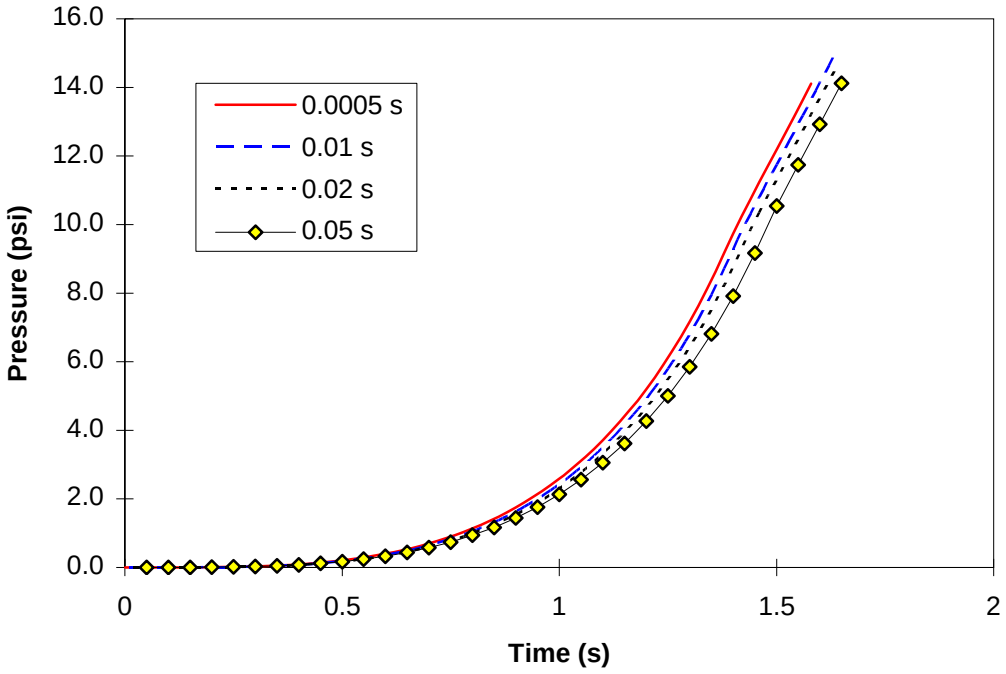

Figure 4.15 Illustration of Convergence with Different Time Steps
30 ft. by 30 ft. Empty Tank, with Methane

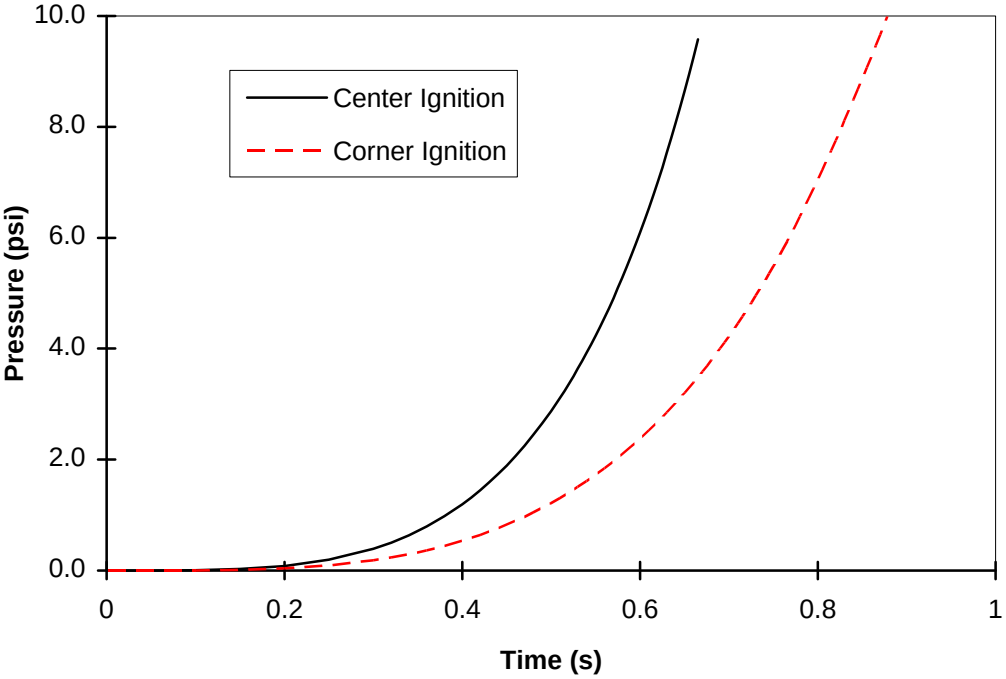

Figure 4.16: Pressure Rise for different Ignition Source Location, for a 20 ft. Diameter by 10 ft. Tall Tank, Empty with Methane at $\Phi = 1.0$

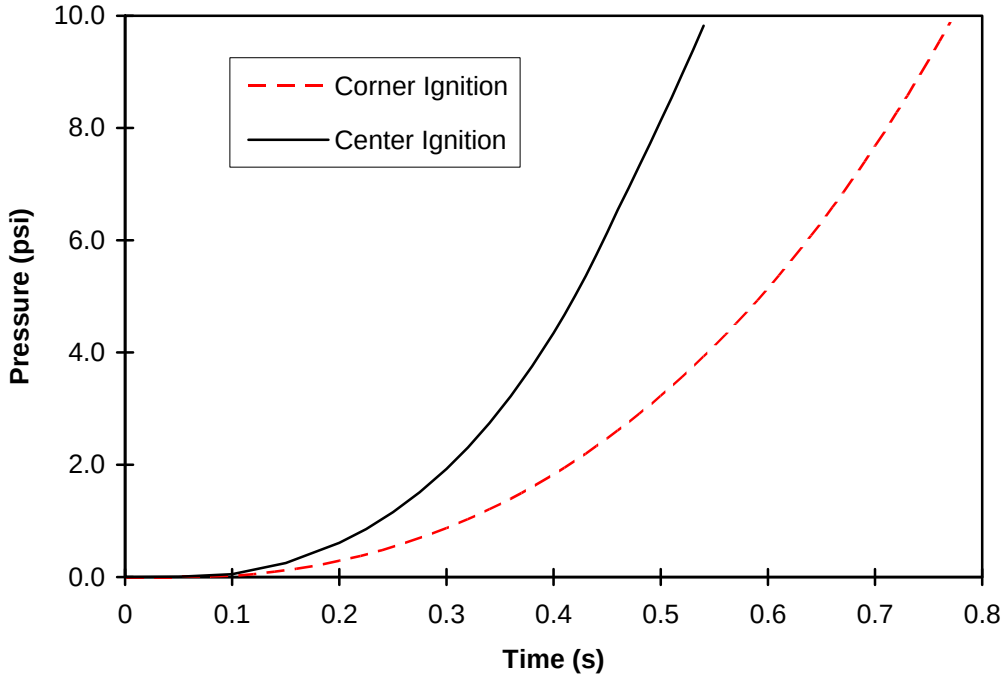

Figure 4.17: Pressure Rise for different Ignition Source Location, for a 20 ft. Diameter by 10 ft. Tall Tank, with 1 ft. Vapor Space of Methane at Φ = 1.0

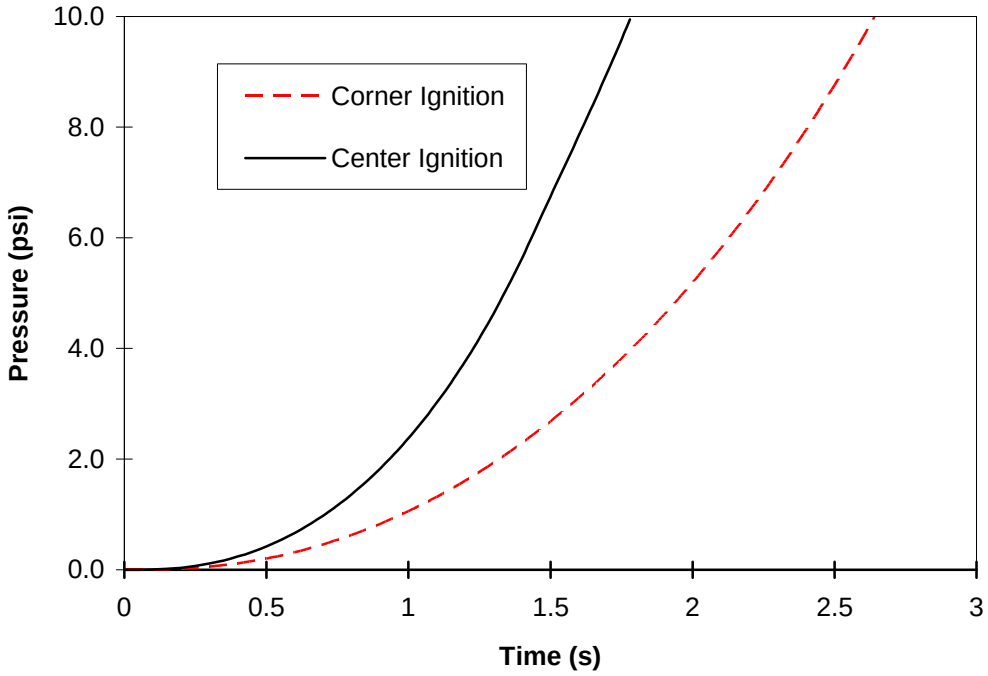

Figure 4.18: Pressure Rise for different Ignition Source Location, for a 80 ft. Diameter by 30 ft. Tall Tank, with 1 ft. Vapor Space of Methane at Φ = 1.0

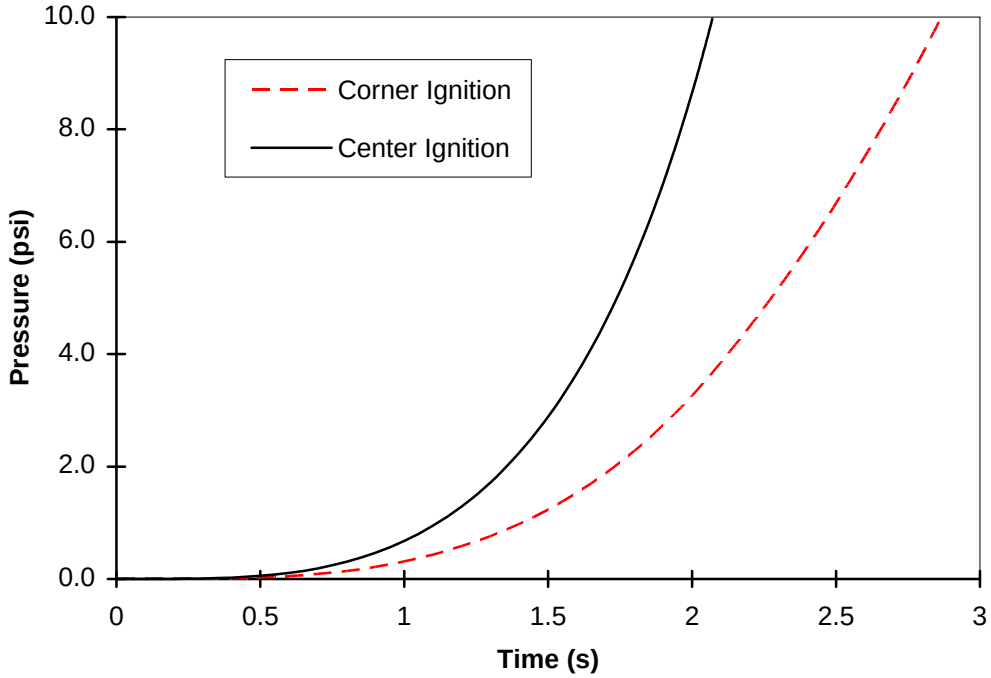

Figure 4.19: Pressure Rise for different Ignition Source Location, for a 80 ft. Diameter by 30 ft. Tall Tank, Empty with Methane at Φ = 1.0

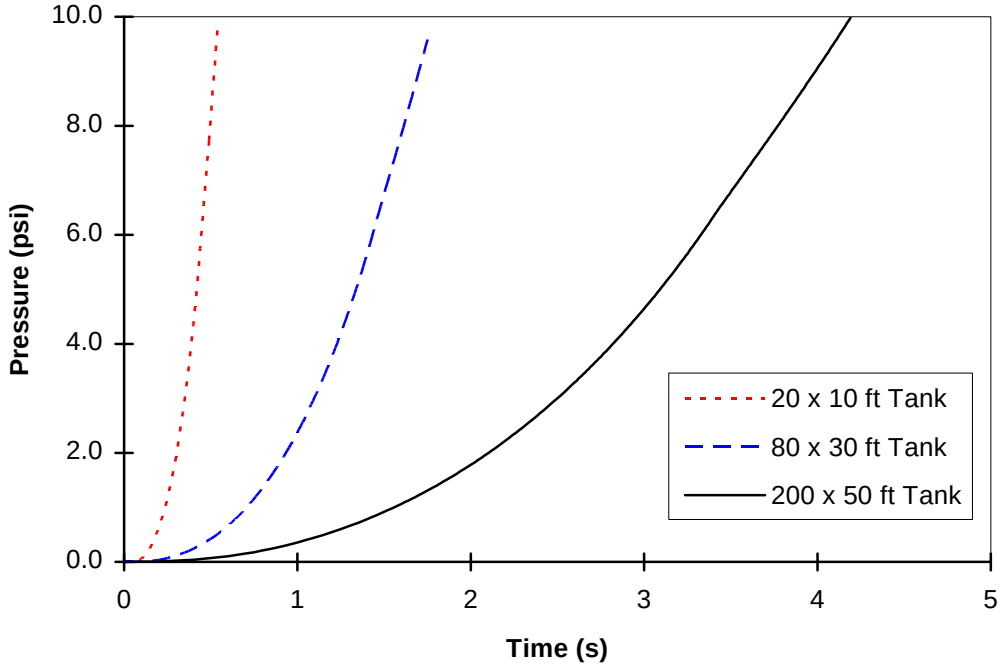

Figure 4.20: Pressure Rise for Different Tank Size
Center Ignition, with 1 ft. Vapor Space of Methane at Φ = 1.0

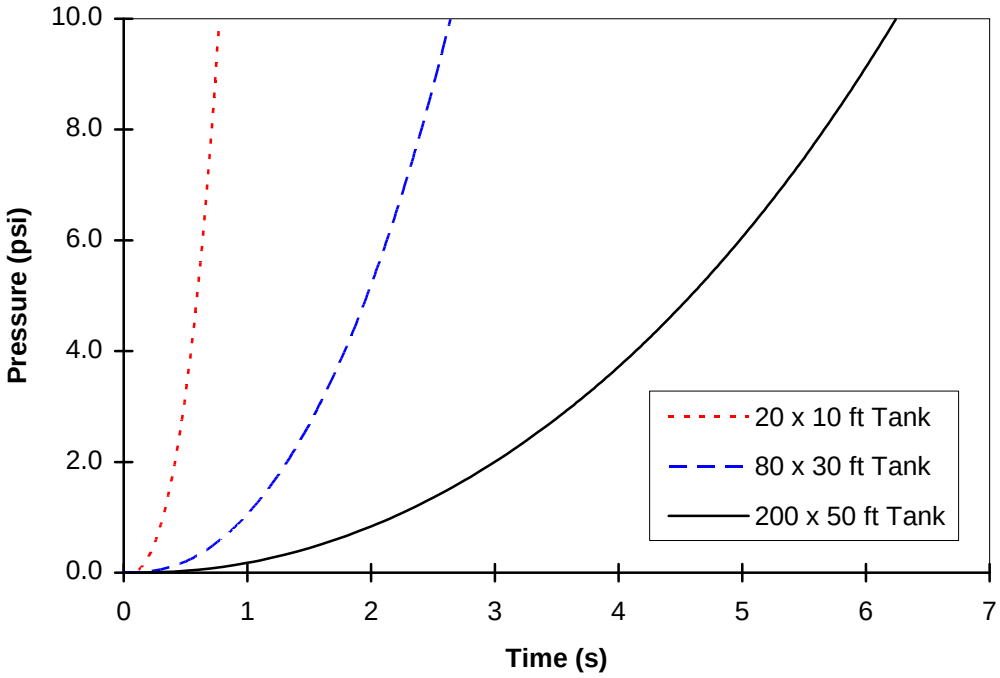

Figure 4.21: Comparison of Pressure Rise for Different Tank Size, Corner Ignition, with 1 ft. Vapor Space of Methane at $\Phi = 1.0$

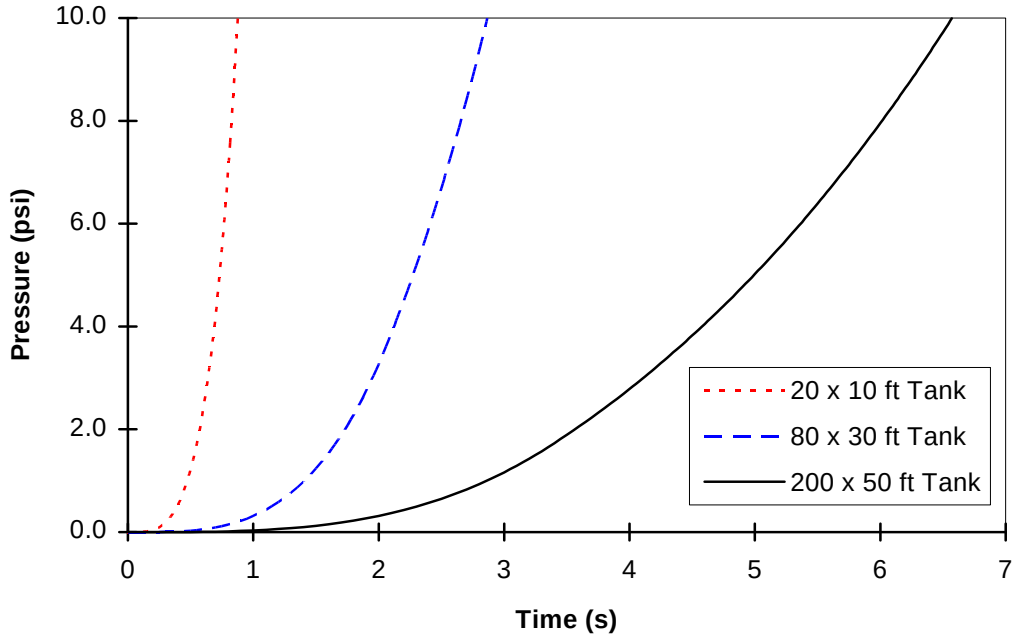

Figure 4.22: Comparison of Pressure Rise for Different Tank Size, Corner Ignition, Empty Tank with Methane Vapor at $\Phi = 1.0$

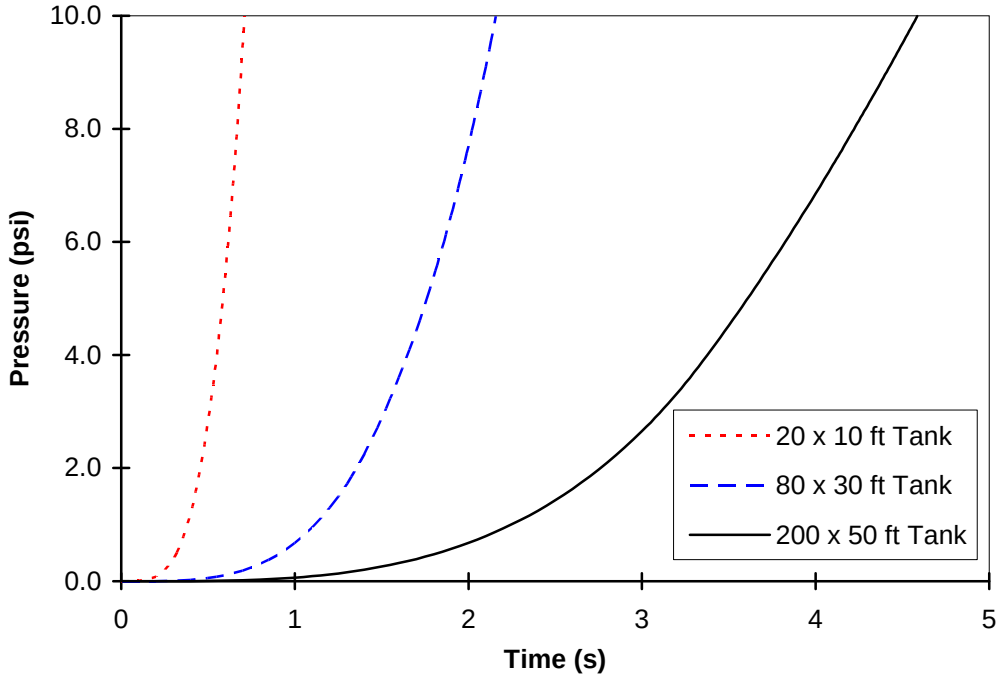

Figure 4.23: Comparison of Pressure Rise for Different Tank Size, Ignition Source Located Halfway between The Center of The Tank's Roof and The Corner, Empty Tank with Methane Vapor at Φ = 1.0

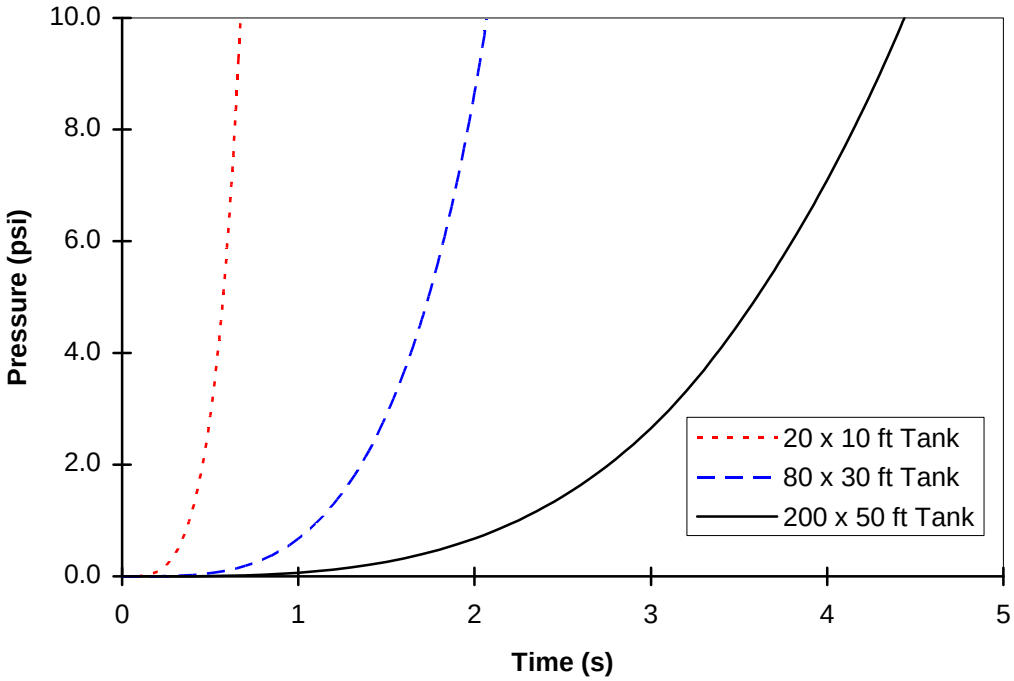

Figure 4.24: Comparison of Pressure Rise for Different Tank Size, Center Ignition, Empty Tank with Methane Vapor at Φ = 1.0

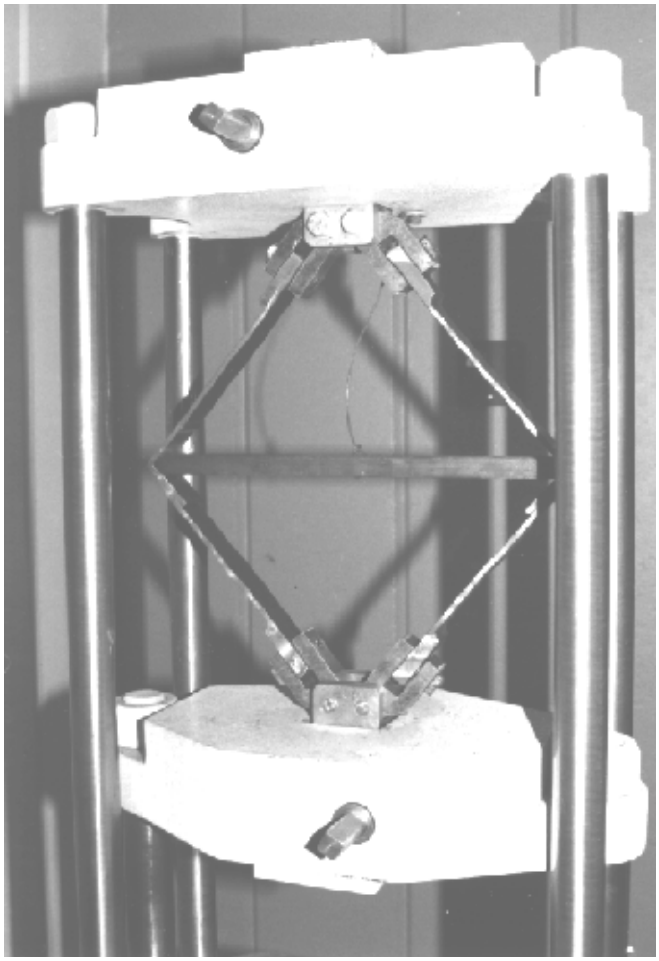

Figure 4.25: Joint Specimen on Testing

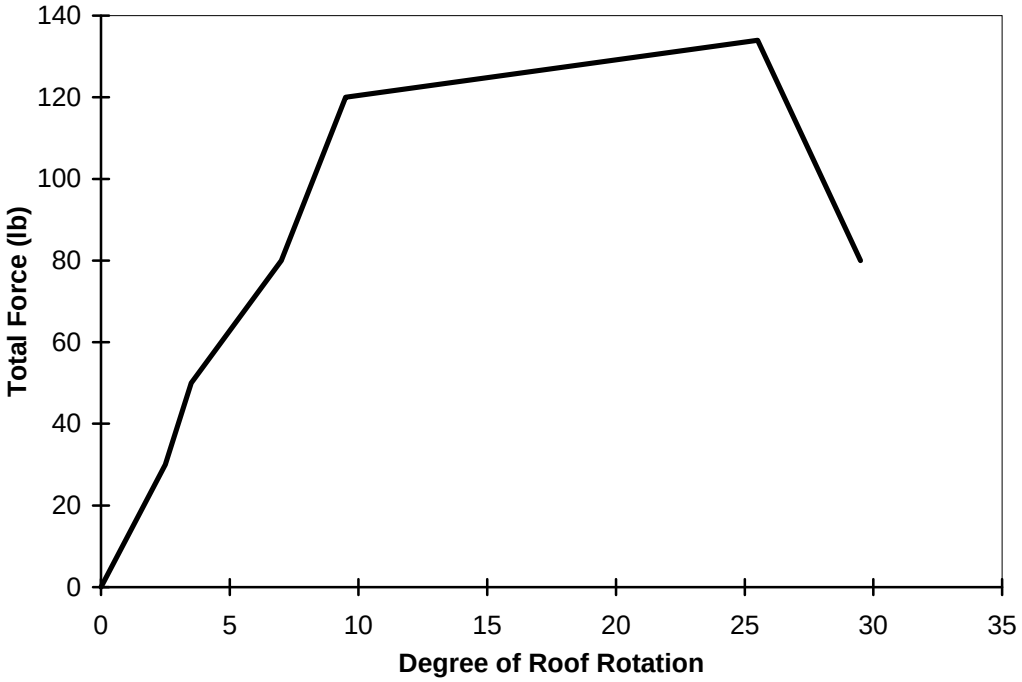

a: loading-rotation relationship

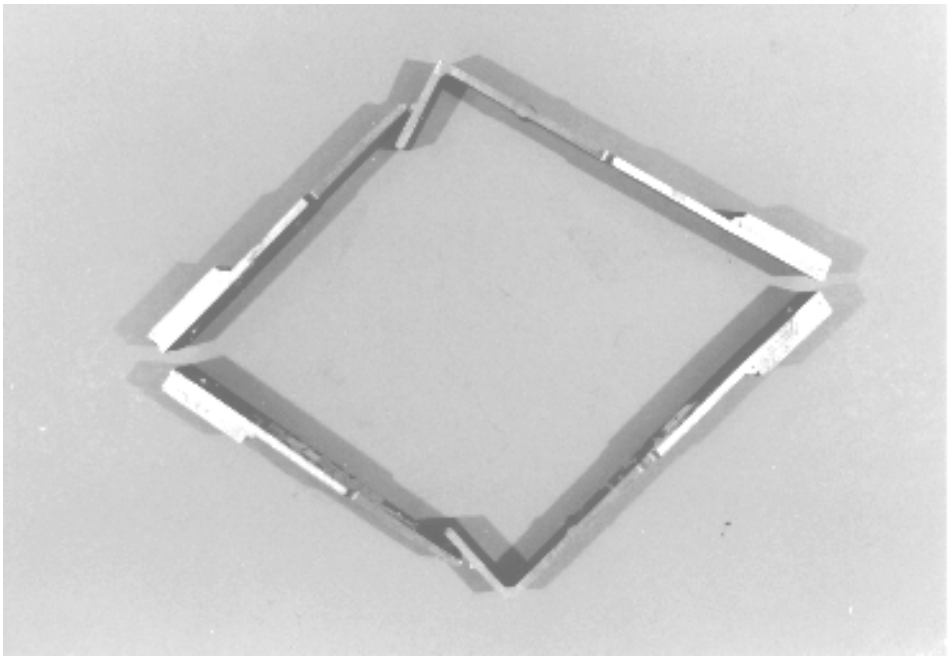

b: specimens after test

Figure 4.26: Tension Test of Small Weld Size Specimens Without Spacer (Bending of roof-to-shell joint)

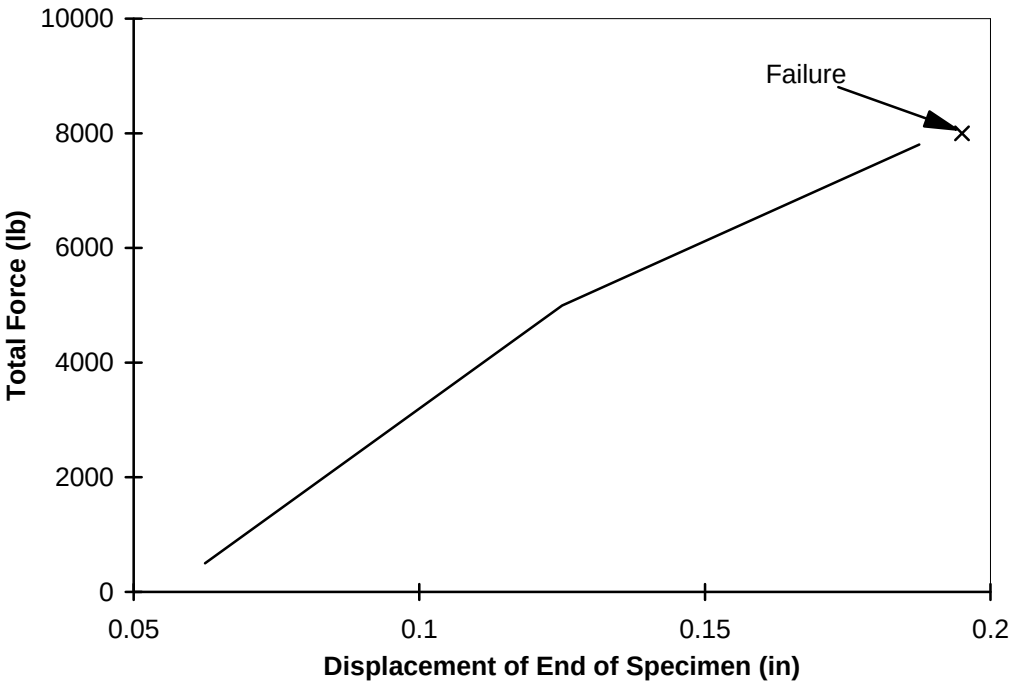

a: displacement-loading curve of test

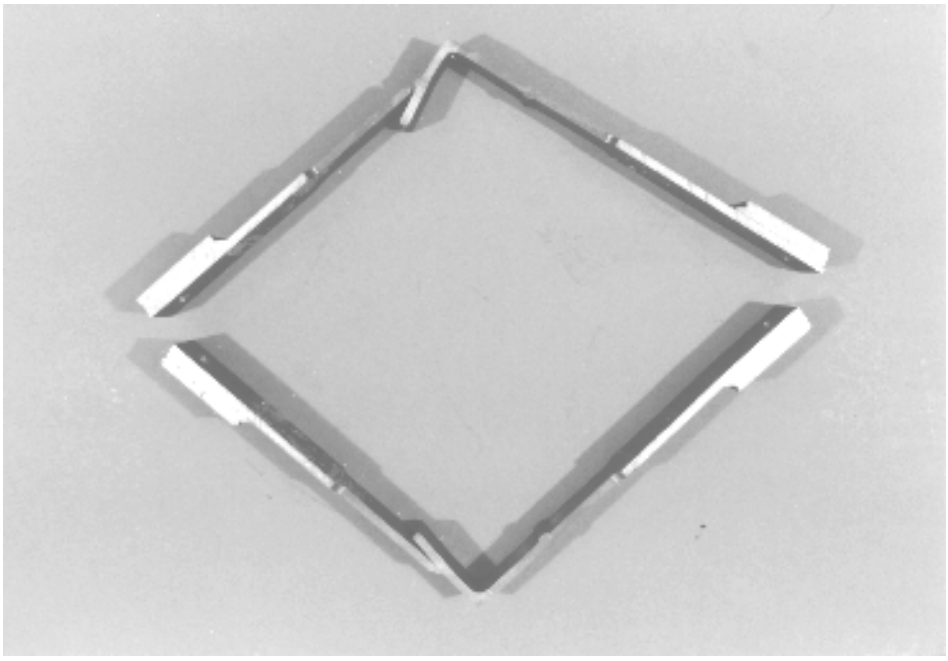

b: specimens after test

Figure 4.27: Tension Test of Small Weld Size Specimens with Spacer (Pulling of roof-to-shell joint)

Figure 4.28: Setting of Small Model Tank Tests

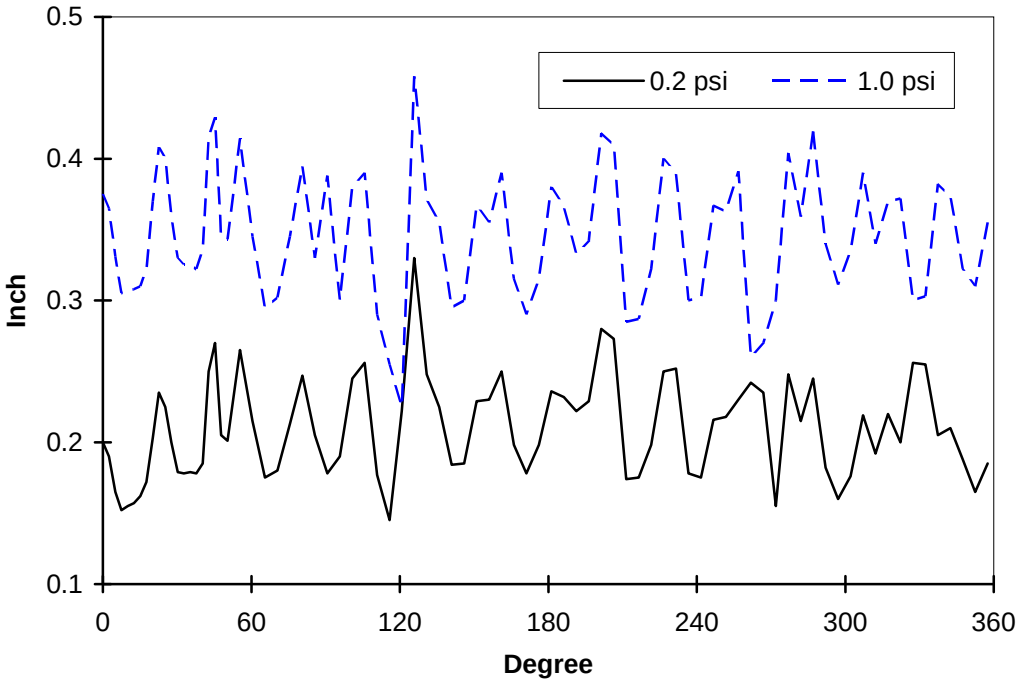

Figure 4.29: Waves Along Circumference at 1/2 inch from Joint on Flat Roof Tank

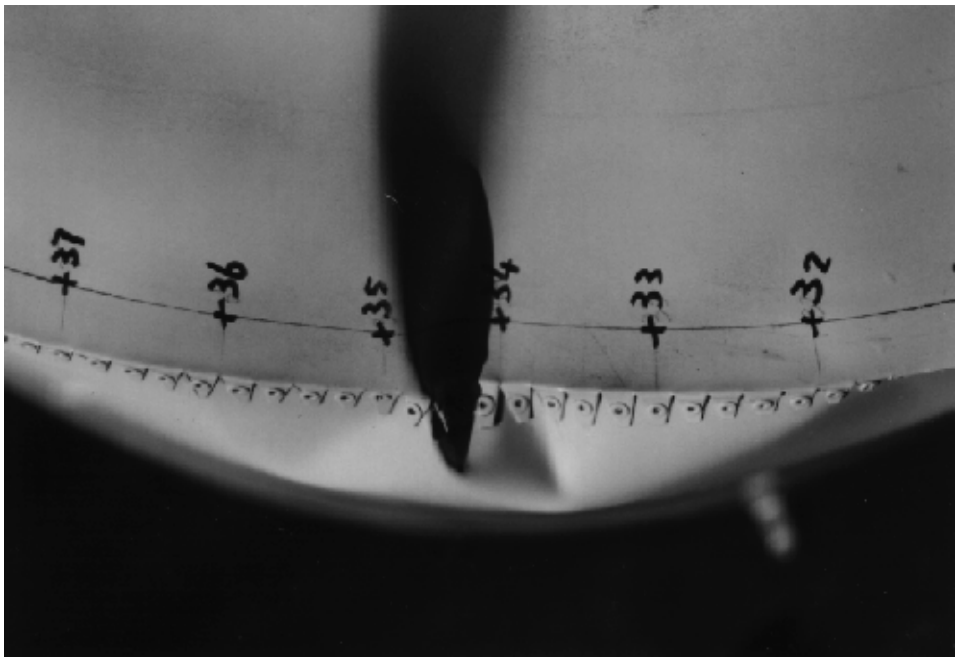

Figure 4.30: First Large Buckling on Flat Roof Tank under 1.2 psi Pressure

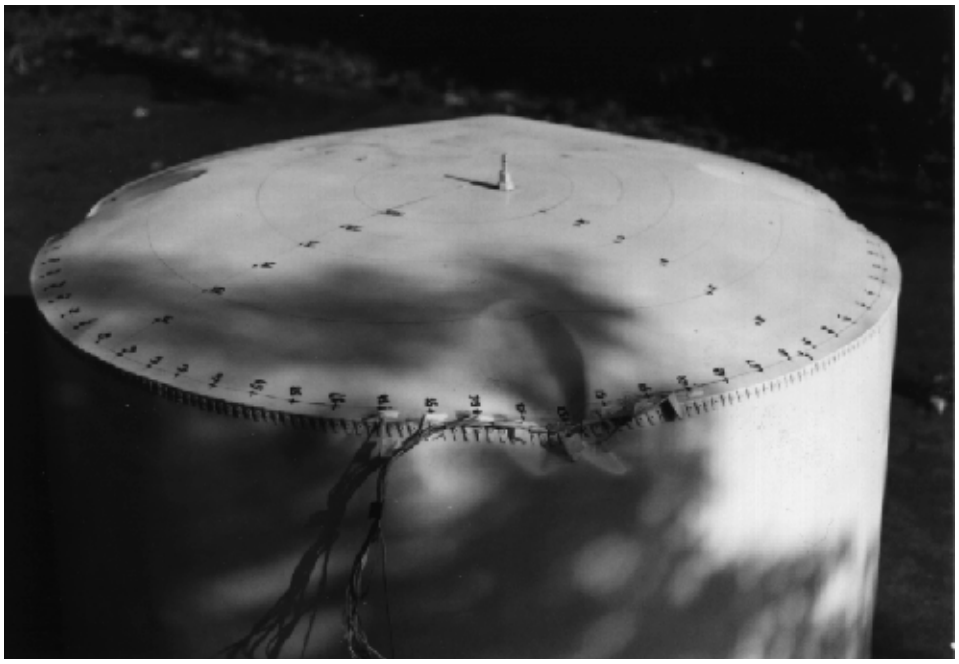

Figure 4.31: Flat Roof Tank after Test

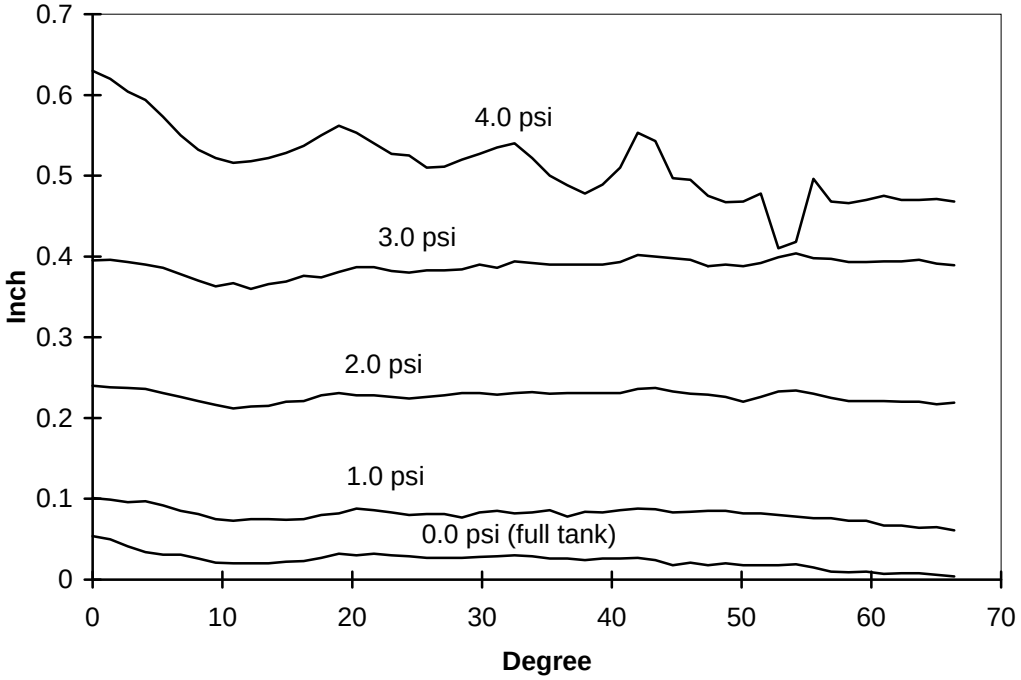

a: measured at 1 inch in from the joint

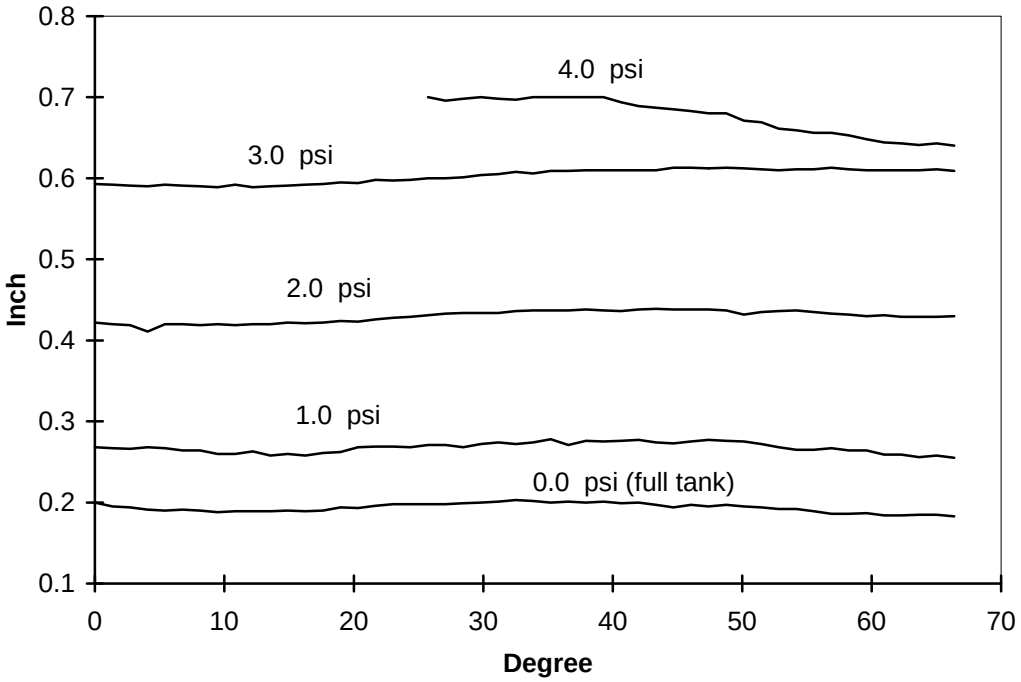

b: measured at 4 inches in from the joint

Figure 4.32: Waves along Circumference on Large Slope Roof Tank

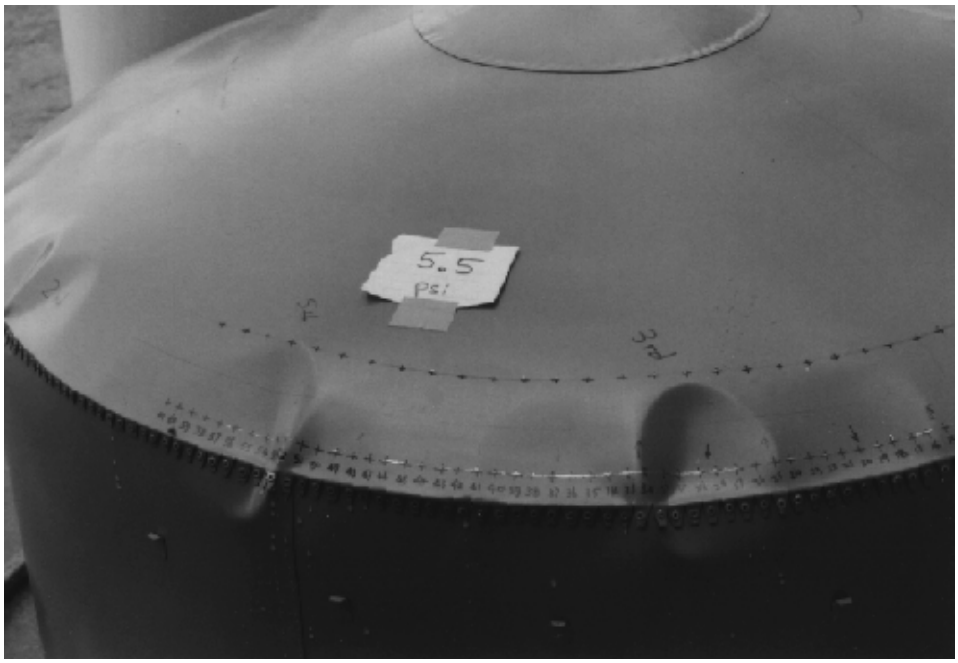

a: under 5.5 psi pressure

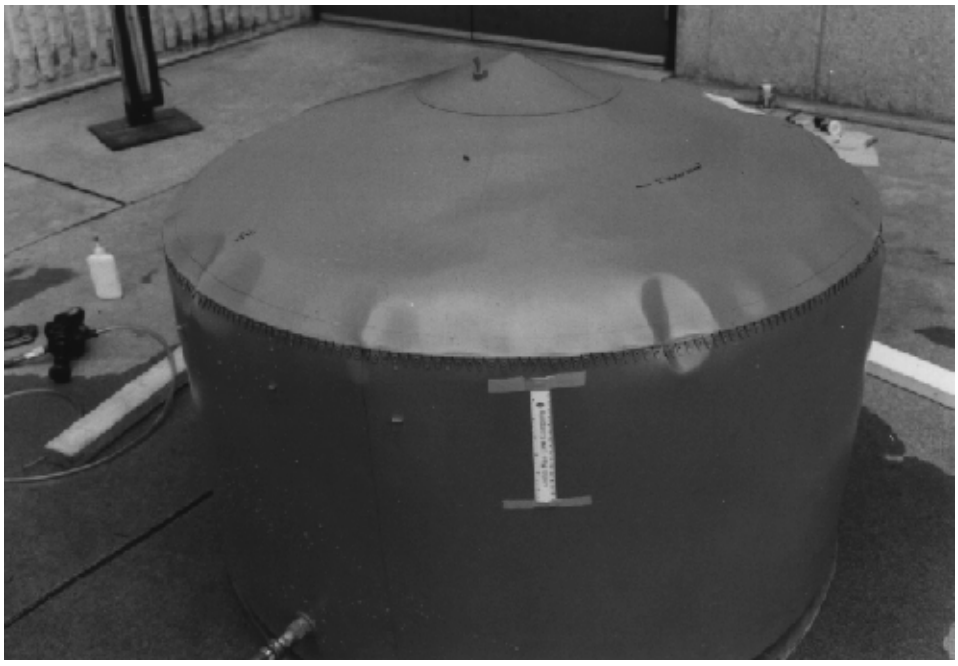

b: after test

Figure 4.33: Large Deformation Buckles on Large Slope Roof Tank

5.0 DYNAMIC TESTING OF MODEL TANKS

To improve understanding of frangible joint behavior, verify analyses, and examine alternative designs, two model tanks were dynamically tested with different roof joints. The dynamic loading of internal burning was simulated by ignition of an air-methane gas mixture. These tests provided data on pressure loads and the response of the tanks. One of the two tanks represented a standard design, while the second one had a stitch welded joint between the top angle and roof.

These tests provide basic data which can be used to evaluate the present design rules. They provide results for comparison with analytical methods to ensure that the appropriate analysis is being used for other designs. Finally the tests provided data to verify the combustion analyses.

5.1 Design of Model Tanks

The design of the scale model tanks was based on existing oil storage tanks but with reduced scale geometry. The basic objective was to simulate the behavior expected in real tanks, while also providing reference data for analysis verification.

Experience has shown that frangible joints function as intended in larger tanks but that smaller tanks may not fail as desired. Therefore, the scale model tanks represented a smaller tank design. The model tanks could not have too thin a thickness, because of the difficulty in welding material less than 1/8 inch thick without causing significant distortion of the tank. Also, considered during the design is the limitation of the volume of the tank for testing safety, it was desired to have the smallest possible volume while still representing real tanks.

Figure 5.1 shows the basic construction of the tank with a continuously welded roof-to-shell joint. The tank is 7.5 feet in diameter and 8 feet high,

with a wall and roof thickness of 1/8 inch. The tanks were made of shell plates and angles made of ASTM A36 steel, which has a minimum yield stress of 36 ksi. The shell plate had an actual measured yield stress of 49 ksi, ultimate stress of 57 ksi, and Young's modulus of 28,000 ksi.

The alternate design tank was of the same size and material but had a stitch welded roof-to-shell joint. Figure 5.2 shows the details of the stitch welding on the second tank.

Assuming a linear stress scaling with respect to thickness and diameter, the minimum 1/8 inch thickness and 7.5 foot diameter models are representative of typical 11.2 foot diameter tanks. Since the model tanks are made of steel, the uplift pressure and diameter to height ratio cannot be both scaled linearly. Eight feet was chosen as the height to make the models similar to a 12 foot high prototype.

Analysis performed on a model tank without a reinforced floor indicated potential uplift and an approximately equal probability of failure at either the roof-to-shell joint or the bottom-to-shell joint. The expected uplift of the tank made it necessary to either anchor the tank to a foundation or to reinforce the bottom so that the bottom joint would not fail during the test.

The tank bottoms and the bottom-to-shell joints were reinforced to ensure failure at the frangible joint. This also provided a strong point for lifting and transporting the tanks. The floors of the models had a thickness of 1/4 inch, thicker than the value of 11/64 inch obtained by a linear 2/3 scaling of a tank. The strengthened floor was reinforced by I beams and C channels. Gussets were welded on the bottom joint of the continuously welded tank model. These reinforcements reduced the deformation of the bottom plate and bottom-to-shell joint and prevented joint failure during the test. The second model tank with a stitch welded roof-to-shell joint had no

gussets, since the reduced strength of the top joint ensured frangible joint failure.

Rafters were included in the tank, both to be representative of a typical tank and to prevent distortion of the roof during transportation. The rafters were supported on the inner edge by a column and at the outer edge by the shell walls. The rafters were scaled linearly from a typical design.

Access into the tanks was provided by one manhole and two nozzles on each tank for routing wires. To prevent pressurization of the tank while filling the balloon, a 1/4 inch hole was drilled in the shell of each tank close to the floor.

5.2 Structural Analysis of Model Tanks

5.2.1 Axisymmetric Large Displacement Static Analysis

Axisymmetric large displacement analyses were performed using shell elements with plastic capability. The model used a bilinear material, with a Young's modulus of 30,000 ksi, Poisson's ratio of 0.3, a yield stress of 36 ksi, and a plastic modulus of 600 ksi. The value of yield stress was the minimum one for the model tank material ASTM A36 steel. The yield stress was later measured as 49 ksi. By resting the bottom on compression only elements, the support of the tank was modeled as an elastic foundation. The foundation had a modulus of 200 psi/in (which is the value for fair to good subgrade), but no resistance to uplift.

Figure 5.3 shows the model and the detail of the roof-to-shell joint. A refined mesh was used in the region of both joints, with an element length of 1/4 inch. The model used 100 shell elements for the bottom, 101 interface elements for the foundation, 100 shell elements for the shell and 60 elements on the roof. The ANSYS 4.4 computer program was used for the calculations.

Since the uplift force is a square function of the tank diameter but the weight of the shell is a linear function, uplift will occur for tanks with small diameters (unless the height-to-diameter ratio is very large). The uplift of the bottom causes bending and compression near the shell-to-bottom joint. Figure 5.4 shows that, for the model tank, the mid-plane equivalent stress at the bottom shell is of the same order as that of the top shell. Without reinforcing the bottom joint, failure could happen at either of the joints.

Figure 5.5 shows the deformed tank with bottom uplift at an internal pressure of 4.5 psi. This was the expected failure pressure for the continuously welded tank, which had the standard roof-to-shell joint and 36 ksi yield stress. Under that pressure, the compression stress at the top joint caused a mid-plane equivalent stress equal to the yielding stress (Figures 5.6). This is confirmed by Figure 5.7, which shows the stresses in the element next to the top shell (element 301 in Figure 5.3.b). Yielding occurs in this element at about 3 psi pressure due to bending, and at about 4.5 psi yielding occurs through the entire element. Compared to linear analyses, nonlinear large displacement solutions give a smaller stress magnitude near the joint. The large displacement stresses also decrease much faster on the roof compared to a linear solution (Young, 1989).

5.2.2 Axisymmetric Large Displacement Dynamic Analysis

Using the predicted no venting pressure time history, as shown in Figure 5.15, a dynamic analysis was performed on the same axisymmetric finite element model. The calculation was done by specifying the time and pressure up to 5 psi in 35 steps. The calculated results were very close to that of static analysis, as shown in Figure 5.8. This can be explained by Figure 5.9, a Fast Fourier Transform analysis of the predicted pressure time history. The 10 decibel band width of the pressure is only about 2 Hz, while the natural frequency of the model tank is calculated to be 35 to 51 Hz as

shown in Figure 5.10. Thus the natural frequency of the tank is significantly higher than the loading frequency, so the tank will respond to the pressure loading as a static load. If the vapor in the tank is not stoichiomentric or venting occurs, the burning process will be slower and even closer to a static load.

5.2.3 3-D Large Displacement Analysis

A 3-D analysis was made of the top joint region of the model tank. The finite element model consisted of 1000 shell elements and represented half of the tank top, with the top angle, rafter gussets. The rafters were modeled by beam elements. The model and boundary conditions are shown in Figure 5.11.

At an internal pressure of 2 psi, buckling calculations were made with and without rafters. These calculations show that the buckling load will be increased by rafters, because they will increase the stiffness of the tank. However, since the calculated first buckling mode of the tank was 17, which means about 3 waves between rafters, the rafters might enhance buckling by exciting mode 18. The calculated linear buckling modes of the tank are shown in Figure 5.12. Although the large buckles occurred on the roof, the shell also buckled with the same mode. The waves on the shell can easily be seen when the roof is not plotted, as shown in Figure 5.13.

5.2.4 Analysis of Stitch Welded Tank

A 3-D finite element model was built for the stitch welded tank. Figure 5.14 shows the contour of the equivalent stress of the shell and roof at 1 psi pressure. The displacement has been scaled up so the openings at the joint can be seen clearly. The calculated maximum opening at the joint is 0.16 inch.

Because the stitch welded joint is not axisymmetric, the failure pressure of the tank cannot be calculated analytically. As can be seen from Figure 5.14, the stresses have a very high gradient near the joint. A much finer mesh in that area would be required to capture stresses accurately. The finite element model shows an equivalent stress of 30 ksi in the top angle near the stitch welds when the internal pressure is 1 psi. This indicates failure would initiate at a pressure of 1.5 to 2 psi.

A simplified prediction was made by assuming that the circumferential stress near the joint of the stitch welded tank was equal to that of a continuously welded tank at the same pressure, but the meridional force on the shell was carried only by the portion of welded joint. Using a linear calculation, the continuously welded tank loaded by 4 psi pressure would have a peak circumferential compression stress of 34.22 ksi and meridional stress of 2.58 ksi, located at the edge of the conical roof. Since the stitch welded tank has a weld to space ratio of 1 to 7 at the joint, a circumferential stress of negative 34.22 ksi and a meridional stress of 20.64 ksi were assumed. The equivalent stress of the joint is 48.0 ksi. Therefore, it is predicted that the tank needed about 4 psi pressure for the average stitch weld stress to reach the yield stress of 49 ksi. Because of the stress concentration, the real failure pressure should be lower than that value.

As discussed, the predicted first buckling mode of the continuously welded tank was 17 as shown in Figure 5.13. Neighboring modes had very close buckling loads. Using 18 equally spaced stitch welded joints was expected to enhance the possibility of exciting the buckling mode that would help lower the failure pressure.

5.2.5 Prediction before test

From our calculations, the predicted failure pressure of the continuously welded tank would be about 4.5 psi. After yielding, the shell

should buckle and the welded joint break. Since the real model tank plate had a measured yield stress of 49 ksi compared to the 36 ksi used in the analysis, the tank would fail at about 6 psi pressure by linear scaling. The design equations in API 650 calculated a 1.32 psi failure pressure of the tank. This was because API 650 design rules were based on material with 32 ksi yield stress and bending moment at the joint was not considered.

It was expected that failure initiation of the stitch welded tank would be between 1.5 and 2.0 psi (the upper bound estimate of failures is 4.0 psi). The failure mode would be the shell buckling followed by tearing of the welded joint.

The dynamic test of scale model tanks confirmed that our calculations and predictions were close to reality.

5.3 Test Description

5.3.1 Combustible Vapor

To control both the air-methane mixture and the magnitude of combustion, the combustible vapor was contained in a weather balloon inside the tank. This balloon was filled with 90 cubic feet of methane and air mixture at stoichiometric conditions, with the total mass of reactants designed to provide the appropriate pressure rise inside the tank. The mass of the air-methane was chosen so that a complete constant volume burning in the tanks would reach a pressure of 20 psi. A point ignition source located at the center of the balloon was used to ignite the methane. The predicted pressure without venting shows a rise time of about 0.4 seconds to a pressure of 10 psi, as shown in Figure 5.15. Also plotted is the predicted pressure rise in the stitch welded tank. The pressure rise was presumed to be much slower with a peak pressure of about 5 psi.

5.3.2 Dynamic Test

The tests were performed in a field, with adequate surrounding space to prevent the danger as a result of the tank fragments. The test procedure consisted of the following steps:

1. Start power generator, computers and amplifier for preheating.
2. Fill the balloon in the tank with methane to the designed volume.
3. Initialize the data acquisition system.
4. Fill the balloon with the compressed air until the mixture reaches the proper mass ratio.
5. Start video camera, high speed camera and data acquisition system, then ignite the mixture.
6. Record strains and pressures, and pictures of the test on films and videos.

5.3.3 Instrumentation

A diagram of the instrumentation is shown in Figure 5.16. The methane from the cylinder and the air from the compressor flowed into the balloon though flow meters at fixed flow rate, adjusted by pressure regulators. Pressure and temperature were monitored and the filling time was controlled to ensure that the correct mass of gases were put into the tank. A solenoid valve was used to control flow into the balloon.

Ignition was by a spark plug mounted at the end of a pipe. Two long probes were used to make a large spark. The spark was controlled by a normally open relay near the tank, which could be closed by pushing the ignition button at a safe distance. When activated, the coil sent a high voltage to the spark plug.

Data acquisition to monitor the pressure and strain was by a 486 computer with a DAS-50 card. The card can sample data at rates up to 1 MHz using an onboard memory with the capability of holding 1 million pieces of data. In our tests, the sample rate of 101 kHz was used. The entire burning and deformation process was recorded in the board and then copied to binary files and stored in the computer. The internal pressure measured by pressure transducers were read through separate channels and eight strain signals were read sequentially into another channel of the DAS-50 by a EXP-16 switch monitored by a Zenith 8080 computer.

The strains were measured by eight strain gauges mounted at the top of the tank shell. The gauges were located two inches down from the roof-to-shell joint along the circumference. There was a 10 inch circumferential space between strain gauges. To capture the buckling of the tank, the strain gauges were in pairs mounted at both inside and outside. The signals were amplified before transmission to the DAS-50 through 100 feet long cables. The output of the amplifiers had a ratio of 4,000 microstrain per volt with a full range output of 5 volts, corresponding to 20 times the yielding strain. The tests were recorded by two high speed cameras (500 frames per second), and three common video cameras (30 frames per second with exposure time of 1/1000 second), placed in positions around the tank.

As will be discussed in the following sections, some difficulties were encountered with data acquisition during the tests. This has been frustrating when evaluating the data. The best effort has been made to recover the data. Unfortunately, there is no opportunity to repeat the tests so we must work with the available data.

5.4 Results of Testing

5.4.1 Open Air Testing of Deflagration

In developing the combustion model, one of the basic assumptions is that the combustion process is by deflagration. Deflagration is a relatively slow process where combustion proceeds in a wave from the ignition point. In contrast, a detonation is extremely rapid, with the combustion essentially occurring simultaneously throughout the space. It was expected that combustion in a storage tank would be by deflagration. To verify that combustion was by deflagration and to test the ignition procedure, open-air tests of balloons were performed.

A total of four open-air tests were performed. The first three tests used balloons filled with 40 cubic feet of air-methane mixture. Ignition was by spark at approximately the center of the balloon. In all cases, the combustion occurred by deflagration. The last test used 90 cubic feet of air-methane and was performed at night. The flame could be seen through the balloon. About 1/3 of a second was required from ignition of the air-methane mixture until the balloon burst, revealing a spherical combustion front, as shown in Figure 5.17. When filled with 90 cubic feet of air-methane mixture, the balloon had a diameter of 5.4 feet. Before bursting, the diameter of the balloon increased to 7 feet. The burning process continued for about another 1/10 of a second. The test in the open air was equivalent to a 100% vented case. The burning process was predicted to be faster in the tanks.

5.4.2 Failure Mode of the Model Tanks

Testing of the two tanks was performed on October 3 and 4, 1992. The continuously welded tank was tested first. As can be seen in the videos and high speed films of the tank, failure was initiated by one local buckle that occurred at the top joint. The buckling bent the roof plate sharply, followed by local failure of the weld. Failure then proceeded from the initiation

location in both directions around the tank. The failure continued until only 4 feet of weld remained intact. The pressure on the opened roof pushed the tank to one side, broke the anchors and nearly tipped the tank over, as shown in Figure 5.18. In this test all four of the rafters in compression were buckled and one of them detached from the shell. The two rafters in tension were both detached from the rafter gussets. Cross sections of the tank are plotted in Figure 5.19 to show the residual deformation. Some of the buckling went more than 1 foot down from the top of the shell. Figure 5.20 is a plot of the deformed tank and Figure 5.21 shows the tank after test. The initial buckle looks very similar to the buckles on the small scale model tanks statically tested.

The failure of the joint of the continuously welded tank was mainly in the base material of the roof plate adjacent to the weld, with portions of the top angle broken, as shown in Figure 5.21.e and 5.21.f. This confirms the tendency of welders to make the weld stronger than needed or possible reduction of strength in the heat effected zone.

In the test of the stitch welded tank, the roof completely separated from the tank due to failure of the stitch welds. High speed photographs of the tank show that venting of the tank occurred before failure. This occurred due to "scalloping" of the roof between the welded joints. One of the welded joints failed first, followed by failure of the adjacent welds. Since the joint was much weaker than the tank shell, the roof was "blown off" from the tank and only the top shell was affected.

Distortion of the top shell of the stitch welded tank was much less than that of the continuously welded tank. The top shell deformed with 18 local buckles corresponding to the stitch welds. The buckling was more severe where the first stitch weld failed. Figure 5.22 shows the tank after the test and Figure 5.23 shows cross sections of the stitch welded tank. Figure 5.23

(a) also shows the locations of stitch weld joints and strain gauges where gauges 1 through 4 were on the inside wall of the tank and gauges 5 through 8 at the outside. As can be seen, the major shell deformations were limited to within 8 inches from the joint and were relatively small. Figure 5.24 is the plot of the deformed tank shell. In the test, all the rafters remained intact, without any buckling.

5.4.3 Pressure Measurements

During the test of the continuously welded tank, the pressure transducer failed, so no direct pressure readings are available. A second pressure transducer was added prior to the stitch welded tank test. The pressure readings for this test are plotted in Figure 5.25. The peak pressure was about 5 psi. The time from ignition until complete tank venting was about 0.5 sec.

From pictures of the stitch welded tank test, it is clear that venting began early in the test. Thus, the stitch welded tank pressures are expected to be lower than that in the continuously welded tank. Figure 5.26 shows the measured pressures in the stitch welded tank and the predicted pressure rise in continuously welded tank using combustion analysis. It appears that the predicted pressures are reasonable for the continuously welded tank, so the prediction will be used in the discussion of the strain data.

5.4.4 Strain Measurements

Strain measurements for the continuously welded tank are shown in Figure 5.27. This figure shows the measured strains (left axis), the predicted pressure (right axis), and the predicted strains using finite element analysis (dots at pressures for which the strains were calculated). The largest pressure used in the finite element analysis was 5.5 psi. Strains at the gauge

locations were calculated using a 2-D large deflection finite element analysis, with the finite element model shown in Figure 5.3. By plotting these together, the pressure in the tank at failure can be estimated.

It is believed that in this test, the active gauges and temperature compensation strain gauges inside the tank were switched, causing the strain readings for channels 1 through 4 to appear positive. The same is believed to be true for gauge 8. The readings for these gauges have been reversed in Figure 5.27. Also note that the time of initiation of combustion is not known for this test, so the starting time of the predicted pressure curve has been shifted to make a reasonable correlation with strain data. During the test, the motors in the high speed cameras introduced a high frequency noise into the data acquisition system. Numerical filtering was used to remove those noises.

The strain readings are initially proportional to the pressure rise, with the severe deformation occurring at about 6 to 8 psi. The cause of the short spike in the readings for the four gauges inside the tank in not known. Considering that venting is not instantaneous following the initial failure of the joint, it is believed that the peak pressure was between 8 and 10 psi. This is reinforced by the comparison between the predicted strains at 5.5 psi and the measure strains.

Results for the stitch welded tank are given in Figure 5.24, with the measured pressure curve superimposed. It can be seen that for several of the gauges the deformation of the shell was in proportion to the pressure until about 5 psi. Beyond that point, the failure of the stitch weld and the stress redistribution of the shell caused uneven deformation.

The predicted strains from 3-D finite element analysis are plotted in Figure 5.29. The calculation was performed on the model shown in Figure

5.11 for 1.0 psi pressure. The curves show that the stitch welds caused a complicated stress-strain field at the joint. The strain gauges at different circumferential locations are expected to have different strain readings. For strain gauges outside the tank, more compression is expected when they are under the stitch welds (gauges 5 and 7 in Figure 5.28-a). Gauges mounted inside the tank between stitch welds should have larger negative readings (gauges 2 and 4 in Figure 5.28-b). The testing results are in qualitative agreement with this calculation.

Strain gauges 1 and 5 were located near a stitch weld. The stitch welds cause the shell to initially bend inwards, with a positive strain inside and negative strain outside. At the end of the test, the shell was flattened and stretched where gauges 1 and 5 were located, so the strain readings show positive residual strain. Gauges 3 and 7 behave initially like gauges 1 and 5. Strain gauges 3 and 7 were close to a weld where the shell was pulled in. The bending changed the curvature, leaving compression strain on the outside and tension strain on the inside. Gauges 2 and 6 were located between two stitch welds, and mainly show compression. Gauges 4 and 8 were between another pair of stitch welds. The shell bent out and the residual strain is the opposite, tension on the outside and compression inside.

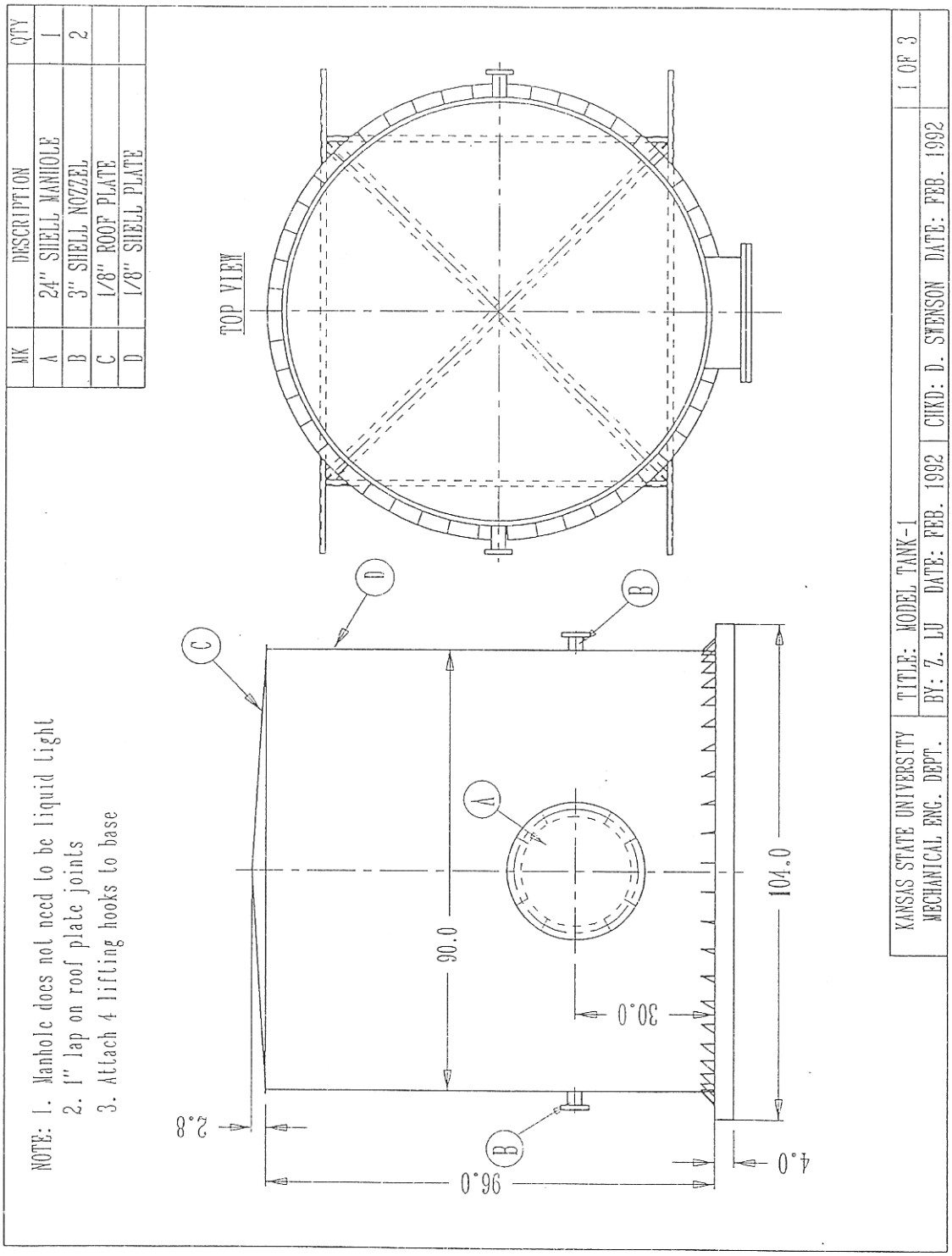

Figure 5.1: Continuous Weld Tank Construction

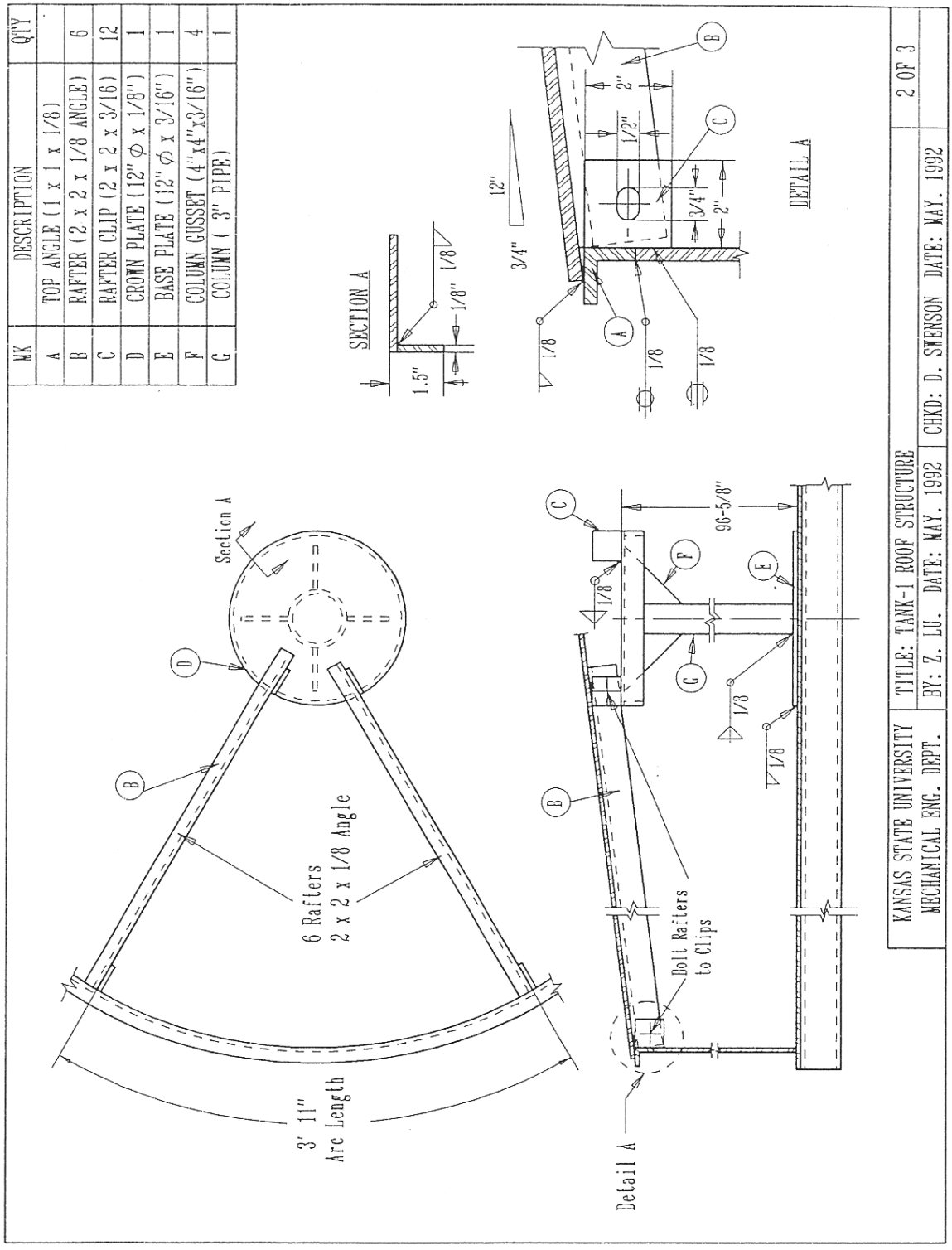

Figure 5.1: (Continued) Continuous Weld Tank Construction

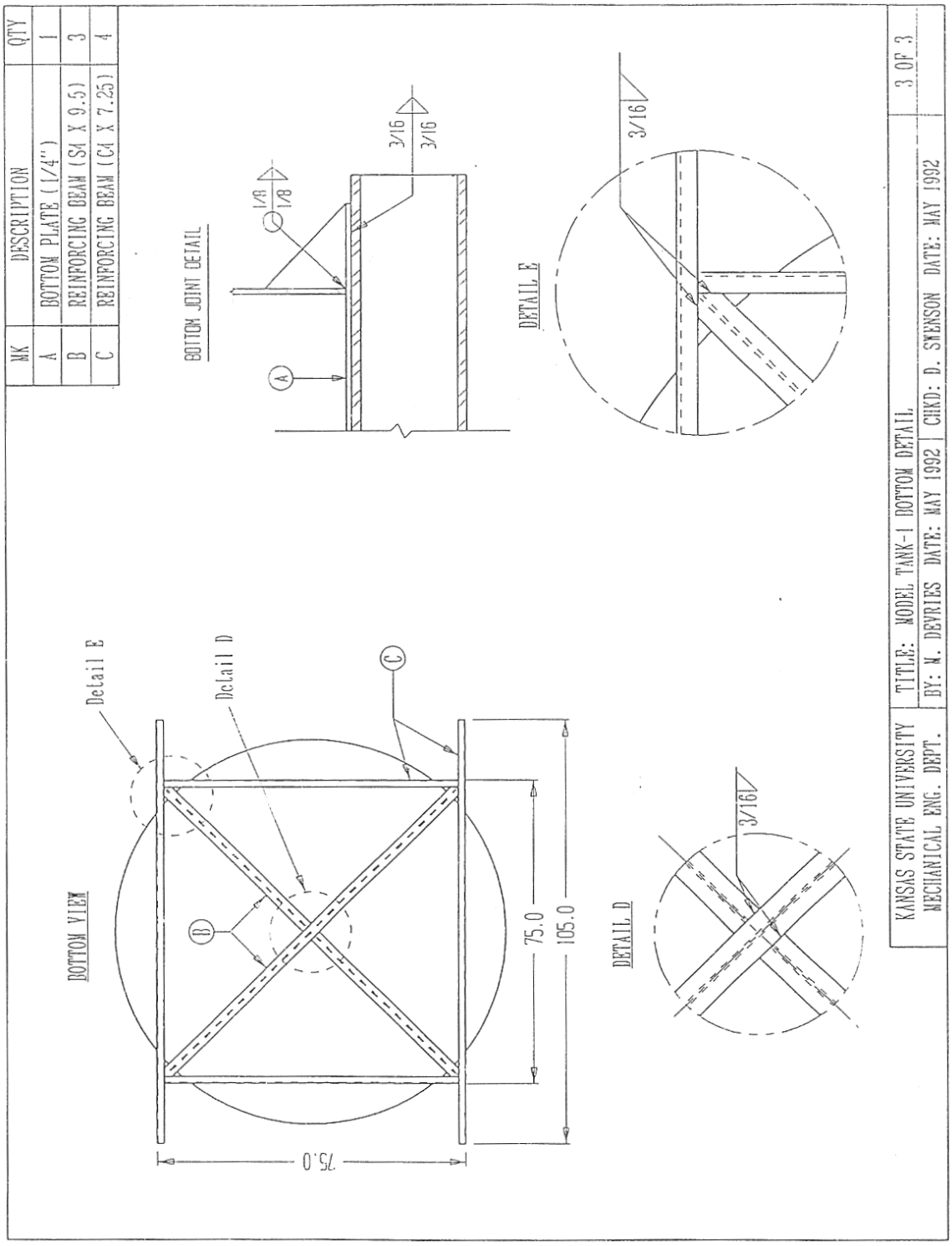

Figure 5.1: (Continued) Continuous Weld Tank Construction

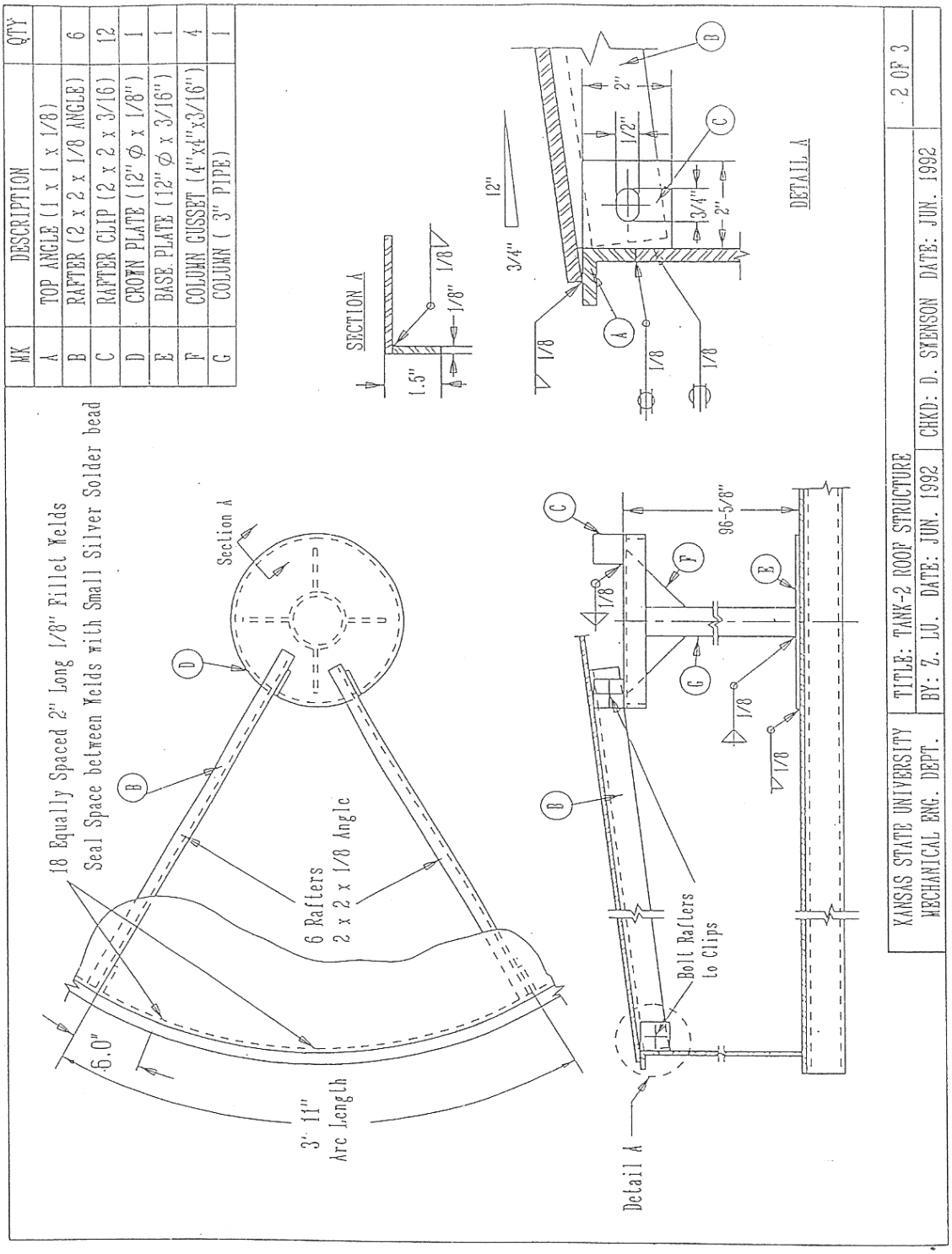

Figure 5.2: Stitch Weld Tank Construction

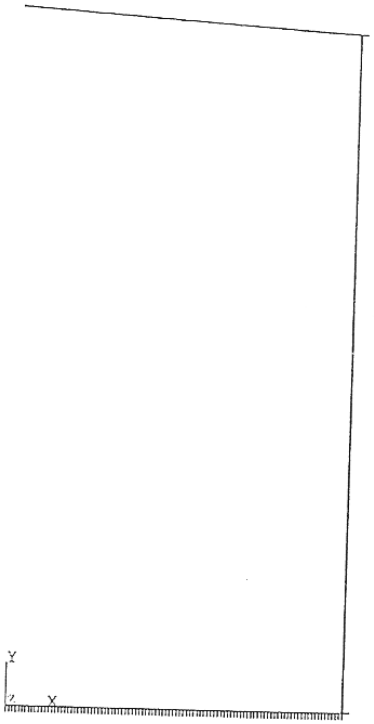

a: Entire Model

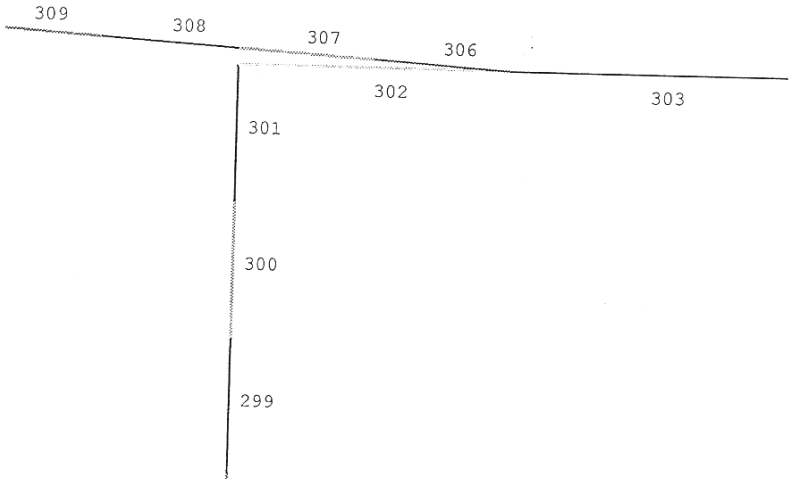

b: Detail at Frangible Joint

Figure 5.3: Finite Element Model Used in 2-D Analysis

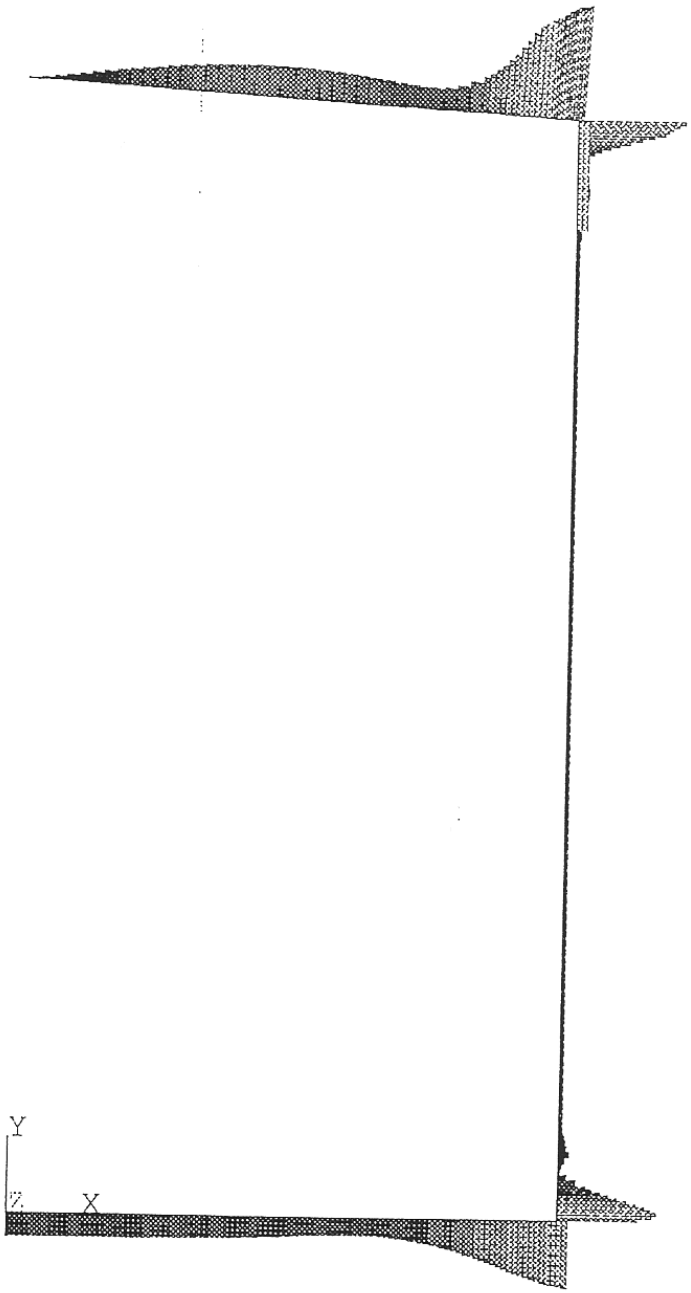

Figure 5.4: The Equivalent Stress of Model Tank under 4.5 psi Pressure At Middle Shell Surface (psi), result by ANSYS

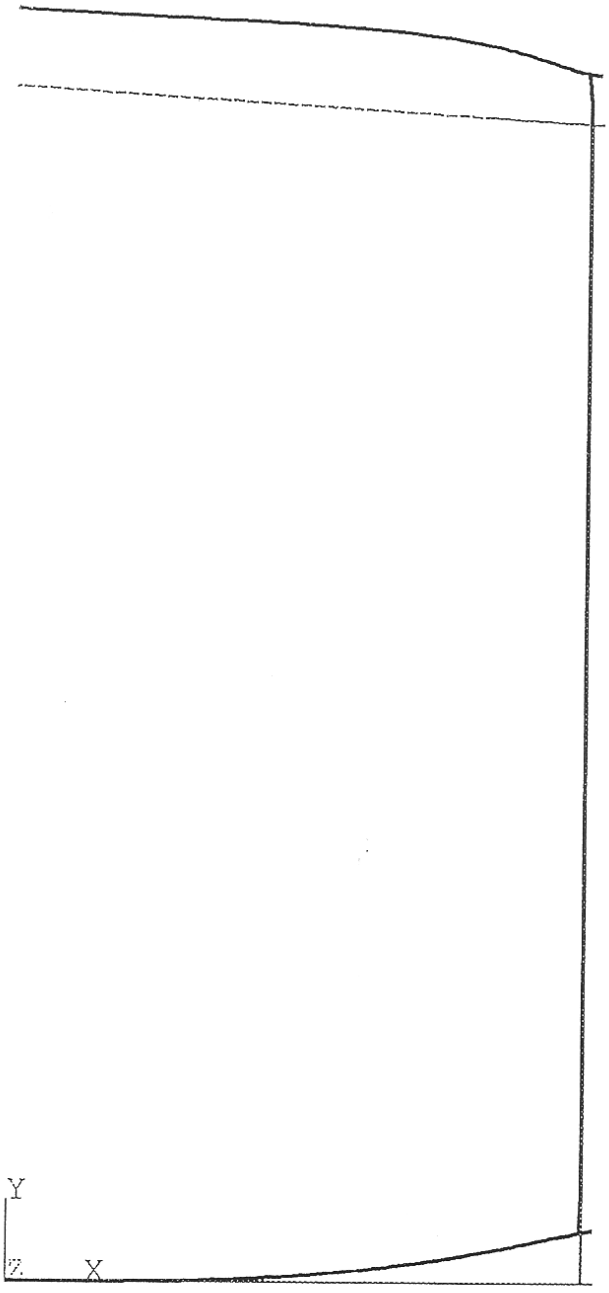

Figure 5.5 Deformed Tank at 4.5 psi Pressure. (Displacement Scale 2.7 : 1)

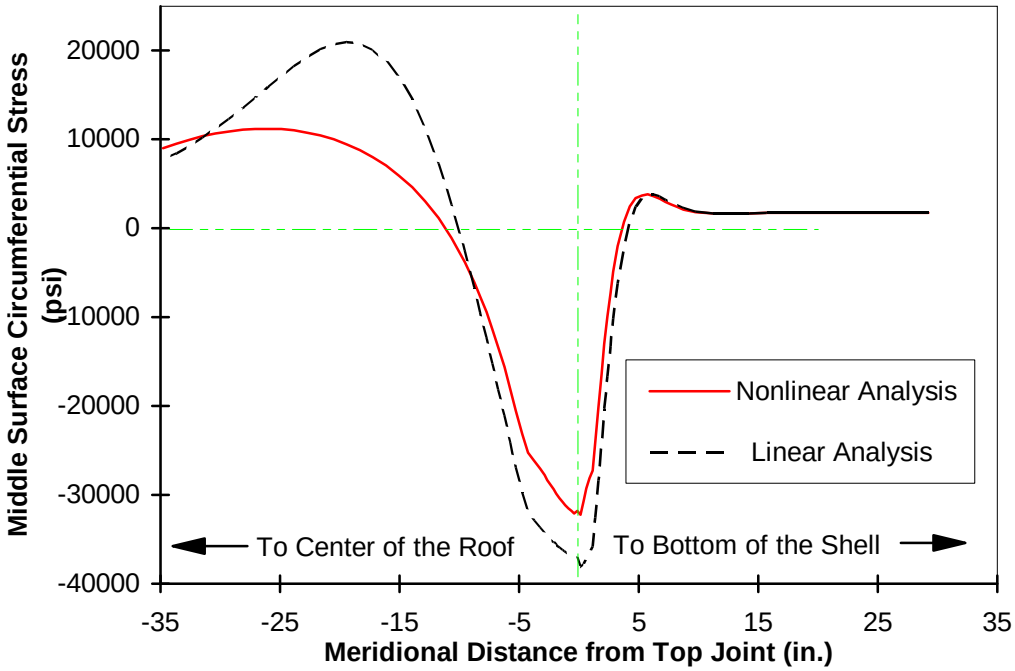

a: Circumferential Stresses

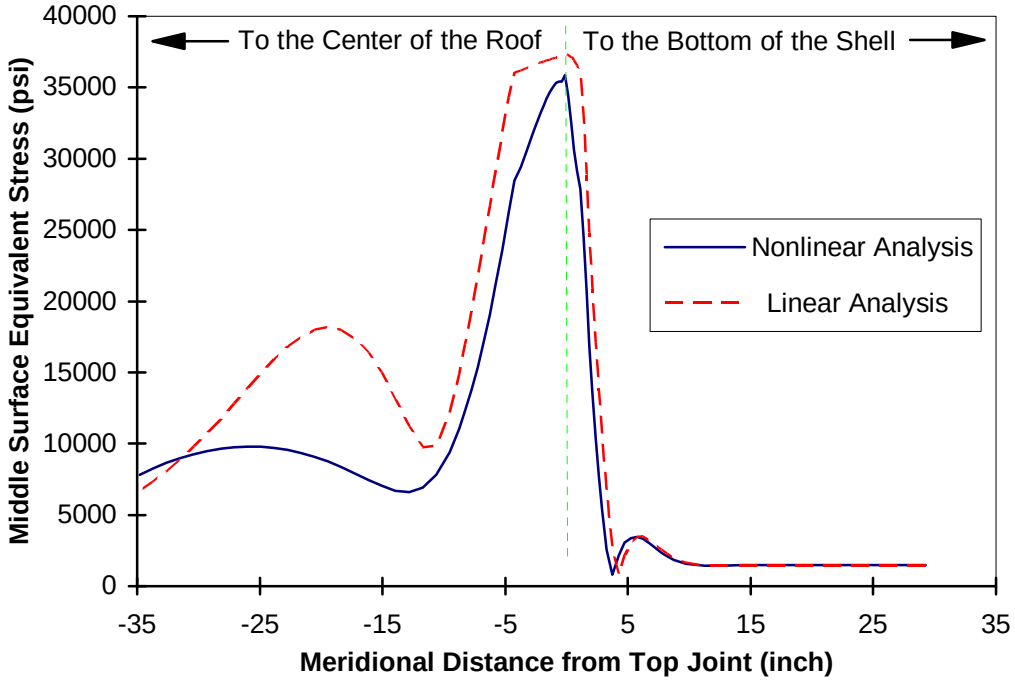

b: Equivalent Stresses

Figure 5.6: Linear and Nonlinear Stresses in Compression Region

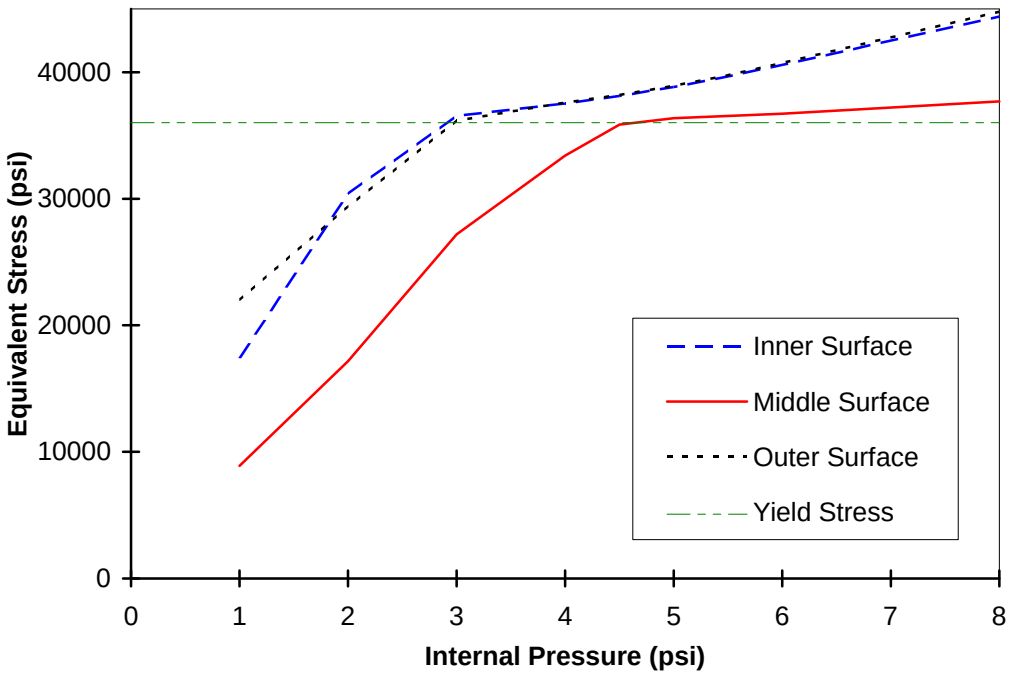

Figure 5.7: Equivalent Stress in Roof Adjacent to Joint

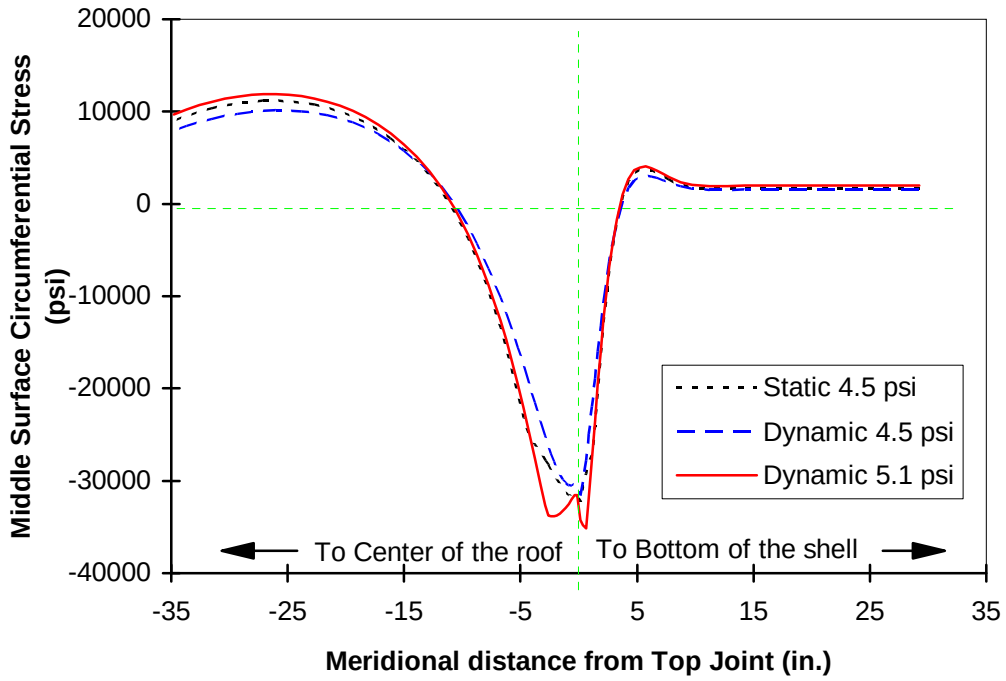

a: Element Circumferential stress

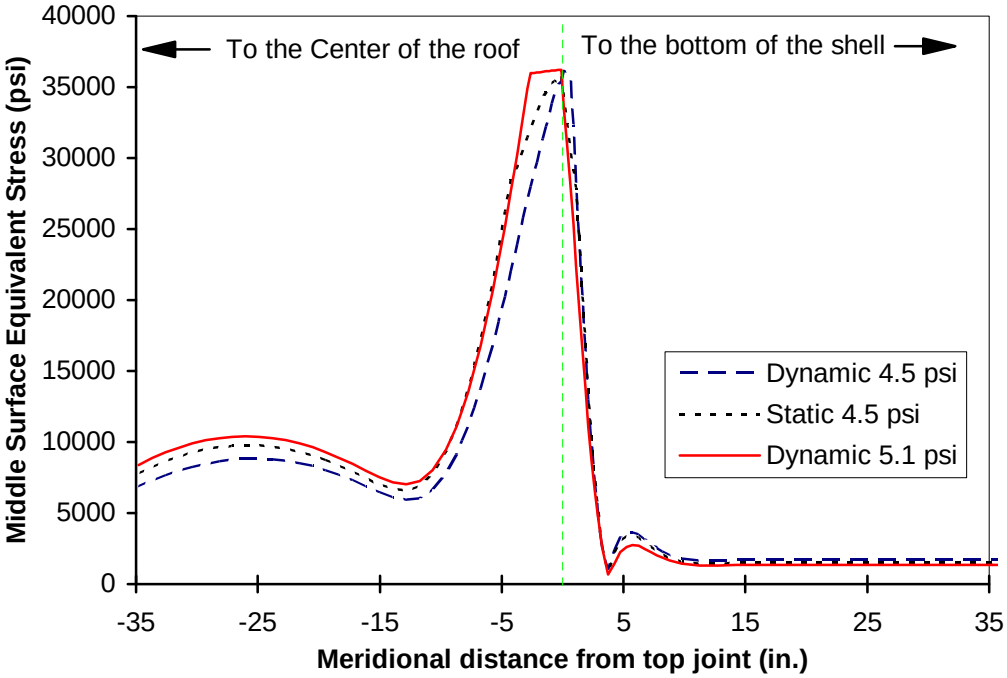

b: Element Equivalent Stress

Figure 5.8: Dynamic Stresses in Compression Region

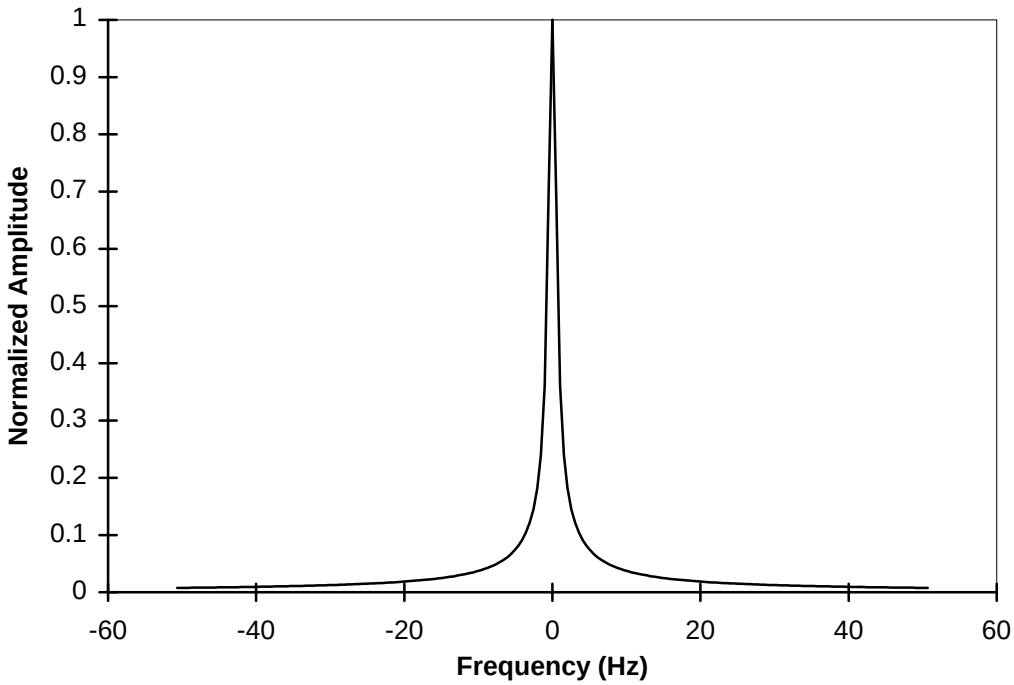

a: Amplitude Spectrum

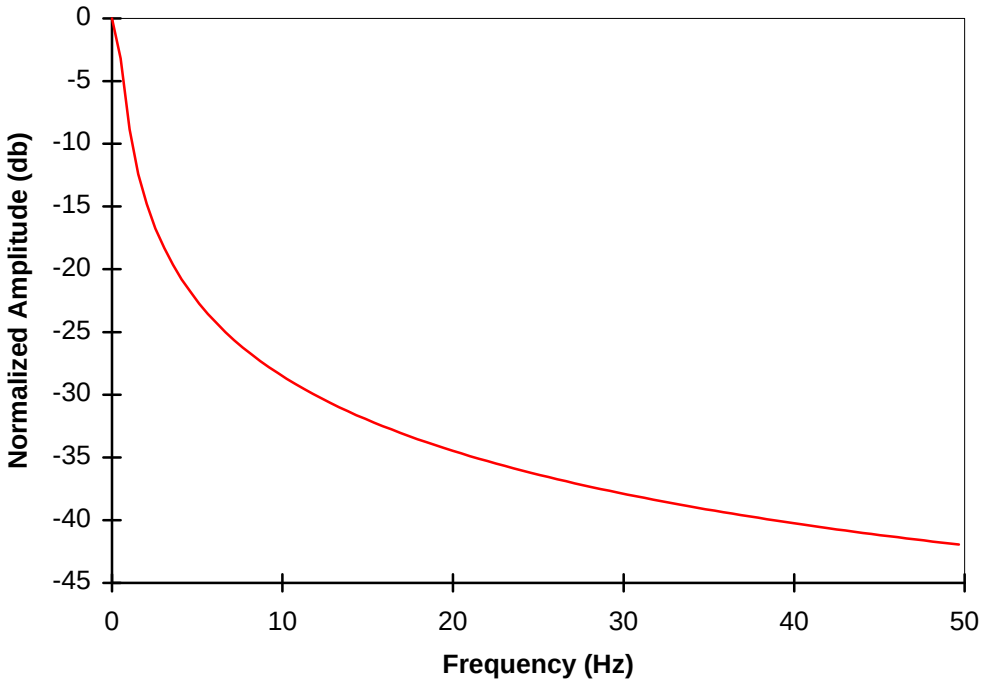

b: Spectrum

Figure 5.9: FFT Analysis of Predicted Pressure Time History

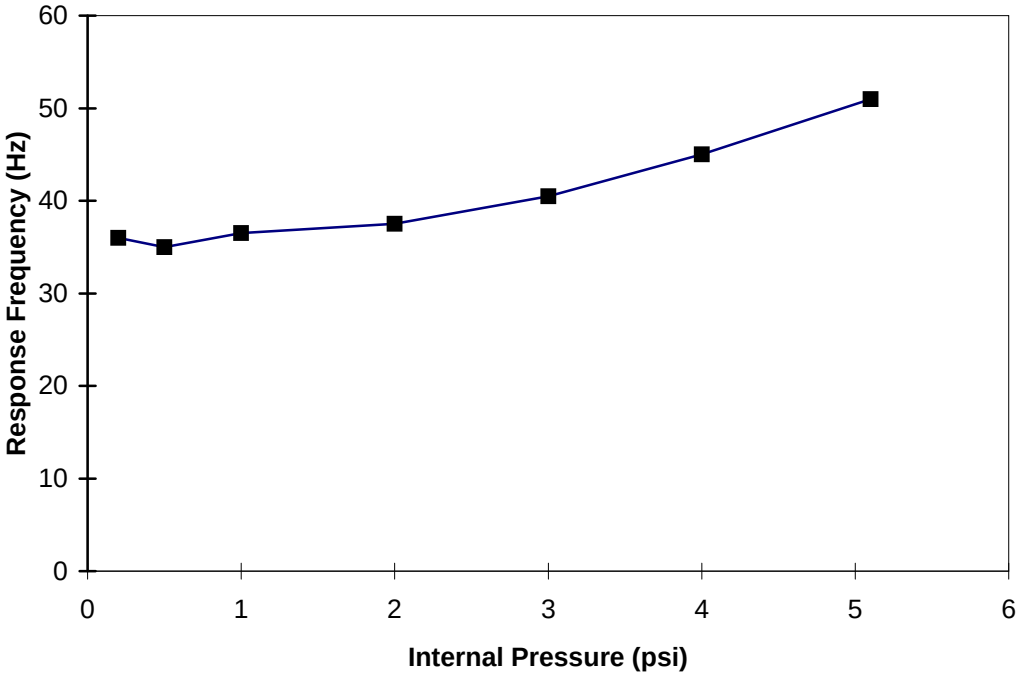

Figure 5.10: The Calculated Natural Frequency of the Model Tank

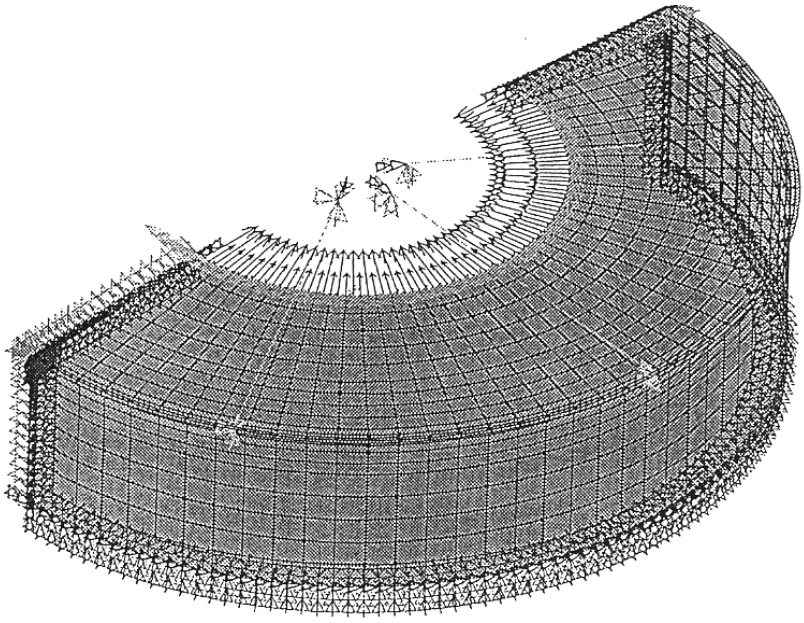

Figure 5.11: The 3-D Finite Element Model

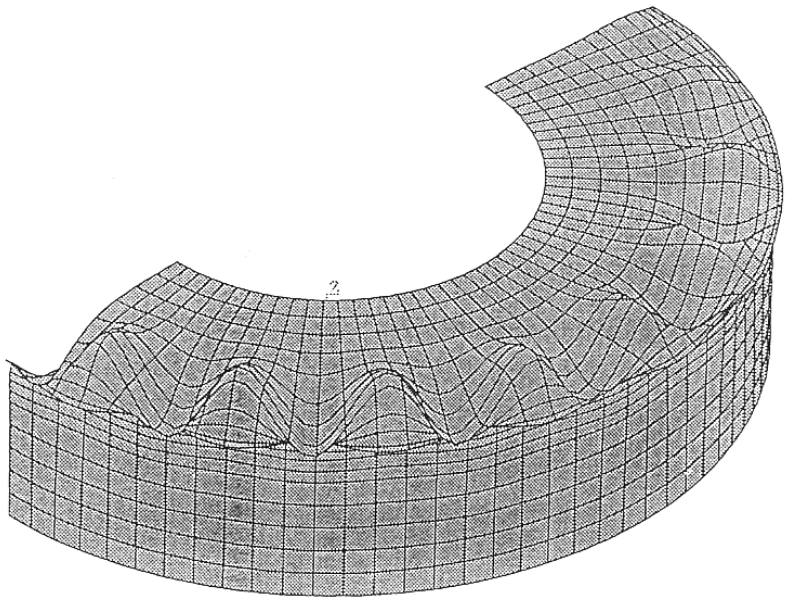

(a) First mode (mode 17) without rafters, critical pressure = 5.16 psi

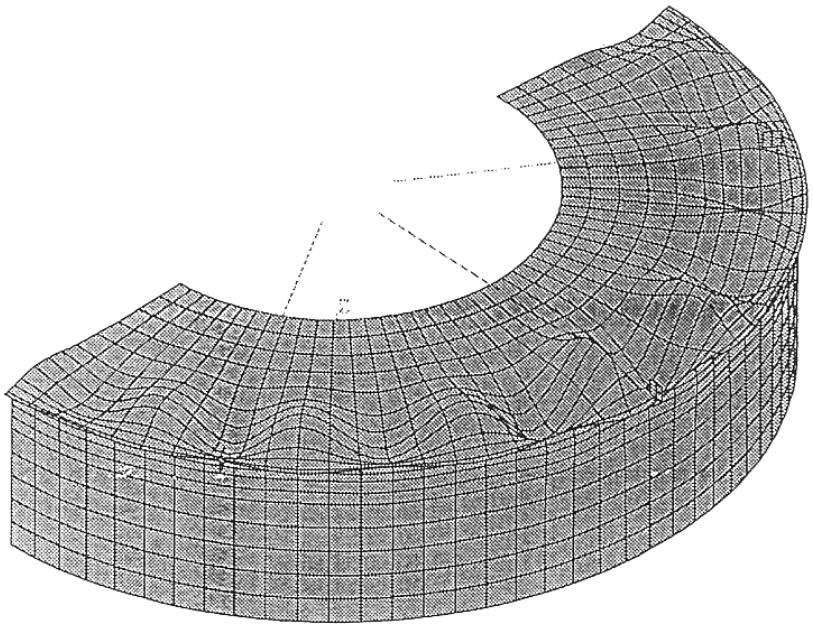

(b) First mode (mode 17) with rafters, critical pressure = 5.31 psi

Figure 5.12: Calculated Buckling Modes of Model Tanks

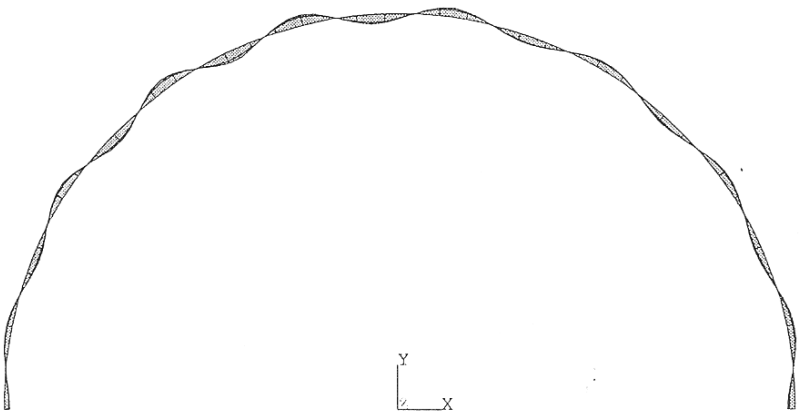

Figure 5.13: Buckling Waves (Mode 16) on The Shell of The Tank
(Roof Is Not Plotted)

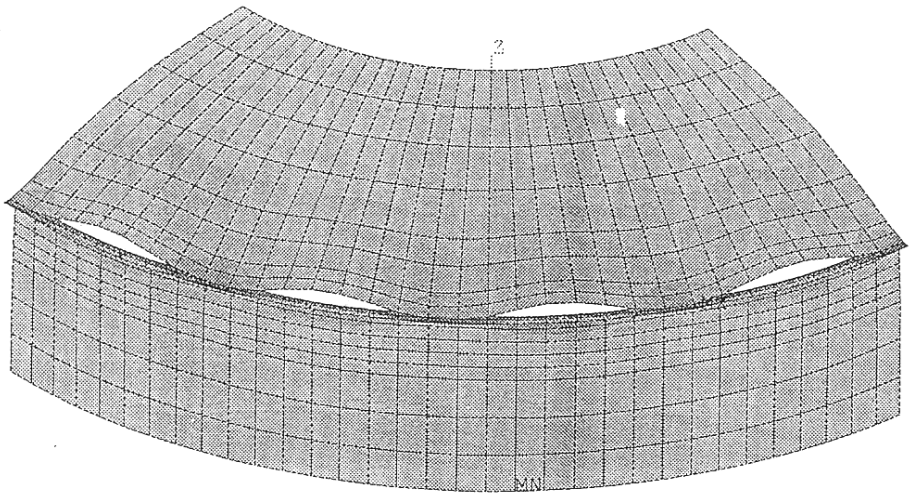

a: Middle surface equivalent stress contour

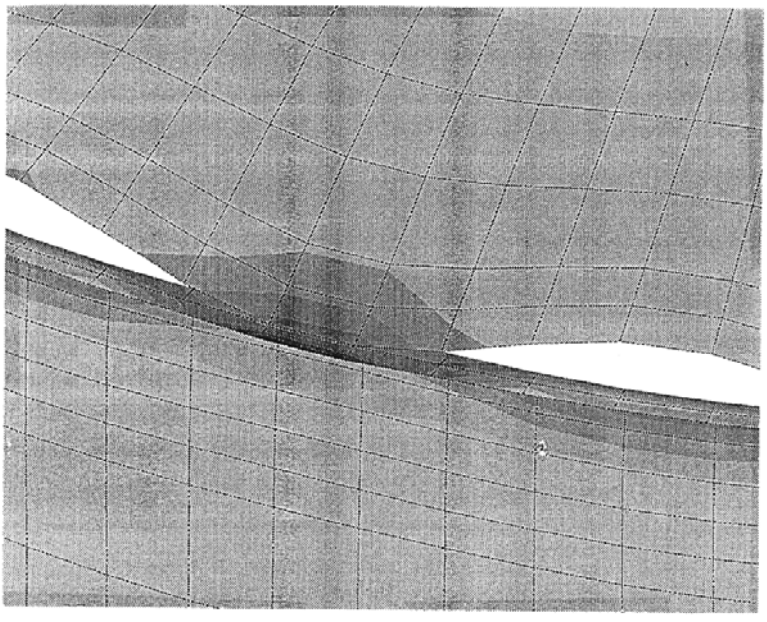

b: Stress contour in detail

Figure 5.14: Stress and Displacement of Stitch Welded Tank under 1 psi Pressure

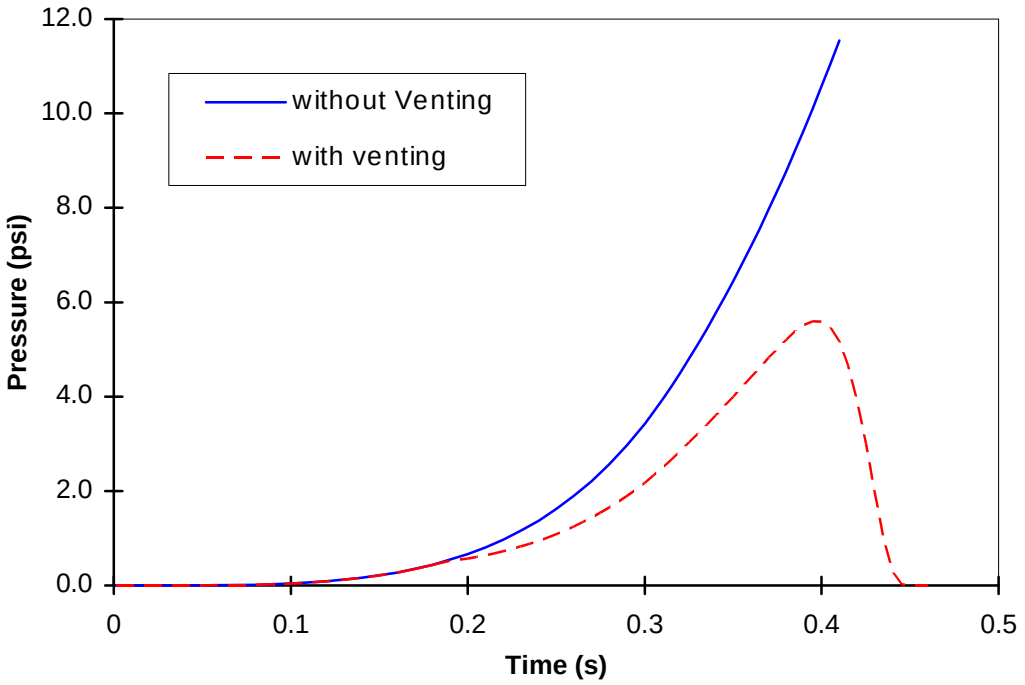

Figure 5.15: Pressure Rise In Model Tanks With And Without Venting

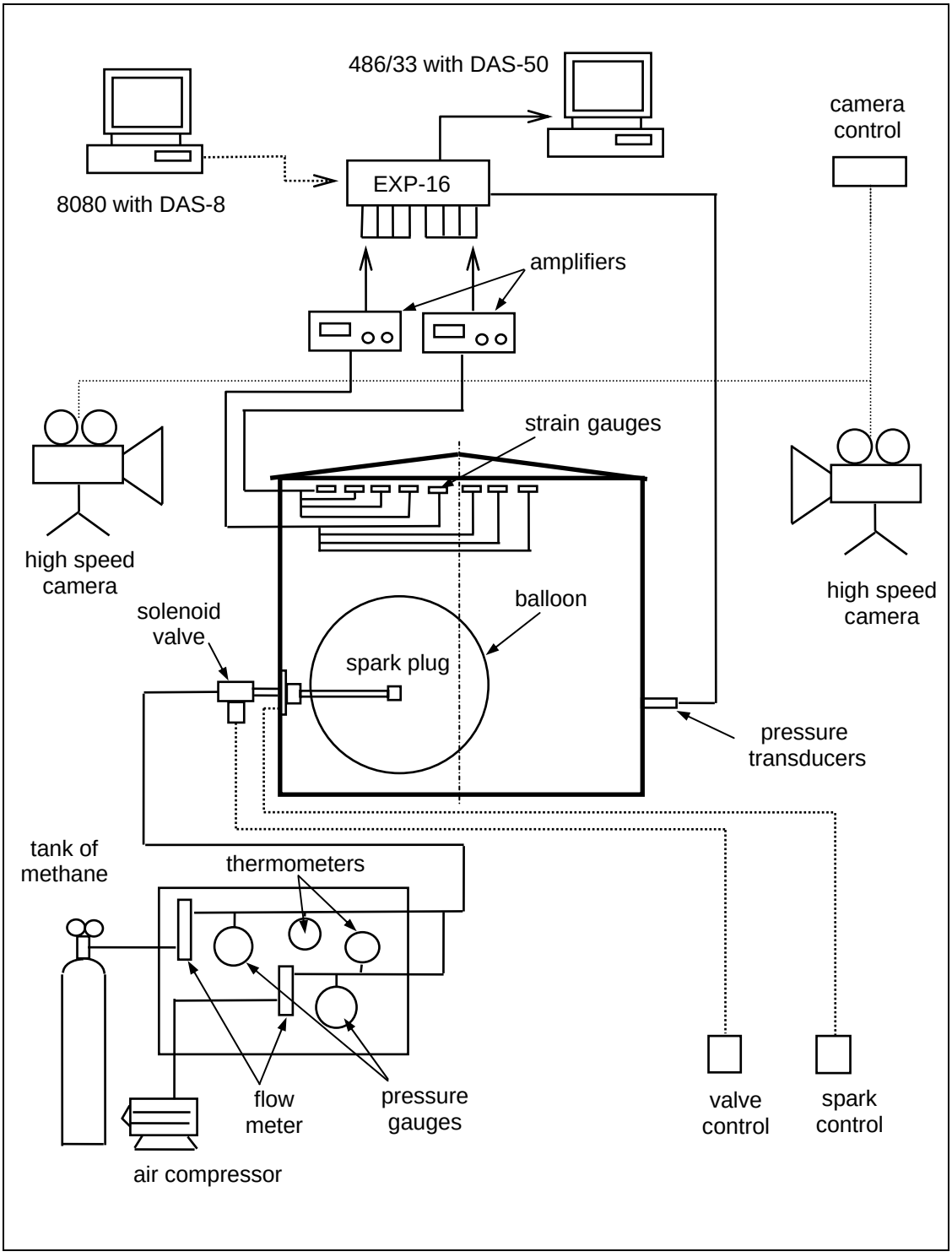

Figure 5.16: Instrumentation

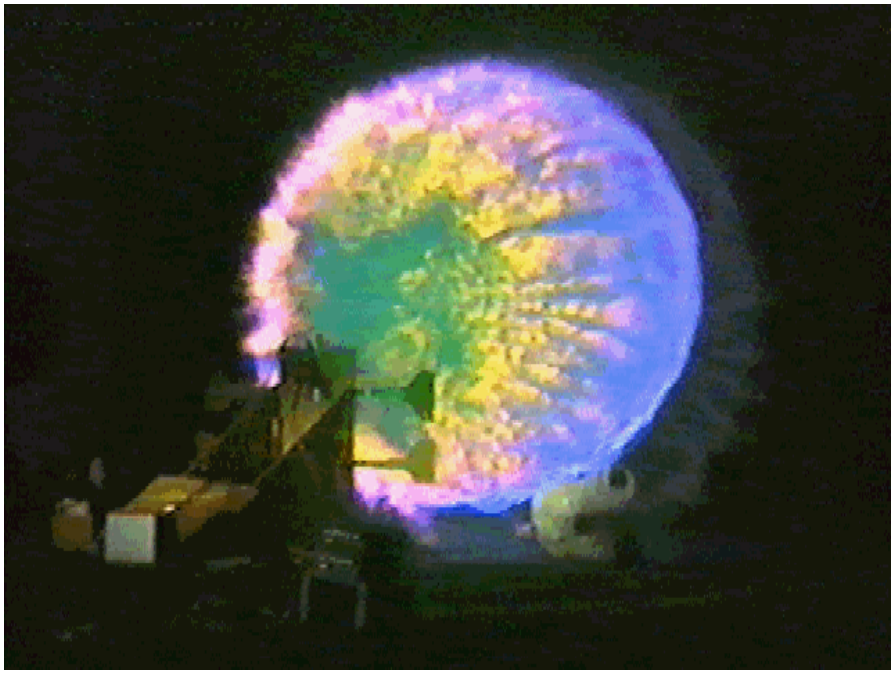

Figure 5.17: Open Air Balloon Test

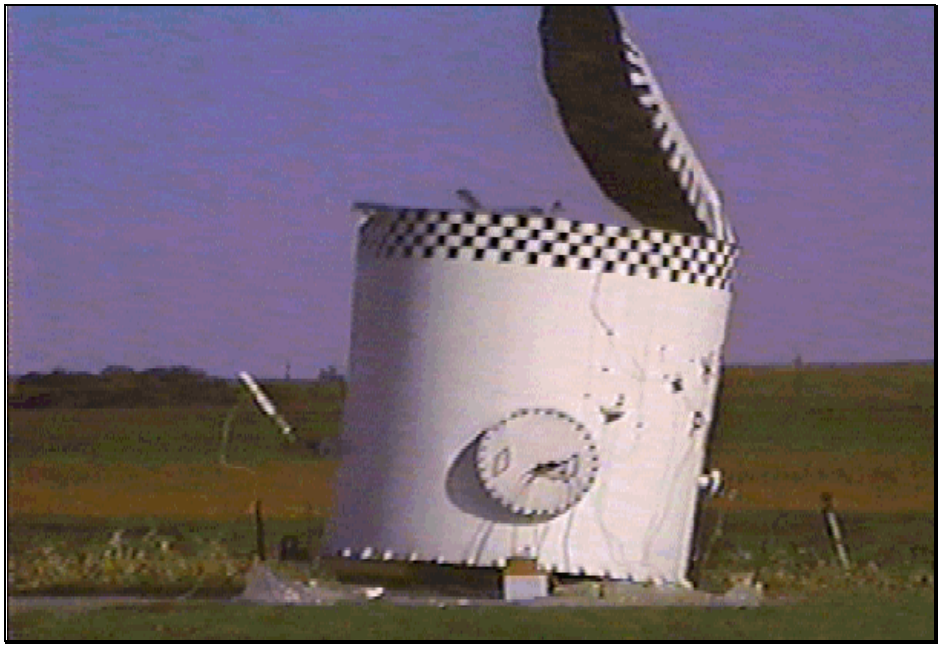

Figure 5.18: Continuously Welded Tank During Test

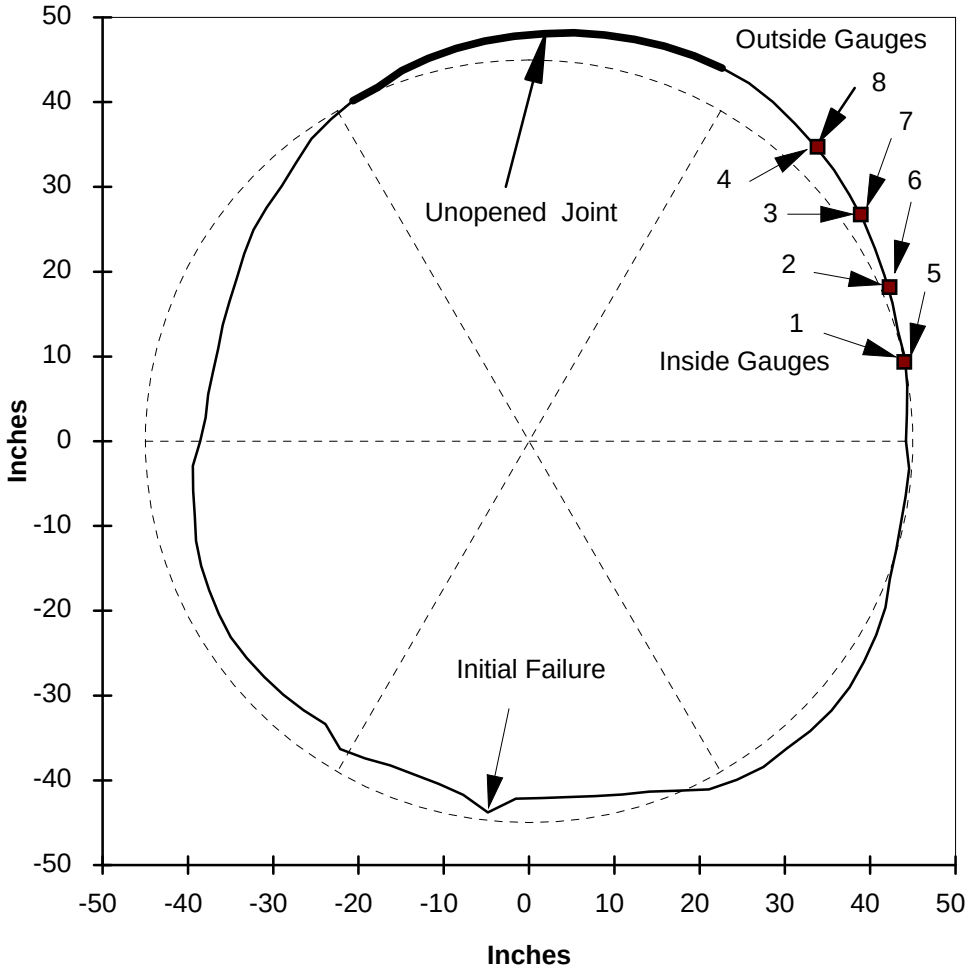

a: At Top of Shell

Figure 5.19: Cross Sections of Continuously Welded Tank

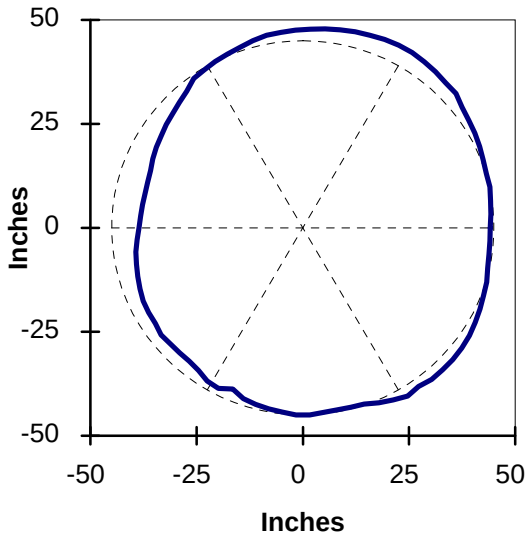

b: 5 Inches Down from the Top

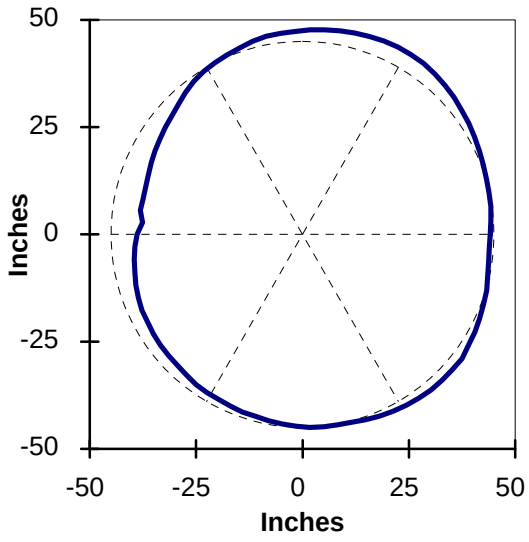

c: 10 Inches Down from the top

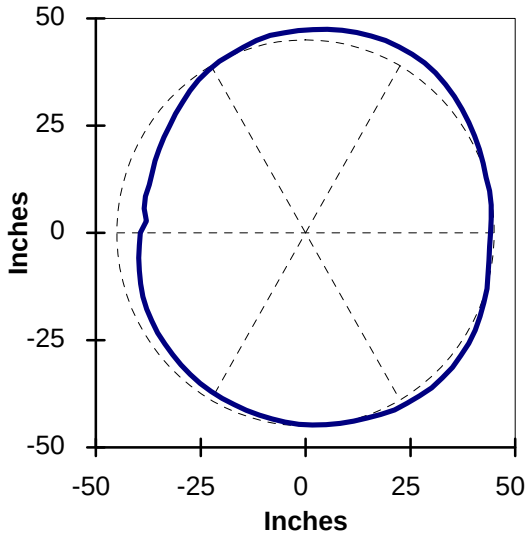

d: 15 Inches Down from the Top

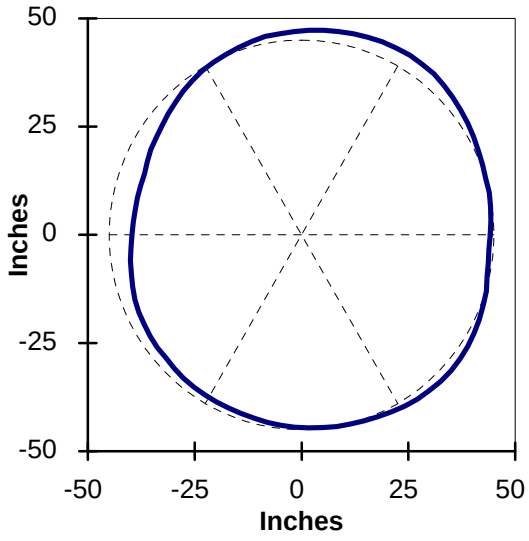

e: 20 Inches Down from the Top

Figure 5.19: (Continued) Cross Sections of Continuously Welded Tank

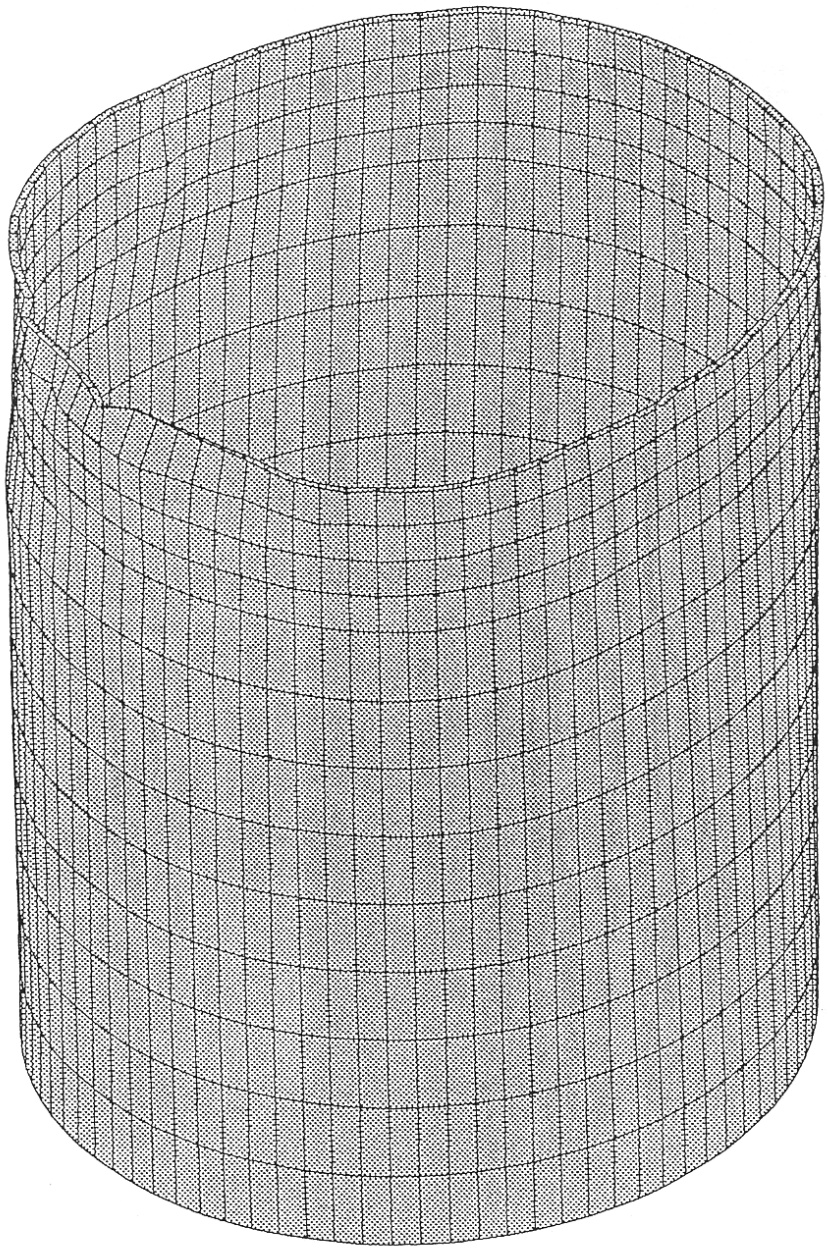

Figure 5.20: Deformation of Continuously Welded Tank

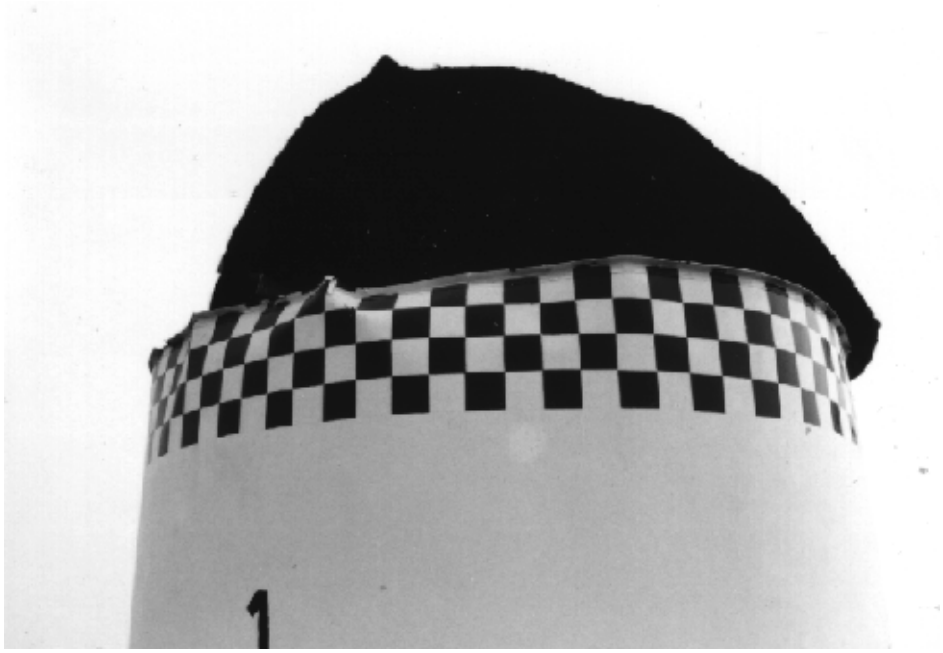

a: View of the Top with the Failure Initiation

b: View of the Top Shell

Figure 5.21: Continuously Welded Tank after Test

c: Buckled Shell and Angle at Failure Initiation

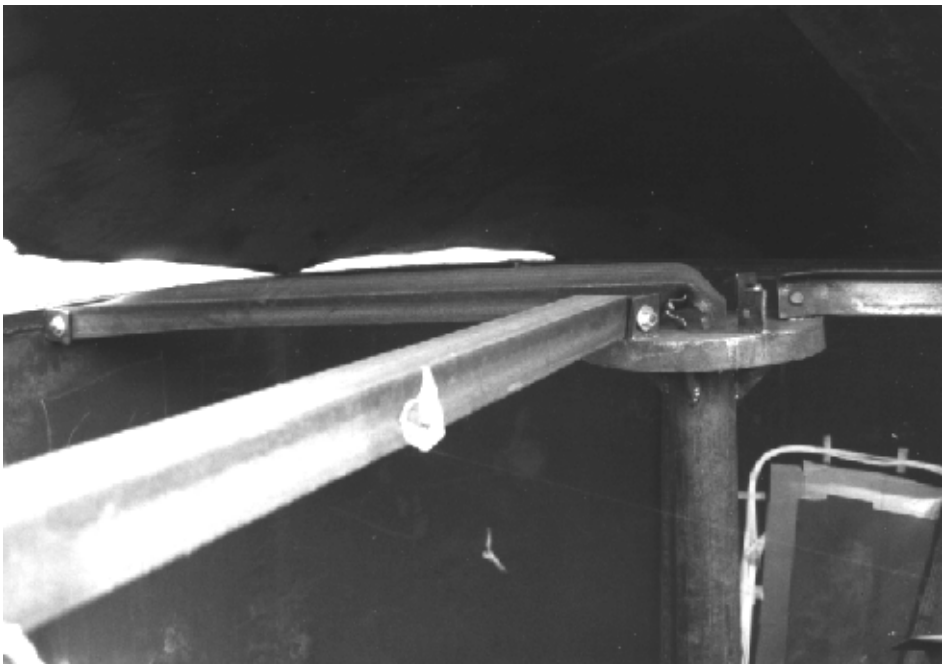

d: Rafters Were Bent and Detached

Figure 5.21: (Continued) Continuously Welded Tank after Test

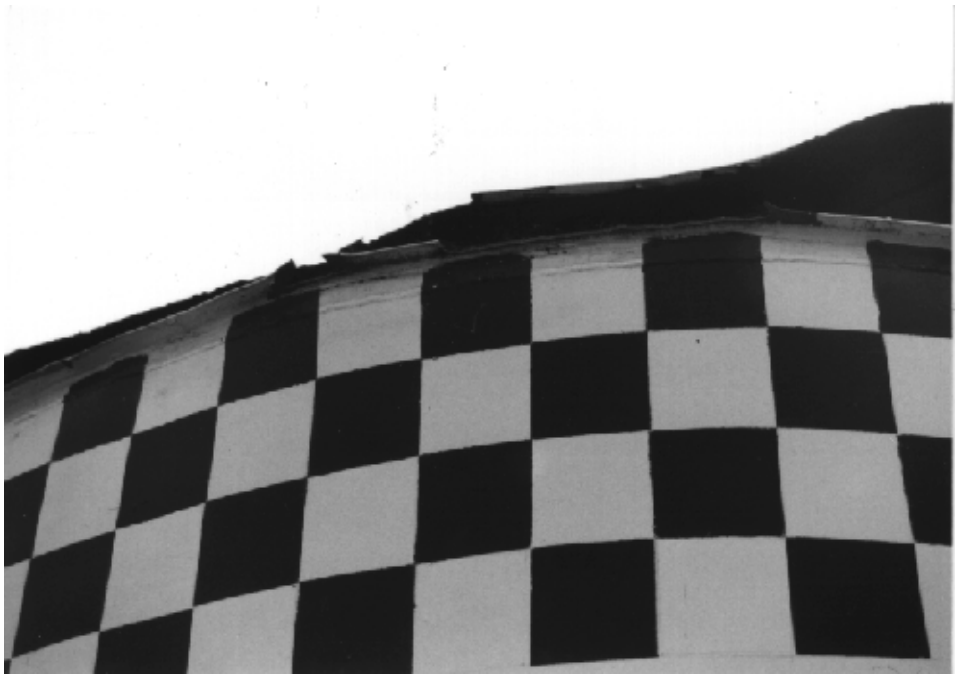

e: Failure Occurred on Roof Plate and Top Angle

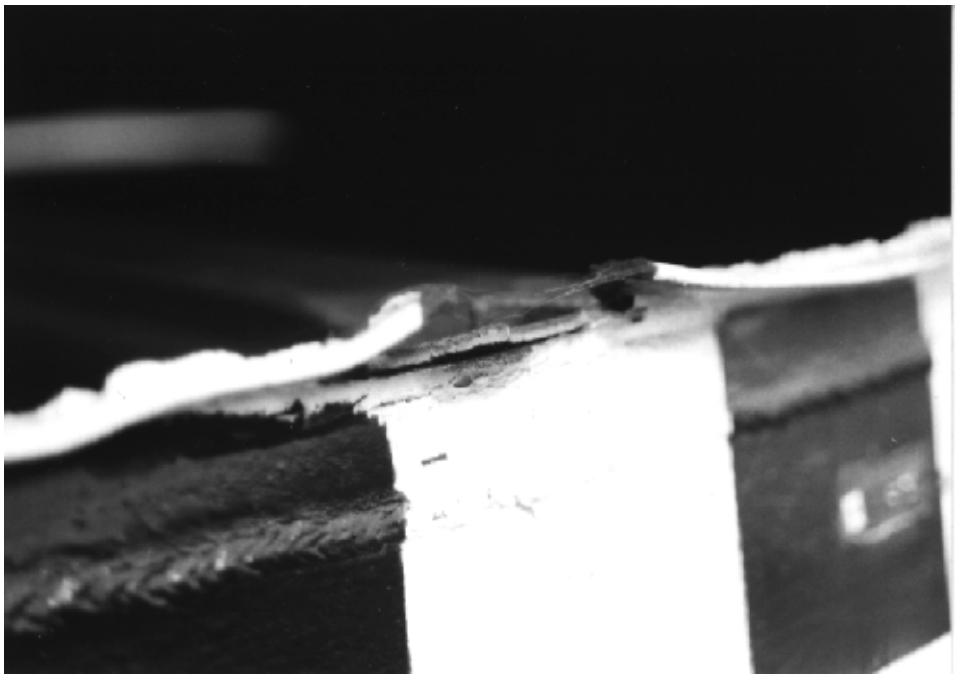

f: Close View of Broken Top Angle

Figure 5.21: (Continued) Continuously Welded Tank after Test

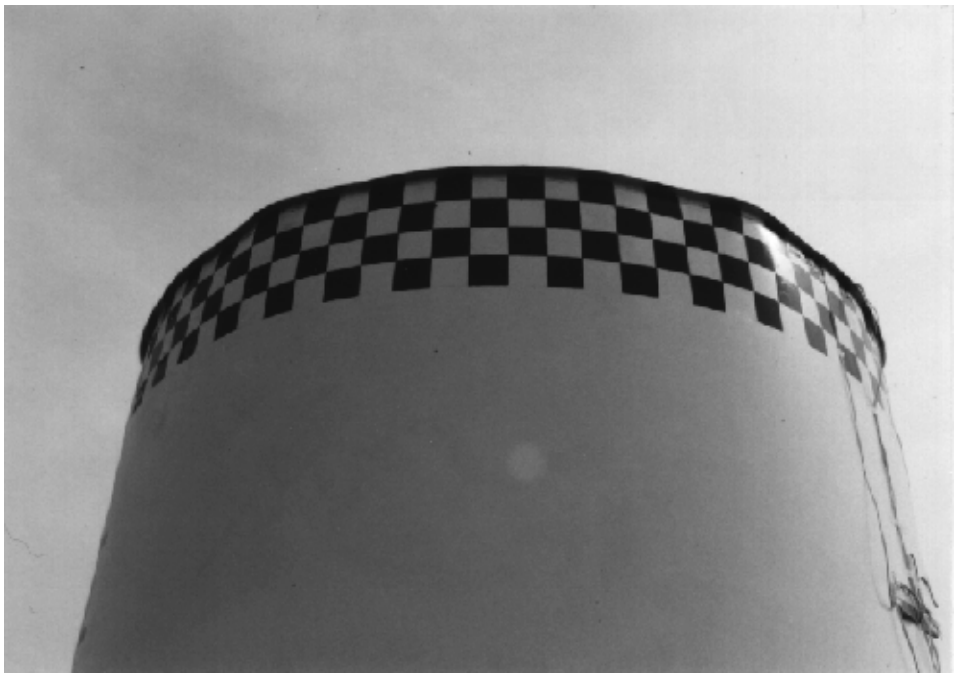

a: View of the Top Shell

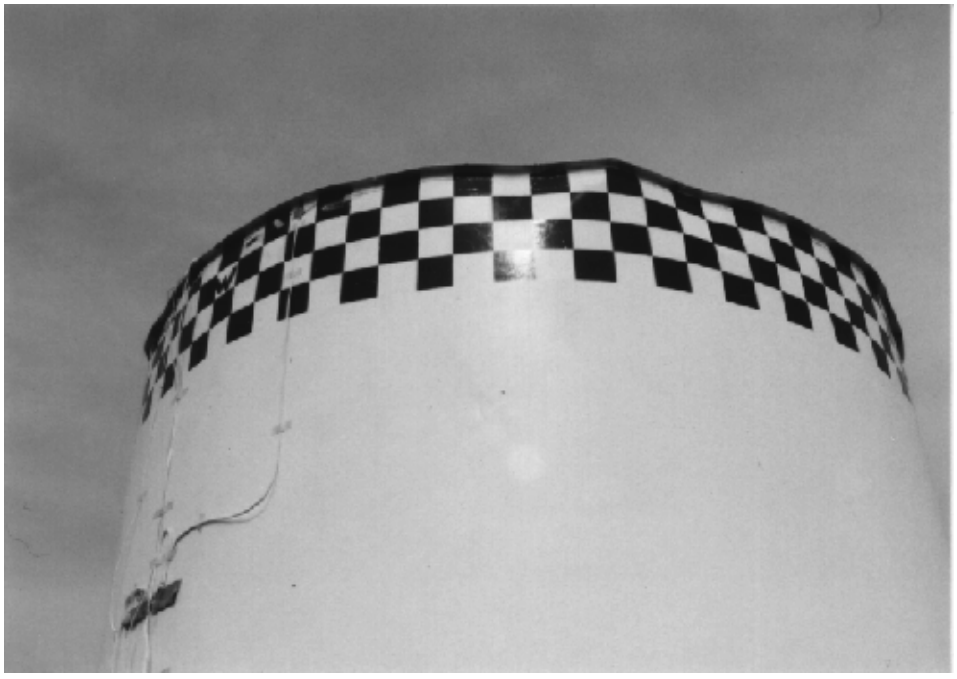

b: View of Top Shell Show the Failure Initiation

Figure 5.22: Stitch Welded Tank after Test

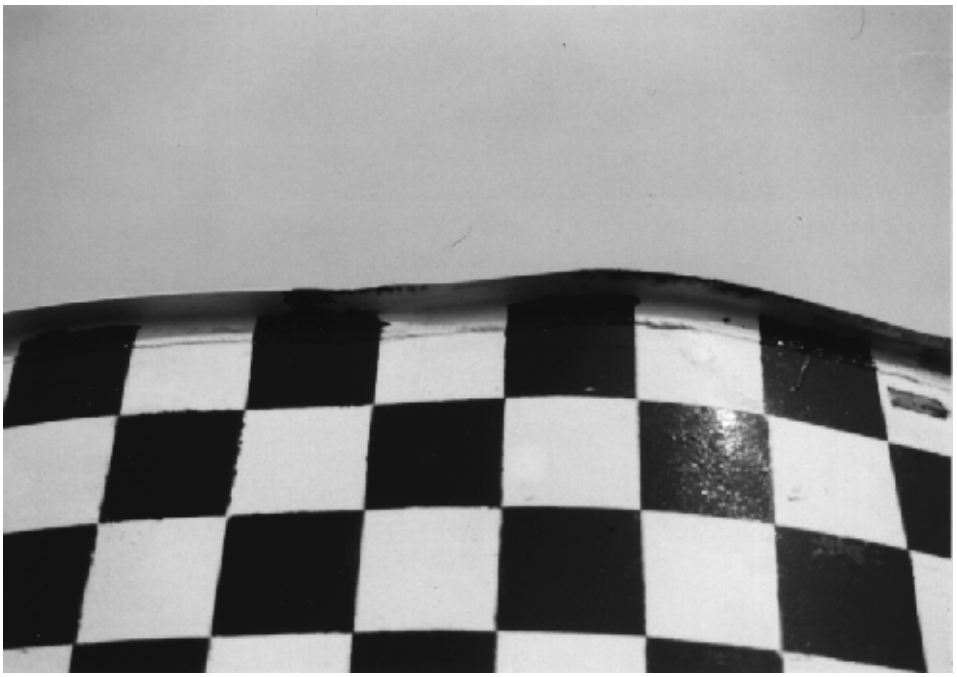

c: Buckling on Top Shell

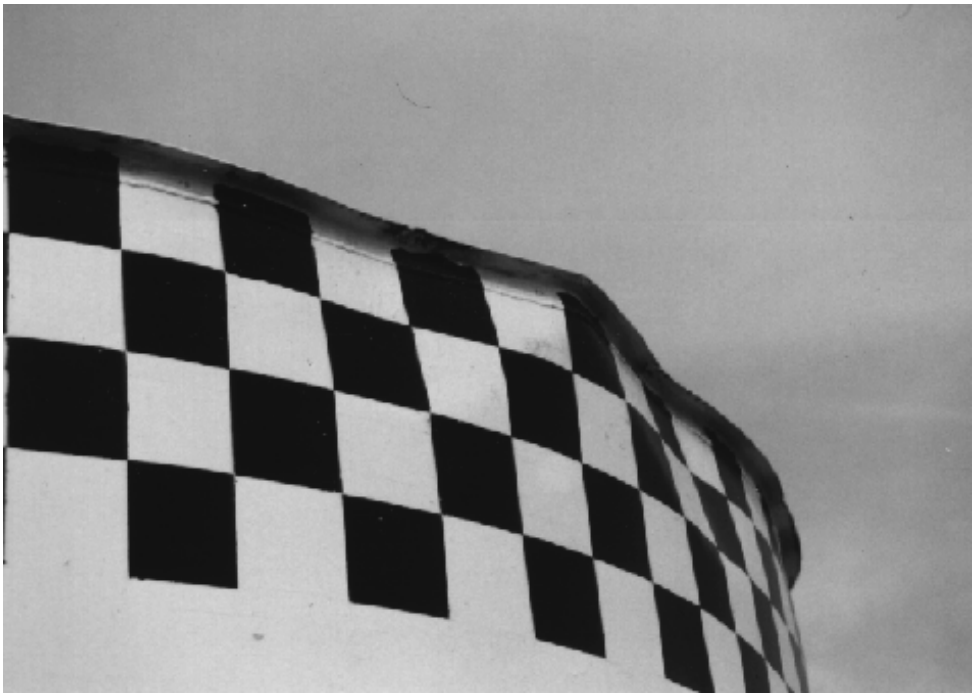

d: First failure Occurred Here

Figure 5.22: (Continued) Stitch Welded Tank after Test

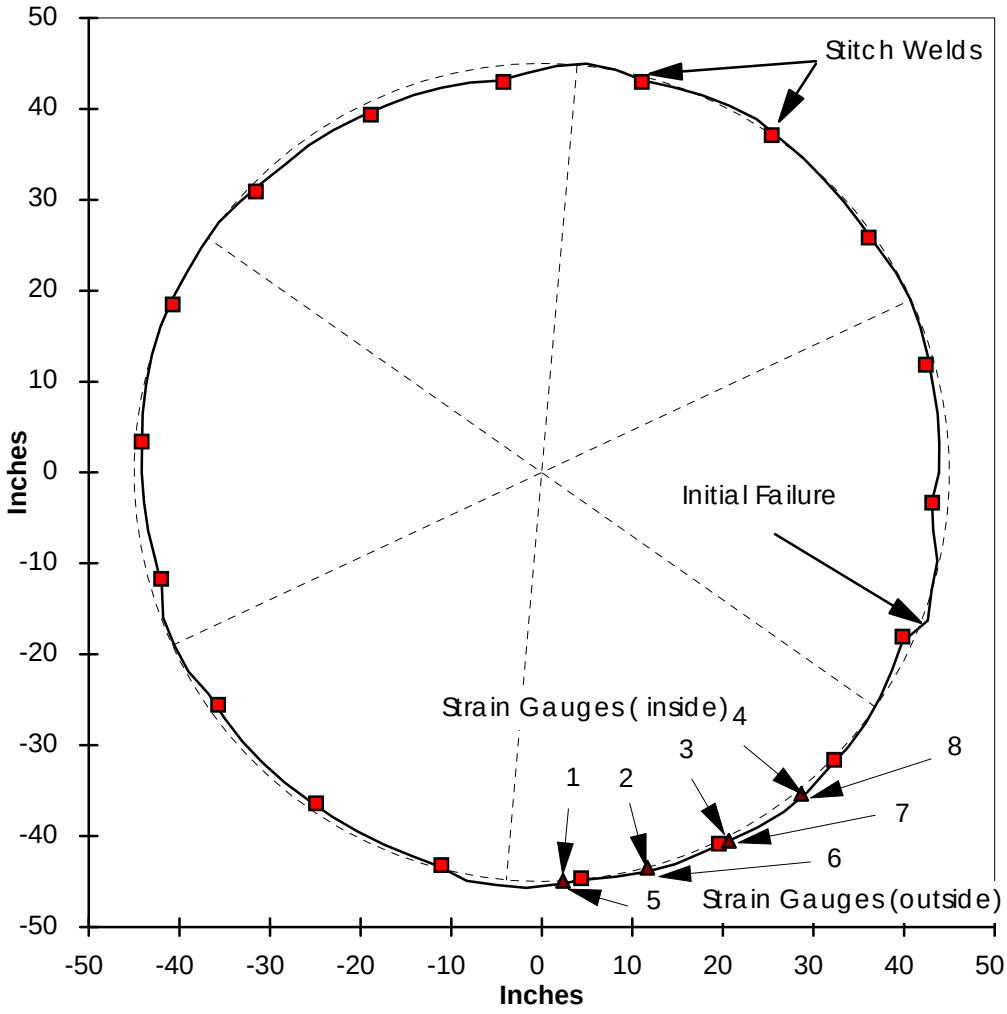

a: At Top of the Shell

Figure 5.23: Cross Sections of Stitch Welded Tank after Test

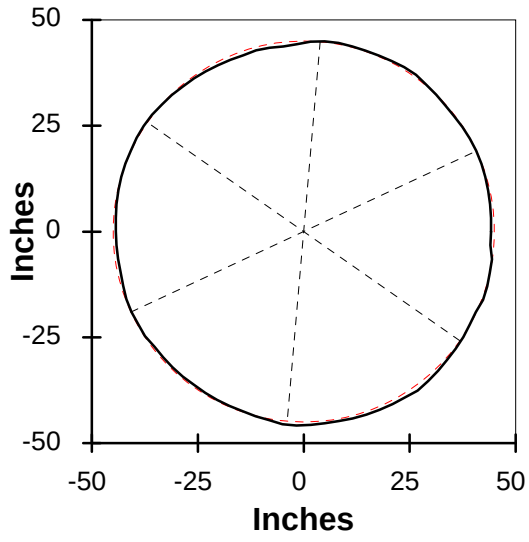

b: 5 Inches Down from the Top

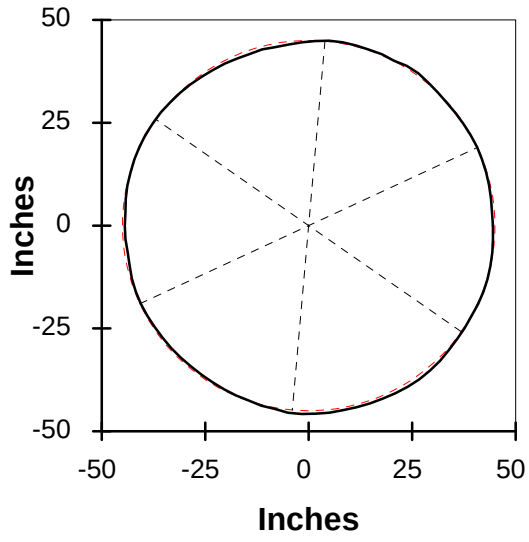

c: 10 Inches Down from the Top

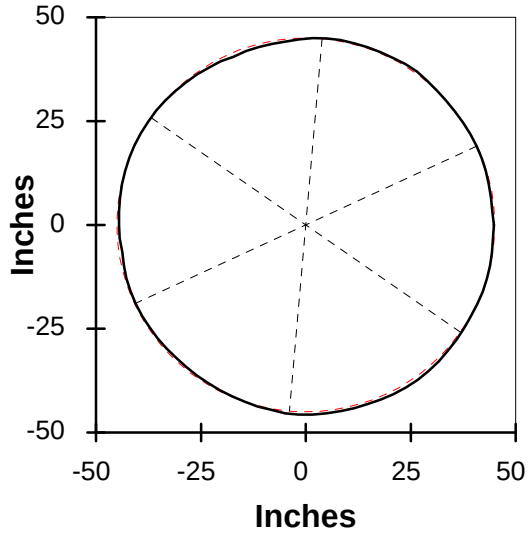

d: 15 Inches Down from the Top

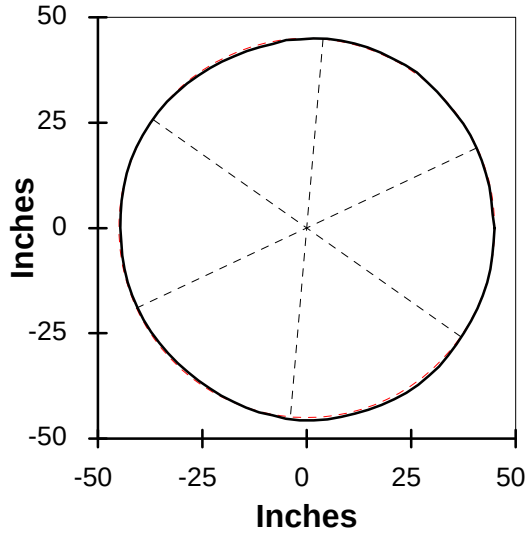

e: 20 Inches Down from the Top

Figure 5.23: (Continued) Cross Sections of Stitch Welded Tank

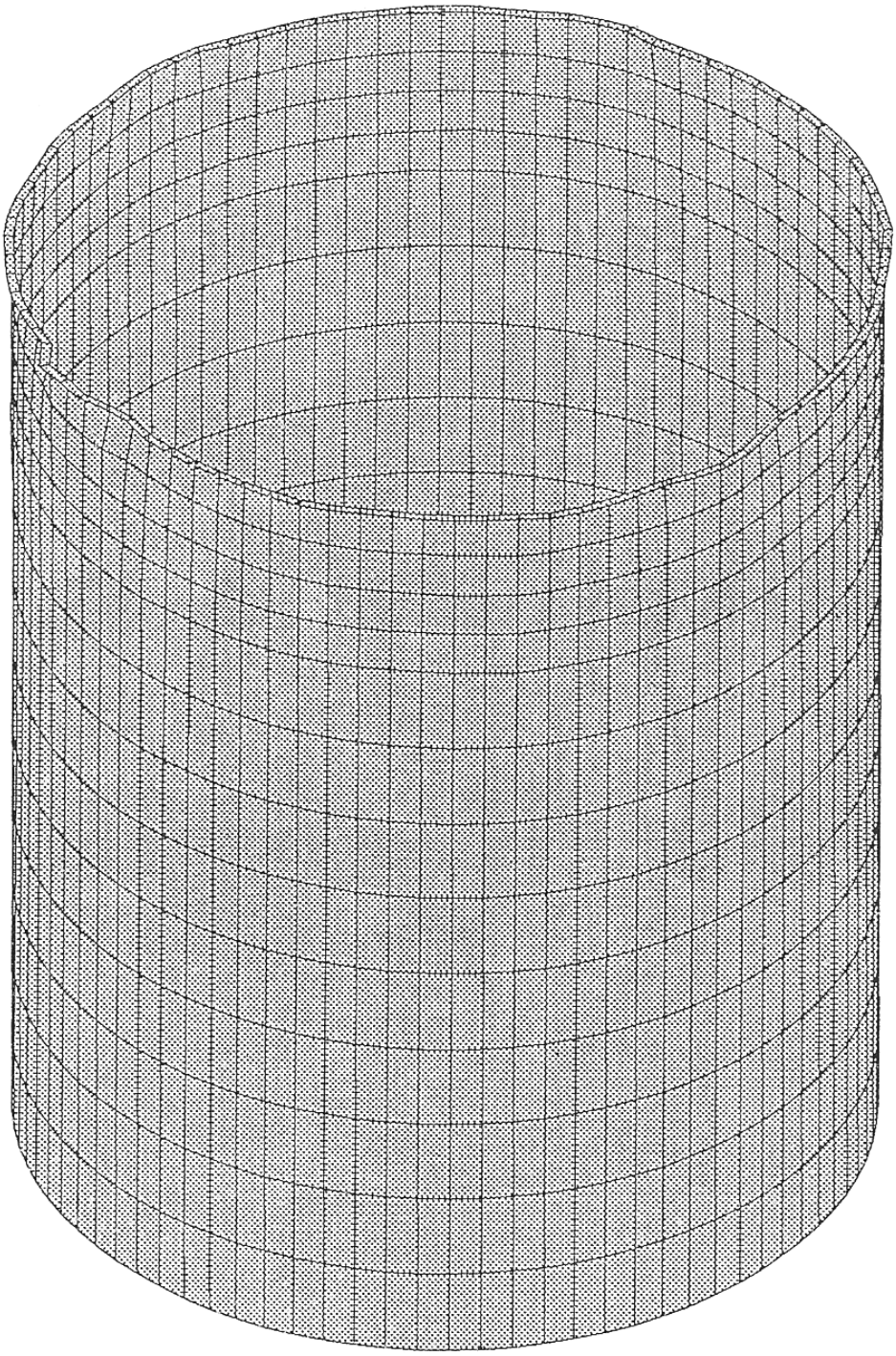

Figure 5.24: Deformation of Stitch Welded Tank

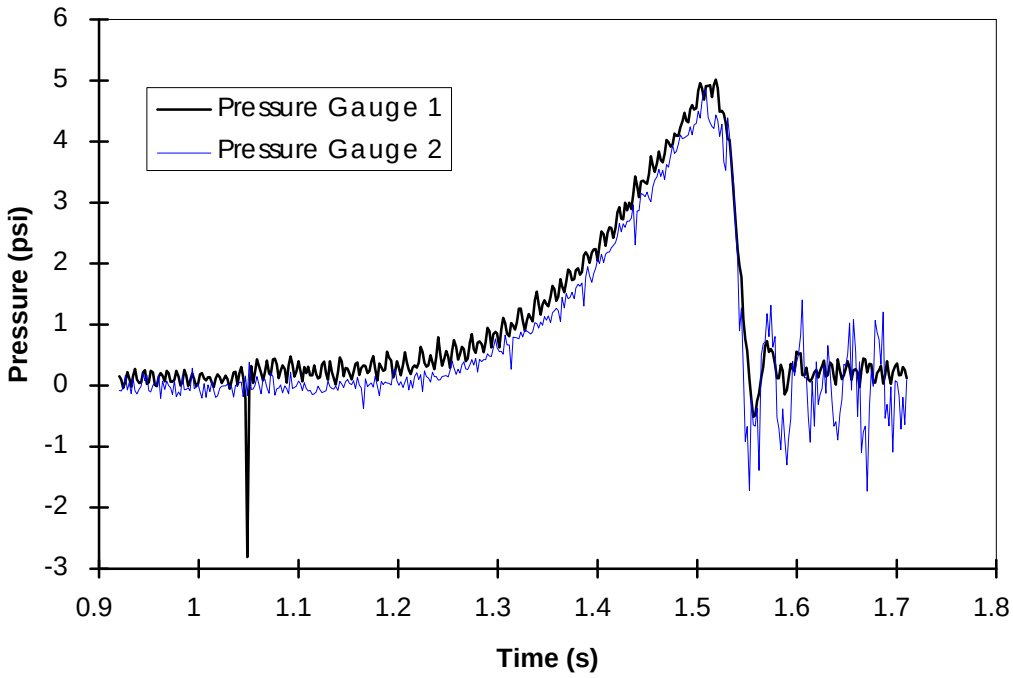

Figure 5.25: Pressure Reading of Stitch Welded Tank Test

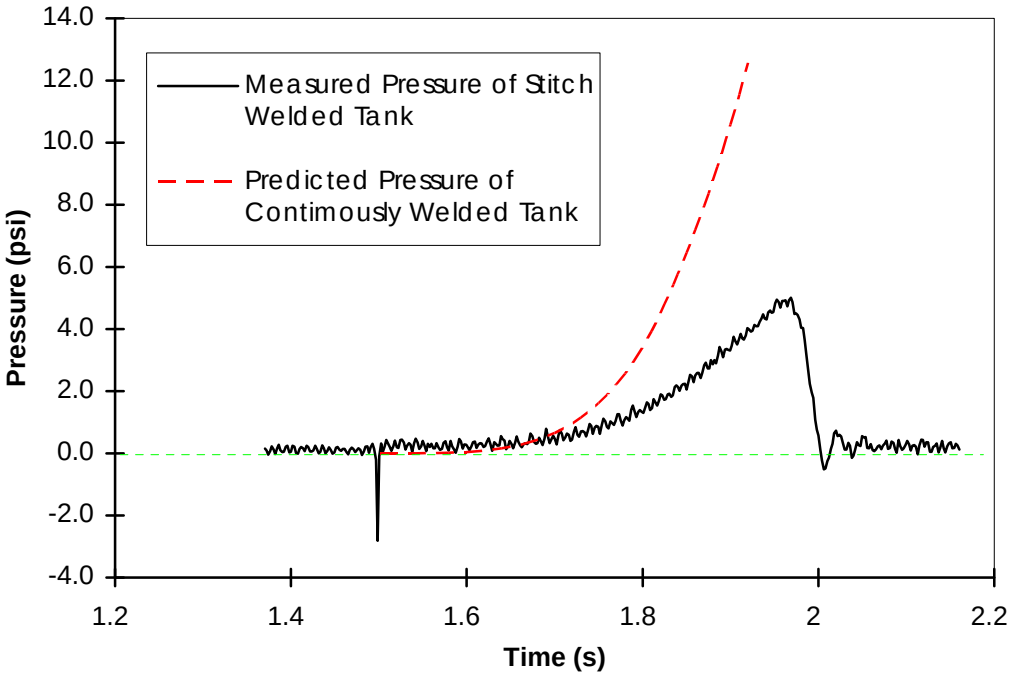

Figure 5.26: Predicted Pressure in Continuously Welded Tank and Measured Pressure in Stitch Welded Tank

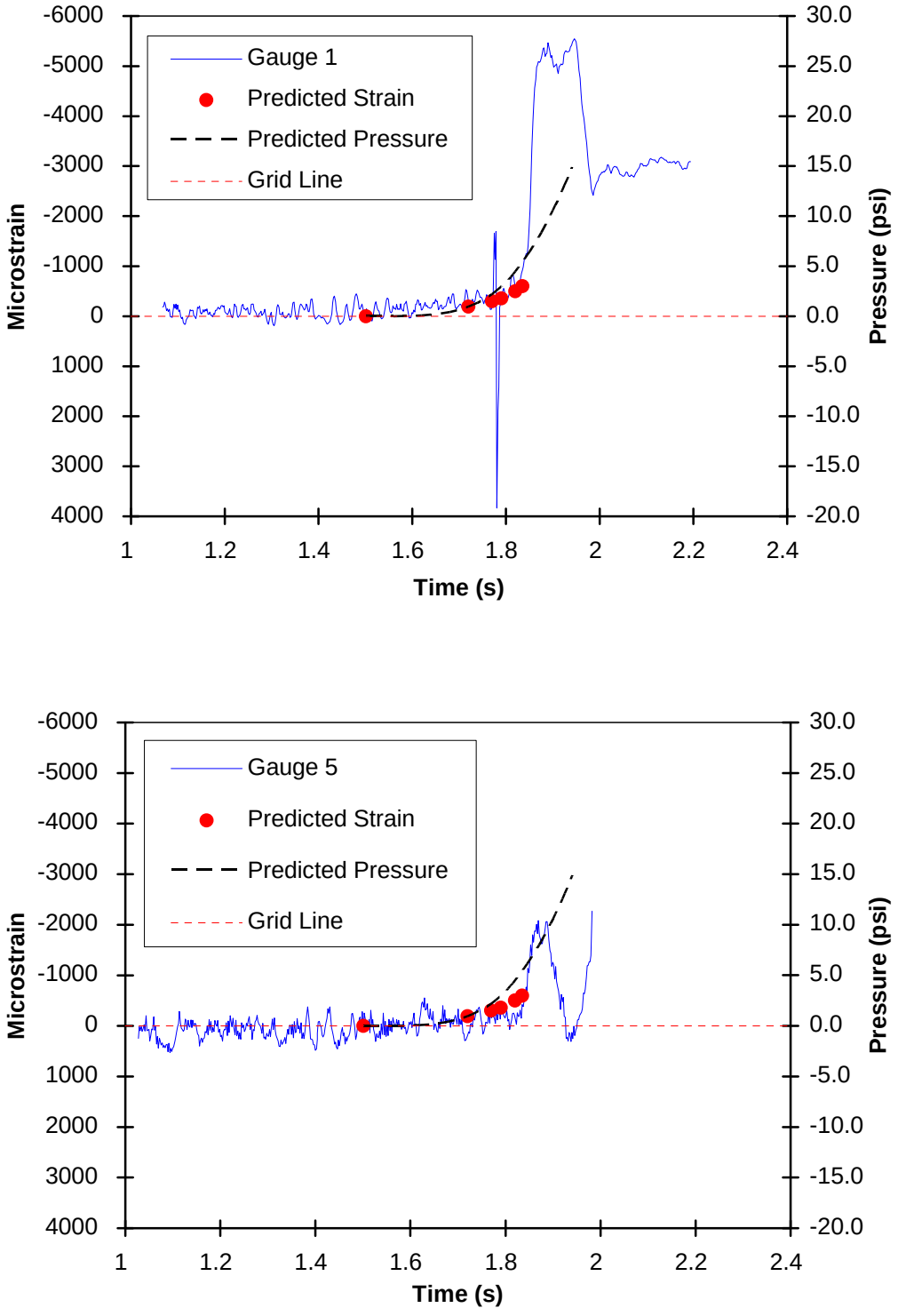

Figure 5.27: Strain and Pressure Readings of Continuously Welded Tank

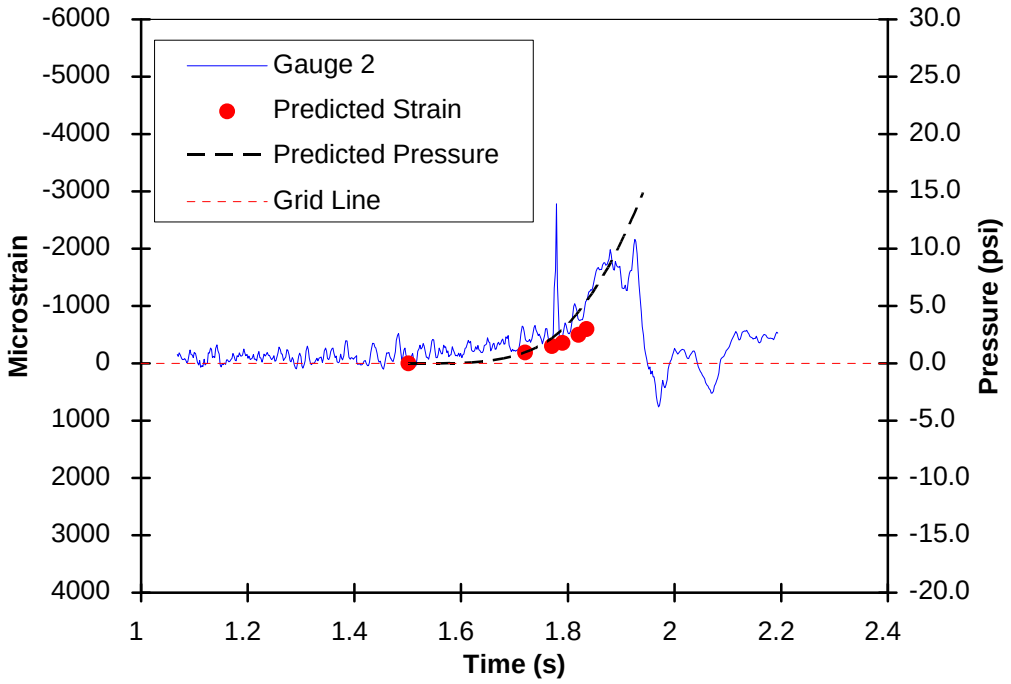

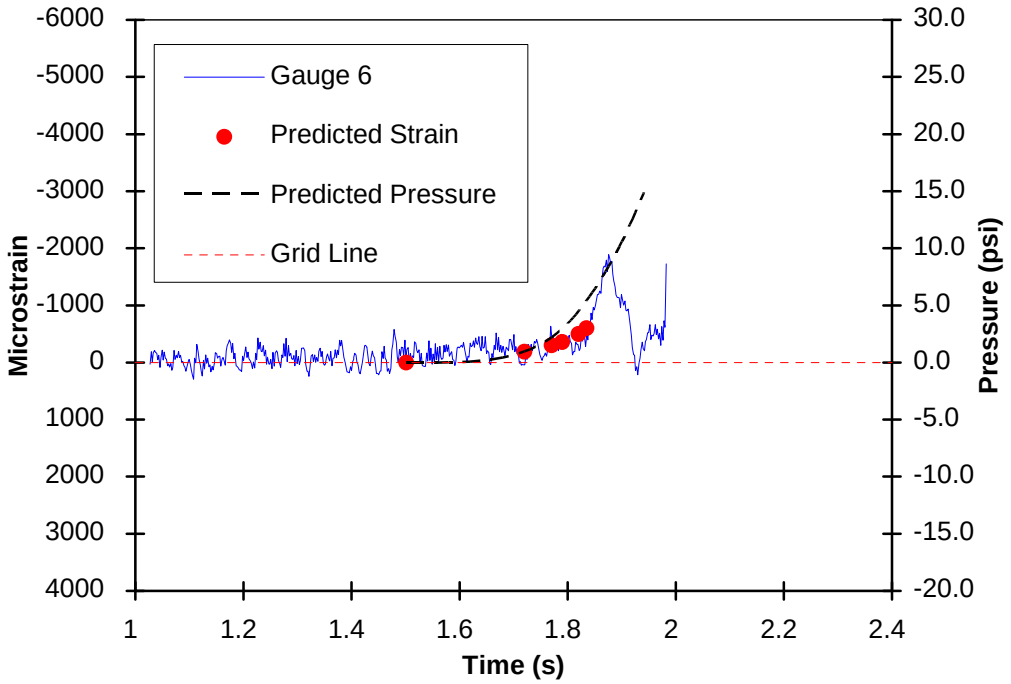

Figure 5.27: (Continued) Strain and Pressure Readings of Continuously Welded Tank

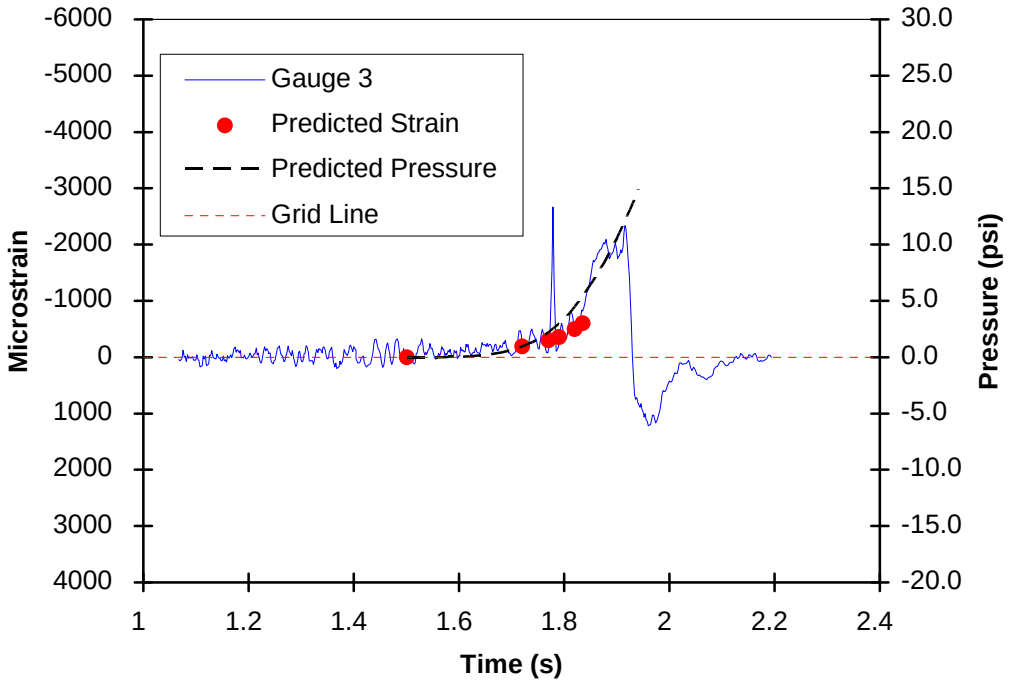

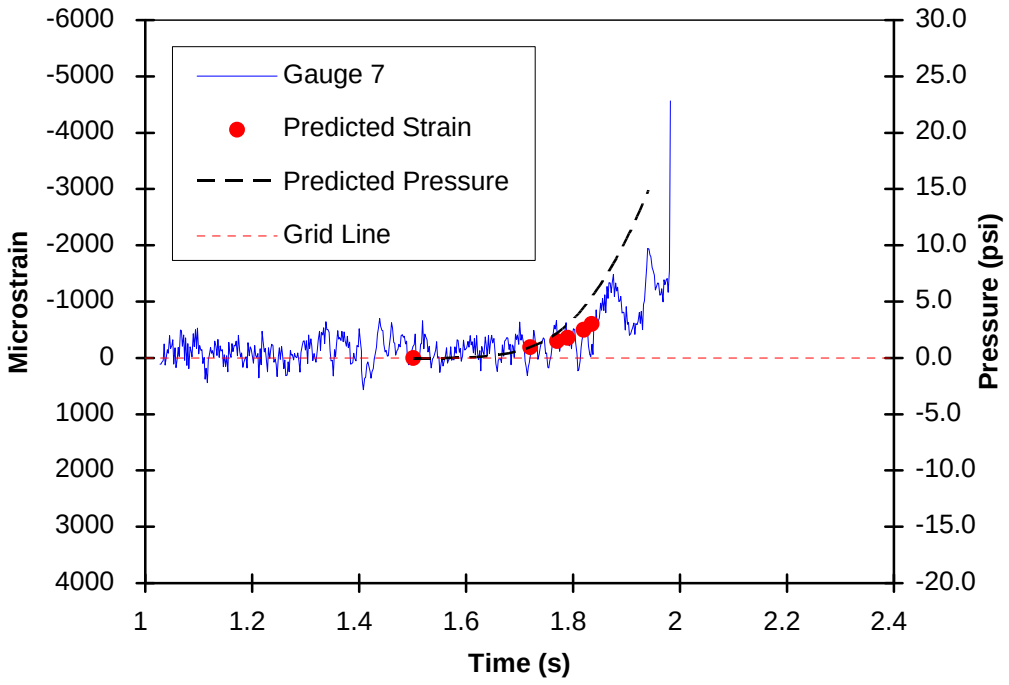

Figure 5.27: (Continued) Strain and Pressure Readings of Continuously Welded Tank

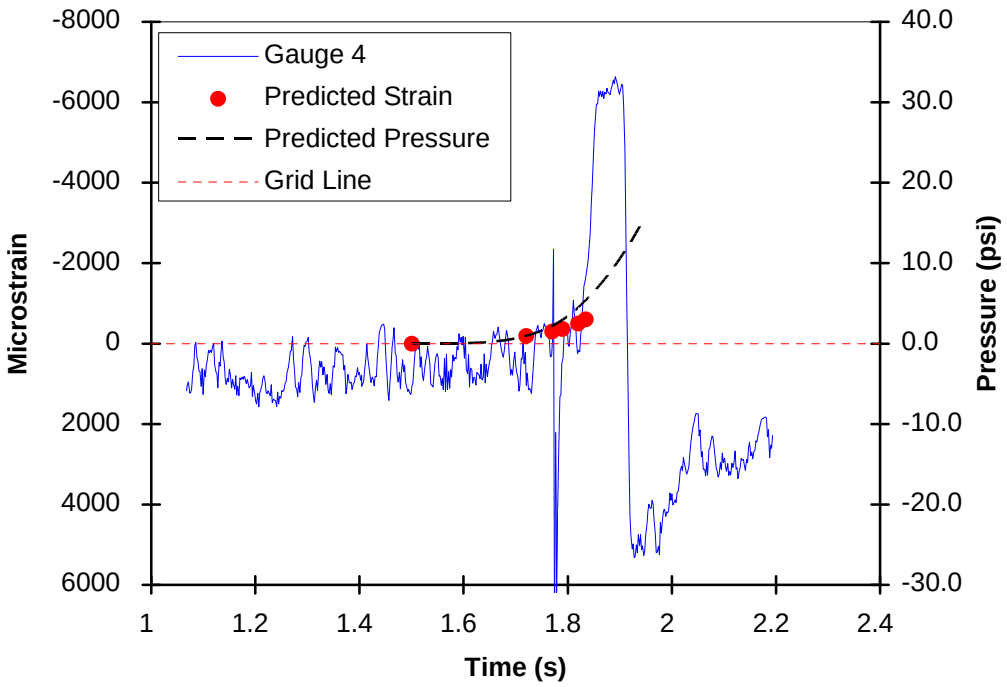

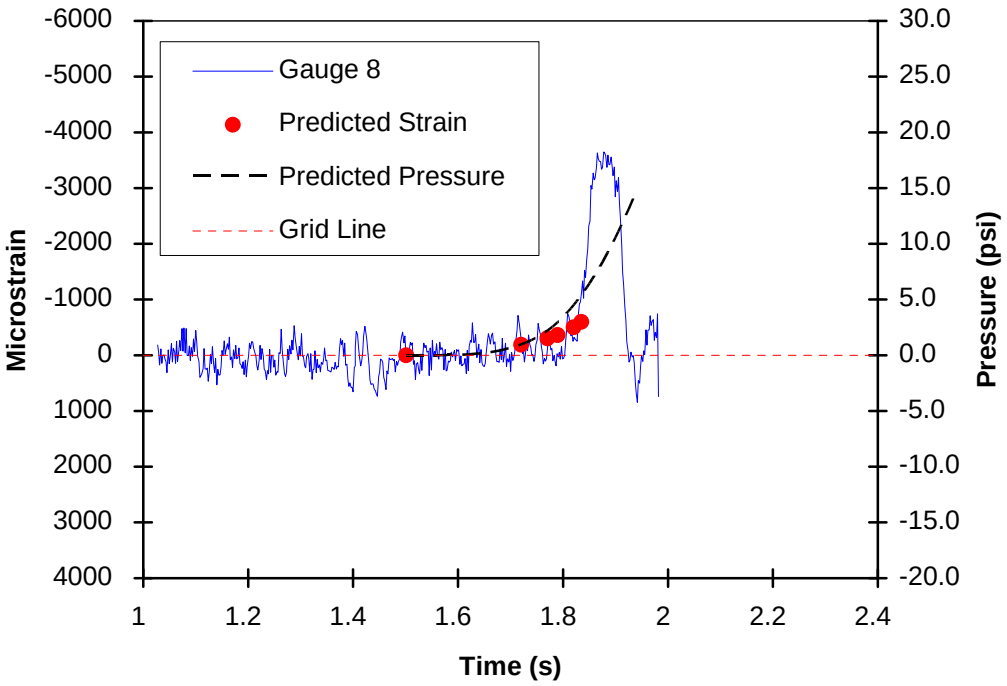

Figure 5.27: (Continued) Strain and Pressure Readings of Continuously Welded Tank

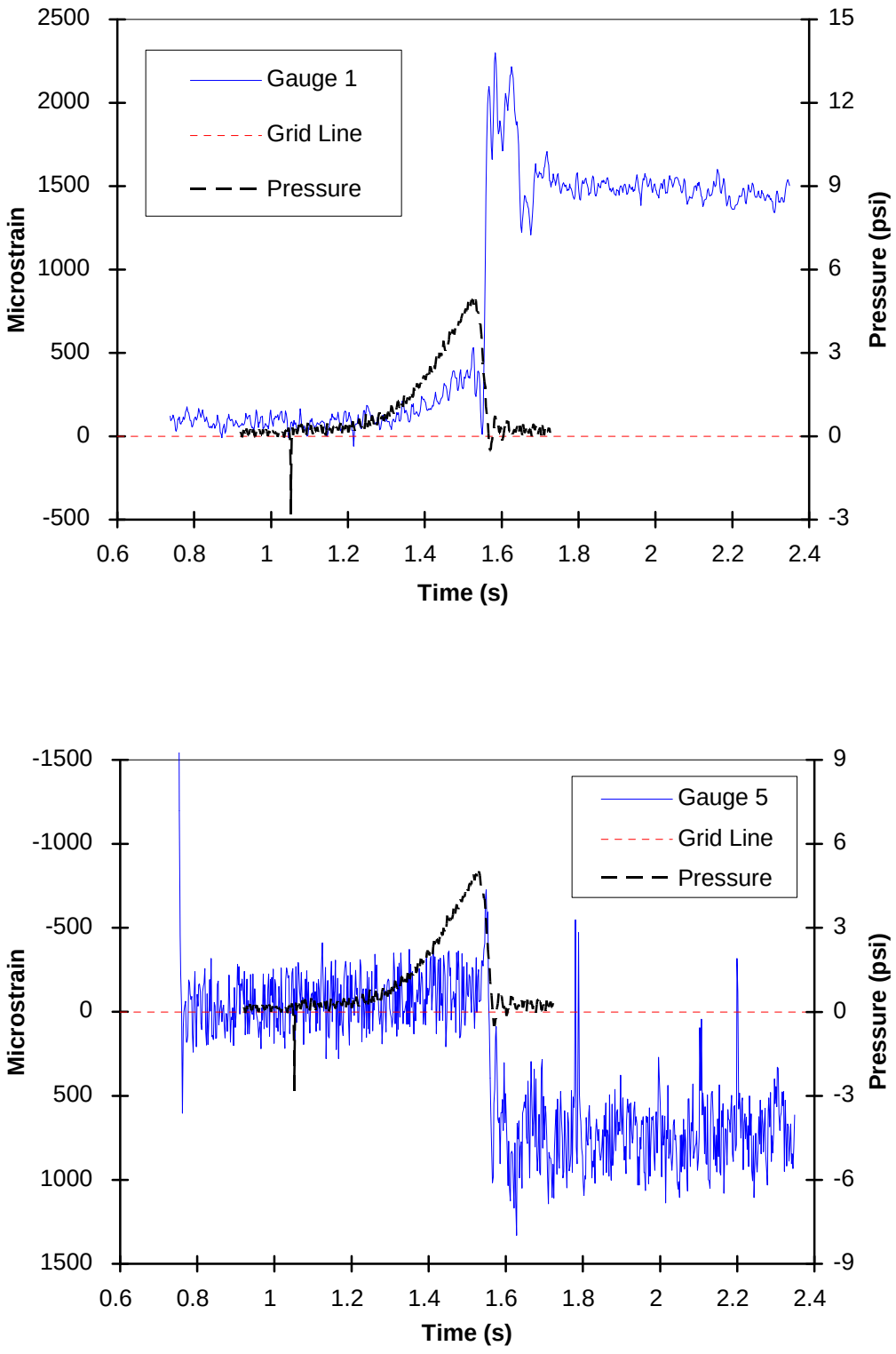

Figure 5.28: Strain and Pressure Readings of Stitch Welded Tank

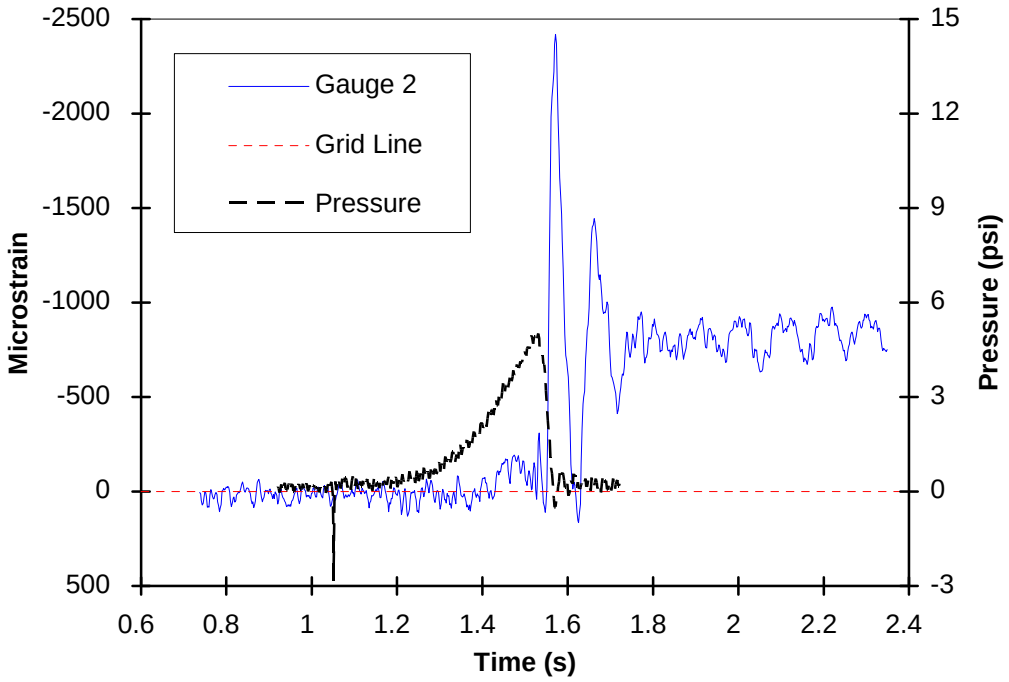

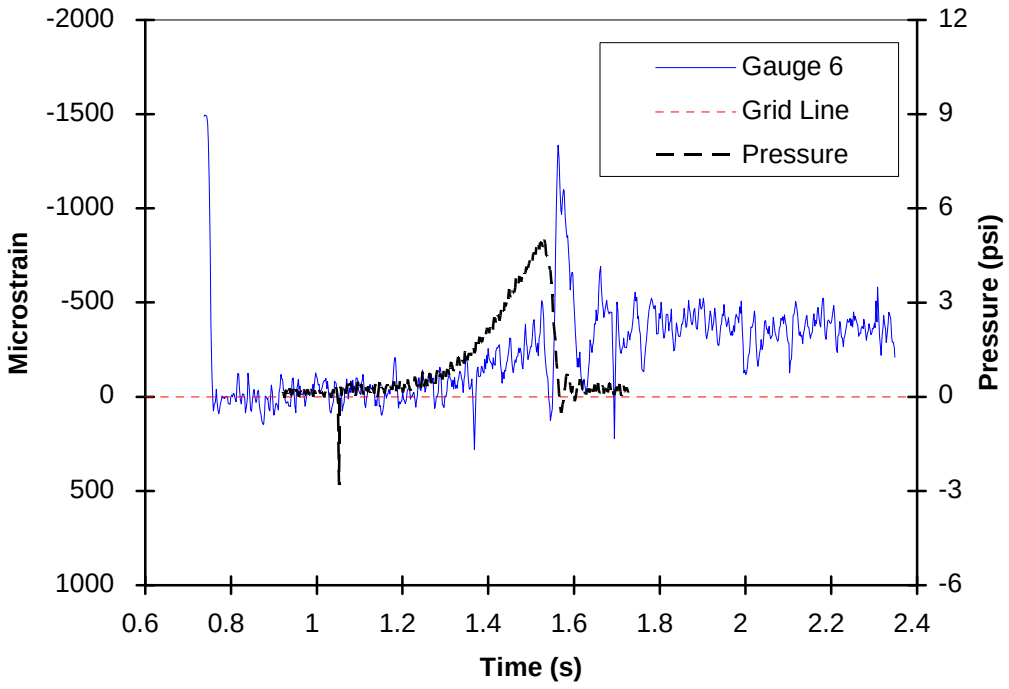

Figure 5.28: (Continued) Strain and Pressure Readings of Stitch Welded Tank

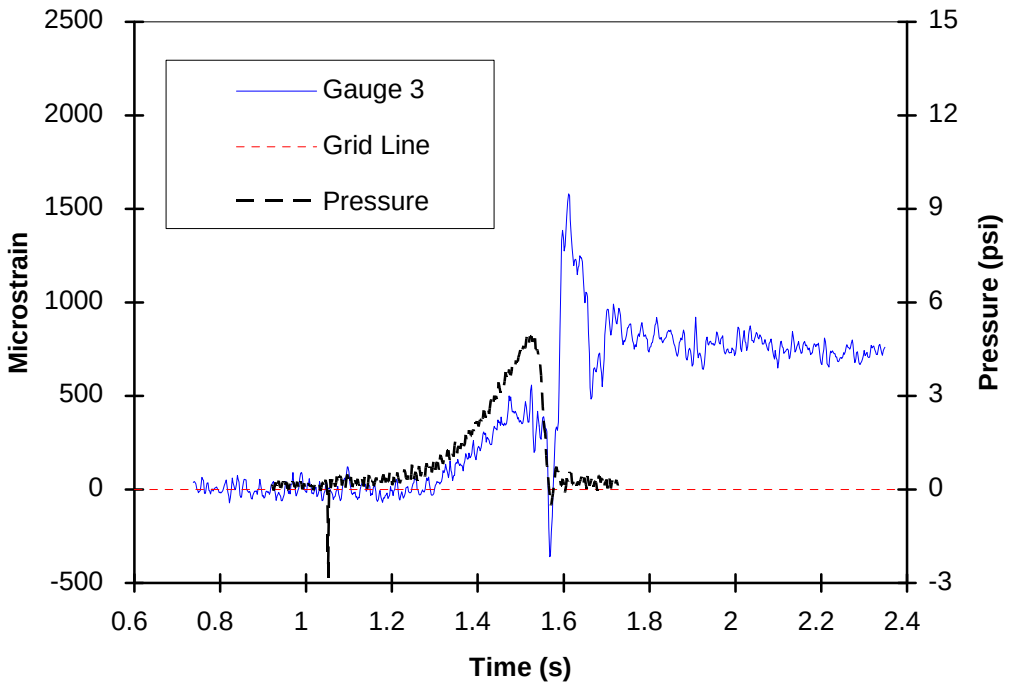

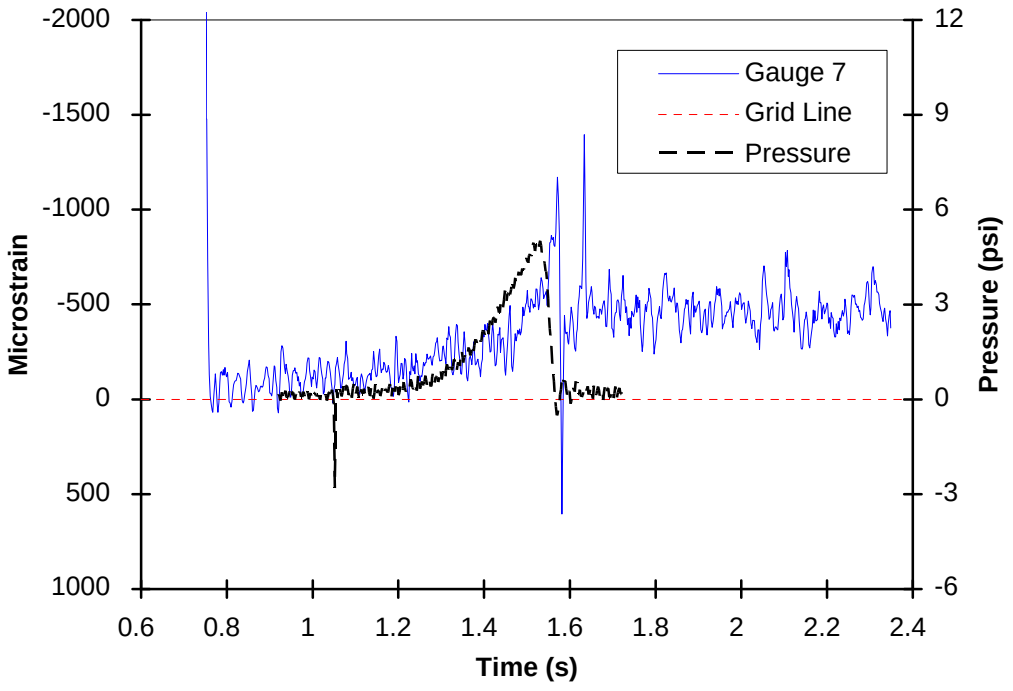

Figure 5.28: (Continued) Strain and Pressure Readings of Stitch Welded Tank

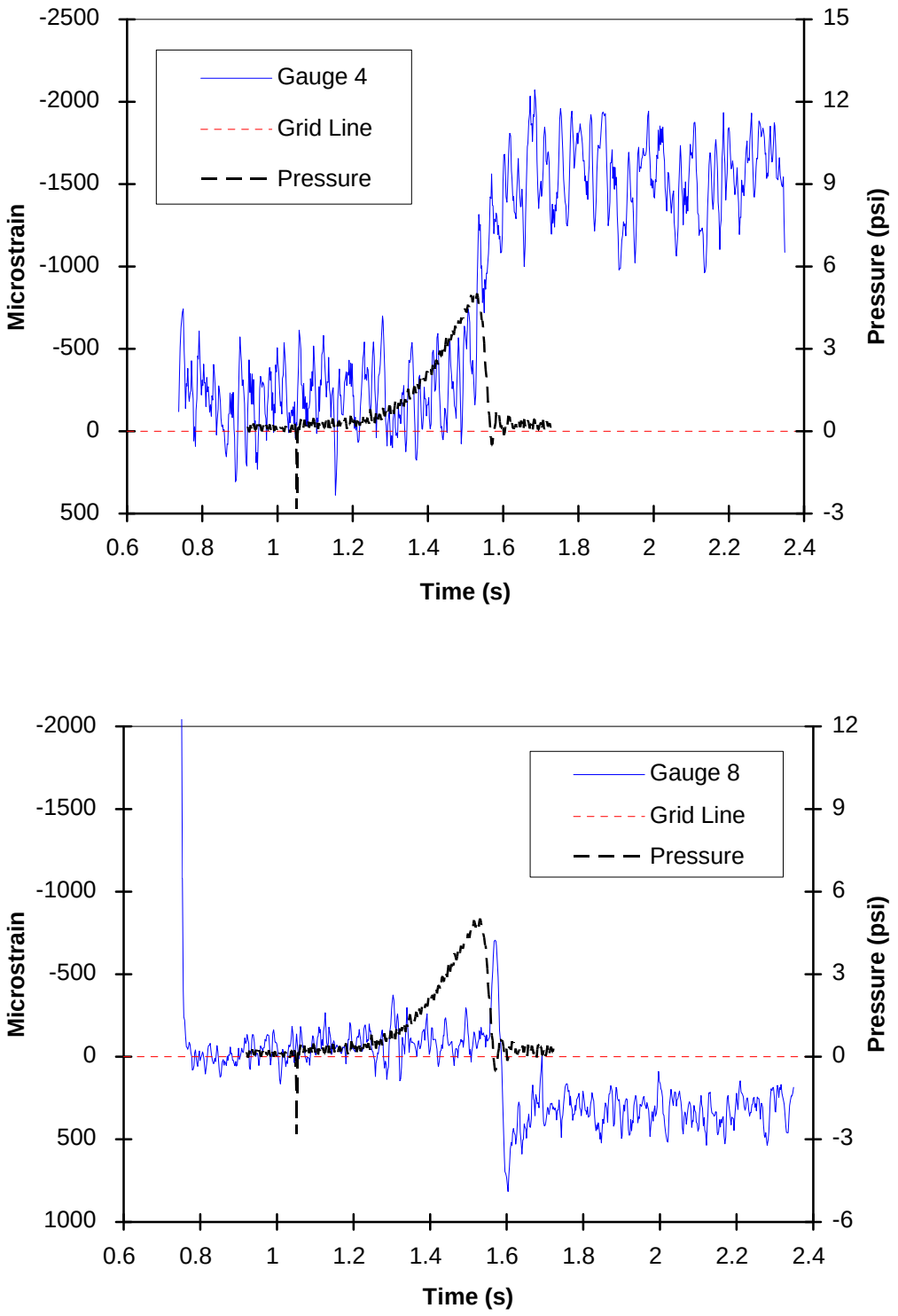

Figure 5.28: (Continued) Strain and Pressure Readings of Stitch Welded Tank

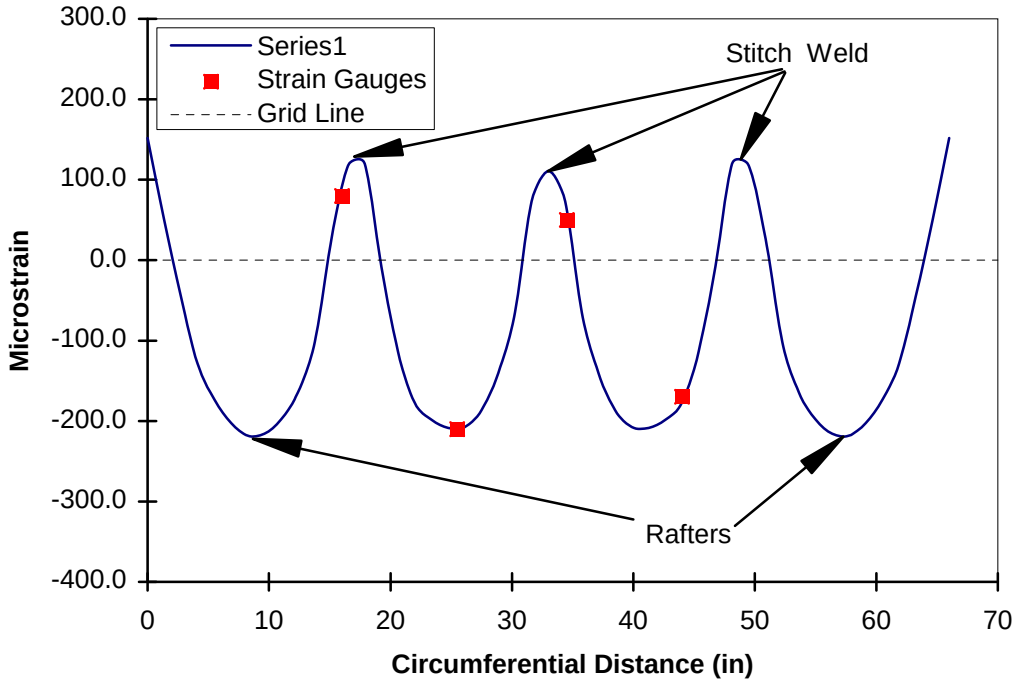

a: Inside Surface

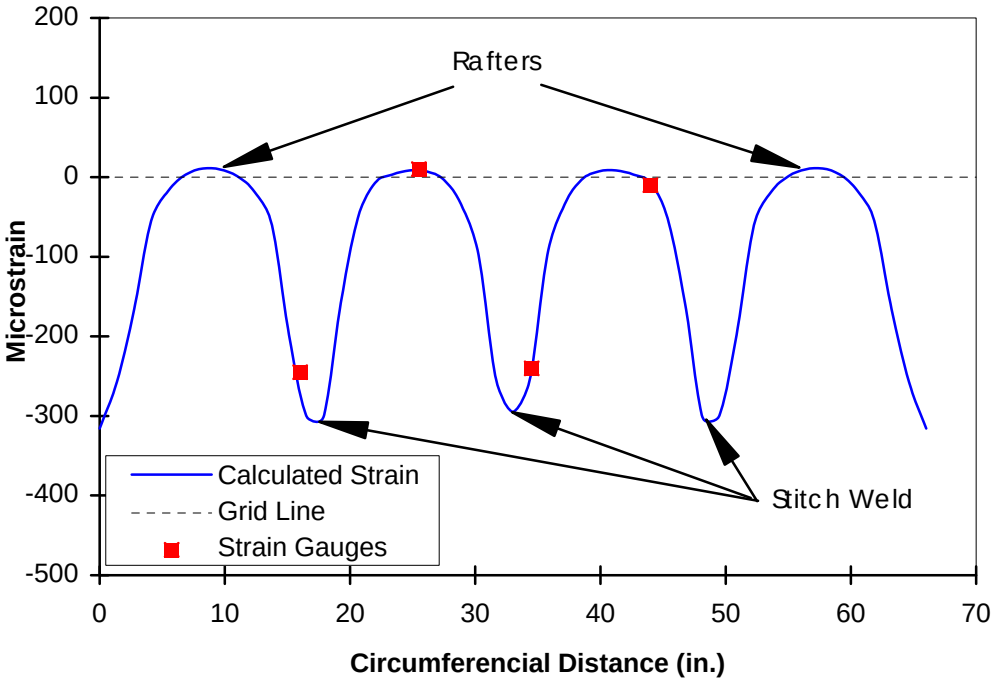

b: Outside Surface

Figure 5.29 Predicted Strain for Stitch Welded Tank under 1 psi Pressure

Located at 2 inches below the Joint

6.0 API-TANK: A PROGRAM FOR THE ANALYSIS OF TANKS WITH FRANGIBLE ROOF JOINTS

6.1. General Description

The failure of storage tanks during internal combustion is a very complicated process. Peak pressure in the tanks will be a fundamental parameter controlling the failure at the joints. It is only when the shell and the bottom of the tank can withstand the peak pressure that the tank will be really safe. The actual failure process is an interaction of the combustion rate, failure initiation and propagation, and venting. A coupled model, taking these phenomena into account, is needed to predict the peak pressure. One object of the research is to develop such a model.

Since the pressure rise in the tanks is relatively slow, static structural analysis is sufficient for the tank until failure initiation. An analytic solution for the whole tank would be very difficult to obtain, if not impossible. Considering that the deflection of the shell at the joint may be an order larger than its thickness, large deformation theory needs to be used and makes the solution even harder to obtain. A 3-D nonlinear finite element analysis can solve the problem but that would require high speed computers and a long computing time.

Since one goal of this project is to develop a simple tool to be used by engineers to design new tanks as well as review existing tanks, a 2-D axisymmetric nonlinear static finite element model is appropriate for the prediction of the initial failure pressure while allowing solution in a relatively short time. Because modal analysis showed that the frequency of pressure rise in the tank is much slower than the natural frequency of storage tanks, dynamic effects are considered not important to the failure initiation and were excluded from the model.

API-Tank has been developed to design and analyze storage tanks with frangible roof joints. API-Tank incorporates the results of this whole research project. It has the ability of designing tanks, evaluating tank behavior, and making hard copies of the results. The program consists of design, analysis, and post-process modules.

The design module will let the user input basic parameters such as diameter and height of the tank and material used. API-Tank will develop a design following API guidelines. The user can either accept the design or make modifications as desired.

A large deflection axisymmetric finite element analysis can be performed in the analysis module. The displacements and stresses of the tank are calculated for given pressure. The pressure for the roof-to-shell joint to yield can be obtained as well as the shell-to-bottom joint yield. The combustion model calculates the pressure rise in the tank. The failure propagation calculation starts when the initial failure pressure is reached. It simulates the failure process of the roof-to-shell joint and calculates the opening area as a function of pressure and time. The venting area is used in the combustion analysis, in which part of the vapor in the tank is vented during the next time step and a new pressure will be obtained. The calculation terminates when the pressure in the tank is totally released or all the vapor in the tank has been burnt. The peak pressure will then be used to calculate the peak stress in the tank. Some design related evaluations defined in API 650 can also be performed in the analysis module, such as overturning stability of the tank and maximum design pressure limited by bottom uplifting.

The post-processing module can generate design tables based on the calculation. It also provides printout of results when needed.

The user can analyze the stresses and displacements in the tank at pressures corresponding to selected tank failure modes. The pressures at each failure mode can be used to help evaluate safety of the tank due to overload pressures.

The following list is the system requirements for API-Tank:

- Any IBM®-compatible machine with an 80286 processor or higher.
- A 3.5-inch or 5.25-inch floppy disk drive.
- A hard disk. The program itself takes about 1 megabytes of disk space. Each analysis generates a set of design and result files. Those files may take 50 to 200 kilobytes of disk space, depending on the size of the tank and number of results obtained.
- A graphics display compatible with Microsoft Windows™ Version 3.1 or later, such as EGA or VGA.
- Four megabytes of memory.
- MS-DOS® version 3.2 or later, and Microsoft Windows™ version 3.1 or later in standard or enhanced mode.
- A Microsoft Windows™ Mouse or compatible pointing device

A printer or plotter is optional. The available output includes the design of the tank structure, evaluation of the deformation and stress at different pressure, as well as API 650 design calculations. The results can be viewed from the window, or be made into hard copy by using a printer or plotter, as listed below:

The available types of plot are:

- Tank design,

- Finite element mesh,
- Pressure-time curve from combustion analysis, if peak pressure has been calculated,
- Deformation of the tank under given pressure,
- Average meridional, circumferential, and equivalent stresses on center, outer, or inner surface of the elements.

The available types of list are:

- Tank design
- Node coordinates of the finite element mesh,
- Element connection and thickness of the finite element mesh,
- Pressure-time data from combustion analysis, if peak pressure has been calculated,
- Nodal displacements under given pressure,
- Meridional, circumferential, and equivalent stresses on center, outer, or inner surface of the nodes,
- Average meridional, circumferential, and equivalent stresses on center, outer, or inner surface of the elements.

6.2 Theory and Implementation

6.2.1 Automatic Design

The automatic design option allows the user to input basic tank parameters, API-Tank will then automatically design a tank to API 650 rules. Two automatic design options, API 650 Section 3 and Appendix F, are available. The basic design parameters are input by the user of the program. The following assumptions are made for the auto-designed tanks:

- 3/16 inch thick roof plate supported by rafters,
- Roof slope 3/4 inch in 12 inches,
- Top angle does not overlap top shell,
- Bottom plate (or annular bottom plate if there is one) projects two inches beyond the shell,
- Shell thickness calculated by one foot method or Appendix A method.

The tank is assumed to rest on a sand foundation with a default modulus of 250 lb/in^2/in. A ringwall with a default modulus of foundation 1000 lb/in^2/in and 6 inches width, measured from the tank shell, is also assumed.

The design can be checked for overturning stability due to a wind velocity of 100 miles per hour (or user specified value) and anchors will be designed if necessary.

6.2.2 Shell Elements

The roof, shell, and bottom of the tank are modeled using axisymmetric conical shell elements (Zenkiewicz and Taylor, 1988), as shown in Figure 6.1. The element has constant thickness with three degrees of freedom at each node: translations in the nodal x and y directions and a rotation about the nodal z axis. The element has membrane and bending capabilities, as well as large deflection capability.

The motion, $\mathbf{u}^n$, of a general point in the element is:

$$\mathbf{u}^n = \begin{Bmatrix} u \\ w \end{Bmatrix} \tag{6.1}$$

where u and w are the in-plane and lateral displacements, respectively. The circumferential displacement v is identically zero due to axisymmetry. The strain at a point is a function of the displacement:

$$\boldsymbol{\varepsilon} = \begin{Bmatrix} \varepsilon_x \\ \varepsilon_y \end{Bmatrix} = \begin{Bmatrix} \dfrac{\partial u}{\partial x} + \dfrac{1}{2}\left(\dfrac{\partial w}{\partial x}\right)^2 \\ \dfrac{1}{r}(u\sin\phi - w\cos\phi) \end{Bmatrix} + y\begin{Bmatrix} -\dfrac{\partial^2 w}{\partial x^2} \\ -\dfrac{\sin\phi}{r}\dfrac{\partial w}{\partial x} \end{Bmatrix} \tag{6.2}$$
$$= \mathbf{A}\,\mathbf{u}^n$$

A is an operator matrix defined in equation (6.3) where the subscripts c, y, and l represent the center surface, bending and large deformation effects, respectively.

$$\mathbf{A} = \mathbf{A}_c + y\mathbf{A}_y + \mathbf{A}_l$$
$$= \begin{bmatrix} \dfrac{\partial}{\partial x} & 0 \\ \dfrac{\sin\phi}{r} & -\dfrac{\cos\phi}{r} \end{bmatrix} + y\begin{bmatrix} 0 & \dfrac{\partial^2}{\partial x^2} \\ 0 & -\dfrac{\sin\phi}{r}\dfrac{\partial}{\partial x} \end{bmatrix} + \begin{bmatrix} 0 & \dfrac{1}{2}\dfrac{\partial w}{\partial x}\dfrac{\partial}{\partial x} \\ 0 & 0 \end{bmatrix} \tag{6.3}$$

For a linear material, the stress-strain relation has the form:

$$\boldsymbol{\sigma} = \mathbf{D}\,\boldsymbol{\varepsilon}$$
$$= \frac{E}{1-\nu^2}\begin{bmatrix} 1 & \nu \\ \nu & 1 \end{bmatrix}\begin{Bmatrix} \varepsilon_x \\ \varepsilon_y \end{Bmatrix} \tag{6.4}$$

Using cubic shape functions for lateral displacement and nodal rotation and linear shape functions for in-plane displacement, the motion of a point $\mathbf{u}^n$ can be interpolated in terms of nodal displacement $\mathbf{u}_l$:

$$\mathbf{u}^{n} = \mathbf{N}\,\mathbf{u}_{l}$$

$$= \begin{bmatrix} 0 & N_3^I & 0 & 0 & N_3^J & 0 \\ N_1^I & 0 & N_2^I & N_1^J & 0 & N_2^J \end{bmatrix} \begin{Bmatrix} w_I \\ u_I \\ \beta_I \\ w_J \\ u_J \\ \beta_J \end{Bmatrix} \tag{6.5}$$

where β is the rotation at the node and the shape functions are:

$$N_1^I = \frac{1}{2} - \frac{s}{4}(3 - s^2),$$

$$N_1^J = \frac{1}{2} + \frac{s}{4}(3 - s^2),$$

$$N_2^I = \frac{L}{8}(1 - s^2)(1 - s),$$

$$N_2^J = -\frac{L}{8}(1 - s^2)(1 + s),$$

$$N_3^I = \frac{1}{2}(1 - s),$$

$$N_3^J = \frac{1}{2}(1 + s). \tag{6.6}$$

The nodal displacements in the local coordinate system can be written in terms of the global system using the following transformation:

$$\mathbf{u}_{l} = \mathbf{T}_{r}\,\mathbf{u}_{e}$$

$$= \begin{bmatrix} \cos\phi & \sin\phi & 0 & 0 & 0 & 0 \\ \sin\phi & -\cos\phi & 0 & 0 & 0 & 0 \\ 0 & 0 & 1 & 0 & 0 & 0 \\ 0 & 0 & 0 & \cos\phi & \sin\phi & 0 \\ 0 & 0 & 0 & \sin\phi & -\cos\phi & 0 \\ 0 & 0 & 0 & 0 & 0 & 1 \end{bmatrix} \begin{Bmatrix} u_X^I \\ u_Z^I \\ \beta^I \\ u_X^J \\ u_Z^J \\ \beta^J \end{Bmatrix} \tag{6.7}$$

The strain-nodal displacement relation can now be written as:

$$\begin{aligned}\boldsymbol{\varepsilon} &= \mathbf{A}\mathbf{N}\mathbf{u}_1 \\ &= (\mathbf{A}_c + y\mathbf{A}_y + \mathbf{A}_1)\mathbf{N}\mathbf{u}_1 \\ &= (\mathbf{B}_c + y\mathbf{B}_y + \mathbf{B}_1)\mathbf{u}_1\end{aligned} \tag{6.8}$$

Assuming a linear material, the total strain energy is the strain energy density integrated over the volume:

$$U = \int_{vol} \frac{1}{2}\boldsymbol{\sigma} : \boldsymbol{\varepsilon}\, d(vol) \tag{6.9}$$

The work done by an external force is the product of force and displacement:

$$V = \mathbf{F} \cdot \mathbf{u} = \mathbf{u}^T \int_{vol} \mathbf{N}^T \mathbf{f}\, d(vol) \tag{6.10}$$

where $\mathbf{f}$ is the external loading on the element.

By applying Hamilton's principle, the shell has the following governing equation:

$$\delta(U + V) = \delta\mathbf{u}^T\mathbf{K}\mathbf{u} - \delta\mathbf{u}^T\mathbf{F} = 0 \tag{6.11}$$

where the global stiffness matrix $\mathbf{K}$ is the integration over the entire volume:

$$\mathbf{K} = \int_{vol} (\mathbf{B}_c + \mathbf{B}_1 + y\mathbf{B}_y)^T \mathbf{D}\, (\mathbf{B}_c + \mathbf{B}_1 + y\mathbf{B}_y)\, d(vol) \tag{6.12}$$

When integrating through the thickness of a conical shell, a factor $(1 + y\frac{\cos\phi}{r})$ needs to be included. For any constant H, we have:

$$\int_{-t/2}^{t/2} H(1 + y\frac{\cos\phi}{r})dy = Ht$$

$$\int_{-t/2}^{t/2} H(1+y\frac{\cos\phi}{r})ydy = H\frac{t^3\cos\phi}{12\,r}$$

$$\int_{-t/2}^{t/2} H(1+y\frac{\cos\phi}{r})y^2dy = H\frac{t^3}{12} \qquad (6.13)$$

The element stiffness matrix in local coordinates is:

$$\begin{aligned}\mathbf{K}_l = & \int_{area} t\,\mathbf{B}_c^T\mathbf{D}\mathbf{B}_c\,d(area) \\ & + \int_{area} \frac{t^3\cos\phi}{12\,r}\left(\mathbf{B}_c^T\mathbf{D}\mathbf{B}_y + \mathbf{B}_y^T\mathbf{D}\mathbf{B}_c\right)d(area) \\ & + \int_{area} \frac{t^3\cos\phi}{12\,r}\left(\mathbf{B}_c^T\mathbf{D}\mathbf{B}_y + \mathbf{B}_y^T\mathbf{D}\mathbf{B}_c\right)d(area) \\ & + \int_{area} \frac{t^3}{12}\mathbf{B}_y^T\mathbf{D}\mathbf{B}_y\,d(area) \\ & + \int_{area} t\left(\mathbf{B}_c^T\mathbf{D}\mathbf{B}_l + \mathbf{B}_l^T\mathbf{D}\mathbf{B}_c + \mathbf{B}_l^T\mathbf{D}\mathbf{B}_l\right)d(area) \\ & + \int_{area} \frac{t^3\cos\phi}{12\,r}(\mathbf{B}_y^T\,\mathbf{D}\,\mathbf{B}_l + \mathbf{B}_l^T\,\mathbf{D}\,\mathbf{B}_y)\,d(area) \qquad (6.14)\end{aligned}$$

The element stiffness matrix in global coordinates will be:

$$\mathbf{K}_e = \mathbf{T}_r^T\mathbf{K}_l\mathbf{T}_r \qquad (6.15)$$

Figure 6.2 shows external loads on an element. The element loads include gravity loads, $\mathbf{F}_1$, pressure loads, $\mathbf{F}_2$, and the secondary effect of pressure load, $\mathbf{F}_3$. The reaction force from the elastic foundation will be converted to stiffness and will be discussed later.

$$\mathbf{F} = \mathbf{F}_1 + \mathbf{F}_2 + \mathbf{F}_3 \qquad (6.16)$$

For an element, the gravity load in local coordinates is:

$$\mathbf{f}_{1l} = -2\pi t\int_0^L r\,\mathbf{N}^T \begin{Bmatrix} \rho g\cos\phi \\ -\rho g\sin\phi \end{Bmatrix} dx \tag{6.17}$$

The element pressure loading vector in local coordinates is:

$$\mathbf{f}_{2l} = -2\pi\int_0^L r\,\mathbf{N}^T \begin{Bmatrix} 0 \\ p_1 - p_2 \end{Bmatrix} dx \tag{6.18}$$

The normal stress due to pressure converted to strain in the plane of the shell has the form:

$$\boldsymbol{\varepsilon}^{pr} = -\frac{\nu}{2E}(p_1 + p_2)\begin{Bmatrix} 1 \\ 1 \end{Bmatrix} - \frac{\nu\, y}{2E\, t}(p_2 - p_1)\begin{Bmatrix} 1 \\ 1 \end{Bmatrix} \tag{6.19}$$

The effect is then handled like a thermal strain. The equivalent load vector is:

$$\mathbf{f}_{3l} = \int_{vol} \mathbf{B}^T\mathbf{D}\,\boldsymbol{\varepsilon}^{pr}\, d(vol) \tag{6.20}$$

6.2.3 Foundation Elements

Foundation elements are used to represent the nonlinear reacting forces on the bottom of the tank by the foundation. The foundation of the tank is modeled as an elastic interface without friction.

The total surface traction force in the global coordinate can be written as an integral over the entire surface:

$$\mathbf{F}^e = \int_S \mathbf{T}_r\,\mathbf{N}^T\mathbf{t}^n\, dS \tag{6.21}$$

where $\mathbf{t}^n$ is the surface traction in local coordinate. The local surface traction and local displacement have the relation:

$$\begin{aligned} \mathbf{t}^n &= -\mathbf{T}\,\mathbf{u}^n \\ &= -\begin{bmatrix} 0 & 0 \\ 0 & k_f \end{bmatrix}\mathbf{u}^n \end{aligned} \tag{6.22}$$

where $\mathbf{T}$ is the interface stiffness matrix and the parameter k_f is a function of the interface opening:

$$k_f = \begin{cases} 0 & \text{with interface open} \\ \text{stiffness of foundation} & \text{with interface closed} \end{cases} \tag{6.23}$$

Substituting equation (6.5), (6.22) and (6.23) into (6.21), we get the foundation force vector and foundation stiffness matrix:

$$\begin{aligned} \mathbf{F}^e &= -\mathbf{K}^e \mathbf{u}_e \\ &= -\int_S \mathbf{T}_r \mathbf{N}^T \mathbf{T} \mathbf{N} \mathbf{T}_r \, dS \, \mathbf{u}_e \end{aligned} \tag{6.24}$$

$$\mathbf{K}^e = \int_S \mathbf{T}_r \mathbf{N}^T \mathbf{T} \mathbf{N} \mathbf{T}_r \, dS \tag{6.25}$$

The foundation stiffness matrix will be evaluated at every iteration and added to the global stiffness matrix.

6.2.4 Finite Element Mesh Generation

The tanks considered in this program are assumed to be at least 5.0 feet in diameter with two shell courses at least 2.5 feet high. Elements near the roof-to-shell joint and the shell-to-bottom joint have the smallest meridonal length of 0.5 inch while much rougher mesh is used for shells away from the joints. The finite element mesh used for modeling the tank is generated as shown in Figures 6.3 and 6.4 and described in Tables 6.1 and 6.2.

6.2.5 Nonlinear Solution Procedure

At the start of the structural analysis, the finite element model is meshed and a linear stiffness matrix formed. For the specified pressure, a global loading vector is obtained and saved. After each iteration, part of the newly obtained displacement will be added to the previous one as the next estimate of the solution. The nonlinear part of the stiffness matrix (due to

the large deflection and elastic foundation) is evaluated using the new solution and then used for the next iteration. If available, a previous solution is used as the first guess. The algorithm can be written as:

do{

$$\mathbf{U}_n^{/} = (\mathbf{K}_0 + \mathbf{K}_1^{n-1})^{-1}\mathbf{F}$$

$$\mathbf{U}_n = (1-\alpha)\mathbf{U}_{n-1} + \alpha\mathbf{U}_n^{/}$$

$$\mathbf{K}_1^n = \mathbf{K}_1^n(\mathbf{U}_n)$$

}while ($\| \mathbf{U}_n - \mathbf{U}_{n-1} \|_\infty \le 0.001 \| \mathbf{U}_n \|_\infty$) (6.26)

where:

$\mathbf{U}_n^{/}$ = new calculated displacement vector

$\mathbf{U}_n$ = displacement vector after n-th iteration

$\mathbf{K}_1^n$ = nonlinear portion of stiffness after n-th iteration

$\mathbf{K}_0$ = linear portion of stiffness, constant for a given mesh

$\mathbf{F}$ = global loading vector, constant for a given pressure

α = relaxation coefficient, changes between 0.05 to 0.5

If the yielding pressure calculation is required for the top joint, a trial pressure will be used first. After the converged displacement has been calculated, the mean equivalent stress at the entire horizontal part of the top angle is calculated and compared to the yielding stress of the material. A new trial pressure is found by Newton's method for the next pressure step until the calculated stress is within $\pm 0.5\%$ of the yielding stress.

The calculation of bottom yield pressure is similar to that of top yield. The equivalent stress is checked for both shell and bottom elements near the joint and the maximum element stress is compared to the yielding stress.

Due to the nonlinearity of the elastic foundation at the bottom, Newton's method does not give a reliable estimate of the bottom uplift pressure while doing the large iteration loop to determine that pressure. An assumed upper and lower bound of pressure is tried first and a new trial pressure is found by reducing the searching region by half. The calculation is completed when the vertical displacement of the bottom joint node is less than 1% of that of the node at the center of the tank bottom or the pressure between the upper and lower bounds is less than 0.02 psi.

To find a peak pressure in the tank during combustion, the top yield pressure is first calculated. Then a combustion analysis is performed with venting beginning when the top yield pressure is reached. The combustion calculation finishes when the pressure in the tank reduces to zero due to venting. The peak pressure during the combustion process is used for the peak stress calculation.

After each set of calculations is done, the displacement is written to a solution file along with the finite element mesh and other analysis parameters that are used by during post-processing.

6.2.6 Combustion Calculation Procedure

The pressure rise in the vapor space inside the tank is calculated by evaluating combustion in small increments of time. The flame front is assumed to grow in a spherical fashion originating from a point source ignition in the tank. The volume of reactants burned in a given time increment is used to determine the pressure after each time increment. To evaluate this pressure, the speed at which the flame front moves is multiplied by a time increment, giving a distance. From this distance, an incremental volume is calculated. This volume is then burned at constant volume combustion and allowed to expand until the pressure inside the tank is uniform.

To calculate the pressure rise during a time increment, an adiabatic flame temperature is calculated for the flame front, assuming constant volume combustion and chemical equilibrium. The pressure inside the volume swept out by the flame front, during a single time increment, increases due to the burning of the reactants at constant volume. The volume swept by the flame front is then allowed to expand, causing the reactants and products to compress, with no mixing, until the pressure inside the tank is uniform. After the pressure inside the tank is balanced, time is incremented and the process repeated. When the internal pressure reaches the roof-to-shell joint yielding pressure, a venting calculation start and part of the combustion products are vented, reducing the pressure. The peak pressure found during the combustion calculation is used for the structural calculation. The combustion calculation continues until the pressure in the tank is reduced to atmospheric pressure.

In these calculations, the tank is assumed to be adiabatic and the tank rigid. The analysis also neglects radiation heat transfer between the flame front and wall of the tank.

The venting calculation starts when the roof-to-shell joint reaches the failure initiation stress. A venting mass flow rate is calculated and the total mass that has left the tank during an individual time step is used to determine the pressure drop due to venting for that given time step. The mass flow rate of the combustion products is calculated assuming constant pressure and temperature inside the tank for the time increment. The pressure and temperature are then recalculated based on the amount of mass that is left inside the tank.

For venting during frangible joint failure, a simplified analysis assuming adiabatic incompressible open-channel flow through a sluice gate is made, as discussed in chapter 4.3 combustion analysis.

With the time increment small, the change in pressure due to venting over the time increment is sufficiently low for the temperature to be assumed to remain constant for venting during each time increment. After the mass flow rate is calculated for each time step, a new pressure is found by the use of the ideal gas law.

6.2.7 Frangible Joint Failure

The frangible joint failure is a very complicated dynamic process. The fracture of the joint will let the combustion products vent out the opening, then the pressure distribution on the tank roof and shell will changing with time. The geometry of the tank after joint failure initial cannot be described by axisymmetrical shell model nor simple formulas. To get a reasonable estimation of the peak pressure in the tank, a simplified frangible joint failure model is used.

After failure initiation, the roof of the tank is assumed to rotate an angle ϕ as a flat annular plate about a point on the roof-to-shell, but the opening is assumed to be the part of the circumference with an opening angle θ, as shown in Figure 6.5. The moments acting on the roof are due to pressure, gravity, air resistance, inertia, edge force, and edge moment, respectively.

The moment due to the weight of the roof to a point on the edge is the product of the total weight of the disk and the horizontal projection of the distance from the center of the disk to the edge point:

$$\begin{aligned} M_w &= \pi R^2 \rho t_h \cdot R\cos\phi \\ &= \rho g t_h \pi R^3 \cos\phi \end{aligned} \tag{6.27}$$

where:

t_h = thickness of the roof,

g = acceleration of gravity,

ρ = density of steel.

After the failure initiation of the roof-to-shell joint, the pressure on the roof has a very complicated distribution. The pressure on the edge of the opening should be lower than that acting on the roof far from the opening. When the roof reaches the vertical position where $\phi = \pi/2$, there should be no pressure moment on the roof. To simplify the problem, one can assume the moment due to the pressure acting on a small strip of the roof (see Figure 6.6) as following:

$$dM_p = 2\,x\,P\,dy \cdot (y + R)\cos\phi \tag{6.28}$$

where:

P = pressure difference between two sides of the roof.

By integration we have:

$$\begin{aligned} M_p &= \int_{-R}^{R} 2\,P\cos\phi\,(y+R)\sqrt{R^2 - y^2}\,dy \\ &= 2\,P\cos\phi\left[\frac{1}{2}y\sqrt{R^2 - y^2} + \frac{1}{2}R^2\sin^{-1}\frac{y}{R}\right]_{-R}^{R} \\ &= \pi R^3\,P\cos\phi \end{aligned} \tag{6.29}$$

The air drag of a flat disk normal to the flow can be calculated by (Fox and McDonald, 1985):

$$f = \frac{1}{2}\rho_{air}V^2 C_D A \tag{6.30}$$

where:

ρ_{air} = density of air,

C_d = drag coefficient, = 1.143 for flat disk.

The moment comes from a small strip as shown in Figure 6.6 and can be written as:

$$dM_r = \frac{1}{2}\rho_{air} V^2 C_D \cdot 2x\,dy \cdot (y + R) \tag{6.31}$$

Integrate over the entire surface gives:

$$\begin{aligned} M_r &= \int_{-R}^{R} \rho_{air} \dot{\phi}^2 C_D (y + r)^3 \sqrt{R^2 - y^2}\, dy \\ &= \rho_{air} C_D \dot{\phi}^2 \int_{-R}^{R} (y^3 + 3Ry^2 + 3R^3 y + R^3)\sqrt{R^2 - y^2}\, dy \\ &= \rho_{air} C_D \dot{\phi}^2 \left[\frac{3}{8} R^5 \sin^{-1} \frac{y}{R} + \frac{1}{2} R^5 \sin^{-1} \frac{y}{R} \right]_{-R}^{R} \\ &= \frac{7}{8} \pi \rho_{air} \dot{\phi}^2 c_D R^5 \end{aligned} \tag{6.32}$$

The moment of inertia of the disk to the rotation axis at the edge is:

$$I = (\frac{1}{4} R^2 + R^2)\pi R^2 \rho t_h$$

Then the inertia moment can be written as:

$$M_i = -\frac{5}{4} \pi R^4 \rho t_h \ddot{\phi} \tag{6.33}$$

Assuming an edge force f_j acting on the unopened portion of the roof-to-shell joint is uniformly distributed and keeps a vertical direction, the edge force will causes a moment about the roof rotation axis, described as:

$$\begin{aligned} M_f &= 2\int_{\theta_o}^{\pi} f_j R\, d\theta (y + R)\cos\phi \\ &= 2 f_j R^2 \cos\phi \int_{\theta_o}^{\pi} (\cos\theta + 1)\, d\theta \\ &= 2 f_j R^2 \cos\phi (\pi - \theta_o - \sin\theta_o) \end{aligned} \tag{6.34}$$

The edge force will keep the same value as evaluated from the root-to-shell joint failure initiation calculation.

There is also a bending moment acting on the edge of the roof, as shown in Figure 6.7 The resulted total moment projection to the axis of the roof rotation can be written in the following integral form:

$$\begin{aligned} M_m &= 2\int_{\theta_o}^{\pi} m_j \cos\theta R\, d\theta \cos\phi \\ &= -2 m_j R \cos\phi \sin\theta \end{aligned} \tag{6.36}$$

The edge moment m_j will be obtained at roof-to-shell joint yield pressure. All the moments project to the axis of rotation ϕ leads to the following relation:

$$M_p - M_w + M_i - M_r - M_f + M_m = 0 \tag{6.37}$$

When the roof has rotated an angle ϕ, the opening will has an angle θ_o from the axis of symmetry. At a given instant, the maximum opening width would be:

$$y_{max} = 2R\sin\phi \tag{6.38}$$

Assume the opening width as the function of θ is:

$$y = \frac{1}{2} y_{max}\left[1 + \cos\left(\frac{\pi\theta}{\theta_o}\right)\right] \tag{6.39}$$

The total opening area can be calculated as:

$$\begin{aligned} A_{open} &= 2\int_0^{\theta_o} y R\, d\theta \\ &= y_{max} R \int_0^{\theta_o} (1 + \cos\frac{\pi\theta}{\theta_o})\, d\theta \\ &= R\, y_{max}\theta_o \end{aligned} \tag{6.40}$$

It is reasonable to say that when $\phi = 0$, we need $\theta_o = 0$ and if the roof rotates $\phi = \pi/2$ then the roof will fly off and $\theta_o = \pi$. If we also assume that

when ϕ equal or larger than $\pi/4$, the opening area will reach its maximum possible value, that is, the cross section area of the tank, we have:

$$\theta_o = \pi \sin\phi \tag{6.41}$$

The opening area can then be written as a function of ϕ only as following and calculated in each step of combustion analysis.

$$A_{open} = 2\pi R^2 \sin^2\phi \tag{6.42}$$

6.3 Verification

Two example/verification problems were performed. The designs used in the calculations are based on actual tank designs. The API-Tank solutions were compared to both analytic and ANSYS solutions.

6.3.1 Example 1: Tank designed following API 650 standard.

The example tank 1 conforms the API 650 standard for frangible roof joint design. It is the same 25 feet diameter tank been analyzed for preliminary calculations (see chapter 4). The design parameters listed by API-Tank are shown in Table 6.3:

The API-Tank finite element model has 240 nodes, 239 shell elements and 61 interface elements.. The same mesh is used in the ANSYS 5.0 finite element model. In ANSYS, the shell is modeled using Shell 51 element and the tank foundation is modeled by Interface 12 element. The input file for the ANSYS calculation is listed in Appendix B.1. Calculations were performed at 0.1 psi and 1.0 psi pressure, respectively. Also calculated is the linear closed form solution of the stresses near the joint of a cortical roof and a cylindrical shell (Young, 1989), with an annular ring representing the top angle. Since the linear closed form solution does not include the gravity loading, its internal pressure was reduced by 0.052 psi, which is the value

required to overcome the weight of the roof. The calculated displacements and stressed are plotted in Figure 6.8 through Figure 6.15.

6.3.2 Example 2: Tank designed violating API 650 standard

The second example tank has 2 inches in 12 inches roof slope and a larger top angle. Its design violated the API 650 standard, but when it caught on fire, the roof-to-shell joint did open up as a frangible one (The liquid level when the fire occurred is unknown). The design parameters are listed in Table 6.4.

The API-Tank finite element model has 274 nodes, 273 shell elements and 70 interface elements.. The same mesh was used in ANSYS 5.0 finite element model, as listed in Appendix B.2. The linear closed form solution was calculated and plotted. In this case, the linear stresses are not precise since the algorithm cannot model the overlapped top angle. The calculated displacements and stressed are plotted in Figure 6.16 through Figure 6.23.

6.3.3 Validity of API-Tank

The verification calculations indicate that API-Tank, ANSYS and linear closed form solution all give similar results at the roof-to-shell joint when the internal pressure is low, as shown in Figures 6.8 through 6.11 and Figures 6.16 through 6.19. In those cases, the deflections are small, so that the nonlinear results are close to that of a linear analysis. There is no linear closed form solution for the shell-to-roof joint calculation since the linear analysis will give a very large lateral deformation but no radial displacement on the circular plate. Only the stresses near the roof-to-shell joint are calculated analytically and compared with finite element models.

Under higher pressure, the nonlinear finite element solutions give smaller stresses than the linear analysis, as shown in Figures 6.13.a, 6.14.a, and 6.15.a. The API-Tank gives somewhat larger displacement than ANSYS, hence larger stresses result. Near the roof-to-shell joint, the differences are

not significant. At the shell-to-bottom joint, API-Tank gives larger uplift of bottom plate and higher stresses than calculated by ANSYS. The reason is API-Tank and ANSYS are using different large deflection formulations. The ANSYS finite element model is stiffer than that of API-Tank. The differences are smaller at the roof-to-shell joint, with both programs giving similar yield pressure. The larger bottom deformation by API-Tank will give a more conservative bottom failure prediction than that by ANSYS. The relative strength of roof-to-shell joint to shell-to-bottom joint calculated by API-Tank will also be a little higher than that by ANSYS. Further comparisons with other large deformation calculations would be useful to further establish the correct solutions, however, the API-Tank calculations are considered valid for predicting the joint behavior.

6.4 Calculated Relative Strength Of Top And Bottom Joints

Calculations using API-Tank show that the relative strength of the roof-to-shell joint and shell-to-bottom joint is a strong function of the liquid level stored in the tank when the overpressurization occurred. The weight of the liquid holds the bottom from being uplifted and reduces the stress at the shell-to-bottom joint. Different tank failure modes were calculated for tanks height of 15, 30, and 45 feet and tank diameters ranging from 15 to 120 feet. The results are shown in Figures 6.24 through 6.29. For empty tanks, the uplift pressure predicted by the API 650 rules and the finite element calculation are essentially identical. In many cases, the uplift will occur before failure initiation at the roof-to-shell joint. The predicted failure pressures on roof-to-shell joint by API-Tank are much higher than that given by API 650 rules. The API-Tank calculations match the ANSYS calculation and observed failure process. The frangible joint failure pressures is usually smaller than the bottom yield pressure, but the safety margin is relatively small for small diameter empty tanks.

The calculations raise some unresolved issues. One problem is for what liquid level in the tank should the evaluation of safety be done. The empty tank has lowest failure pressure and smaller bottom to top joint strength ratio, but less damage will be expected if the bottom failure did occur. On the other hand, the full, higher tank has larger bottom to top joint strength, but the consequences of bottom failure will be much worse than that of an empty tank. The recommended values are yet to be determined.

Another question is how to bring complex results into simple design criteria. During the combustion process, the internal pressure will rise beyond the value needed to cause roof-to-shell joint to yield. We think that it might be useful to take the relative strength ratio of the two joints as a requirement, say, the safe design should have the bottom yielding pressure twice as much as the top yielding one.

Region	Number of Elements	Size of Elements	Condition
N_1	12	0.5	Always
N_2	12	1.0	Always
N_3	(R-18)/2 6	Calculated 2.0	24 < R < 33 33 < R
N_4	0 (R-30)/3 6	- Calculated 3.0	R < 33 33 < R < 52 52 < R
N_5	0 (R-48)/4 12	- Calculated 4.0	R < 52 52 < R < 102 102 < R
N_6	0 (R-96)/6 10	- Calculated 6.0	R < 102 102 < R < 168 168 < R
N_7	0 (R-156)/12	- Calculated	R < 168 168 < R
N_8	2 2	0.5 1/3 Angle Width	Angle Width > 1 Angle Width < 1
N_9	Angle Width -1 1	0.5 1/3 Angle Width	Angle Width > 1 Angle Width < 1
N_{10}	2 x Angle Width 1	0.5 2 x Shell Thick	Angle not overlap shell Angle overlap shell
N_{11}	12	0.5	Always
N_{12}	12	1.0	Always
N_{13}	6	2.0	Always
N_{14}	6 (Top course height-30)/3+1	4.0 Calculated	Top course height > 48 102 < R < 168
N_{15}	0 (Top course height-48)/2+1	- Calculated	Top course height < 48 Top course height > 48
N_{16}	10	Calculated	All intermediate courses

Table 6.1: Finite element mesh on upper part of tank

Region	Number of Elements	Size of Elements	Condition
N_{16}	10	Calculated	All intermediate courses
N_{17}	0 (Bottom course height-48)/2+1	- Calculated	Bottom course < 48 Bottom course > 48
N_{18}	6 (Bottom course height-48)/3+1	4.0 Calculated	Bottom course < 48 30 < Bottom course < 48
N_{19}	6	2.0	Always
N_{20}	12	1.0	Always
N_{21}	12	0.5	Always
N_{22}	2	Calculated	Always
N_{23}	12	0.5	Always
N_{24}	12	1.0	Always
N_{25}	(R-18)/2 6	Calculated 2.0	24 < R < 33 33 < R
N_{26}	0 (R-30)/3 6	- Calculated 3.0	R < 33 33 < R < 52 52 < R
N_{27}	0 (R-48)/4 12	- Calculated 4.0	R < 52 52 < R < 102 102 < R
N_{28}	0 (R-96)/6 10	- Calculated 6.0	R < 102 102 < R < 168 168 < R
N_{29}	0 (R-156)/12	- Calculated	R < 168 168 < R

Table 6.2: Finite element mesh on lower part of tank

```
Diameter of the tank:    26.000   ft.
Height of the tank:    36.000   ft.
Roof slope:     0.750   inch in 12 inches
Thickness of roof plate:    0.1875   in.
Top angle width:     2.000   in.
Top angle thickness:    0.1875   in.
Top angle at outside of tank
Angle does not overlap top shell
Number of courses:    4
Course     Height (in.)   Thickness (in.)

       1      108.000          0.2500
       2      108.000          0.2500
       3      108.000          0.2500
       4      106.000          0.1875

Thickness of bottom plate:    0.2500   in.
Bottom plate beyond shell:      2.00   in.
No annular bottom plate
Inner radius of ringwall:    12.500   ft.
Stiffness of ringwall:    1000.0   psi/in.
Stiffness of sand foundation:     250.0   psi/in.
Material of the tank plate:   ASTM A36
Minimum yielding strength:     36.00   ksi
```

Table 6.3: Design Parameters of Tank 25

Diameter of the tank: 41.000 ft.
Height of the tank: 50.000 ft.
Roof slope: 2.000 inch in 12 inches
Thickness of roof plate: 0.1875 in.
Top angle width: 2.500 in.
Top angle thickness: 0.3125 in.
Top angle at outside of tank
Top angle overlap top shell
Number of courses: 7

Course	Height (in.)	Thickness (in.)
1	95.000	0.3125
2	97.000	0.2500
3	97.000	0.2500
4	97.000	0.2500
5	71.500	0.1875
6	71.500	0.1875
7	70.620	0.1875

Thickness of bottom plate: 0.2500 in.
Bottom plate beyond shell: 1.50 in.
No annular bottom plate
Inner radius of ringwall: 20.000 ft.
Stiffness of ringwall: 1000.0 psi/in.
Stiffness of sand foundation: 250.0 psi/in.
Material of the tank plate: ASTM A36
Minimum yielding strength: 36.00 ksi

Table 6.4: Design Parameters of Tank 55

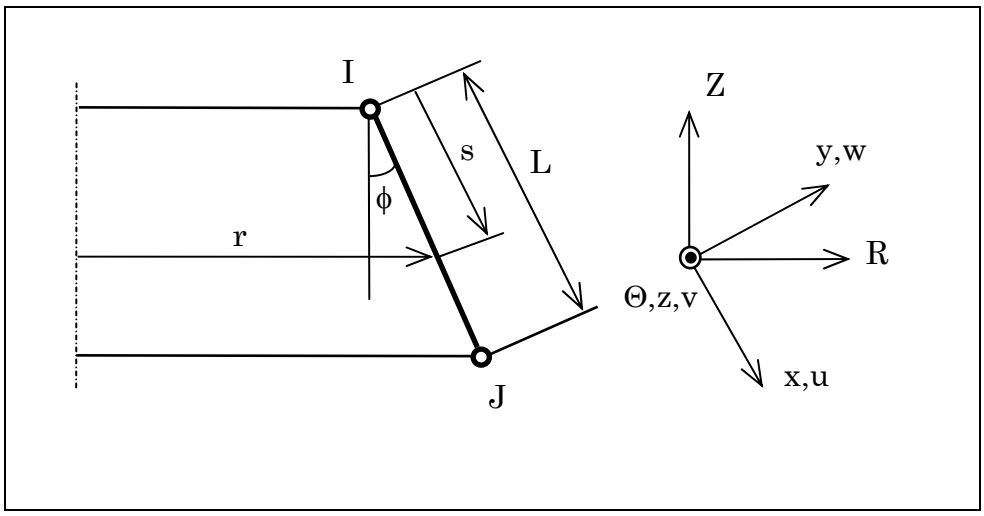

Figure 6.1: Axisymmetric Shell Element

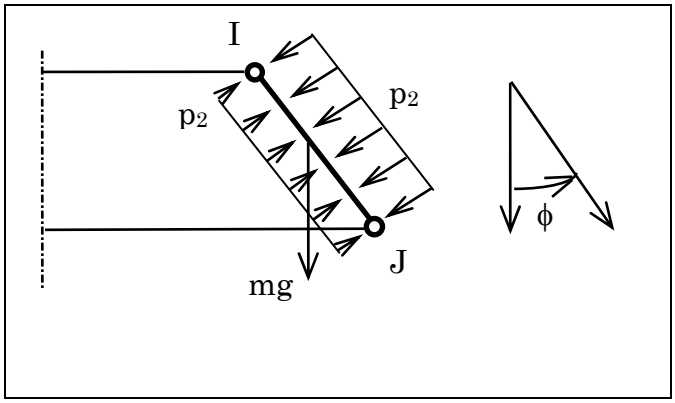

Figure 6.2: Loading on Element

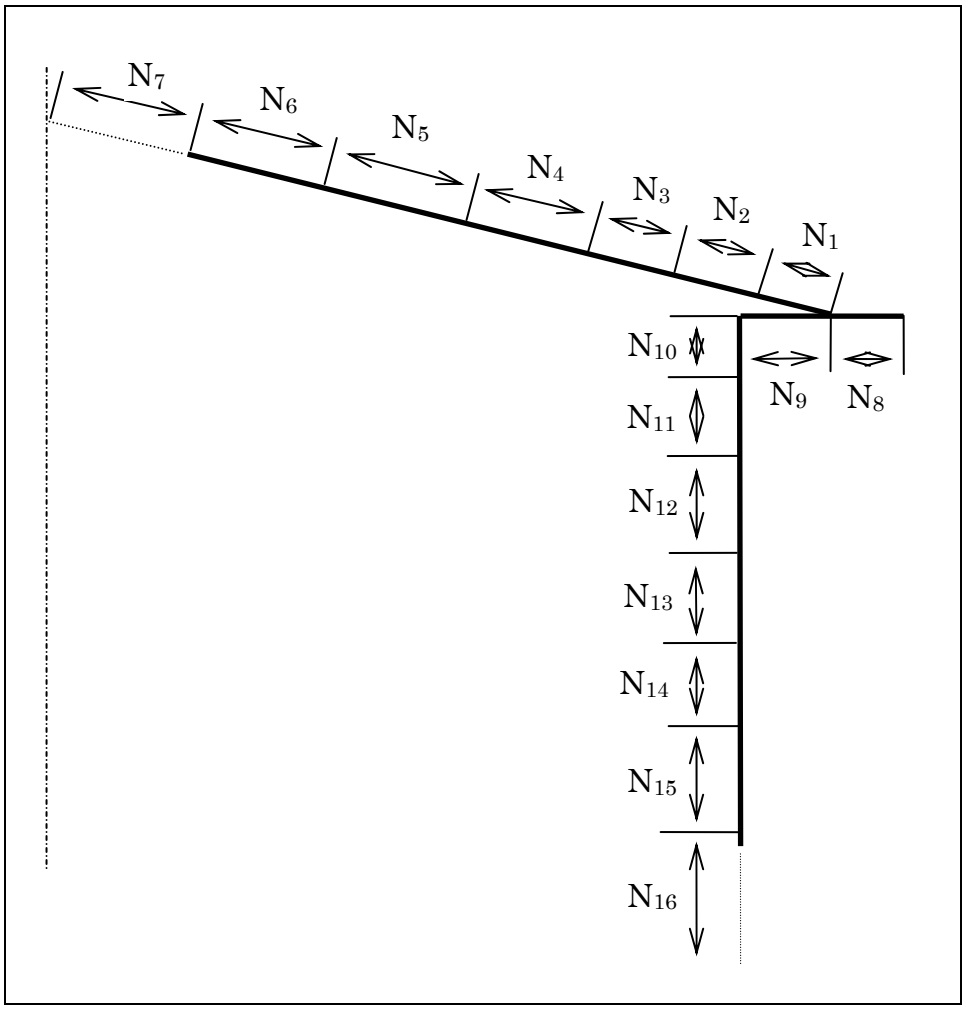

Figure 6.3: Finite Element Mesh on Upper Part of the Tank

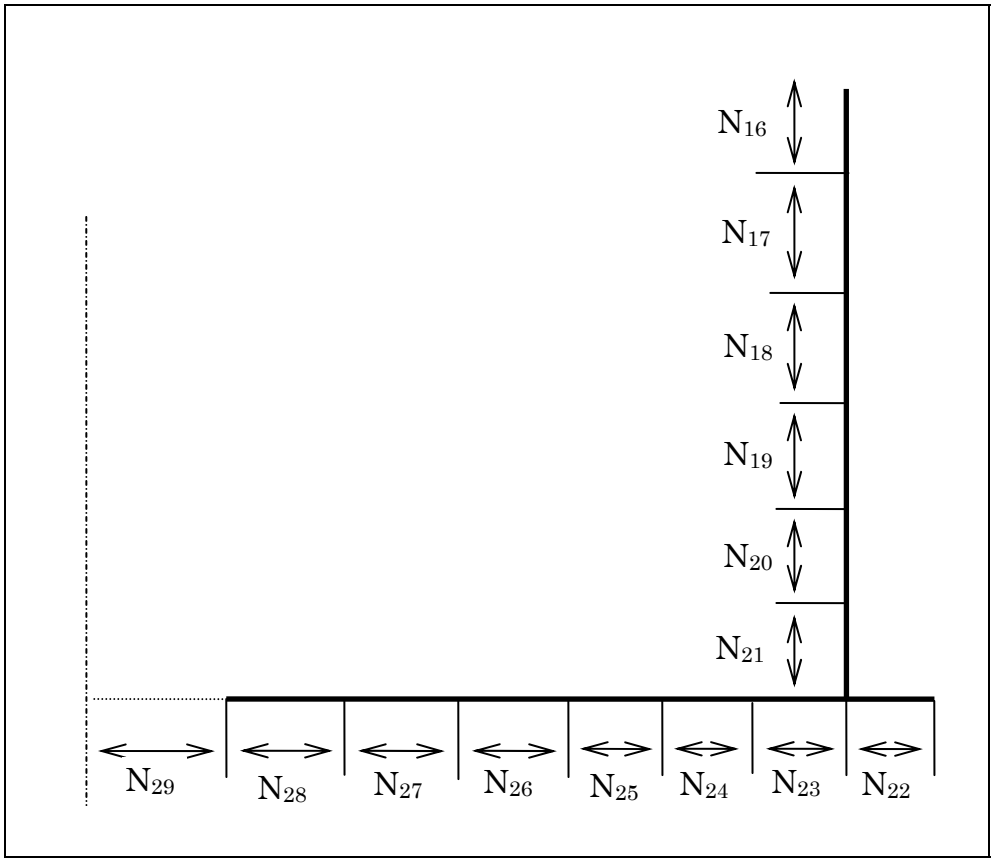

Figure 6.4: Finite Element Mesh on Lower Part of the Tank

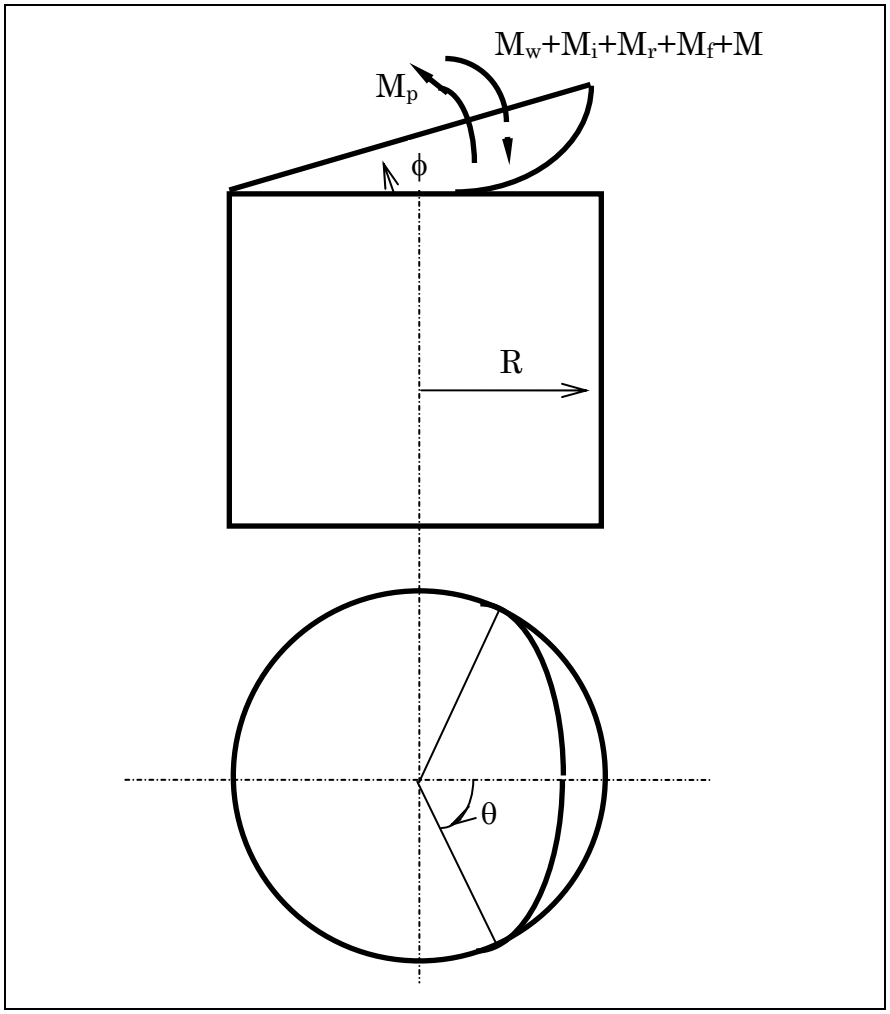

Figure 6.5: Forces Acting on Roof During Venting

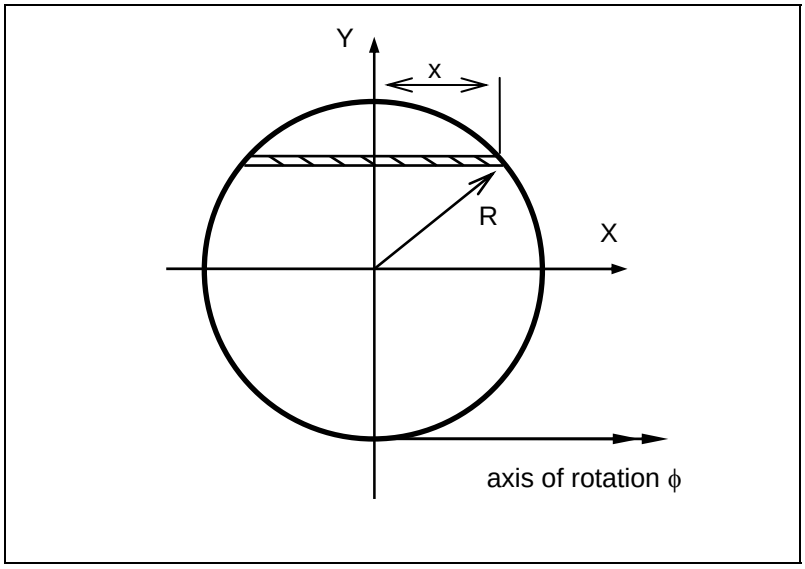

Figure 6.6 Integration Of A Strip Area about Axis of Rotation

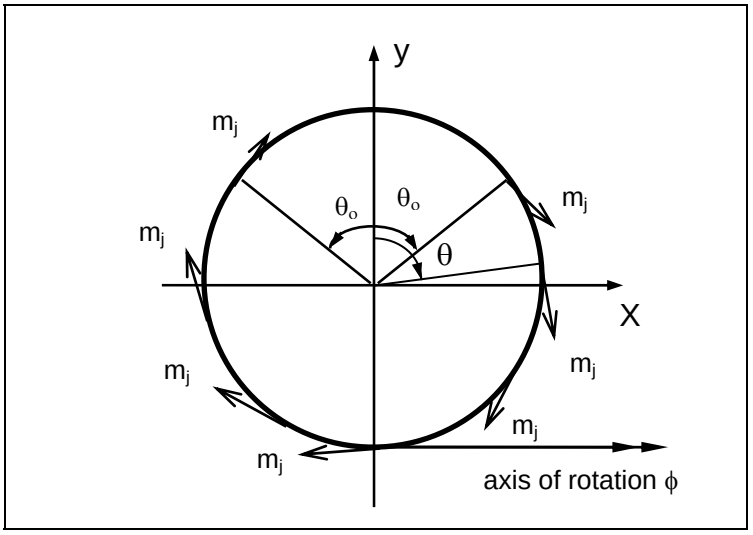

Figure 6.7 Edge Moment On Tank Roof

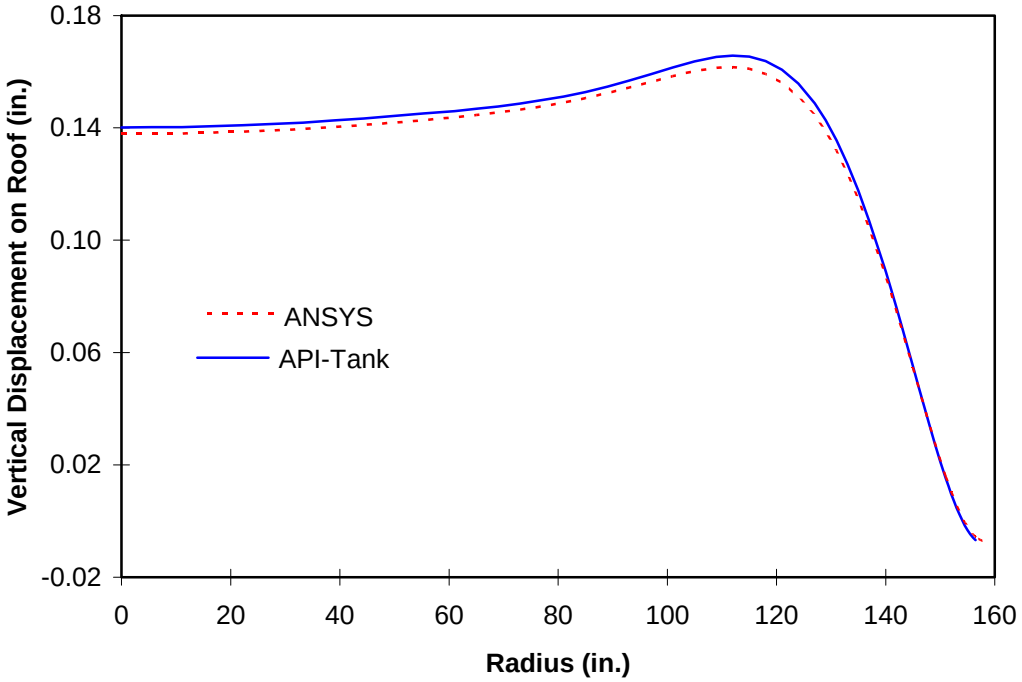

a: Deformation on the roof

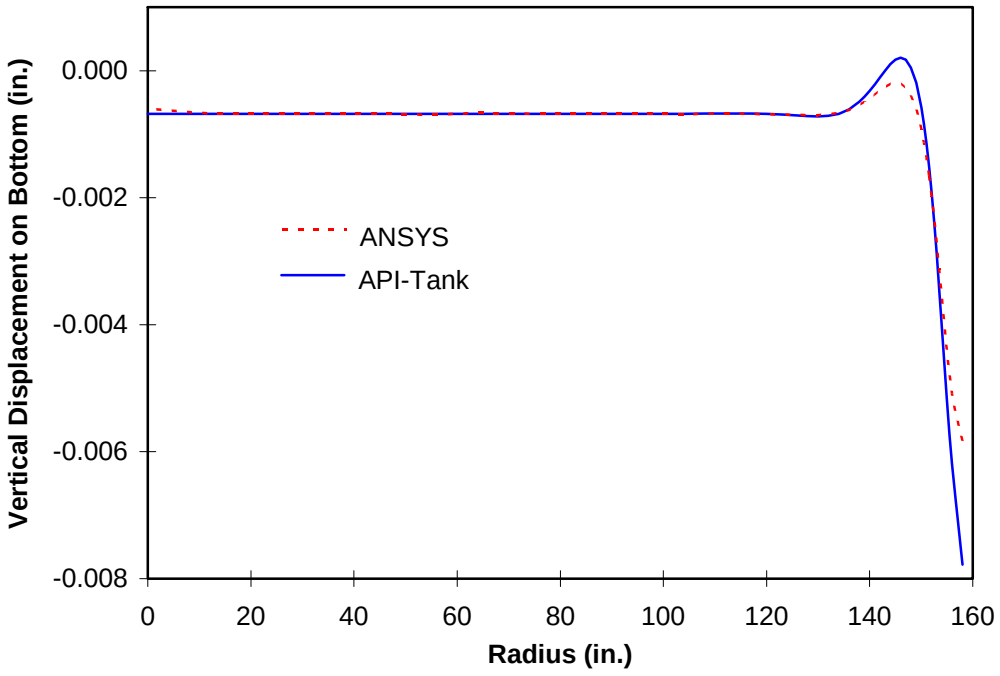

b: Deformation on the bottom

Figure 6.8: Deformation of Example Tank 1, Empty with 0.1 psi Pressure

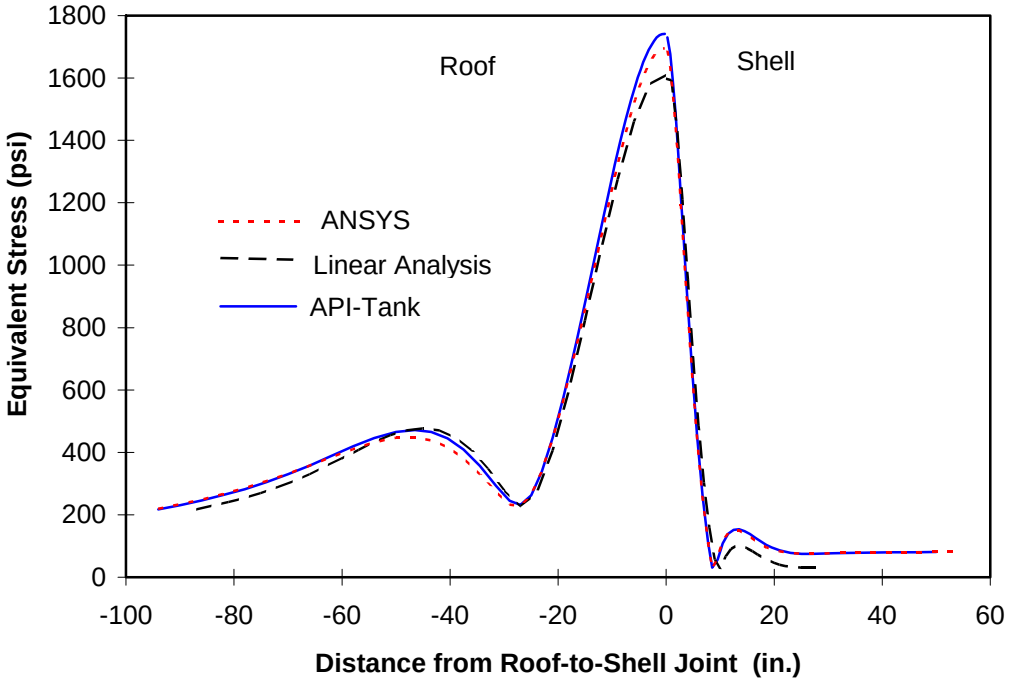

a: Near the roof-to-shell joint

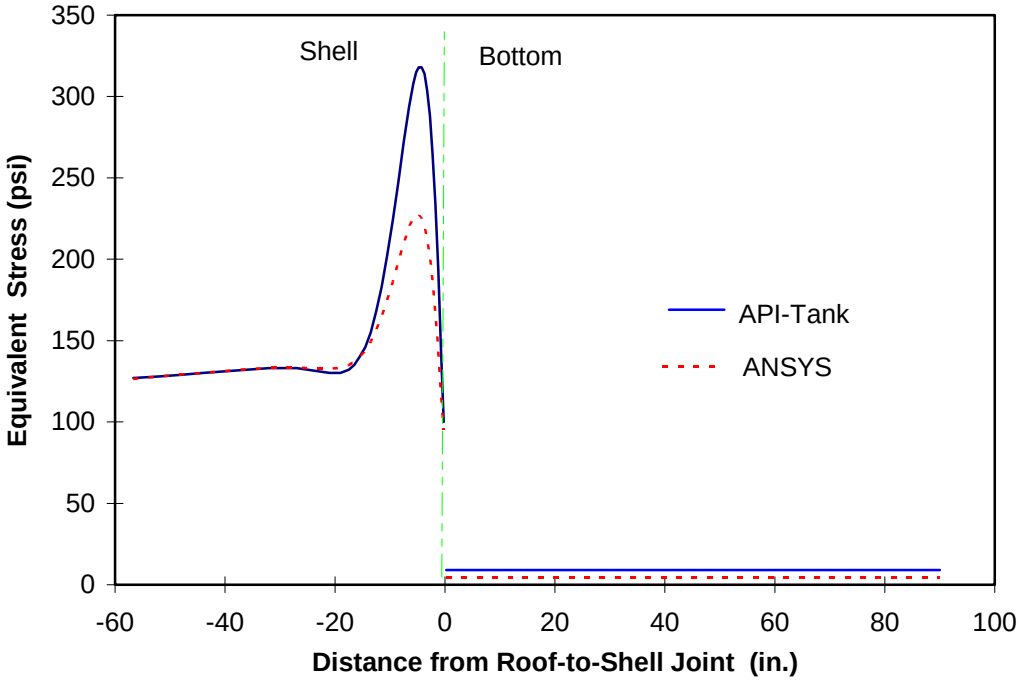

b: Near the shell-to-bottom joint

Figure 6.9: Equivalent Stress in Example Tank 1, Empty with 0.1 psi Pressure

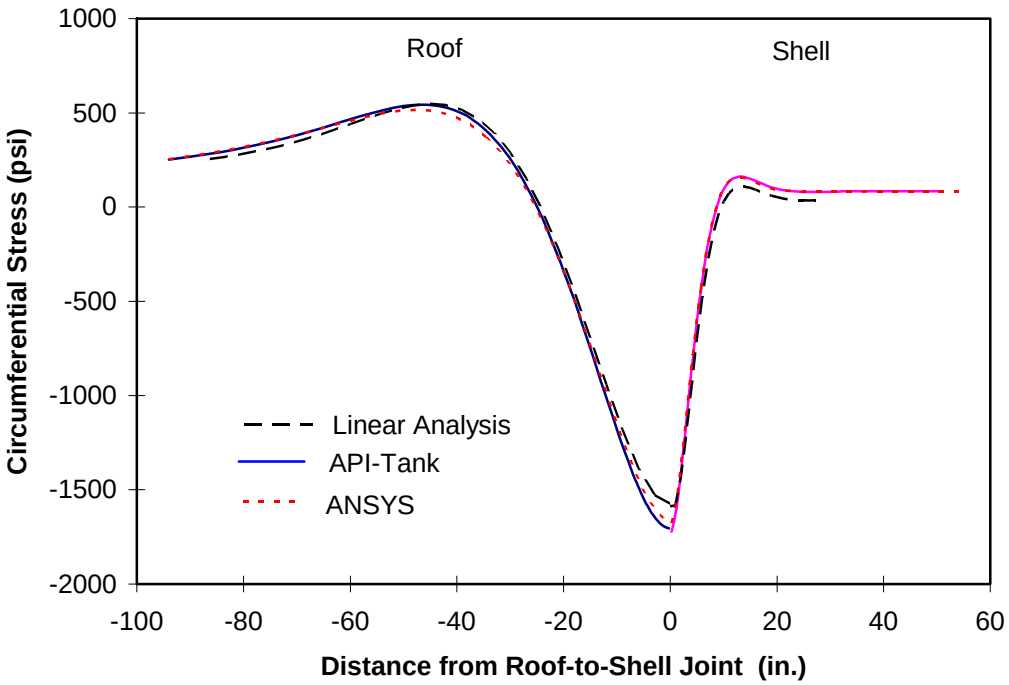

a: Near the roof-to-shell joint

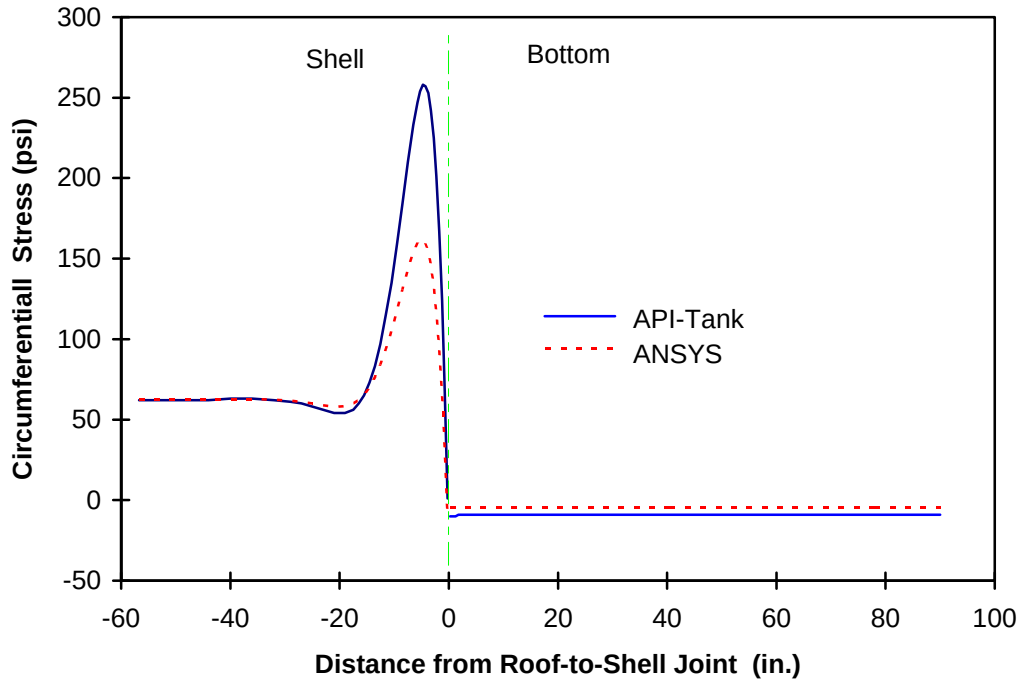

b: Near the shell-to-bottom joint

Figure 6.10: Circumferential Stress in Example Tank 1, Empty with 0.1 psi Pressure

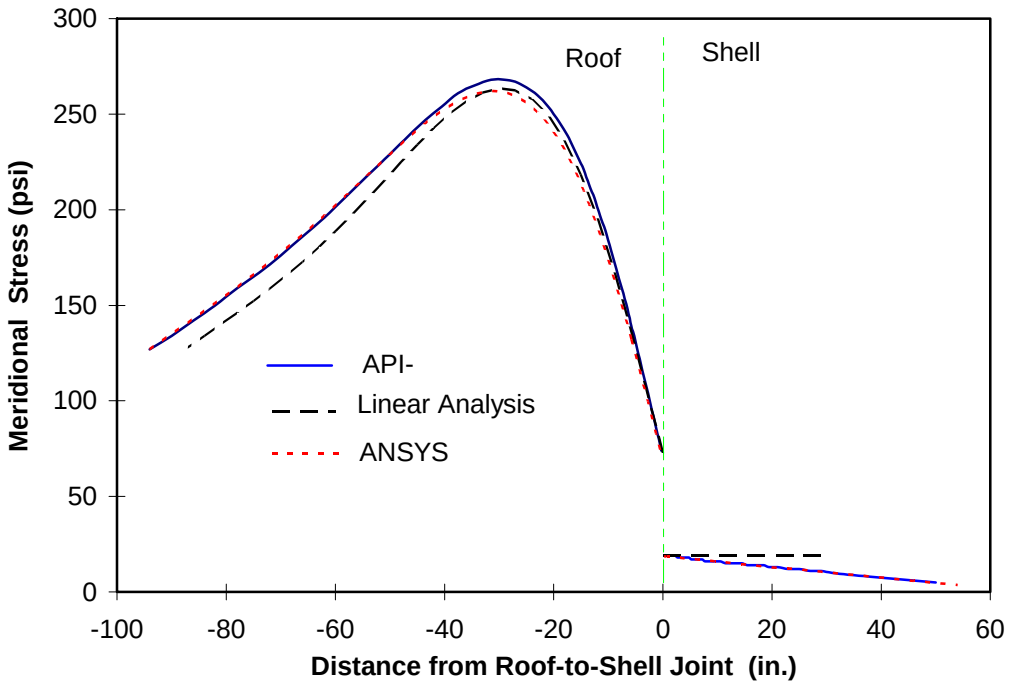

a: Near the roof-to-shell joint

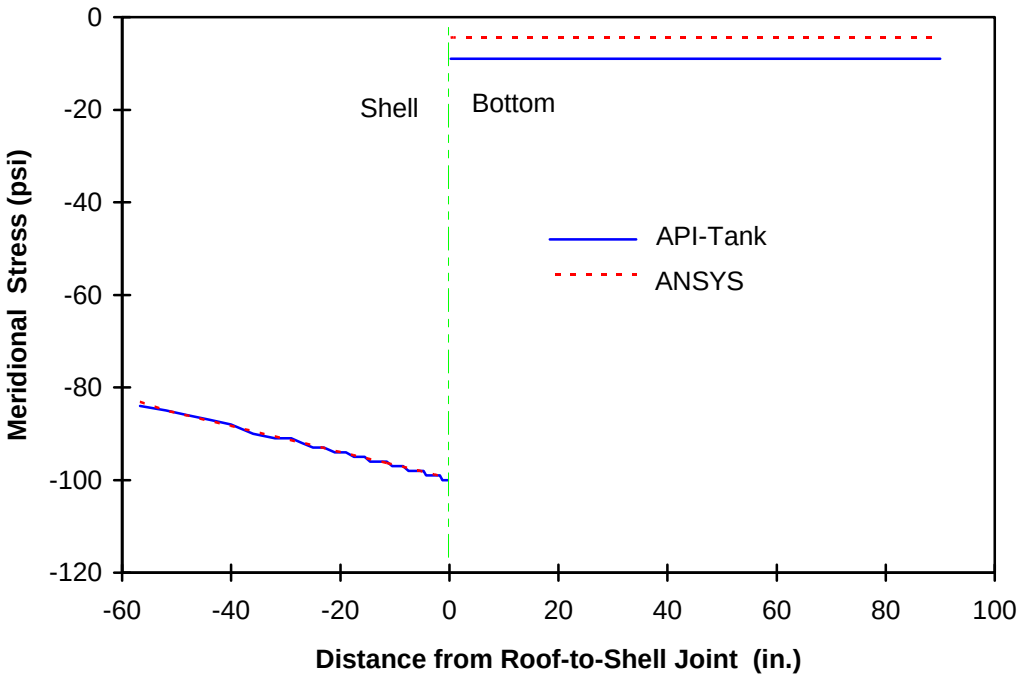

b: Near the shell-to-bottom joint

Figure 6.11 Meridional Stress in Example Tank 1, Empty with 0.1 psi Pressure

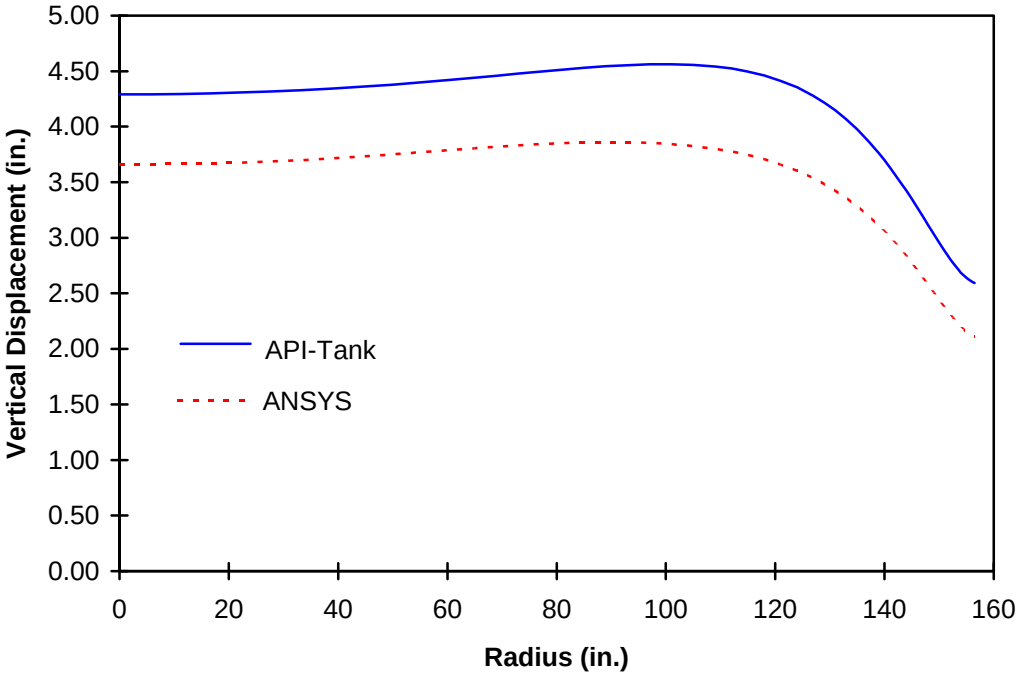

a: Deformation on the roof

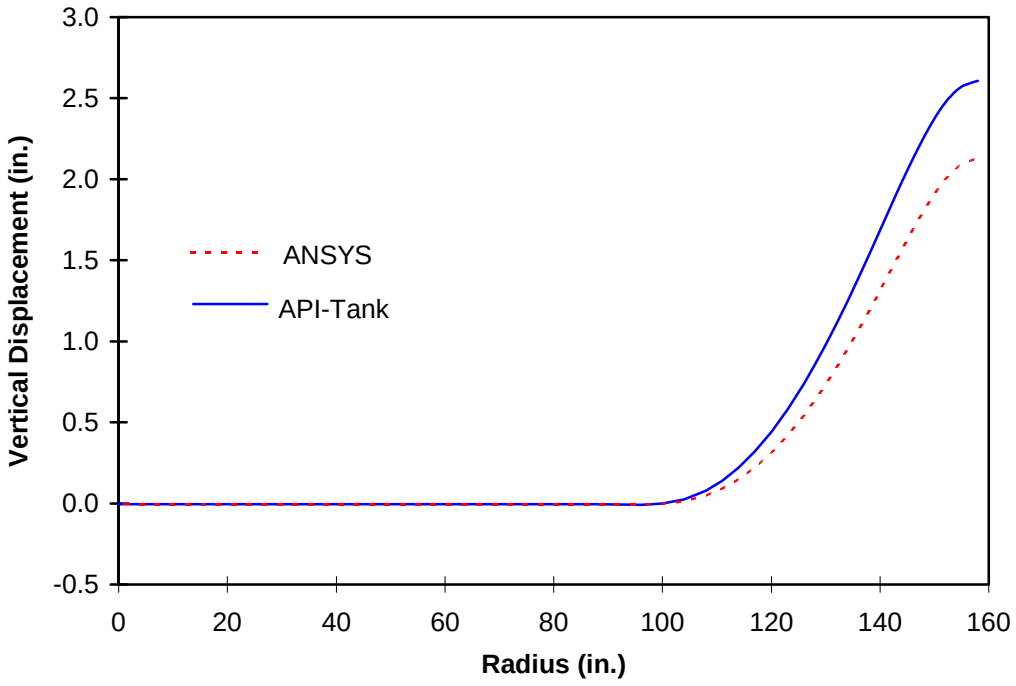

b: displacement on the bottom

Figure 6.12: Displacement of Example Tank 1, Empty with 1.0 psi Pressure

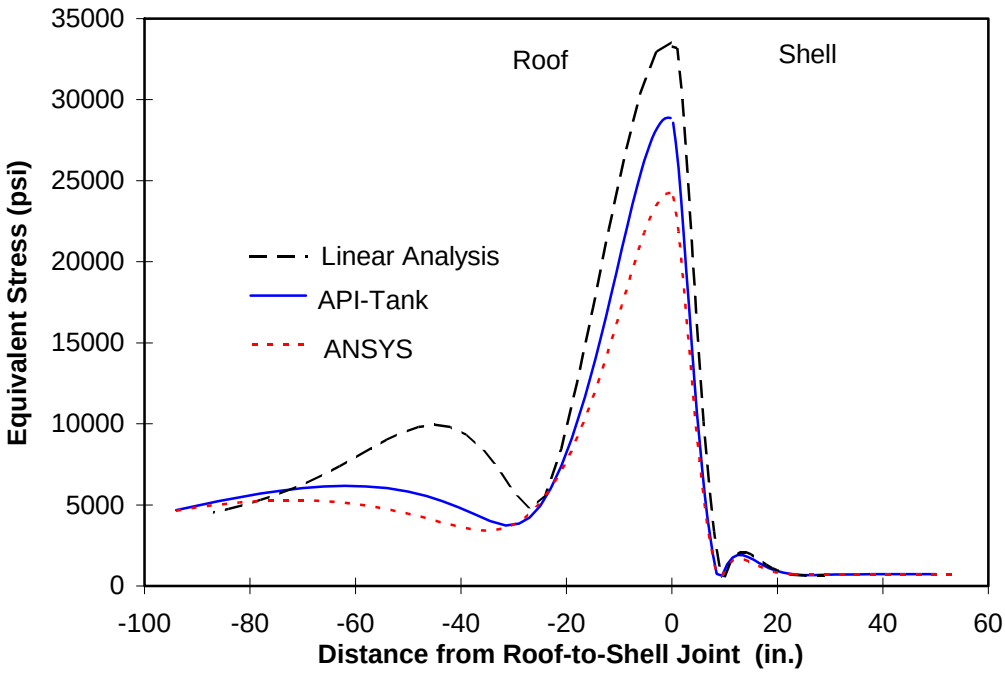

a: Near the roof-to-shell joint

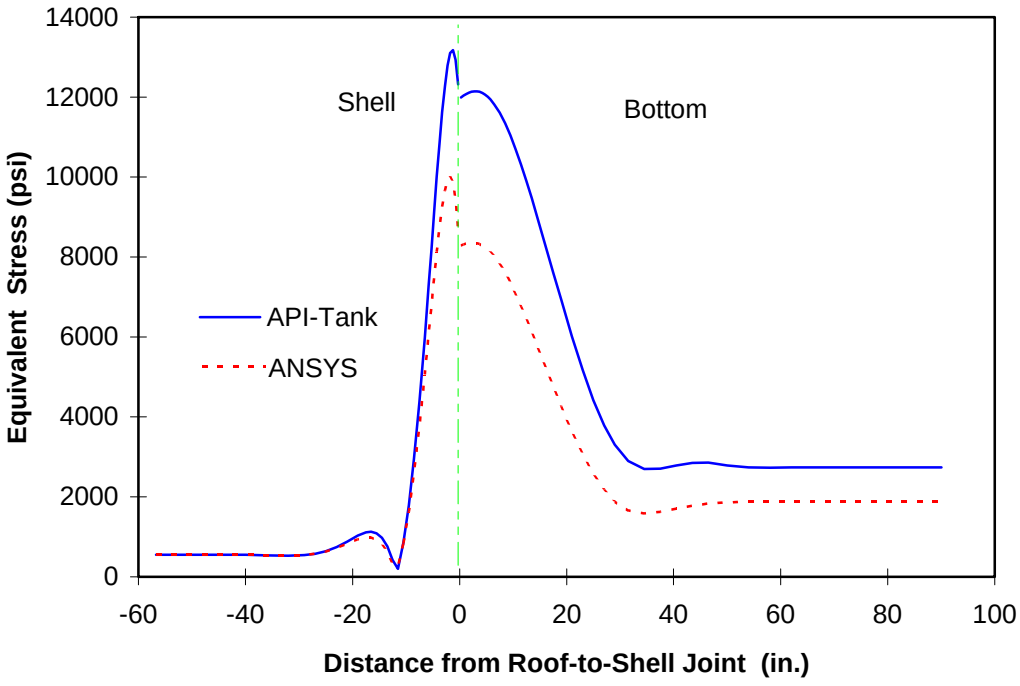

b: Near the shell-to-bottom joint

Figure 6.13: Equivalent Stress in Example Tank 1, Empty with 1.0 psi Pressure

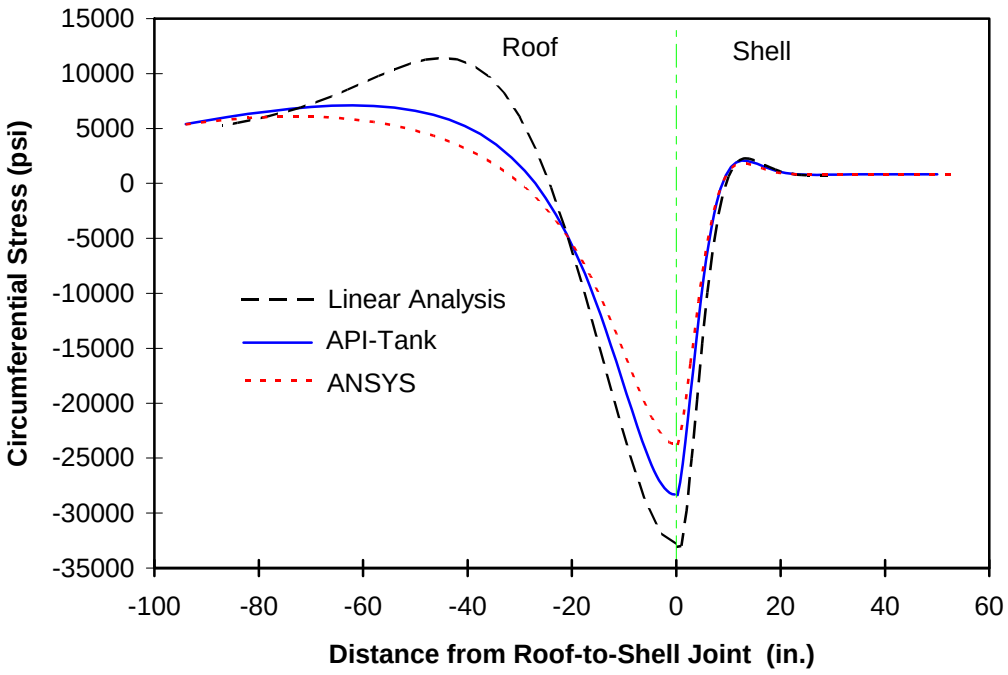

a: Near the roof-to-shell joint

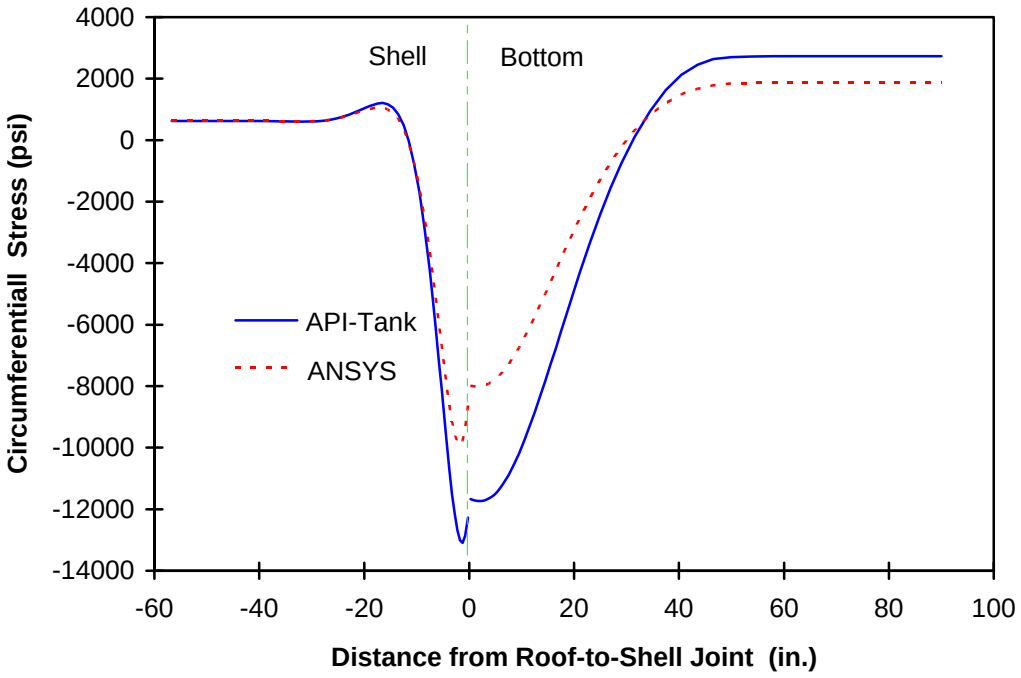

b: Near the shell-to-bottom joint

Figure 6.14: Circumferential Stress in Example Tank 1, Empty with 1.0 psi Pressure

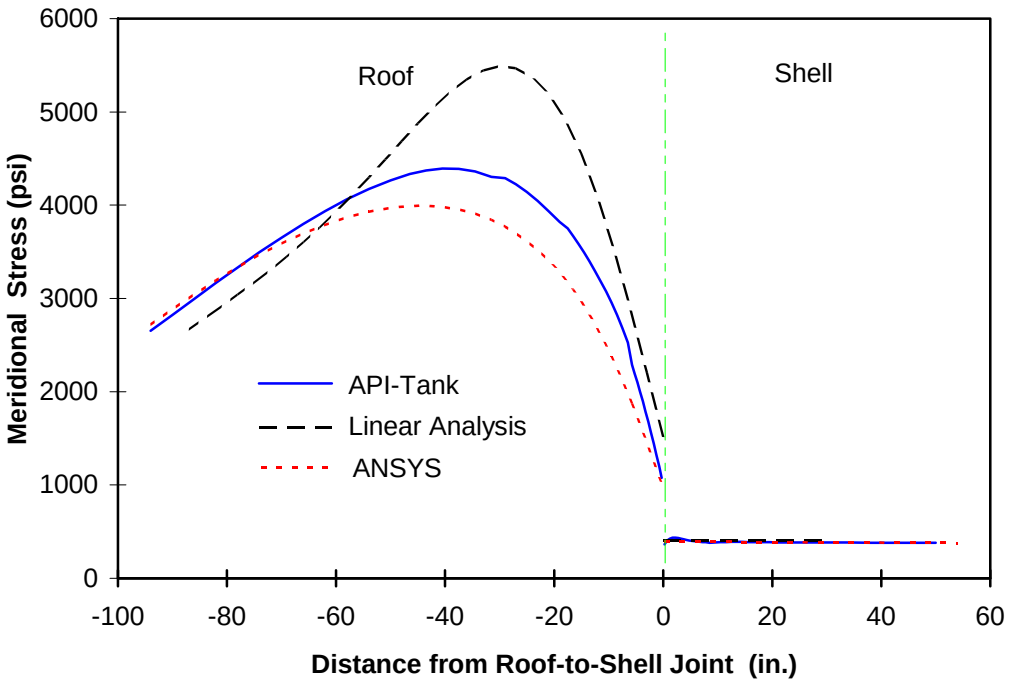

a: Near the roof-to-shell joint

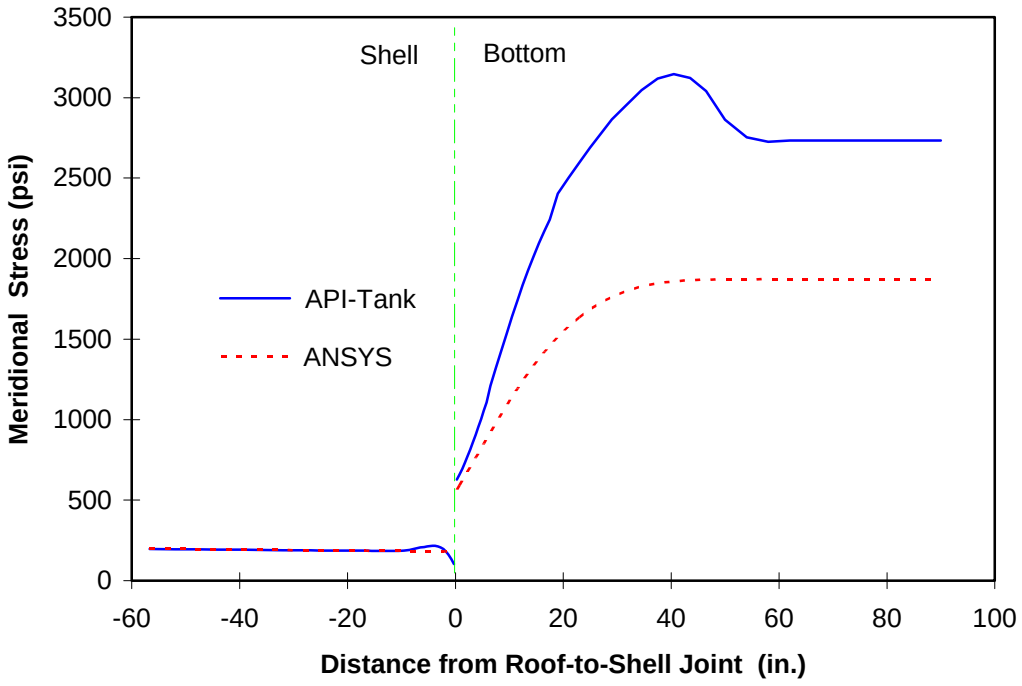

b: Near the shell-to-bottom joint

Figure 6.15: Meridional Stress in Example Tank 1, Empty with 1.0 psi Pressure

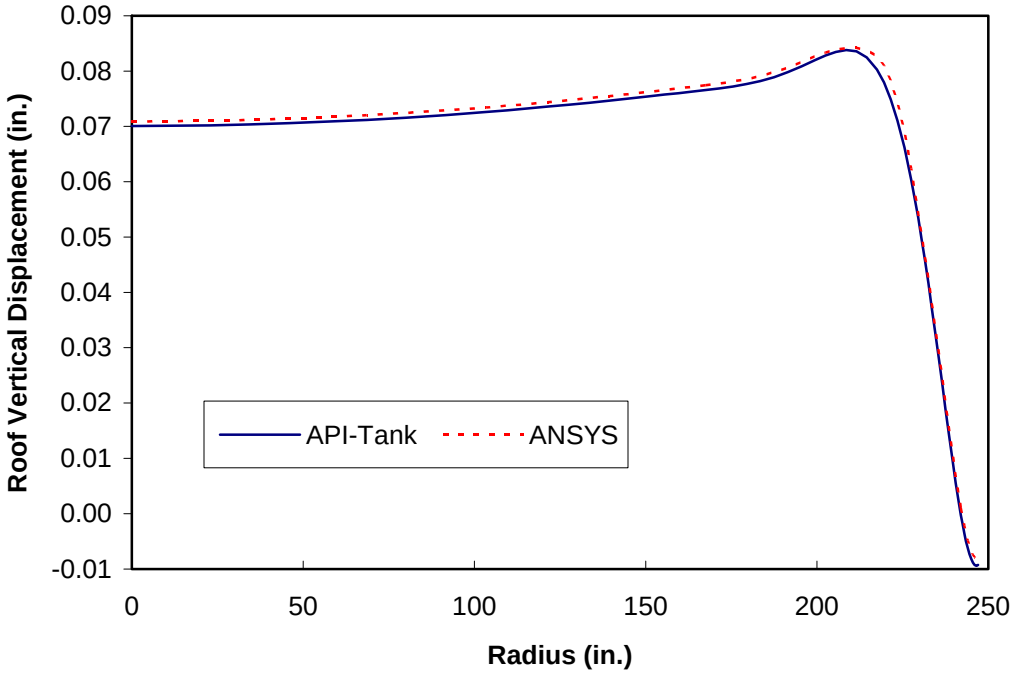

a: displacement on the roof

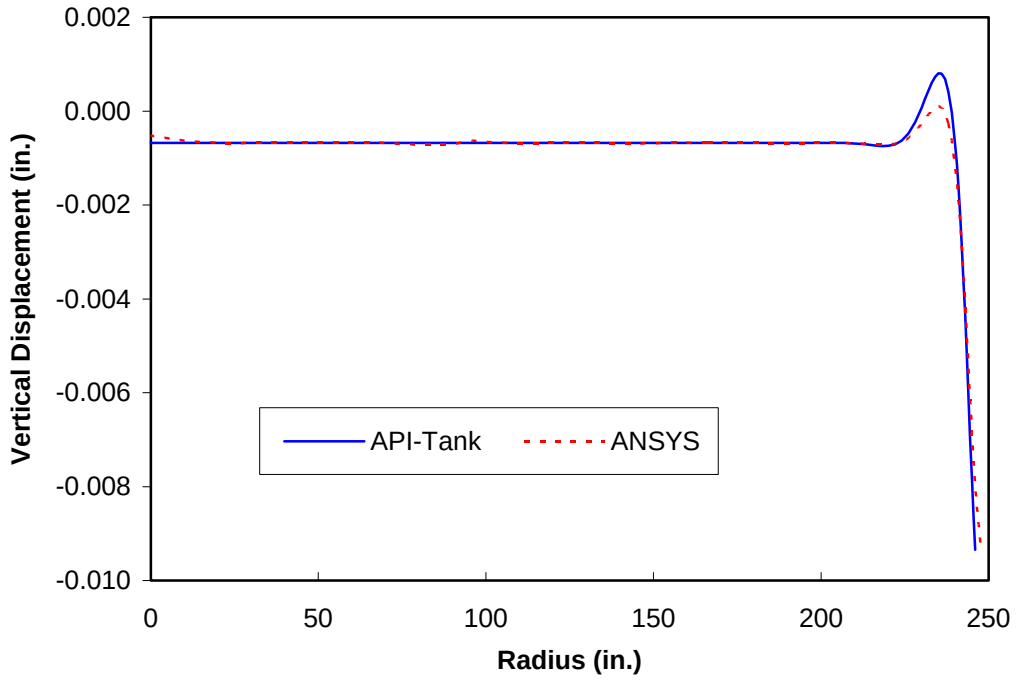

b: displacement on the bottom

Figure 6.16: Deformation of Example Tank 2, Empty with 0.1 psi Pressure

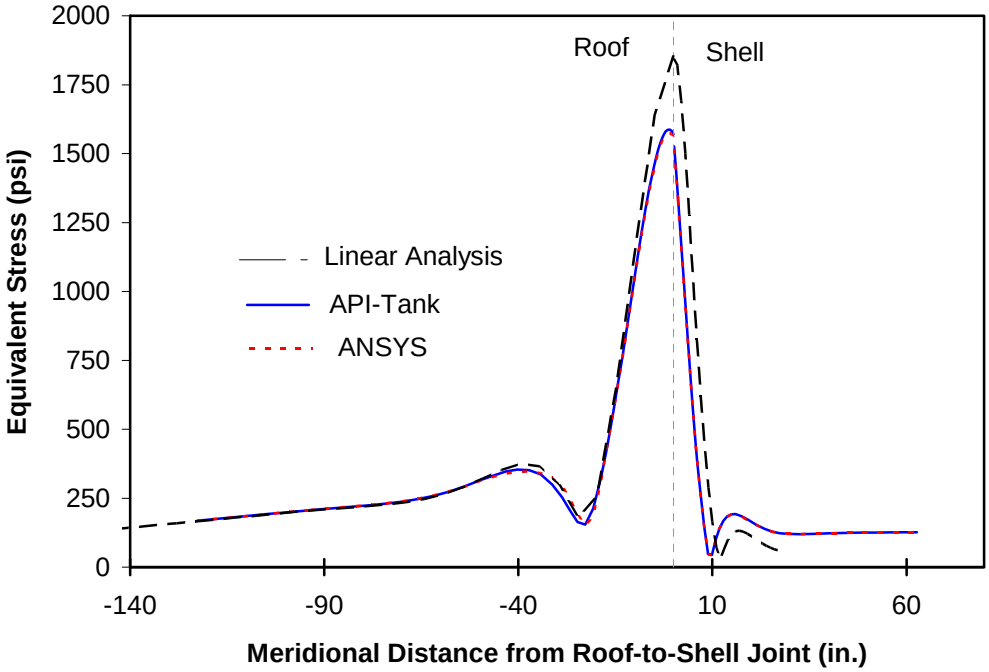

a: Near the roof-to-shell joint

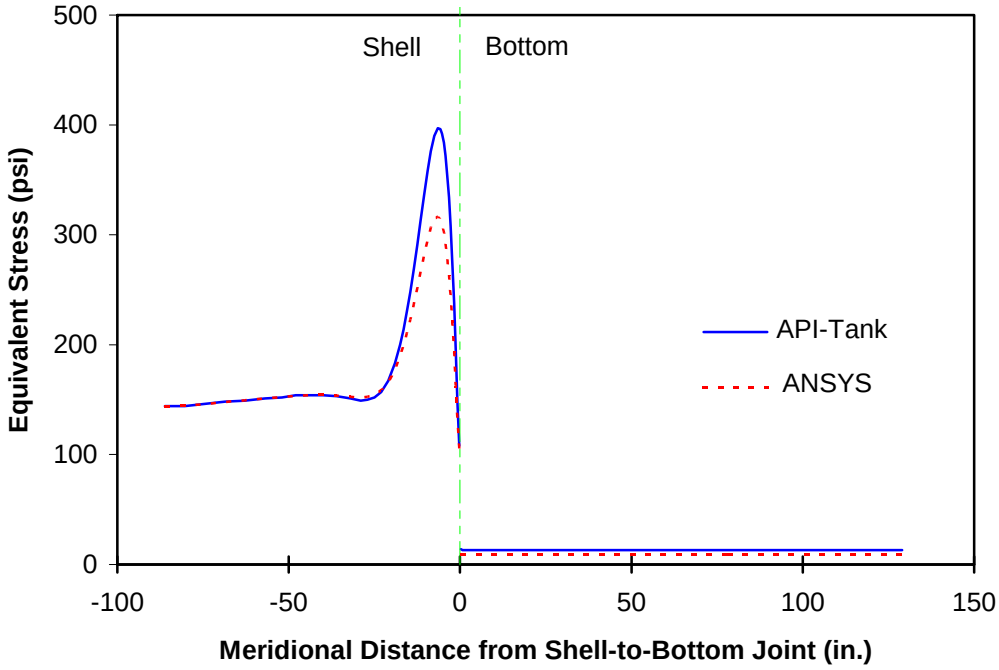

b: Near the shell-to-bottom joint

Figure 6.17: Equivalent Stress in Example Tank 2, Empty with 0.1 psi Pressure

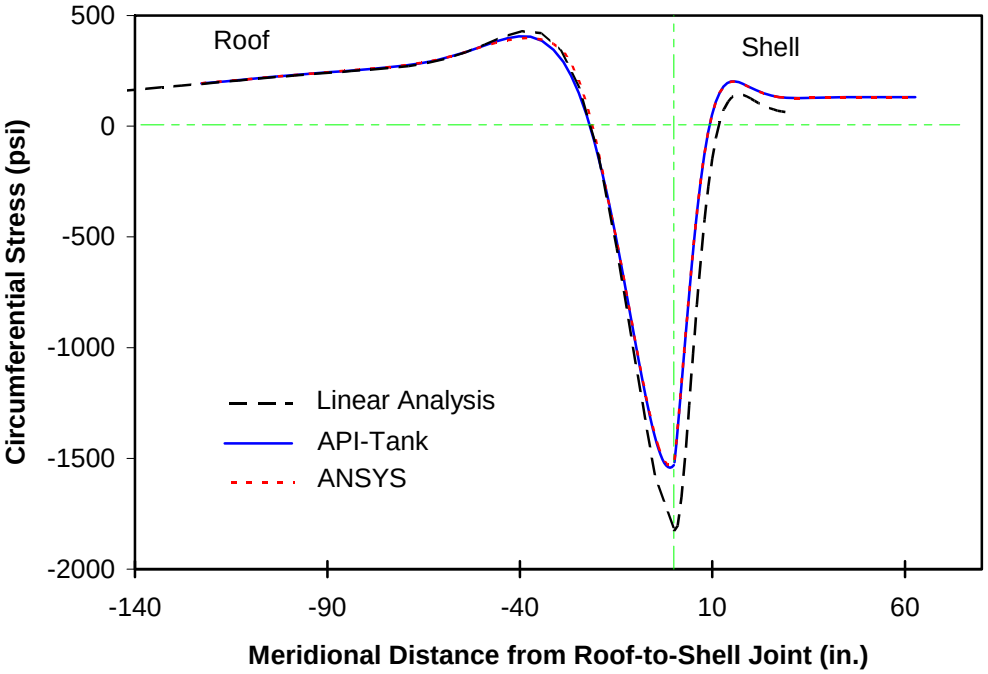

a: Near the roof-to-shell joint

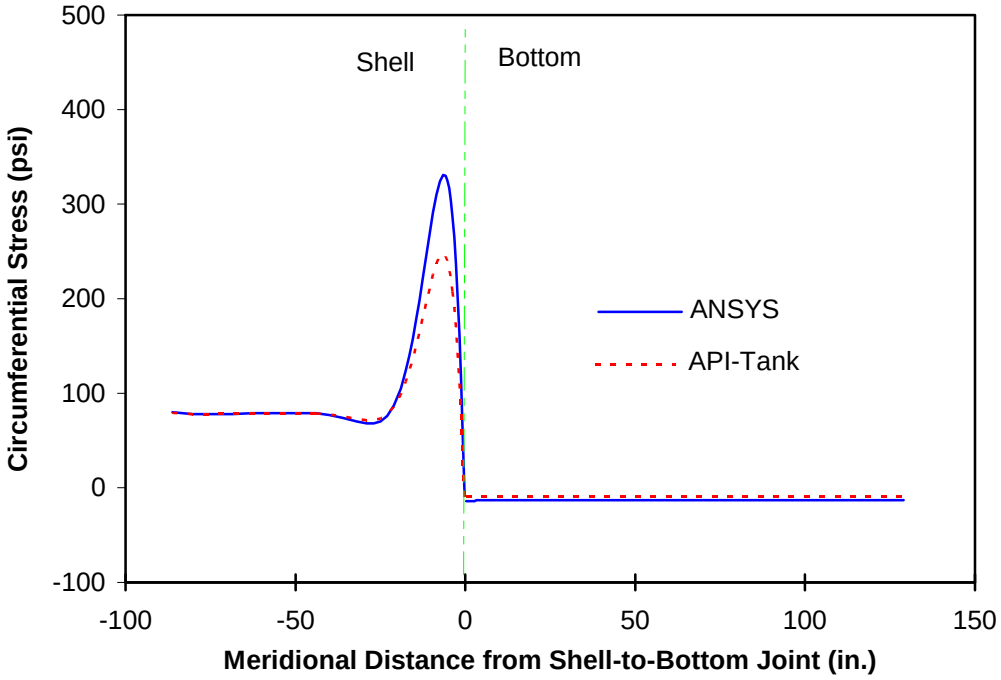

b: Near the shell-to-bottom joint

Figure 6.18: Circumferential Stress in Example Tank 2, Empty with 0.1 psi Pressure

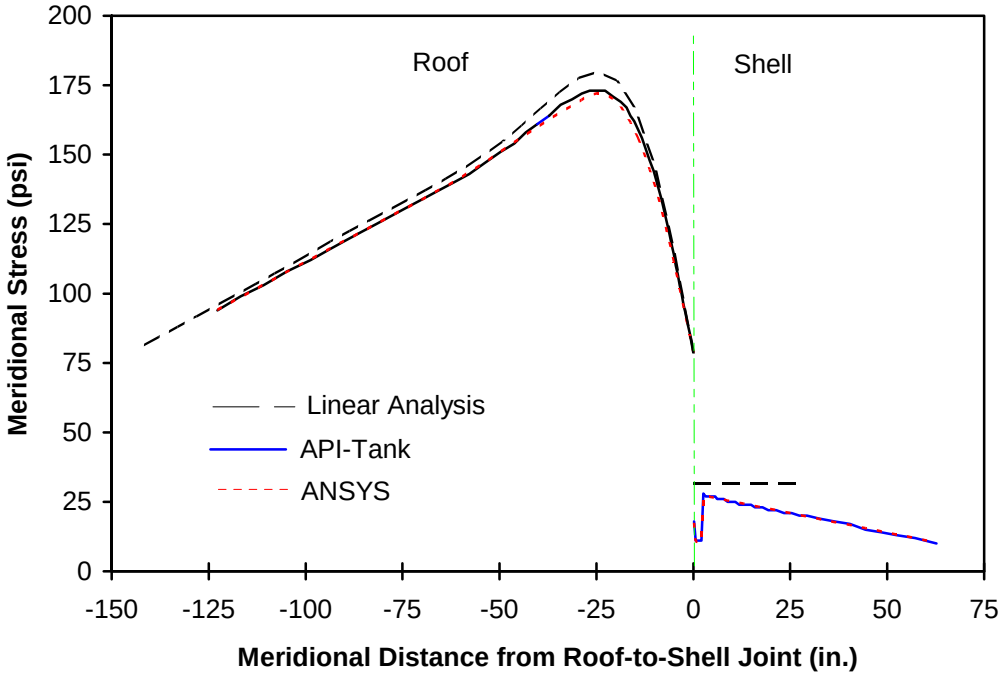

a: Near the roof-to-shell joint

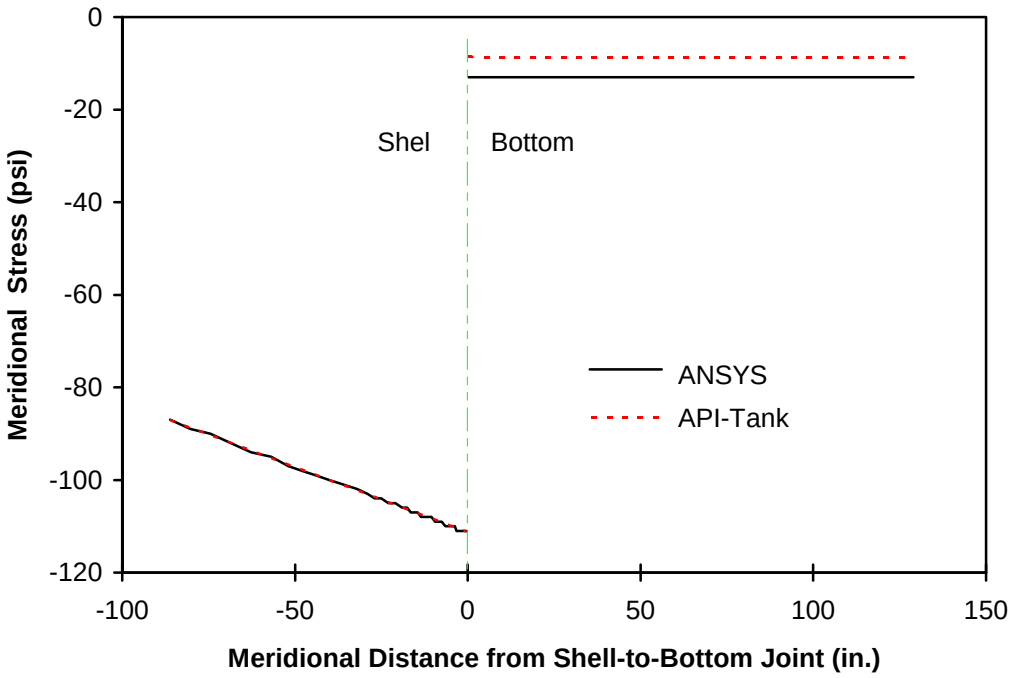

b: Near the shell-to-bottom joint

Figure 6.19: Meridional Stress in Example Tank 2, Empty with 0.1 psi Pressure

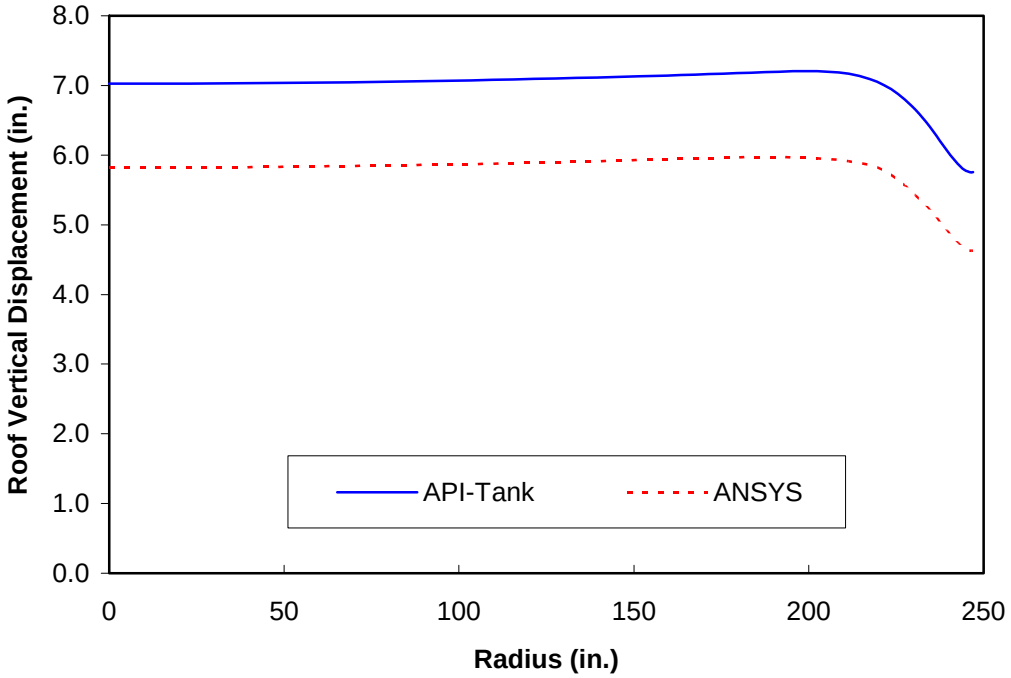

a: displacement on the roof

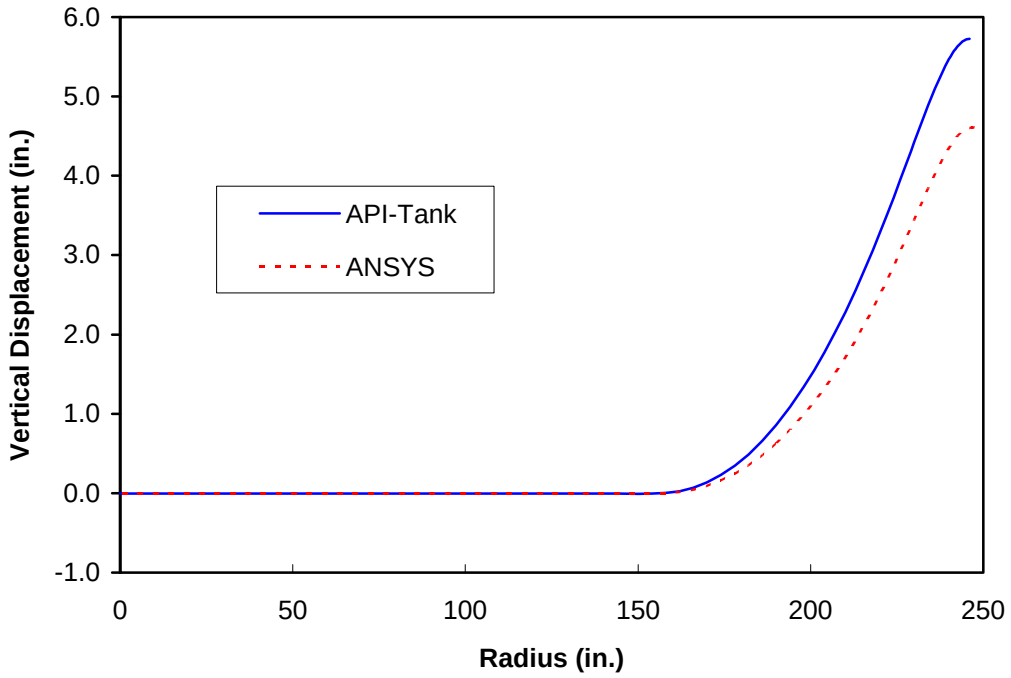

b: displacement on the bottom

Figure 6.20: Deformation of Example Tank 2, Empty with 1.0 psi Pressure

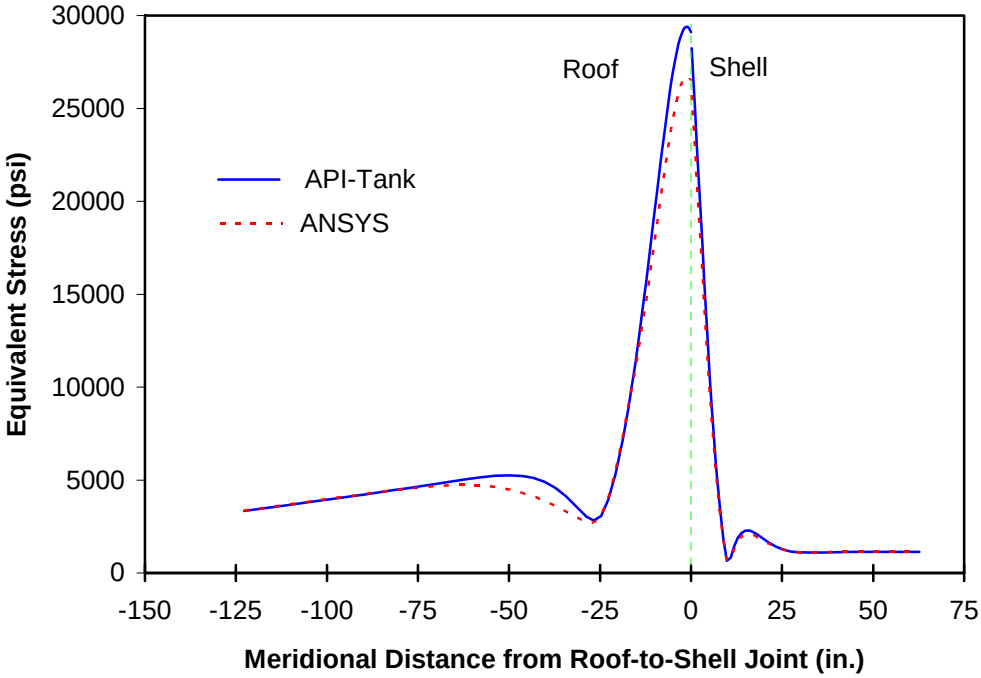

a: Near the roof-to-shell joint

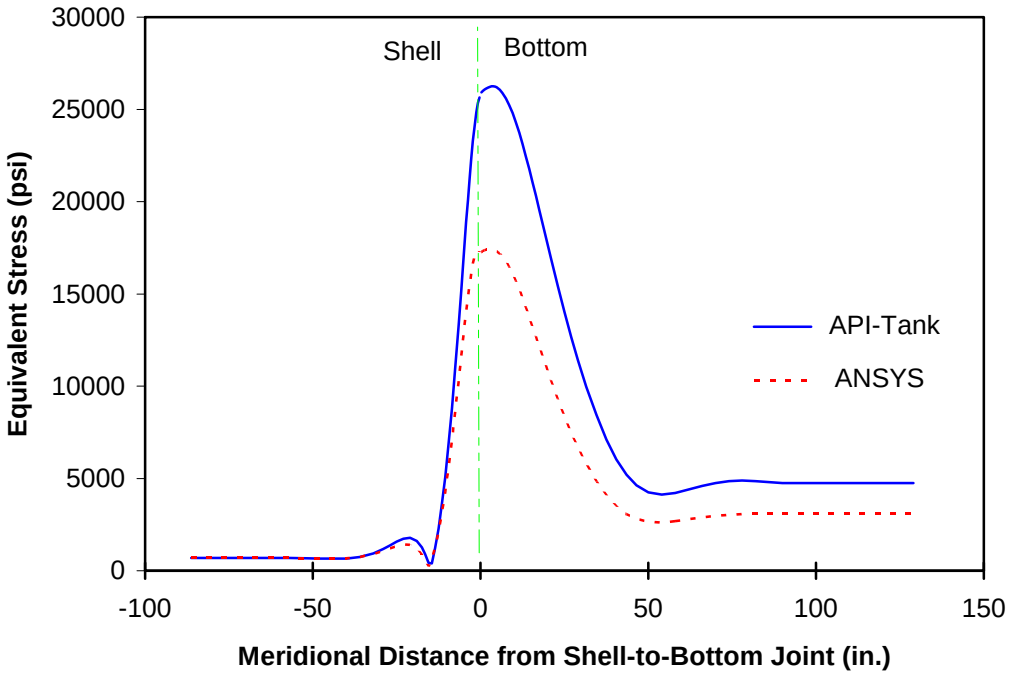

b: Near the shell-to-bottom joint

Figure 6.21: Equivalent Stress in Example Tank 2, Empty with 1.0 psi Pressure

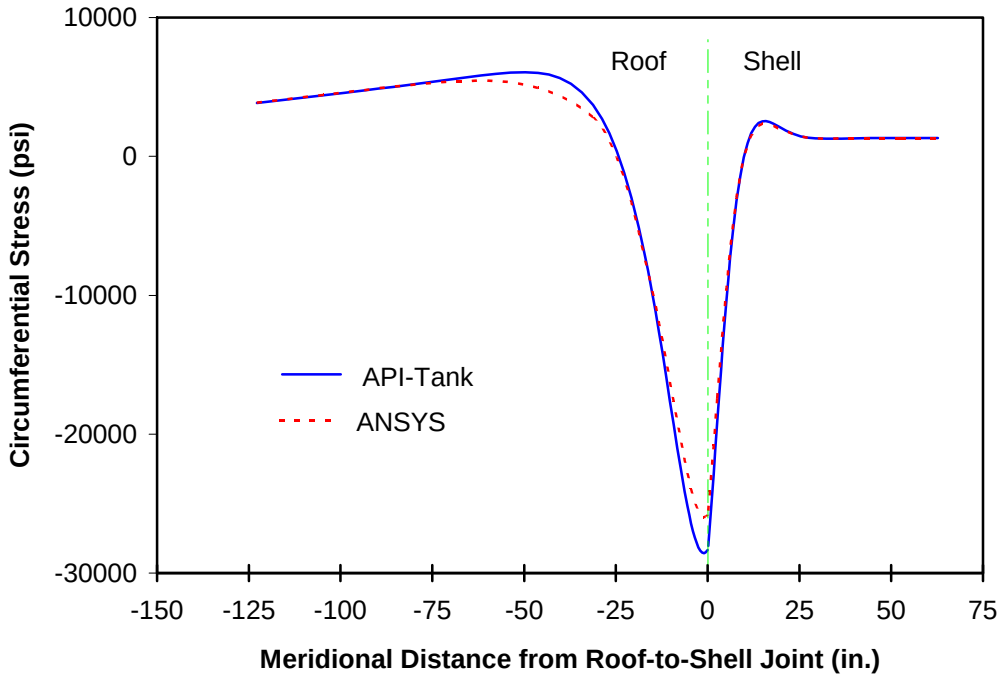

a: Near the roof-to-shell joint

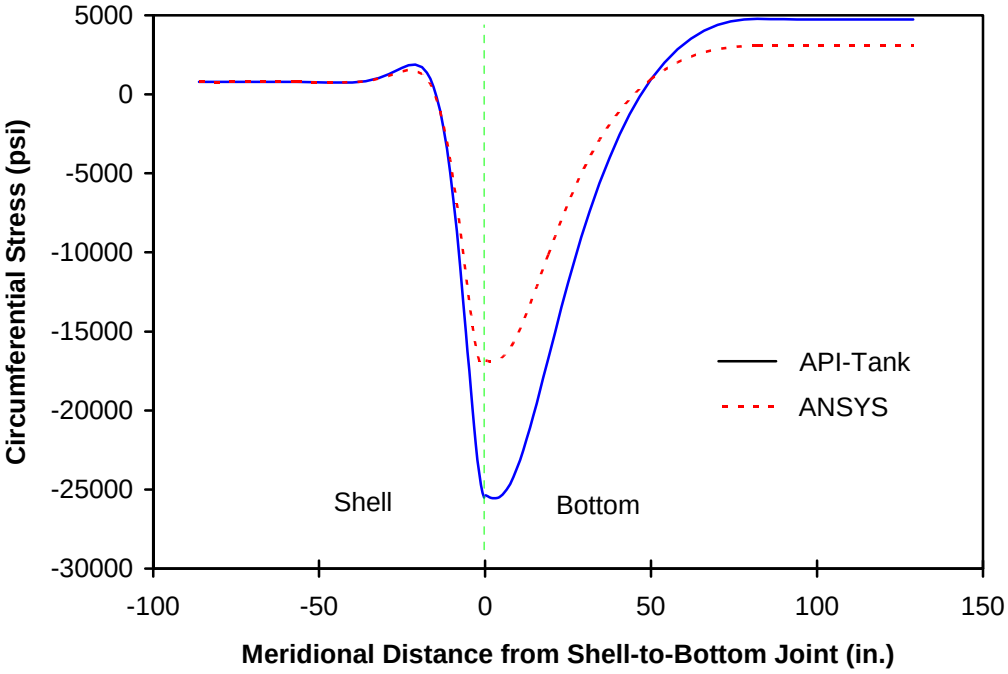

b: Near the shell-to-bottom joint

Figure 6.22: Circumferential Stress in Example Tank 2, Empty with 1.0 psi Pressure

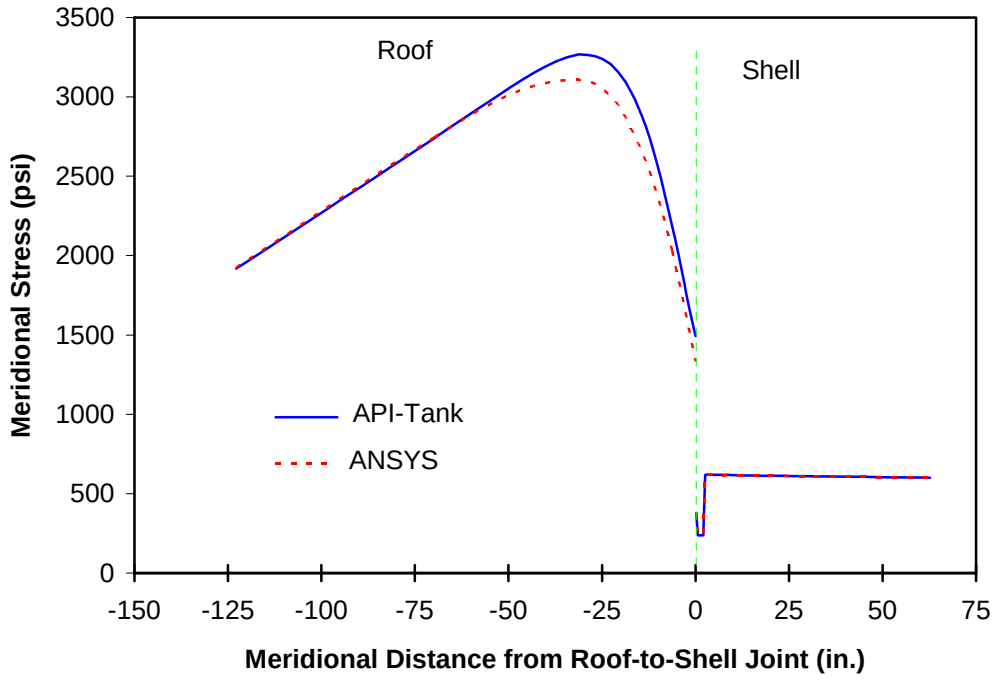

a: Near the roof-to-shell joint

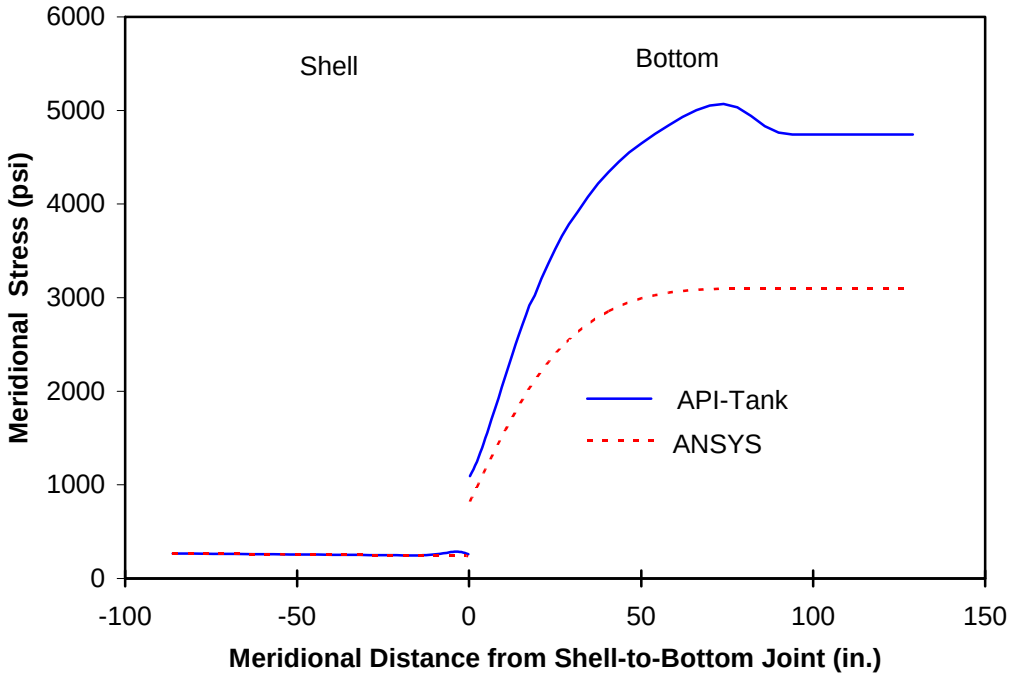

b: Near the shell-to-bottom joint

Figure 6.23: Meridional Stress in Example Tank 2, Empty with 1.0 psi Pressure

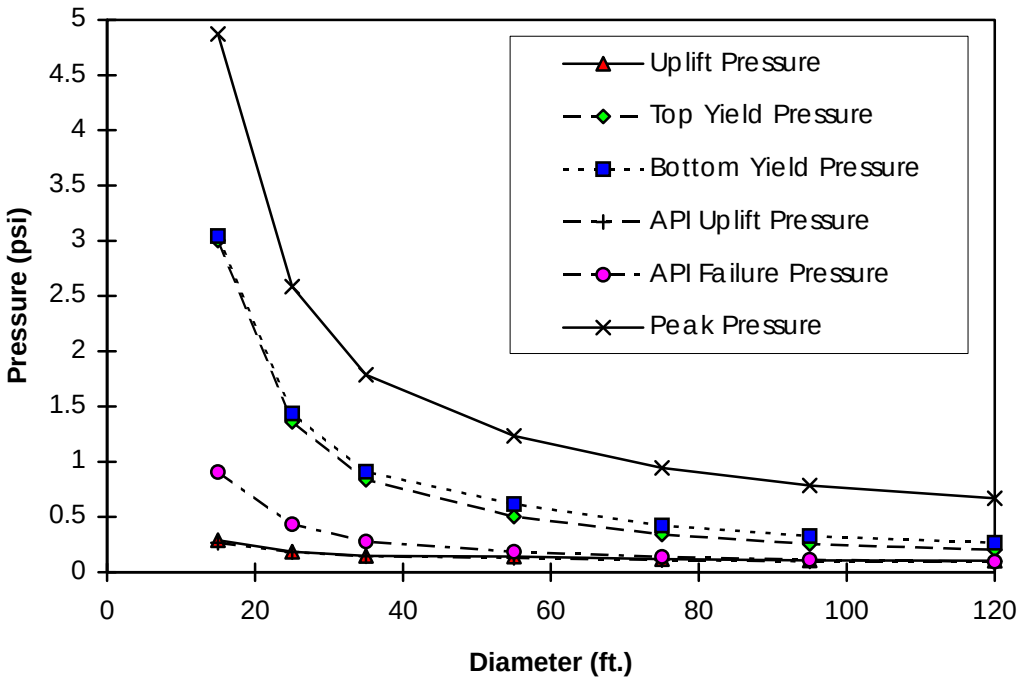

Figure 6.24: Critical Pressures for 15 Feet High Empty Tanks

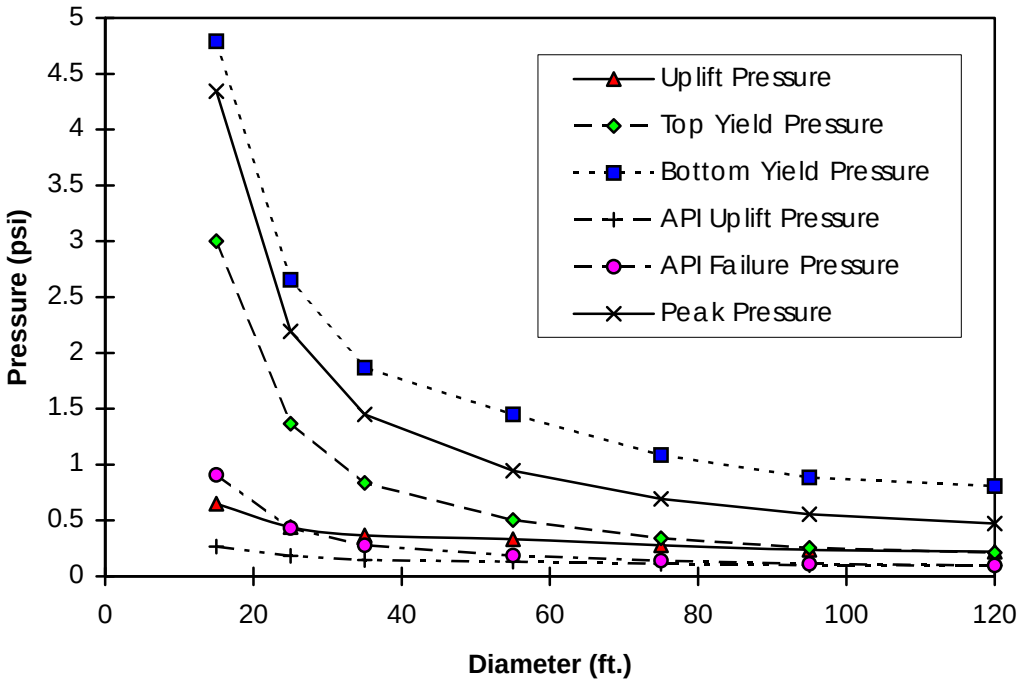

Figure 6.25: Critical Pressures for 15 Feet High Full Tanks

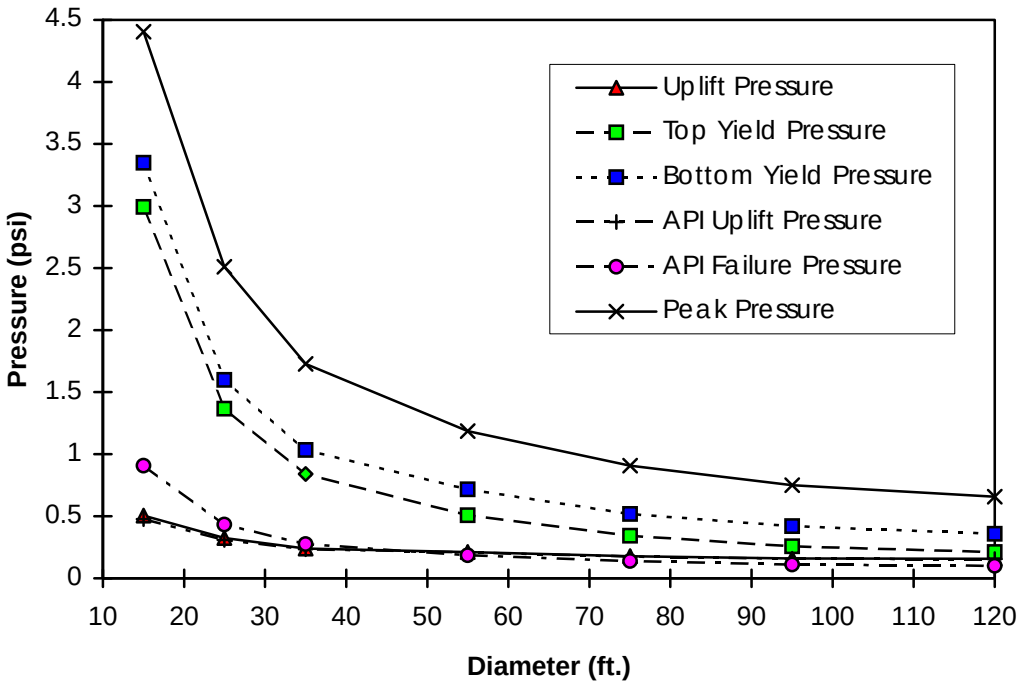

Figure 6.26: Critical Pressures for 30 Feet High Empty Tanks

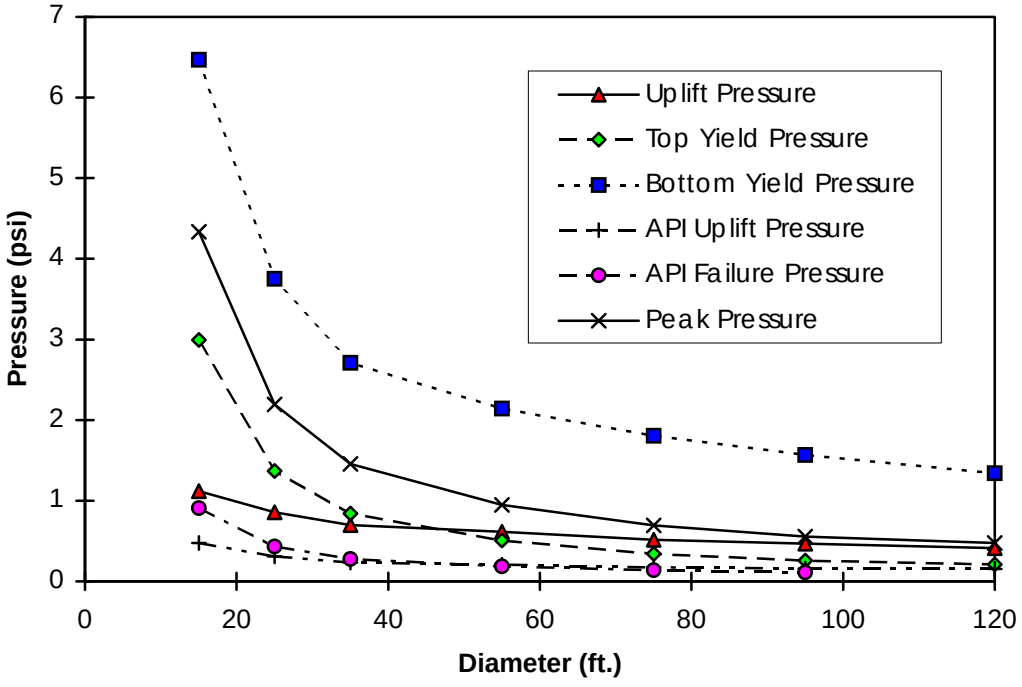

Figure 6.27: Critical Pressures for 30 Feet High Full Tanks

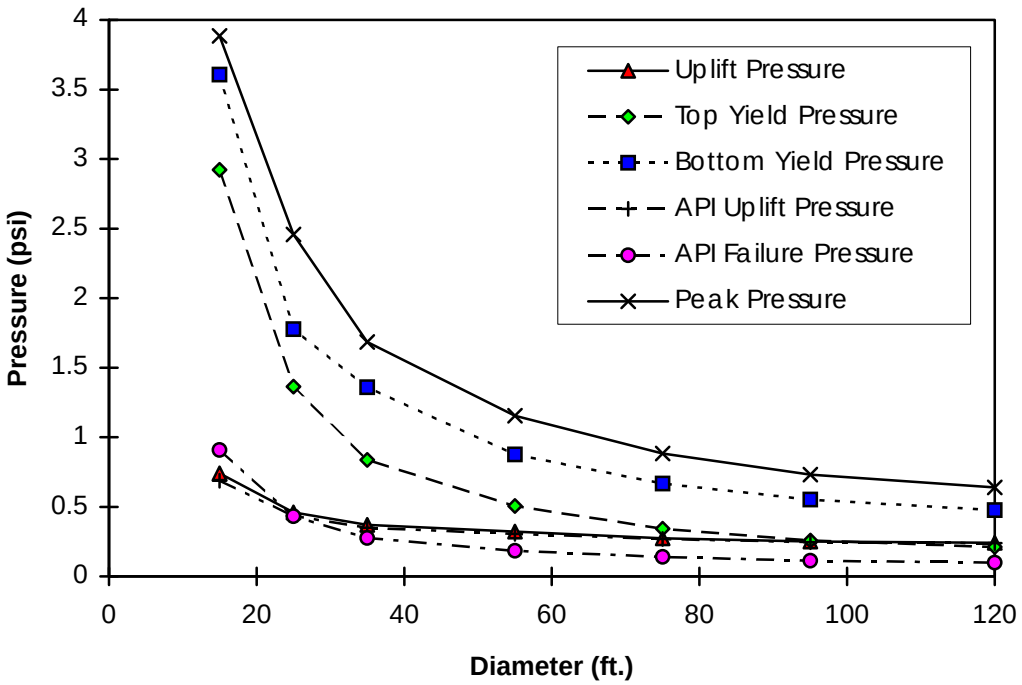

Figure 6.28: Critical Pressures for 45 Feet High Empty Tanks

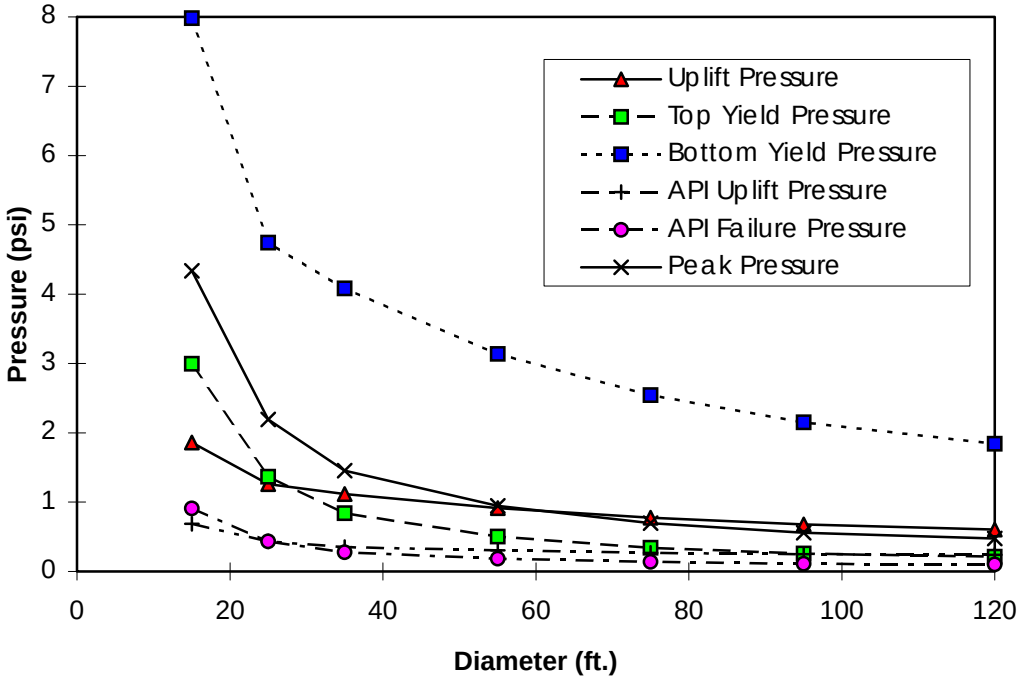

Figure 6.29: Critical Pressures for 45 Feet High Full Tanks

7.0 CONCLUSIONS

This study yields the following conclusions:

With respect to API 650 design rules:

- API 650 design equations for frangible roof joints are based on compressive yielding of the roof-to-shell joint.
- The compression area lengths W_c and W_h in API 650 can be derived by simple linear calculations. W_c is the length where the compression stress reduces to 1/3 of the peak value on the shell, while W_h is half of the length from the edge of a conical shell to where the compression stress reduces to 1/3 of the peak value.
- The failure pressure calculated using API 650 rules is significantly lower than that predicted using finite element analysis or observed in testing. This is not conservative for design.
- British research results support the PVRC research findings.

With respect to the analysis:

- Combustion of the mixture occurred by deflagration. The amount of turbulence significantly affects the burn rate. We expect a relatively small turbulence in the tanks due to the quiescent conditions in the tank.
- The combustion process took approximately several tenths of a second to several seconds to fail a tank. This means that loads on the structure, before failure, are essentially static.
- Buckling loads significantly depend on the slope of the roof. Increasing the slope increases the critical buckling pressure. As a

result, shallow roofs will initially buckle elastically, while steep roofs will not.

- The elastic buckling leads to a new stable configuration. The consequence of this buckling is that compressive circumference stresses in the buckled region are reduced and additional load is placed on the compression ring. However, loading can then continue until yielding of the ring occurs.
- The loading rate in the tank during deflagration will be slowed by venting of the tank. The pressure rise of an empty tank will be slower than a full tank.
- The tanks are expected to respond statically to the deflagration loading. This is because the natural frequencies of tanks are much higher than the loading frequencies.
- Most empty tanks will uplift before frangible joint failure. Uplift at the bottom will not necessarily fail the bottom.
- The relative strength of the roof-to-shell joint and shell-to-bottom joint is a strong function of the liquid level stored in the tank when the overpressurization occurred. The weight of the liquid holds the bottom from being uplifted and reduces the stress at the shell-to-bottom joint. The frangible joint failure pressure is usually smaller than the bottom yield pressure, but the safety margin is relatively small for small diameter empty tanks.

With respect to testing:

- The fillet weld on the roof-to-shell joint tends to be as strong as the plates.

- Failure of the continuously welded tank occurred as expected, initiated by a local inelastic buckle, followed by general failure of the weld. The exact pressure of failure is not known, but it clearly was higher than the stitch welded tank. We believe the first buckling occurred at about 5 psi and the peak pressure was between 8 and 10 psi. If the tank would not have been designed with a reinforced bottom-to-shell joint, it is probable that failure would have also occurred in the bottom-to-shell joint.
- The rafters of the continuously welded tank had no apparent effect on failure pressure or location for either tank.
- Failure of the stitch welded tank occurred at a peak pressure of 5 psi. The roof completely detached, with much less distortion of the upper shell.
- Calculations were basically confirmed by the test and can be used to predict the behavior of the oil storage tanks.
- A video of the testing was prepared.

Some unresolved issues:

- For what liquid level in the tank should the evaluation of safety be done? The empty tank has the lowest failure pressure and smaller bottom to top joint strength ratio, but less damage will be expected if bottom failure does occur. The full, higher tank has higher bottom failure pressure, but worse consequences.
- How to bring complex results into simple design criteria is still a question. It might be useful to use the relative strength of the two joints as a design requirement. For example, a safe design should

have the bottom yielding pressure twice as much as the top yielding one.

8.0 REFERENCES

American Petroleum Institute, 1988, “API Standard 650: Welded Steel Tanks for Oil Storage," 8th ed., 1220 L. Street, Northwest, Washington, DC.

American Petroleum Institute, 1993, “API Standard 650: Welded Steel Tanks for Oil Storage," 9th ed., 1220 L. Street, Northwest, Washington, DC.

Abdel-Gayed, R.G., Bradley, D. and Lawes, M., 1987, "Turbulent Burning Velocities: a General Correlation in terms of straining rates," Department of Mechanical Engineering, University of Leeds, Leeds LS2 9JT, U.K.

ASTM, 1987*, Industrial Dust Explosions: Symposium on Industrial Dust Explosions*, ASTM Special Technical Publication 958, Philadelphia, PA.

Baalman, J., “Pressure Rise in Large Fuel Storage Tanks Due to Combustion,” Master’s Thesis, Kansas State University, Manhattan, Kansas.

Barnett, H.C. and R.R. Hibbard, 1957, "Basic Considerations in the Combustion of Hydrocarbon Fuels with Air," Rept. 1300, Propulsion Chem. Div., Lewis Flight Propulsion Lab., NASA, Cleveland, OH.

Bartknecht, W., 1989, *Dust Explosions Course, Prevention, Protection*, Springer-Verlag Berlin Heidelberg,

Bert, C. and Martindale J., February, 1988, “An Accurate Simplified Method for Analyzing Thin Plates Undergoing Large Deflections”, AIAA Journal, Vol. 26, No. 2.

Bone, J.,1993, “Case analysis of Tank Fire,” Terminals Proprietary, Ltd., New south Wales, Australia.

British Standards Institution, British Standard BS 2654: *Manufacture of Vertical Steel Welded Storage Tanks with Butt-Welded Shells for the Petroleum Industry*, 2 Park Street, London W1A 2BS, 1984.

Famili, J., August 1965, "Asymmetric Buckling of Finitely Deformed Conical Shells", AIAA Journal, Vol. 3, No. 8.

Ferguson, C.R., 1986, *Internal Combustion Engines*, John Wiley and Sons, New York, NY.

Fox, R. W. and McDonald, A. T., 1985, Introduction to Fluid Mechanics, 3rd ed. John Wiley & Sons, Inc., New York, NY.

Gordon, S. and McBride, B., 1971, "Computer Program for Calculations of Complex Chemical Equilibrium Compositions, Rocket Performance, Incident and Reflected Shocks, and Chapman-Jouquet Detonations," NASA SP-273,

Gugan, K., 1978, *Unconfined Vapor Cloud Explosions*, The Institution of Chemical Engineers, London.

Kanury, A.M., 1975, *Introduction to Combustion Phenomena*, Gordon and Breach Science Publishers, New York, NY.

Krtzig, W., 1990, *Computational Mechanics of Nonlinear Response of Shells*, Springer Series in Computational Mechanics, New York.

Kuo, K.K., 1986, *Principles of Combustion*, John Wiley and Sons, New York, NY.

Lee, H.S., 1984, "Physics of Explosions - Lecture Notes," Shock Wave Physics Research Lab., Mech. Eng. Dept., McGill Univ., Montreal, Canada.

Lind, C.D. and Whitson, J.C., 1977, "Explosion Hazards Associated with Spills of Large Quantities of Hazardous Materials. Phase II," Final

Report, Rept. No. CG-D-85-77, Dept. of Transportation, U.S. Coast Guard.

Liu, W. K. and Uras, R. A., 1989, "Transient Buckling analysis of Liquid Storage Tanks Part I: Theory," PVP Conference in Honolulu, Hawaii.

Morgenegg, E.E., 1978, "Frangible Roof Tanks", Monsanto Company, St. Louis, MO.

Nagashima, H., August 1989, "Experimental Study on Dynamic Buckling of Cylindrical Tanks," Journal of Japanese Society of Mechanical Engineering, Vol. 55.

NASA, December 1962, "Collected Papers on Instability of Shell Structures", NASA TN D-1510

Niordson F. I., 1985, *Shell Theory*, Elsevier Science Publishers B. V., The Netherlands

Obert, E. F., 1973, *Internal Combustion Engines and Air Pollution*, 3rd Ed. Harper & Row, Publishers, Inc.

Prager, M., 1991, "Summary of Frangible Roof Failure Experiences," Provided information., Pressure Vessel Research Council, 345 East 47th., New York, NY, 10017, May 6.

Ringer, M., 1991, Provided Information on Frangible Roofs for Storage Tanks, Monsanto Company, St. Louis, MO.

Sherman, M., 1991, Private Communication with Joe Baalman, Sandia National Lab., Albuquerque, NM, June 11.

Swenson, D., Fenton, D., Lu. Z., and Baalman, J., 1992, "Evaluation of Design Criteria for Frangible Storage Tank Roof Joints," Phase one report, Kansas State University, Manhattan, KS 66506.

Swenson, D., Fenton, D., Lu. Z., Ghori, Asif., and Baalman, J., 1993, "Evaluation of Design Criteria for Storage Tanks with Frangible Roof

Joints," Phase two report, Kansas State University, Manhattan, KS 66506.

Taylor, C., April 1974, "Simplification of the Analysis of Stress in Conical Shells", Dept. of Theoretical and Applied Mechanics, University of Illinois at Urbana-Champaign.

The Tank Committee of the Engineering Equipment and Materials Users Association, U. K., 1990, "Frangible roof joints for fixed roof tanks," 14-15 Belgrave Square, London-SWIX 8 PS.

Timoshenko, S. P., and Woinowsky-Krieger, S., 1959*, Theory of Plates and Shell*, McGraw-Hill Book Company, New York, NY.

Tranter, C. J., 1968, *Bessel Functions with Some Physical Applications*, The English University Press Ltd.

Vol'mir, A., April 1967, *A Translation of Flexible Plates and Shells*, Dept. of Engineering Science and Mechanics, University of Florida.

Yamaki, N. 1984, *Elastic Stability of Circular Cylindrical Shells*, Elsevier Science Publishers B. V., The Netherlands.

Yisguda, S. and Miyoshi, T., 1992, "Bifurcation Buckling of the Top end Closure of Oil Storage Tanks under Internal Pressure," PVP. Vol. 230, Stress Classification Robust Methods and Elevated Temperature Design, ASME

Yoshida, S. and Miyoshi, T., April 1990, "Buckling Analysis of the Inner Shell Plate of a Multi-Walled Coaxial Cylindrical Tank for Oil Storage under External Liquid Pressure," Journal of Japanese Society of Mechanical Engineering, Vol. 56

Young, W. C., 1989, *Roark's Formulas for Stress and Strain*, 6th ed. McGraw-Hill Book Company, New York, NY.

Zienkiewicz, O. C., and Taylor, R. L., 1991, *The Finite Element Method*, 4th ed. McGraw-Hill Book Company, New York, NY.

APPENDIX A: COMBUSTION WAVE GEOMETRY

Consider a tank of radius R with height of vapor space H as shown in Figure A.1. The ignition source is located at point O, which is distance e from center line of the tank shell and distance h below the roof of the tank. At a given instant, the radius of the fireball is r. Using a cylindrical coordinate system with the origin at the ignition source and the z axis up, the cross section area of the fireball S at height z can be determined analytically. The total volume of the fireball V can be obtained using the following integration:

$$V = \int_{\max(h-H,-r)}^{\min(h,r)} S\,dz \tag{A.1}$$

When the ignition source is on the centerline of the tank, the value of e equals zero and the cross section at any z location will be a circle with radius:

$$\rho = \min(\sqrt{r^2 - z^2}, R) \tag{A.2}$$

When e is not zero, the calculation of cross sectional area can be performed for three cases. When the fireball and the tank shell do not touch each other for the given z coordinate, the cross sectional area is that of a circle with radius ρ, as given in (A.2). Otherwise, the cross sectional area is the common part of two circles. The fireball in the tank is shown in Figure 3.1. The projection of the radius of the fireball at position z is ρ_o:

$$\rho_o = \sqrt{r^2 - z^2} \tag{A.3}$$

The tank shell in the given coordinate system can be written as:

$$(\rho\cos\theta - e)^2 + (\rho\sin\theta)^2 = R^2 \tag{A.4}$$

Solving for ρ we get:

$$\rho = e\cos\theta \pm \sqrt{e^2\cos^2\theta + R^2 - e^2} \tag{A.5}$$

Since ρ > 0, θ can be obtained from (A.5) by taking the positive sign:

$$\theta = \frac{\rho^2 + e^2 - R^2}{2e\rho} \tag{A.6}$$

At point A where the surface of the fireball contacts the tank shell, θ_0 can be obtained by substituting (A.3) into (A.6):

$$\theta_0 = \cos^{-1}\left(\frac{r^2 - z^2 + e^2 - R^2}{2e\sqrt{r^2 - z^2}}\right) \tag{A.7}$$

From geometry relations shown in Figure A.1, we have:

$$\overline{AO} = \sqrt{r^2 - z^2}$$

$$\overline{DO} = -\sqrt{r^2 - z^2}\cos\theta_0 = \frac{R^2 - e^2 - r^2 + z^2}{2e}$$

$$\overline{AD} = \sqrt{r^2 - z^2}\sin\theta_0 = \sqrt{r^2 - z^2 - \frac{(r^2 - z^2 + e^2 - R^2)^2}{4e^2}}$$

$$\sin\alpha = \frac{\overline{AD}}{\overline{AF}} = \frac{1}{R}\sqrt{r^2 - z^2 - \frac{(r^2 - z^2 + e^2 - R^2)^2}{4e^2}}$$

The area of AECO is:

$$S_{AECO} = \rho_0^2\,\theta_0 = (r^2 - z^2)\cos^{-1}\left(\frac{R^2 - e^2 - r^2 + z^2}{2e}\right) \tag{A.8}$$

The area of ABCD is:

$$\begin{aligned} S_{ABCD} &= R^2\alpha - \overline{AD}\sqrt{R^2 - \overline{AD}^2} \\ &= R^2\sin^{-1}\left[\frac{1}{R}\sqrt{r^2 - z^2 - \frac{(r^2 - z^2 + e^2 - R^2)^2}{4e^2}}\right] \\ &\quad - \sqrt{r^2 - z^2 - \frac{(r^2 - z^2 + e^2 - R^2)^2}{4e^2}}\sqrt{R^2 - r^2 + z^2 + \frac{(r^2 - z^2 + e^2 - R^2)^2}{4e^2}} \end{aligned} \tag{A.9}$$

The triangle area AOC is:

$$
\begin{aligned}
S_{AOC} &= \overline{AD} \times \overline{AO} \\
&= -\rho_0^2 \sin\theta_0 \cos\theta_0 \\
&= \frac{R^2 - e^2 - r^2 + z^2}{2e} \sqrt{r^2 - z^2 - \frac{(r^2 - z^2 + e^2 - R^2)^2}{4e^2}}
\end{aligned}
\tag{A.10}
$$

The total cross section area S at height z is:

$$
\begin{aligned}
S &= S_{AECO} + S_{ABCD} + S_{AOC} \\
&= (r^2 - z^2)\cos^{-1}\left(\frac{R^2 - e^2 - r^2 + z^2}{2e}\right) \\
&+ R^2 \sin^{-1}\left[\frac{1}{R}\sqrt{r^2 - z^2 - \frac{(r^2 - z^2 + e^2 - R^2)^2}{4e^2}}\right] \\
&- \sqrt{r^2 - z^2 - \frac{(r^2 - z^2 + e^2 - R^2)^2}{4e^2}} \sqrt{R^2 - r^2 + z^2 + \frac{(r^2 - z^2 + e^2 - R^2)^2}{4e^2}} \\
&+ \frac{R^2 - e^2 - r^2 + z^2}{2e} \sqrt{r^2 - z^2 - \frac{(r^2 - z^2 + e^2 - R^2)^2}{4e^2}}
\end{aligned}
$$

(A.11)

Equation (A.11) is valid for $\alpha < \pi/2$, that is, cross section with z coordinate satisfies the following relations:

$$
(R - e)^2 < r^2 - z^2 < R^2 + e^2 \tag{A.12}
$$

In case α is bigger than $\pi/2$, the geometry of the cross section is shown in Figure A.2. Notice that when $\theta_0 < \pi/2$ the area S_{AOC} is negative in value, the total area of the cross section will be:

$$
S = S_{OAEC} + S_{AOC} + S_{ABC} \tag{A.13}
$$

The angle β in Figure 3.2 can be calculated as:

$$
\beta = \sin^{-1}\frac{\overline{AD}}{R} = \sin^{-1}\left[\frac{1}{R}\sqrt{r^2 - z^2 - \frac{(r^2 - z^2 + e^2 - R^2)^2}{4e^2}}\right] \tag{A.14}
$$

The area S_{ABC} can be written as:

$$
\begin{aligned}
S_{ABC} &= \pi R^2 - (R^2\beta - \overline{A\,D}\sqrt{R^2 - \overline{\overline{A\,D}}} \\
&= \pi R^2 - R^2 \sin^{-1}\left[\frac{1}{R}\sqrt{r^2 - z^2 - \frac{(r^2 - z^2 + e^2 - R^2)^2}{4e^2}}\right] \\
&+ \sqrt{r^2 - z^2 - \frac{(r^2 - z^2 + e^2 - R^2)^2}{4e^2}}\sqrt{R^2 - r^2 + z^2 + \frac{(r^2 - z^2 + e^2 - R^2)^2}{4e^2}}
\end{aligned}
$$

(A.15)

The total cross sectional area then calculated will be:

$$
\begin{aligned}
S &= (r^2 - z^2)\cos^{-1}\left(\frac{r^2 - z^2 + e^2 - R^2}{2e\sqrt{r^2 - z^2}}\right) \\
&+ \frac{R^2 - e^2 + z^2 - r^2}{2e}\sqrt{r^2 - z^2 - \frac{(r^2 - z^2 + e^2 - R^2)^2}{4e^2}} \\
&+ \pi R^2 - R^2 \sin^{-1}\left[\frac{1}{R}\sqrt{r^2 - z^2 - \frac{(r^2 - z^2 + e^2 - R^2)^2}{4e^2}}\right] \\
&+ \sqrt{r^2 - z^2 - \frac{(r^2 - z^2 + e^2 - R^2)^2}{4e^2}}\sqrt{R^2 - r^2 + z^2 + \frac{(r^2 - z^2 + e^2 - R^2)^2}{4e^2}}
\end{aligned}
$$

(A.16)

The calculated area S is then integrated with respect to z coordinate using Runge-Kutta-Gill method. The step length is set to 1/150 of the z domain, which will give an error equal or less than $0.42 \times 10^{-9} r^5$.

Figure A.1 Geometry of the Fireball at Position z
when $(R - e)^2 < r^2 - z^2 < R^2 + e^2$

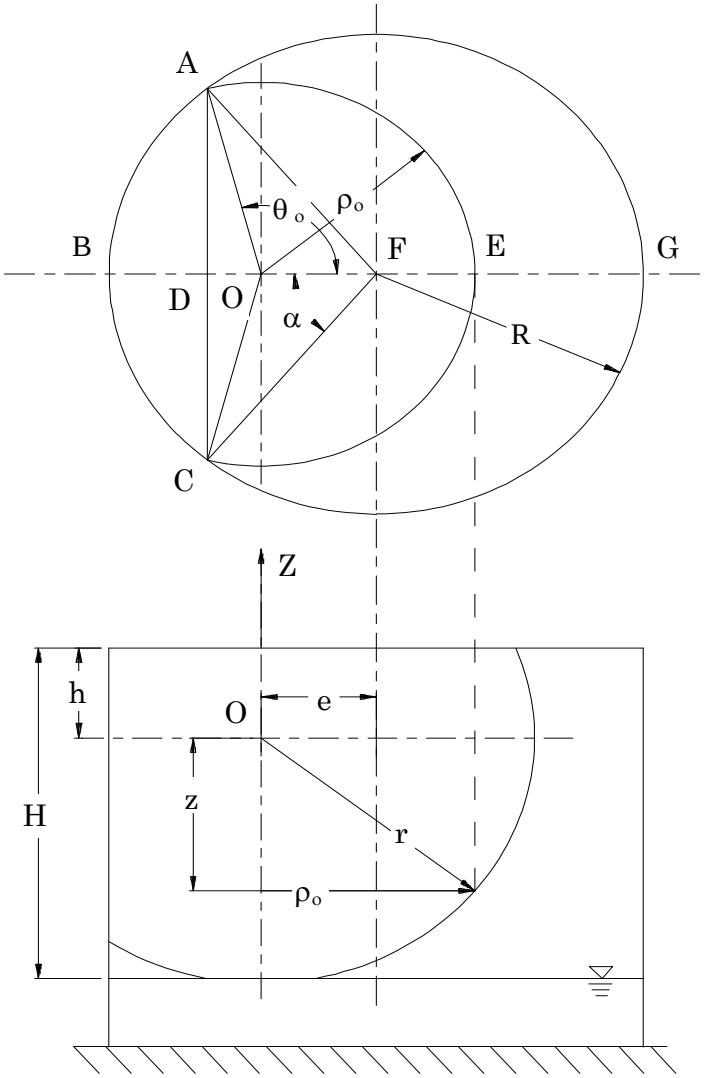

Figure A.2: Geometry of the Fireball at Position z

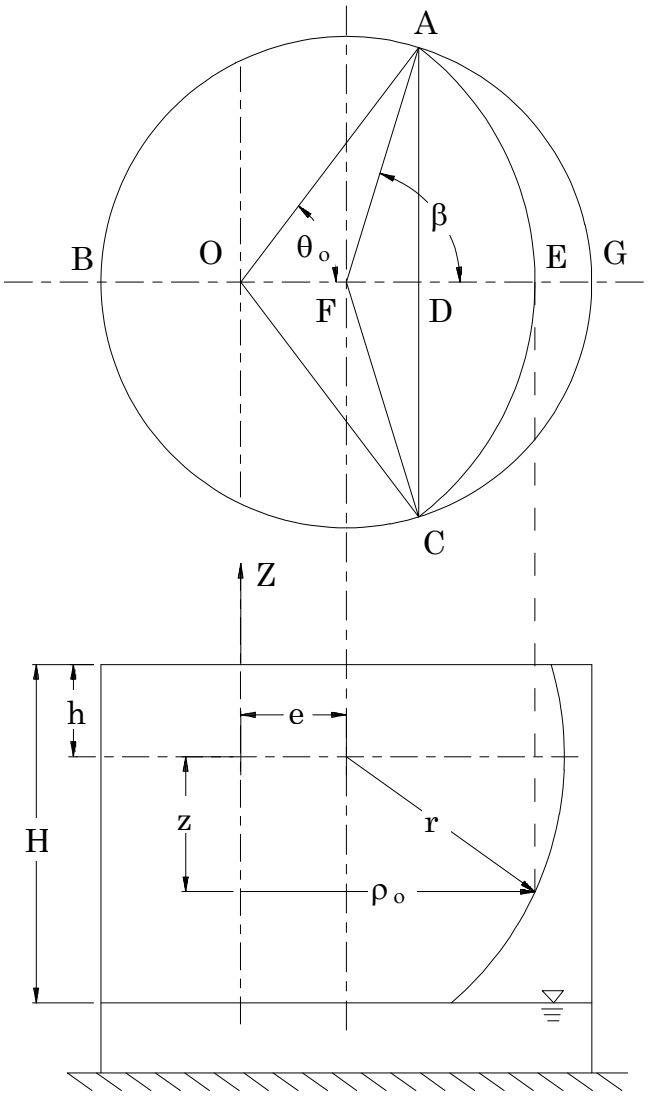

when $R^2 + e^2 < r^2 + z^2 < (R + e)^2$

APPENDIX B: LIST OF ANSYS FILES FOR VERIFICATION

B.1 Input file for Tank 25

```
/COM This is the input file of the analysis of tank 25
/PREP7
/COM elastic analysis
KAN,0
/COM  large displacement analysis (nonlinear)
KAY,6,1
/COM  stress stiffening included
KAY,8,1
/COM  shell 51: plastic axisymmetric conical shell
ET,1,51,
/COM  interface 12 : used to model the elastic foundation
ET,2,12,,,
/COM  thickness of the roof and upper shell plate
R,1,0.1875
/COM  the thickness of the bottom part of the shell and bottom
R,2,0.25
MP,EX,1,3e7
MP,NUXY,1,.3
MP,DENS,1,0.000727
/COM  the different stifnesses are used for the interface
/COM  element to model the elastic foundtion
R,    3, ,  330450.4, ,   1
R,    4, ,  659034.1, ,   1
R,    5, ,  656241.6, ,   1
R,    6, ,  571974.6, ,   1
R,    7, ,  488517.2, ,   1
R,    8, ,  486946.5, ,   1
R,    9, ,  485375.7, ,   1
R,   10, ,  483804.9, ,   1
R,   11, ,  482234.1, ,   1
R,   12, ,  480663.3, ,   1
R,   13, ,  479092.5, ,   1
R,   14, ,  477521.7, ,   1
R,   15, , 297273, ,   1
R,   16, ,  296291.2, ,   1
R,   17, ,  295309.5, ,   1
R, 18, ,   176518.1, ,  1
R, 19, ,   234048.5, ,  1
R, 20, ,   232477.7, ,  1
R, 21, ,   230906.9, ,  1
R, 22, ,   229336.1, ,  1
R, 23, ,   227765.3, ,  1
R, 24, ,   226194.5, ,  1
R, 25, ,   224623.7, ,  1
R, 26, ,   223052.9, ,  1
R, 27, ,   221482.1, ,  1
R, 28, ,   219911.3, ,  1
R, 29, ,   218340.5, ,  1
R, 30, ,   324369.2, ,  1
R, 31, ,   427256.2, ,  1
R, 32, ,   420973.1, ,  1
R, 33, ,   414689.9, ,  1
R, 34, ,   408406.7, ,  1
R, 35, ,   402123.5, ,  1
R, 36, ,   493491.4, ,  1
R, 37, ,   579623.4, ,  1
```

```
R, 38, ,   565486.2, ,  1
R, 39, ,    551349, ,  1
R, 40, ,   537211.9, ,  1
R, 41, ,   523074.7, ,  1
R, 42, ,   591927.9, ,  1
R, 43, ,   653450.7, ,  1
R, 44, ,    628318, ,  1
R, 45, ,   603185.3, ,  1
R, 46, ,   578052.6, ,  1
R, 47, ,   552919.8, ,  1
R, 48, ,   527787.1, ,  1
R, 49, ,   502654.4, ,  1
R, 50, ,   477521.7, ,  1
R, 51, ,    452389, ,  1
R, 52, ,   427256.2, ,  1
R, 53, ,   402123.5, ,  1
R, 54, ,   466002.5, ,  1
R, 55, ,   508937.6, ,  1
R, 56, ,    452389, ,  1
R, 57, ,   395840.3, ,  1
R, 58, ,   339291.7, ,  1
R, 59, ,   282743.1, ,  1
R, 60, ,   226194.5, ,  1
R, 61, ,   169645.9, ,  1
R, 62, ,   113097.2, ,  1
R, 63, ,   56548.62, ,  1
R, 64, ,    9424.77, ,  1
/COM  generating nodes
N, 1,  0, 441.8125
N,12,  61.0, 438.0
FILL
N,24,  109.0, 435.0
FILL
N,30,  127.0, 433.875
FILL
N,36,  139.0, 433.125
FILL
N,48,  151.0, 432.375
FILL
N,59,   156.5, 432.03125
FILL
N,60,  158.0, 432
N,64, 156.0,  432.0
FILL
N,80,156.0, 424.0
FILL
N,93, 156.0, 410.0
FILL
N,98, 156.0,  400.0
FILL
N,104, 156.0, 376.0
FILL
N,113, 156.0, 324.0
FILL
N,143, 156.0, 54.0
FILL
N,149, 156.0, 30.0
FILL
N,155, 156.0, 18.0
FILL
N,167, 156.0, 6.0
FILL
N,178, 156.0, 0.50
FILL
N,179, 158, 0.0
```

```
N,182, 156.0, 0.0
FILL
N,194, 150.0, 0.0
FILL
N,206, 138.0, 0.0
FILL
N,212,  126.0, 0.0
FILL
N,218,  108.0, 0.0
FILL
N, 230, 60.0, 0.0
FILL
N,240,  0.0, 0.0
FILL
/COM 62 nodes for foundation
NGEN,2,62,179,240,1,0.0,,0.0
NPLOT
MAT,1
/com thickness 3/16"
REAL,1
TYPE,1
/com generating elements
E,1,2
ENGEN,1,58,1,1
/COM ENGEN,IINC,ITIME,NINC,IEL1,IEL2,IEINC,MINC,TINC,RINC,CINC
EN,59,59,62
EN,60,60,61
/com element 61-112
ENGEN,1,53,1,60,
MAT,1
TYPE,1
/COM thickness 1/4"
REAL,2
EN,113,113,114
ENGEN,1,65,1,113
EN,178,178,182
EN, 179,179,180
ENGEN,1,61,1,179
TYPE,2
REAL,3
MAT,2
EN,240,241,179
ENGEN,1,62,1,240,,,,,1
EPLOT
WSORT
WAVES
D,ALL,UZ
D,1,UX
D,1,ROTZ
D,240,UX
D,240,ROTZ
D,241,ALL,,,302,1
EP,1,2,0.1,,59,1
EP,62,2,0.1,,178,1
EP,182,2,0.1,,239,1
ACEL,,386
WSORT
CNVR,0.0005,,,,,100
SAVE
FINISH
/com start solution process
/SOLU
ANTYP,0
STAT
PSTRES,ON
```

```
TIME,1
NSUBST,2
KBC,0
NCNV,0
NEQIT,20
LSWRITE,1
/com 10 stepes (35 substepes total) from 0 to 1.0 psi
TIME,2
EP,1,2,0.2,,59,1
EP,62,2,0.2,,178,1
EP,182,2,0.2,,239,1
LSWRITE,2
TIME,3
EP,1,2,0.3,,59,1
EP,62,2,0.3,,178,1
EP,182,2,0.3,,239,1
LSWRITE,3
TIME,4
EP,1,2,0.4,,59,1
EP,62,2,0.4,,178,1
EP,182,2,0.4,,239,1
LSWRITE,4
TIME,5
EP,1,2,0.5,,59,1
EP,62,2,0.5,,178,1
EP,182,2,0.5,,239,1
LSWRITE,5
TIME,6
NSUBST,5
EP,1,2,0.6,,59,1
EP,62,2,0.6,,178,1
EP,182,2,0.6,,239,1
LSWRITE,6
TIME,7
EP,1,2,0.7,,59,1
EP,62,2,0.7,,178,1
EP,182,2,0.7,,239,1
LSWRITE,7
TIME,8
EP,1,2,0.8,,59,1
EP,62,2,0.8,,178,1
EP,182,2,0.8,,239,1
LSWRITE,8
TIME,9
EP,1,2,0.9,,59,1
EP,62,2,0.9,,178,1
EP,182,2,0.9,,239,1
LSWRITE,9
TIME,10
EP,1,2,1.0,,59,1
EP,62,2,1.0,,178,1
EP,182,2,1.0,,239,1
LSWRITE,10
LSSOLVE,1,10,1
/FINISH
/POST1
SET,LAST
ETABLE,smer,ls,5
ETABLE,sh,ls,7
ETABLE,se,NMIS,10
PRETAB,GRP1
PRITER
/output,t5510,dat
PRNSOL,U
PRETAB,GRP1
```

```
PRITER
/output
FINISH
```

B.2 Input File for Tank 55

```
/COM This is the input file of the analysis of tank 55
/PREP7
/COM elastic analysis
KAN,0
/COM  large displacement analysis (nonlinear)
KAY,6,1
/COM  stress stiffening included
KAY,8,1
/COM  stiff 51: plastic axisymmetric conical shell
ET,1,51,
/COM  stiff 12: 2-D interface element
ET,2,12,
/COM  thickness of the bottom plate
R,1,0.25
/COM  roof thickness
R,2,0.1875
/COM  the thickness of the bottom part of the shell and top angle
R,3,0.3125
/COM the thickness of the top angle plus top shell
R,4,0.5
/COM the interface element properties
R,   5, ,  388510, ,  1
R,   6, ,  775972.7, ,  1
R,   7, ,  774401.9, ,  1
R,   8, ,  772831.1, ,  1
R,   9, ,  771260.3, ,  1
R,  10, ,  769689.6, ,  1
R,  11, ,  768118.8, ,  1
R,  12, ,  766548, ,  1
R,  13, ,  764977.2, ,  1
R,  14, ,  763406.4, ,  1
R,  15, ,  761835.6, ,  1
R,  16, ,  760264.8, ,  1
R,  17, ,  473987.4, ,  1
R,  18, ,  473005.6, ,  1
R,  19, ,  472023.9, ,  1
R,  20, ,  282546.8, ,  1
R,  21, ,  375420, ,  1
R,  22, ,  373849.2, ,  1
R,  23, ,  372278.4, ,  1
R,  24, ,  370707.6, ,  1
R,  25, ,  369136.8, ,  1
R,  26, ,  367566, ,  1
R,  27, ,  365995.2, ,  1
R,  28, ,  364424.4, ,  1
R,  29, ,  362853.6, ,  1
R,  30, ,  361282.9, ,  1
R,  31, ,  359712.1, ,  1
R,  32, ,  536426.5, ,  1
R,  33, ,  709999.3, ,  1
R,  34, ,  703716.2, ,  1
R,  35, ,  697433, ,  1
R,  36, , 691149.8, ,  1
R,  37, , 684866.6, ,  1
R,  38, , 846920.3, ,  1
R,  39, , 1003738, ,  1
R,  40, ,  989600.9, ,  1
```

```
R,  41, ,  975463.7, ,  1
R,  42, ,  961326.5, ,  1
R,  43, ,  947189.4, ,  1
R,  44, , 1086728, ,  1
R,  45, , 1218937, ,  1
R,  46, , 1193804, ,  1
R,  47, , 1168671, ,  1
R,  48, , 1143539, ,  1
R,  49, , 1118406, ,  1
R,  50, , 1093273, ,  1
R,  51, , 1068141, ,  1
R,  52, , 1043008, ,  1
R,  53, , 1017875, ,  1
R,  54, , 992742.4, ,  1
R,  55, , 967609.7, ,  1
R,  56, , 1172860, ,  1
R,  57, , 1357167, ,  1
R,  58, , 1300618, ,  1
R,  59, , 1244070, ,  1
R,  60, , 1187521, ,  1
R,  61, , 1130972, ,  1
R,  62, , 1074424, ,  1
R,  63, , 1017875, ,  1
R,  64, , 961326.5, ,  1
R,  65, , 904777.9, ,  1
R,  66, , 1195620, ,  1
R,  67, , 1391626, ,  1
R,  68, , 1192822, ,  1
R,  69, ,  994018.7, ,  1
R,  70, ,  795215, ,  1
R,  71, ,  596411.2, ,  1
R,  72, ,  397607.5, ,  1
R,  73, ,  198803.7, ,  1
R,  74, ,  33133.96, ,  1
/COM  the material properties of the plates
MP,EX,1,3e7
MP,NUXY,1,.3
MP,DENS,1,0.000727
/COM  start from the roof, using the API-Tank mesh
N, 1,   0.0, 641.250
N, 9,  91.5, 626.0
FILL
N,19, 151.5, 616.0
FILL
N,31, 199.5, 608.0
FILL
N,43, 229.5, 603.0
FILL
N,55, 241.5, 601.0
FILL
N,66, 247.0, 600.08333
FILL
N,67, 248.5, 600.0
N,72, 246.0, 600.0
FILL
N,73, 246.0, 599.625
N,85, 246.0, 593.625
FILL
N,97, 246.0, 581.625
FILL
N,103, 246.0, 569.625
FILL
N,109, 246.0, 545.625
FILL
N,112, 246.0, 529.0
```

```
FILL
N,122, 246.0, 457.5
FILL
N,132, 246.0, 386.0
FILL
N,142, 246.0, 289.0
FILL
N,152, 246.0, 192.0
FILL
N,162, 246.0, 95.0
FILL
N,169, 246.0, 54.0
FILL
N,175, 246.0, 30.0
FILL
N,181, 246.0, 18.0
FILL
N,193, 246.0, 6.0
FILL
N,204, 246.0, 0.5
FILL
N,205, 247.5, 0.0
N,220, 240.0, 0.0
FILL
N,232, 228.0, 0.0
FILL
N,238, 216.0, 0.0
FILL
N,244, 198.0, 0.0
FILL
N,256, 150.0, 0.0
FILL
N,266, 90.0, 0.0
FILL
N,274, 0.0, 0.0
FILL
/COM  70 interface elements 275 - 344
NGEN,2,70,205,274,1,0.0,0,0.0
NPLOT
MAT,1
REAL,2
TYPE,1
E,1,2
ENGEN,1,65,1,1
EN,66,66,69
REAL, 3
EN,67,67,68
ENGEN,1,6,1,67
REAL,4
EN,73,73,74
/COM ENGEN,IINC,ITIME,NINC,IEL1,IEL2,IEINC,MINC,TINC,RINC,CINC
ENGEN,1,4,1,73
REAL,2
EN,77,77,78
ENGEN,1,55,1,77
/COM thickness 1/4"
REAL,1
EN,132,132,133
ENGEN,1,30,1,132
REAL,3
EN,162,162,163
ENGEN,1,42,1,162
EN,204,204,208
REAL,1
EN,205,205,206
```

```
ENGEN,1,69,1,205
TYPE,2
REAL,5
MAT,2
EN,274,275,205
ENGEN,1,70,1,274,,,,,1
EPLOT
WSORT
WAVES
D,ALL,UZ
D,1,UX
D,1,ROTZ
D,274,UX
D,274,ROTZ
D,275,ALL,,,344,1
EP,1,2,0.1,,66,1
EP,69,2,0.1,,204,1
EP,208,2,0.1,,273,1
ACEL,,386
WSORT
LSWRITE,10  CNVR,0.0005,,,,,100
SAVE
FINISH
/com start solution process
/SOLU
ANTYP,0
STAT
PSTRES,ON
TIME,1
NSUBST,2
KBC,0
NCNV,0
NEQIT,30
LSWRITE,1
TIME,2
NSUBST,2
KBC,0
NCNV,0
NEQIT,25
EP,1,2,0.2,,66,1
EP,69,2,0.2,,204,1
EP,208,2,0.2,,273,1
LSWRITE,2
TIME,3
EP,1,2,0.3,,66,1
EP,69,2,0.3,,204,1
EP,208,2,0.3,,273,1
LSWRITE,3
TIME,4
EP,1,2,0.4,,66,1
EP,69,2,0.4,,204,1
EP,208,2,0.4,,273,1
LSWRITE,4
TIME,5
NSUBST,5
EP,1,2,0.5,,66,1
EP,69,2,0.5,,204,1
EP,208,2,0.5,,273,1
LSWRITE,5
TIME,6
NSUBST,10
EP,1,2,0.6,,66,1
EP,69,2,0.6,,204,1
EP,208,2,0.6,,273,1
LSWRITE,6
```

```
TIME,7
EP,1,2,0.7,,66,1
EP,69,2,0.7,,204,1
EP,208,2,0.7,,273,1
LSWRITE,7
TIME,8
EP,1,2,0.8,,66,1
EP,69,2,0.8,,204,1
EP,208,2,0.8,,273,1
LSWRITE,8
TIME,9
EP,1,2,0.9,,66,1
EP,69,2,0.9,,204,1
EP,208,2,0.9,,273,1
LSWRITE,9
TIME,10
EP,1,2,1.0,,66,1
EP,69,2,1.0,,204,1
EP,208,2,1.0,,273,1
LSWRITE,10
LSSOLVE,1,10,1
/FINISH
```